

# Sheffield Hallam University

*Deposition and characterisation of (Ti,Zr) based hard compound and multi-layer PVD films.*

DOHUE, Lee Adrian.

Available from the Sheffield Hallam University Research Archive (SHURA) at:

<http://shura.shu.ac.uk/19570/>

## A Sheffield Hallam University thesis

This thesis is protected by copyright which belongs to the author.

The content must not be changed in any way or sold commercially in any format or medium without the formal permission of the author.

When referring to this work, full bibliographic details including the author, title, awarding institution and date of the thesis must be given.

Please visit <http://shura.shu.ac.uk/19570/> and <http://shura.shu.ac.uk/information.html> for further details about copyright and re-use permissions.

101 441 778 3



Sheffield Hallam University

**REFERENCE ONLY**

ProQuest Number: 10694451

All rights reserved

INFORMATION TO ALL USERS

The quality of this reproduction is dependent upon the quality of the copy submitted.

In the unlikely event that the author did not send a complete manuscript and there are missing pages, these will be noted. Also, if material had to be removed, a note will indicate the deletion.



ProQuest 10694451

Published by ProQuest LLC (2017). Copyright of the Dissertation is held by the Author.

All rights reserved.

This work is protected against unauthorized copying under Title 17, United States Code  
Microform Edition © ProQuest LLC.

ProQuest LLC.  
789 East Eisenhower Parkway  
P.O. Box 1346  
Ann Arbor, MI 48106 – 1346

**DEPOSITION AND CHARACTERISATION  
OF (Ti,Zr) BASED HARD COMPOUND AND  
MULTI-LAYER PVD FILMS.**

**Lee Adrian Donohue.**

**A thesis submitted in partial fulfilment of the  
requirements of  
Sheffield Hallam University  
for the degree of Doctor of Philosophy.**

**November 1995.**

**Collaborating organisation:  
Hauzer Techno Coating Europe B.V.**

## **ABSTRACT.**

Industrial recognition of the importance of optimising engineering component performance has recently led to a significant increase in the use of surface coating technologies. An important process for the production of such coatings is Physical Vapour Deposition (PVD) which has proved to be a consistent, reliable and improving technique for industry. In the area of advanced wear resistant coatings however, fundamental research to improve deposition efficiency and enhance coating performance has been required. This thesis describes research investigating the following three areas:-

A series of experiments was carried out to study the design, metallurgy and performance of TiZr, ZrMo and TiMo segmented targets for use in steered cathodic arc evaporation and unbalanced magnetron sputter PVD techniques. A hot isostatic pressing technique was used to manufacture a range of prototype targets by diffusion bonding of appropriate metallic segments to controllable depths. In steered arc evaporation trials, a deleterious evaporation phenomenon occurred at segment interfaces when the cathode spot traversed from high vapour pressure to low vapour pressure materials. Analysis of the spot motion has led to the proposal of a simple model. Reactive unbalanced magnetron sputtering trials successfully produced a range of TiZrN, TiMoN and ZrMoN coatings of compositions in good agreement with Monte-Carlo simulation predictions. However, preferential poisoning of the high reactivity metal segments on TiMo and ZrMo targets was found to occur during high N<sub>2</sub> partial pressure processes. A comparative study of unbalanced magnetron sputtering, steered arc evaporation and the hybrid arc-bond sputter technique has been made during deposition trials on the ternary TiZrN hard coating system. Examination of the influence of two process parameters, substrate bias voltage and nitrogen partial pressure, on the mechanical and physical properties of TiZrN coatings is also reported. Stoichiometric TiZrN films were generally found to exhibit a <111> single phase, face centred cubic structure with lattice parameters which followed Vegard's law. Alteration of the elemental composition of the alloy could be achieved by altering the power to individual magnetron cathodes or varying the current of the arc discharge during co-deposition. Solid solution strengthening mechanisms produced high hardness values (2500-3600H<sub>k</sub>) which maximised as the alloy composition approached Ti<sub>0.6</sub>Zr<sub>0.4</sub>. Further studies have been undertaken where Al was partially substituted for Zr within the lattice to enhance oxidation resistance properties and a range of fully adherent TiAlZrN quaternary films on high speed steel substrates were produced. The development of an original technique for industrial scale fabrication of a range of hard, low period (<150Å) multi-layer PVD thin films is outlined and the effects of substrate rotation velocity, type of rotation (1-fold or 3-fold) and deposition rate have been investigated. The high level of lattice mis-match and substantial differences in dislocation line energy and shear modulus has given rise to TiAlN-ZrN films exhibiting Knoop micro-hardness in excess of 4000H<sub>k</sub>. Bulk and micro-analysis techniques have indicated a reproducible lamella coating structure can be formed, with accurate control of the layer period. Excellent levels of coating adhesion were implemented by a metal ion etch substrate pre-treatment and the deposition of a sputtered base layer and films exhibited relatively low surface roughness and high density. A coating strategy, based upon the reactivity of the individual target materials and the characteristics of arc evaporated and magnetron sputtered vapour fluxes, has been determined which provides high flexibility in the coating elemental composition. The investigations clearly indicate that the multi-layer coating methods utilised allow the deposition of 3rd generation films without a productivity loss in comparison to 1st generation and 2nd generation hard coatings.

## ADVANCED STUDIES.

As part of the course of study I attended the following conferences and workshops combined with a number of informal research seminars presented at Sheffield Hallam University by academic staff from the Materials Research Institute and the Division of Applied Physics.

- *"3rd International Conference on Advances in Coatings and Surface Engineering for Corrosion and Wear Resistance"*, May 1992, Newcastle Polytechnic.
- *"Hard Coatings by PVD Methods and Evaluation Techniques Workshop"*, October 1992, Sheffield Hallam University.
- *"21st International Conference on Metallurgical Coatings and Thin Films"*, April 1993, San Diego, California, United States of America.
- *"International Conference on Advanced Materials and Processing Technologies"*, August 1993, Dublin City University, Dublin, Eire.
- *"22nd International Conference on Metallurgical Coatings and Thin Films"*, April 1994, San Diego, California, United States of America.
- *"4th International Conference on Plasma Surface Engineering"*, October 1994, Garmisch-Partenkirchen, Germany,
- *"3rd European Workshop on Plasma Surface Engineering"*, June 1995, Wurzburg, Germany.
- *"International Conference on Advanced Materials and Processing Technologies"*, August 1995, Dublin City University, Dublin, Eire.

## PUBLICATIONS.

*"Design and performance of a hot isostatically pressed Ti-Zr segmented cathode for electromagnetically steered arc physical vapour deposition".*

L.A.Donohue, J.Cawley, J.S.Brooks - Surface and Coating Technology, 63, 1994, 49-56. Presented at ICMCTF-93, San Diego, California, USA, April 1993 and The Iron and Steel Institute of Japan, Tokyo, 1993.

*"Fabrication and Performance of novel segmented cathodes for arc evaporative and magnetron sputter physical vapour deposition".*

J.Cawley, L.A.Donohue, J.S.Brooks - Presented at AMPT-93, Dublin, Eire, August 1993.

*"Design and assessment of segmented targets in PVD".*

L.A.Donohue, J.Cawley, J.S.Brooks - Poster presented at EAST conference, Schwäbisch Gmünd, F.R.G, 1993.

*"Deposition and characterisation of Arc-Bond Sputter TiZrN coatings from pure metallic and segmented targets".*

L.A.Donohue, J.Cawley, J.S.Brooks - Surface and Coating Technology, 72, 1995, 128-138. Presented at ICMCTF-94, San Diego, California, USA, April 1994.

*"Deposition and characterisation of TiAlZrN films produced by a combined steered arc and unbalanced magnetron sputtering technique".*

L.A.Donohue, J.Cawley, J.S.Brooks, W-D.Münz - Surface and Coating Technology, 74-75, 1995, 123. Presented at Plasma Surface Engineering-94, Garmisch-Partenkirchen, F.R.G, 1994 and the satellite meeting of LCS-94, Ehime University, Matsuyama, Japan, 1994.

*"Investigation of superlattice coatings deposited by a combined steered arc evaporation and unbalanced magnetron sputtering technique".*

L.A.Donohue, J.Cawley, D.B.Lewis, J.S.Brooks, W-D.Münz - In press Surface and Coating Technology. Presented at ICMCTF-95, San Diego, California, USA, April 1995.

*"Large scale fabrication of hard superlattice thin films by combined steered arc evaporation and unbalanced magnetron sputtering".*

L.A.Donohue, W-D.Münz, J.Cawley, T.Hurkmans, T.Trinh, I.Petrov, J.E.Greene - Presented at 3rd European Workshop on Plasma Surface Engineering, Wurzburg, Germany, June 1995. In press Surface and Coatings Technology.

*"Characterisation of TiAlN-ZrN superlattice thin films produced by variable PVD deposition regimes".*

J.Cawley, L.A.Donohue, J.M.Titchmarsh, W-D.Münz, G.E.Gregory - Presented at AMPT-95, Dublin City University, Dublin , Eire, August 1995. In press Surface and Coatings Technology.

## ACKNOWLEDGEMENTS.

The author would like to sincerely thank the following people and collaborating establishments for their helpful discussions and advice during the period of study:

- Dr J.Cawley, Professor J.S.Brooks, Professor W-D.Münz & the staff of the Materials Research Institute, Sheffield Hallam University, United Kingdom.
- T.Hurkmans & T.Trinh - Hauzer Techno Coating Europe B.V, Venlo, Netherlands.
- Dr H.Jehn, Dr B.Rother, H.Kappl & staff - Forschungsinstitut für Edelmetalle und Metallchemie, Schwäbisch-Gmünd, F.R.G.
- Deutscher Akademischer Austauschdienst (DAAD), Bonn, F.R.G.
- Professor Allan Matthews & staff - Research Centre for Surface Engineering, Hull University, United Kingdom.
- Dr Sue King - H.I.P. Infutec Ltd, Chesterfield, United Kingdom
- Atomic Energy Authority, Harwell, Oxford, United Kingdom.
- The Department of Metallurgy, University of Sheffield, United Kingdom.
- Dr Ivan Petrov - University of Illinois at Urbana-Champaign, Urbana, USA.
- IBM Research, Yorktown Heights, New York, USA.
- Dr M.Ives, Dr C.Blomfield (The lads at 157), Dr P.Walke and the rest of the MRI and Physics research students - For the laughter and entertainment they have provided throughout the years.
- Higher Education Funding Council England (HEFCE) for funding this project.

Finally, I would like to thank my mother, father & family for their constant and selfless support and motivation throughout the highs and lows of my education and research.

# CONTENTS

## **Chapter One: Introduction.....1**

- 1.1. Surface engineering.
- 1.2. Physical vapour deposition (PVD).
- 1.3. PVD hard coating developments.
- 1.4. Present work.

## **Chapter Two: Literature Review.....9**

- 2.1. Sputtering techniques.
  - 2.1.1. Sputtering processes and energetic particle interactions.
  - 2.1.2. D.C. diode sputtering - the self-sustained glow discharge.
  - 2.1.3. Glow discharge characteristics.
  - 2.1.4. D.C. triode sputtering
  - 2.1.5. Magnetron enhanced sputtering.
  - 2.1.6. The unbalanced magnetron.
  - 2.1.7. Multi-cathode systems and closed field geometry.
  - 2.1.8. Reactive sputtering.
- 2.2. Arc evaporation techniques.
  - 2.2.1. The random cathodic arc.
  - 2.2.2. The cathode spot life cycle.
  - 2.2.3. The types of cathode spot.
  - 2.2.4. The spot diameter and current density.
  - 2.2.5. Spot splitting.
  - 2.2.6. The types of erosion
  - 2.2.7. The random spot motion.
  - 2.2.8. The steered arc.
  - 2.2.9. The filtered arc.
  - 2.2.10. Arc evaporation of multi-elemental targets.
- 2.3. The Arc-Bond Sputter (ABS™) technique.

- 2.4. Film deposition.
  - 2.4.1. Nucleation and growth mechanisms.
  - 2.4.2. Structure zone models and film microstructure.
  - 2.4.3. Ar<sup>+</sup>sputter etching and metallic interlayers.
  - 2.4.4. Bias edge effects.
  - 2.4.5. Residual stress.
- 2.5. Coating Systems.
  - 2.5.1. First generation of PVD hard coatings.
  - 2.5.2. Second generation of PVD hard coatings.
  - 2.5.3. Third generation of PVD hard coatings.
- 2.6. Summary.

**Chapter Three: Experimental.....67**

- 3.1. Physical vapour deposition equipment.
  - 3.1.1. The electromagnetic steered arc evaporation PVD unit.
  - 3.1.2. The unbalanced magnetron sputter PVD unit.
  - 3.1.3. The arc-bond sputter PVD unit.
- 3.2. Target manufacturing technique.
- 3.3. Sample preparation for coating.
- 3.4. Sample preparation techniques for analysis.
  - 3.4.1. Scanning electron microscopy fracture cross-sections.
  - 3.4.2. Transmission electron microscope coating cross-sections.
- 3.5. Characterisation techniques.
  - 3.5.1. X-ray diffraction.
  - 3.5.2. Scanning electron microscopy.
  - 3.5.3. Transmission electron microscopy.
  - 3.5.4. Glow discharge optical emission spectroscopy (GDOES).
  - 3.5.5. Vickers hardness test.
  - 3.5.6. Knoop microhardness test.
  - 3.5.7. Coating thickness Calotest.

- 3.5.8. Scratch adhesion testing.
- 3.5.9. Rockwell indentation adhesion testing.
- 3.5.10. Colourimetry.
- 3.5.11. Surface roughness profiling.

3.6. Summary of equipment and techniques.

**Chapter Four: Investigation of TiZr, TiMo & ZrMo segmented targets.....104**

4.1. TiZr Model alloy investigations.

- 4.1.1. Alloy manufacture, preparation and equilibrium studies.
- 4.1.2. Results of 20%Ti / 80%Zr alloy investigations.
- 4.1.3. Results of 50%Ti / 50%Zr alloy investigations.
- 4.1.4. Results of 80%Ti / 20%Zr alloy investigations.

4.2. Mechanical and physical properties of TiZr, TiMo and ZrMo segmented targets.

- 4.2.1. X-ray diffraction results.
- 4.2.2. Microstructural analysis.
- 4.2.3. Interfacial microscopy.
- 4.2.4. Interfacial diffusion analysis by X-ray line-scanning.
- 4.2.5. Hardness measurements.

4.3. Segmented target performance in steered arc evaporation trials.

- 4.3.1. TiZr target performance.
- 4.3.2. TiMo target performance.
- 4.3.3. ZrMo target performance.

4.4. Simulation of segmented target sputter and ion etching performance.

- 4.4.1. Sputter yields and ion ranges.
- 4.4.2. Simulation of substrate ion etching.
- 4.4.3. Simulation of substrate sputter coating.
- 4.4.4. Simulation of substrate arc coating.

4.5. Target performance in unbalanced magnetron sputtering trials.

- 4.5.1. The influence of preferential target poisoning.

- 4.5.2. Mechanical and physical properties of TiMoN and ZrMoN ternary coatings.
- 4.5.3. Flux distribution analysis

**Chapter Five: Investigation of the TiZrN system.....147**

- 5.1. Examination of  $Ti_xZr_yN$  coatings deposited by SCAE, UBM and ABS techniques.
  - 5.1.1. X-ray diffraction results.
  - 5.1.2. GDOES results.
  - 5.1.3. Scanning electron microscopy results.
  - 5.1.4. Mechanical and physical properties.
  
- 5.2. Parameter study.
  - 5.2.1. X-ray diffraction results.
  - 5.2.2. GDOES results.
  - 5.2.3. Scanning electron microscopy results.
  - 5.2.4. Mechanical and physical properties.
  
- 5.3. Investigation of the TiAlZrN system.
  - 5.3.1. Experimental conditions.
  - 5.3.2. X-ray diffraction results.
  - 5.3.3. GDOES results.
  - 5.3.4. Scanning electron microscopy results.
  - 5.3.5. Mechanical and physical properties.

**Chapter Six: Growth and characterisation of TiAlN-ZrN and TiAlN-TiN multi-layer thin films.....197**

- 6.1. Multi-layer process conditions.
  
- 6.2. The effect of rotation velocity and type of rotation on TiAlN-ZrN multi-layer films.
  - 6.2.1. X-ray diffraction results.
  - 6.2.2. GDOES results.
  - 6.2.3. Scanning electron microscopy results.
  - 6.2.4. Transmission electron microscopy results.

- 6.2.5. Knoop micro-hardness results.
- 6.2.6. Surface roughness results.
- 6.2.7. Thickness and deposition rate.
- 6.2.8. Rockwell and scratch adhesion results.
- 6.2.9. Colour measurements.
  
- 6.3. The effect of arc current on the period of TiAlN-ZrN multi-layer films.
  - 6.3.1. X-ray diffraction results.
  - 6.3.2. GDOES analysis.
  - 6.3.3. Mechanical and physical properties.
  
- 6.4. The deposition and properties of arc / magnetron TiAlN-TiN coatings.
  - 6.4.1. X-ray diffraction results.
  - 6.4.2. GDOES analysis.
  - 6.4.3. Mechanical and physical properties.
  
- 6.5. Multi-layer fabrication by co-sputter deposition without combined steered arc evaporation.
  - 6.5.1. X-ray diffraction results.
  - 6.5.2. GDOES analysis.
  - 6.5.3. Mechanical and physical properties.
  
- 6.6. Bias current measurements.
  
- 6.7. Modelling of the substrate rotation and coating flux density.

**Chapter Seven: Discussion and conclusions .....241**

- 7.1. The fabrication and performance of segmented targets.
- 7.2. The TiZrN system.
- 7.3. The growth and characterisation of pseudo-ceramic multi-layer thin films.

7.4. Conclusions.

7.5. Further work.

**Appendix 1. ABS coating flux density and substrate rotation model.....258**

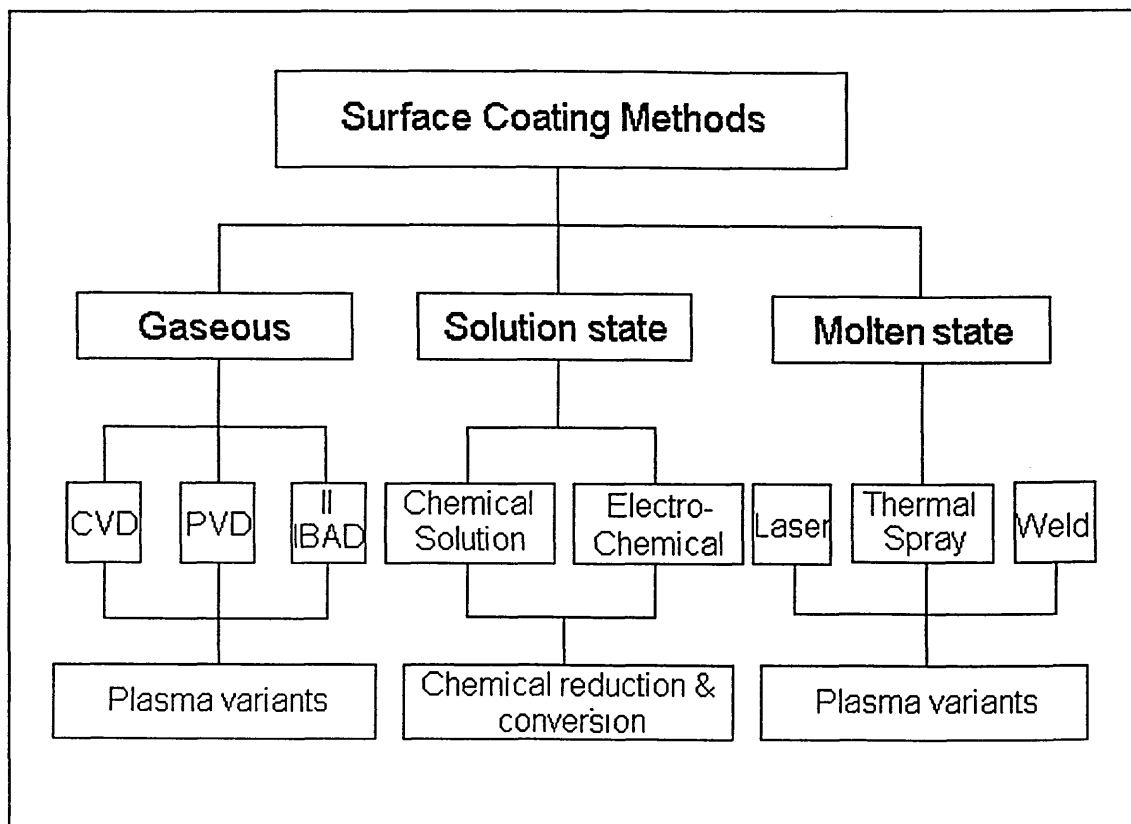
# **CHAPTER ONE**

## **INTRODUCTION.**

### **1.1. Surface engineering.**

The demands from industry to produce components capable of operating in extreme working environments with high performance and enhanced efficiency has provided a large increase in the research and development of surface engineering techniques. Most surface engineering methods rely on the fabrication of a composite system (i.e. thin coating deposited on a substrate) to cause a surface modification which improves the engineering performance to a level which cannot be achieved by either the coating or substrate alone (1). However, some techniques create improved component properties and greater longevity by physical alteration of its surface through diffusion, substitution or implantation of extrinsic atoms to controllable matrix depths. Other methods cause substrate hard-facing through various spraying and welding treatments, whilst many processes utilise a mechanical approach (shot-peening and polishing) to improve wear properties and enhance repair efficiency. This large number of surface engineering methods can be categorised by 3 broad generic surface engineering groups (figure 1.1).

Figure 1.1 The surface engineering generic groups



The diversity of well proven, so-called "wet" surface engineering treatments currently being utilised by industry is vast, ranging from simple painting techniques to more complex electro-plating and salt bath nitriding methods. These traditional techniques have been intensively studied since the early 1900's and exhibit high reproducibility and excellent reliability. However, the wet methods are restricted in the types of coatings they can deposit and can suffer from serious environmental problems.

The last 30 years has seen the emergence of "dry" advanced surface engineering techniques many of which extensively utilise plasmas to deposit coatings. Most of these techniques have their origins in the semi-conductor and micro-electronics industries where accurate control of the coating composition and growth rate is critical. Nearly all dry methods involve treatment under vacuum conditions in the presence of inert and / or reactive gases and are characterised by high versatility and flexibility in the processing conditions and materials which can be applied.

The applications of surface engineering coatings to industrial components has now become widespread (2) ranging from high technology operations in the compact disc and aeronautics industries to low technology processes such as the decoration of watch cases and glasses frames. Coatings are routinely used as thermal barriers on gas turbine blades and provide erosion, abrasion, corrosion and oxidation resistance to a wide variety of cutting and forming tools. Anti-reflective coatings are used as filters on many optical devices and thin films have also been produced for their superconducting properties.

A key dry surface engineering technique showing outstanding scientific and commercial potential in the coating of industrial components is physical vapour deposition (PVD) and will be discussed in greater detail.

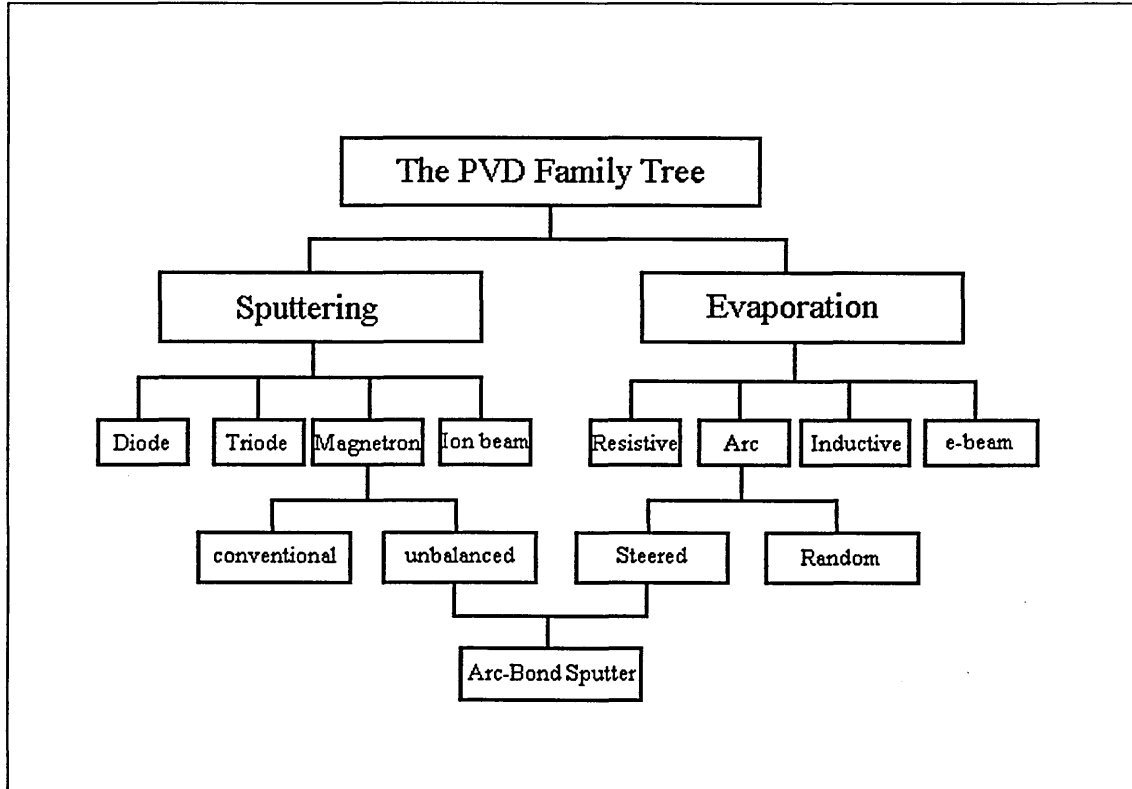
### 1.2. Physical vapour deposition.

The term physical vapour deposition (PVD) covers a multitude of techniques which have the common feature of processing under partial vacuum conditions where at least one of the coating species is atomised from the solid state within a chamber. Generally these methods are plasma assisted and capable of processing at relatively low temperatures (150-500°C), allowing the deposition of metals, alloys, ceramics and non-conducting (radio frequency) coatings to a wide variety of temperature sensitive substrates. PVD techniques allow unprecedented control of the coating-substrate interface and an ability to tailor the coating characteristics (i.e. thickness, micro-

structure and composition) to fine tolerances. Two main deposition methods can be used, sputtering (3-6) or evaporation (7-10) (figure 1.2).

Sputter PVD is a process in which the atomisation of coating material is achieved by energetic bombardment of the surface of a solid target with ions or neutral particles. Collisions between the incoming particles and the atoms in the near surface layers of a solid cause complex momentum transfer and the possibility of atomic ejection.

Figure 1.2. The PVD family tree.



Evaporative PVD is a process in which coating material is produced by either resistive heating, inductive heating, the application of an electron beam or the controlled interaction of an electric arc with a solid to create joule heating and subsequent evaporation and liberation of metal species into the vapour phase.

Recently efforts have been made to combine the steered arc evaporation and unbalanced magnetron sputtering cathode arrangements into a single assembly, resulting in the unification of the PVD family tree with the development of Arc-Bond Sputter (ABS™) PVD (11).

Generally, ion or electron beam evaporation takes place under high vacuum conditions ( $<10^{-5}$  mbar) whilst arc evaporation and magnetron sputtering techniques utilise inert (Ar) and / or reactive gases ( $N_2$ ) to back-fill the chamber to a total pressure of around  $10^{-3}$  mbar. A negative bias voltage (50-200V) is typically applied to the substrate during coating, to cause positive ions (usually  $Ar^+$ ) to be accelerated towards the growing film and provide an enhancement in the surface mobility of adatoms, densification of the film micro-structure and a decrease in the level of film roughness.

This thesis will concentrate on the theory, practical arrangement and utilisation of three of the PVD techniques - steered arc evaporation, unbalanced magnetron sputtering and arc-bond sputtering.

### 1.3. PVD hard coating developments.

The first generation of PVD hard coatings has been extensively studied since the early 1980's and their utilisation in industrial applications has become widespread. This class of coating is characterised by the binary pseudo-ceramic (metal / non-metal compound) materials such as TiN (12), TiC (13) and  $TiB_2$ (14). Most early PVD fundamental research and applications have centred around the properties and characteristics of the TiN system due to its high hardness, excellent wear resistance and gold colour. However, interest was quick to spread to the deposition of other transition and refractory metal systems combined with a wide variety of reactive gases ( $CH_4$ ,  $N_2$ , and  $O_2$ ). Further developments in coating technology started to occur during 1986 with the introduction of multi-component materials, now considered to be the second generation of PVD hard coatings. Ternary and quaternary (15) films were produced by the addition of further metal elements to the binary systems to form substitutional alloy nitrides and carbides, or by the mixing of reactive gases ( $N_2$  &  $CH_4$ ) to produce metal carbo-nitride films. Research has demonstrated that the use of coatings such as  $TiAlN$  (16) or  $TiCN$  (17) can produce greater improvements in the engineering performance of a broad range of components when compared against the binary systems due to superior hardness, oxidation and wear resistance properties. However, problems have been encountered during the deposition of multi-elemental films in various PVD techniques. Reactive sputtering systems can suffer from target cross-contamination, large differences in sputter yields and preferential target poisoning. Evaporation techniques can suffer from preferential erosion problems, differences in evaporation rates and "spitting".

The latest development in PVD hard coating technology is the production of multi-layer and superlattice thin films (18-20) and is considered to be the third generation. This type of coating can be fabricated in two different classes:

- Metal / ceramic multilayers produced by reactive gas partial pressure control - e.g. Ti/TiN.
- Ceramic / ceramic multilayers produced by reactive co-deposition of different target materials - e.g. TiN/ZrN.

The academic and commercial interest of this type of film lies in their considerably enhanced mechanical and physical properties and crack deflection mechanisms. However, the present level of understanding in third generation coatings is deficient and industrial scale deposition is still commercially unavailable.

Other emerging coating groups currently under investigation include the superhard (hardness ranging from 5000-10000H<sub>v</sub>) and low friction coatings. Examples of the superhard class of coatings are diamond, diamond like carbon (DLC), cubic boron nitride (cBN) and carbon nitride films (CN), whilst MoS<sub>2</sub> and Si<sub>3</sub>N<sub>4</sub> films show excellent tribological properties.

#### 1.4. Present work.

At present, knowledge and understanding of the production and characteristics of second and third generation coating systems is far from complete. Arc evaporation systems suffer from preferential erosion problems during the deposition of multi-elemental coatings and provide inefficient utilisation of the target materials. One suggested method to overcome some of the evaporation problems is the use of a segmented target consisting of concentric circular sections into which a cathodic arc may be steered by use of a suitable magnetic arrangement (21-23). The use of a segmented target in sputter PVD may also be a cost effective method for studying preferential poisoning mechanisms prevalent in co-deposition systems.

Fundamental investigation of simple ternary and quaternary coating systems produced by various sputtering and evaporation techniques is also necessary to gain a detailed understanding of the physical processes developing during deposition and their relationships with coating properties.

The recent development of Arc-bond sputter PVD technology has led to a capability to independently coat by both the steered arc evaporation and unbalanced magnetron sputtering techniques. This uniquely allows the combination of two different line-of-sight PVD techniques during a single process and may provide a method for the deposition of low period multi-layer coatings at industrial scale.

Thus, the following three areas were identified in which further research was required:

- (i) Fundamental studies on the fabrication and performance of multi-elemental segmented targets in arc evaporation and magnetron sputtering. Specifically to investigate the cathode spot motion across dissimilar metal junctions and examine deformation and interfacial phenomena occurring during steered arc evaporation. Analysis of preferential segmented target poisoning in reactive sputter processes and investigation of the advanced PVD coating properties.
- (ii) Critical examination of the second generation  $Ti_xZr_yN$  ternary coating system deposited by unbalanced magnetron sputtering, steered arc evaporation and arc-bond sputter PVD. Study of the production and characteristics of arc-bond sputter  $Ti_xZr_yN$  coatings modified by the addition of Al.
- (iii) Development and investigation of a new industrial scale combined arc evaporation / unbalanced magnetron sputter technique for the deposition of third generation superlattice coatings. Analysis of the relationships between substrate rotation velocity, fold of rotation, superlattice period and the mechanical and physical properties of  $TiAlN-ZrN$  and  $TiAlN-TiN$  coatings.

This thesis describes work performed in these areas and consists of a further 7 chapters :

- Chapter 2 reviews experimental results and theoretical models obtained from literature and surveys developments in steered and random arc evaporation, conventional and unbalanced magnetron sputtering and advanced coating systems.
- Chapter 3 reviews the experimental techniques employed and a detailed description of the experimental apparatus.

- Chapter 4 consists of experimental work performed on fabrication and performance analysis of segmented targets. This chapter includes results from investigations of target phenomena and coating properties during steered arc and unbalanced magnetron sputter deposition trials.
- Chapter 5 consists of experimental work performed during critical examination of the  $Ti_xZr_yN$  coating system deposited by arc-bond sputter (ABS<sup>TM</sup>), steered arc and unbalanced magnetron sputter PVD. The influence of aluminium substitution in the  $Ti_xZr_yN$  coating lattice and the mechanical and physical properties of the film is also considered.
- Chapter 6 contains a description of a new industrial scale technique for the deposition of superlattice thin films by combined steered arc evaporation and unbalanced magnetron sputtering. This chapter presents results on the mechanical and physical properties of TiAlN-ZrN and TiAlN-TiN superlattice films and the influence of planetary rotation velocity and the type of rotation on the superlattice period.
- Chapter 7 contains a discussion of the literature reviewed and experimental work reported in this thesis. This chapter also defines the major conclusions from the investigations and makes suggestions of relevant areas for further work.

## References.

1. D.S.Rickerby, A.Matthews - "*Advanced Surface Engineering*", 1991, Blackie Press.
2. A.Matthews, R.J.Artley, P.Holliday, P.Stevenson - "*The UK Engineering Coatings Industry in 2005*", Department of Trade and Industry / University of Hull, August 1992.
3. B.N.Chapman - "*Glow Discharge Processes*", 1980, Wiley Interscience Press.
4. J.Musil, S.Kadlec, J.Vyskocil, V.Poulek - *Surf.Coat.Tech*, 1989, 39-40, 301-314.
5. U.König - *Surf.Coat.Tech*, 1987, 33, 91-103.
6. J.L.Vossen, W.Kern - "*Thin Film Processes*", 1978, Academic Press.
7. G.Ecker - "*Vacuum Arcs - Theory and Application*", 1980, Wiley Interscience Press.
8. E.Ertürk, O.Knotek, W.Burgmer, H.-G.Prenzel, H.-J.Heuvel, H.G.Dederichs, C.Stössel - *Surf.Coat.Tech*, 1991, 46, 1, 39-46.
9. P.D.Swift, D.R.Mckenzie, I.S.Falconer - *J.Appl.Phys*, 1989, 66(2), 505.
10. H.K.Pulker - "*Coatings on Glass*", 1984, Elsevier Press.
11. W-D.Münz, F.J.M.Hauzer, D.Schulze, B.Buil - *Surf.Coat.Tech*, 1991, 49, 161.
12. W.D.Sproul, P.J.Rudnik, M.E.Graham - *Surf.Coat.Tech*, 1989, 39/40, 355-363.
13. P.A.Steinmann, H.E.Hintermann - *J.Vac.Sci.Technol*, 1985, A3(6), 2394-2400.
14. O.Knotek, F.Löffler, M.Böhmer, R.Breidenbach, C.Stöbel - *Surf.Coat.Tech*, 1991, 49, 263-267.
15. O.Knotek, W-D.Münz, T.Leyendecker - *J.Vac.Sci.Technol*, 1987, A5(4), 2173-2179.
16. W-D.Münz - *J.Vac.Sci.Technol*, 1986, A4(6), 2717-2725.
17. E.Damond, P.Jacquot, J.Pagny - *Materials Science and Engineering*, 1991, A140, 838-841.
18. S.A.Barnett - "*Physics of thin films*", 1993, 17, 1-77, Academic Press.
19. H.Holleck, M.Lahres, P.Woll - *Surf.Coat.Tech*, 1990, 41, 179.
20. X.Chu, M.S.Wong, W.D.Sproul, S.L.Rohde, S.A.Barnett - *J.Vac.Sci.Technol*, 1992, A10(4), 1604-1609.
21. P.Jewsbury, S.Ramalingam, R.F.Chang - *Proc. Eng.Mat.Adv.Friction and Wear App.Conf*, 1988, 107.
22. A.I.Bushik, B.Jüttner, H.Pursch, V.A.Shilov - *Akademie der Wissenschaften der DDR, Zentralinstitut für Elektronenphysik Preprint 83-1*, 1983, 1-38.
23. V.A.Batalin, Y.N.Volkov, T.V.Kulevoi, S.V.Petrenko - *Instrumental and Experimental Techniques*, 1992, 35(6), 1108-1110.

## CHAPTER TWO

### LITERATURE REVIEW.

#### 2.1. Sputtering Techniques.

##### 2.1.1. Sputtering processes and energetic particle interactions.

Sputtering is the removal of atomised material from a solid due to energetic bombardment of its surface layers by ions or neutral particles (1). The phenomenon was first discovered by W.R.Grove (2) in 1842, who noticed the build up of a metallic deposit on the glass walls of a discharge tube. However, it took an additional 50 years before the physical process involved in sputtering was recognised (3) and another 100 years for a quantitative description of the sputtering events to be developed (4-7).

Generally, an incoming particle will collide with atoms at the surface of a solid causing an energy transfer to the atomic nuclei such that :

$$T = \frac{4 m_i m_t}{(m_i + m_t)^2} E_0 \sin^2 \frac{\Theta}{2} \quad \text{.....equation 2.1}$$

where T = Energy transfer function for a binary collision.

$m_i$  and  $m_t$  = Masses of the incident and target atoms.

$\Theta$  = Projectile scattering angle.

$E_0$  = Initial energy of the atom.

If more energy is transferred than the binding energy at a lattice site, primary recoil atoms may be created which can collide with other target atoms and distribute their energy via a collision cascade. A surface atom becomes sputtered if the energy transferred to it normal to the surface is larger than the surface binding energy (approximately equal to the heat of sublimation).

The ability of a material to be sputtered is measured by a quantity known as the sputtering yield (Y). This may be simply defined as the mean number of atoms removed per incident particle:

$$Y = \frac{\text{No. of atoms removed}}{\text{No. of incident particles}} \quad \text{.....equation 2.2.}$$

The yield is dependent not only on the characteristics of the target material, but also on the incident angle, ion energy and ion mass and may be approximated (8), assuming normal incidence, using the equation;

$$Y = \frac{3E_t \alpha E_i}{4\pi^2 U_0} \dots \text{equation 2.3.}$$

where  $E_t$  = Energy transferred in a binary collision.

$\alpha$  = Function of the colliding atomic masses.

$U_0$  = Surface binding energy of the target.

$E_i$  = Energy of the incident ion.

The importance and measurement of the sputtering yield was first recognised around 125 years ago (9) and has been the subject of investigation ever since (10). Whilst the variation in sputtering yield can be as much as one order of magnitude, it is considerably lower than variations in the evaporative yields from solid and liquid sources, which often reach several orders of magnitude (11,12) and evaporation techniques generally provide higher deposition rates. However, sputter processes provide a number of key advantages over evaporative processing techniques including:-

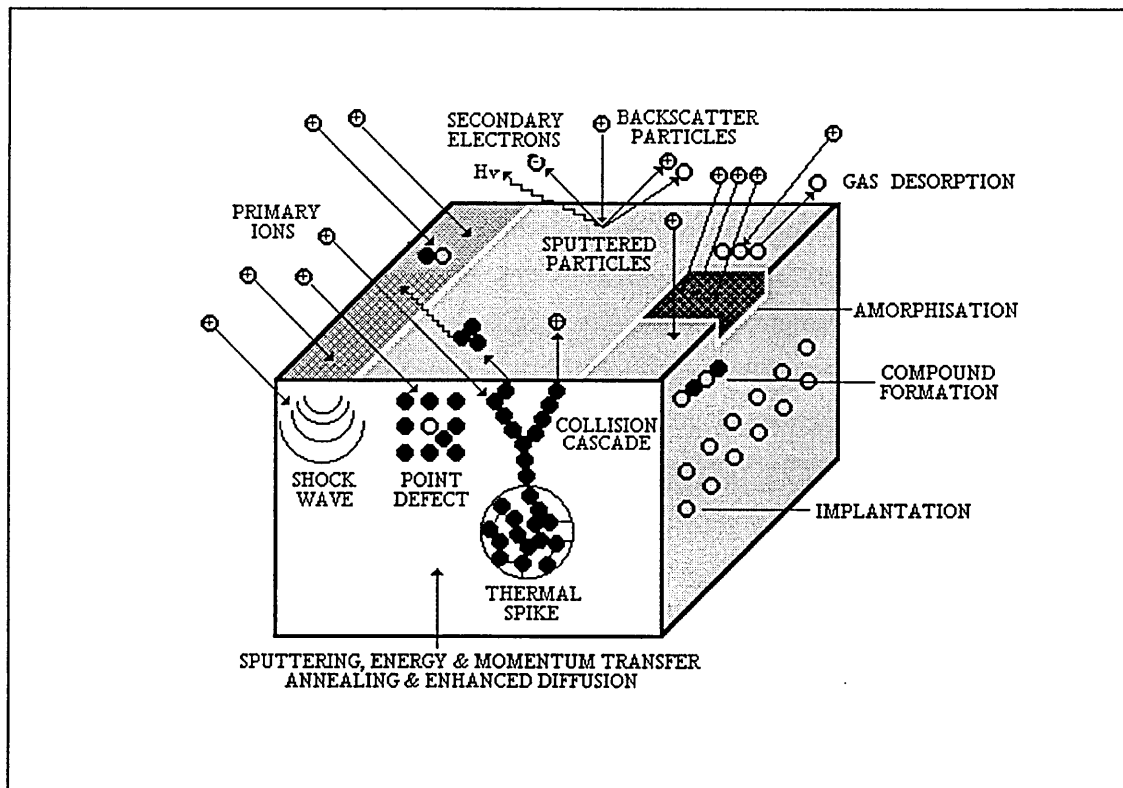
- (1) Higher thickness uniformity.
- (2) Deposition of a wide variety of materials.
- (3) Smooth films (no spitting or macro-particle formation).
- (4) Large target areas.

The sputtering process has almost no restrictions in the target materials which can be used, ranging from pure metals (d.c power supply) to semi-conductors and insulators (r.f.power supply). Deposition can be carried out in either non-reactive (inert gases only) or reactive discharges (inert & reactive gases) with single or multi-elemental target materials, allowing an extension of the possible combinations and compositions of coatings even further. For more detailed aspects of sputter processing the reader is referred to a series of excellent reviews (13-16) and the later sections of this thesis (section 2.1.2-2.1.4).

It is important to note that a wide range of other physical interaction events (figure 2.1) at the target surface can be caused by energetic particle bombardment (16).

Possible particle ejection events include liberation of neutral atoms, backscattering, X-ray emission, photon generation, secondary electron emission and desorption of gas atoms. Processes within the target itself include amorphisation, implantation, compound formation, localised heating and the creation of point defects.

Figure 2.1. Interaction events due to energetic particle bombardment.



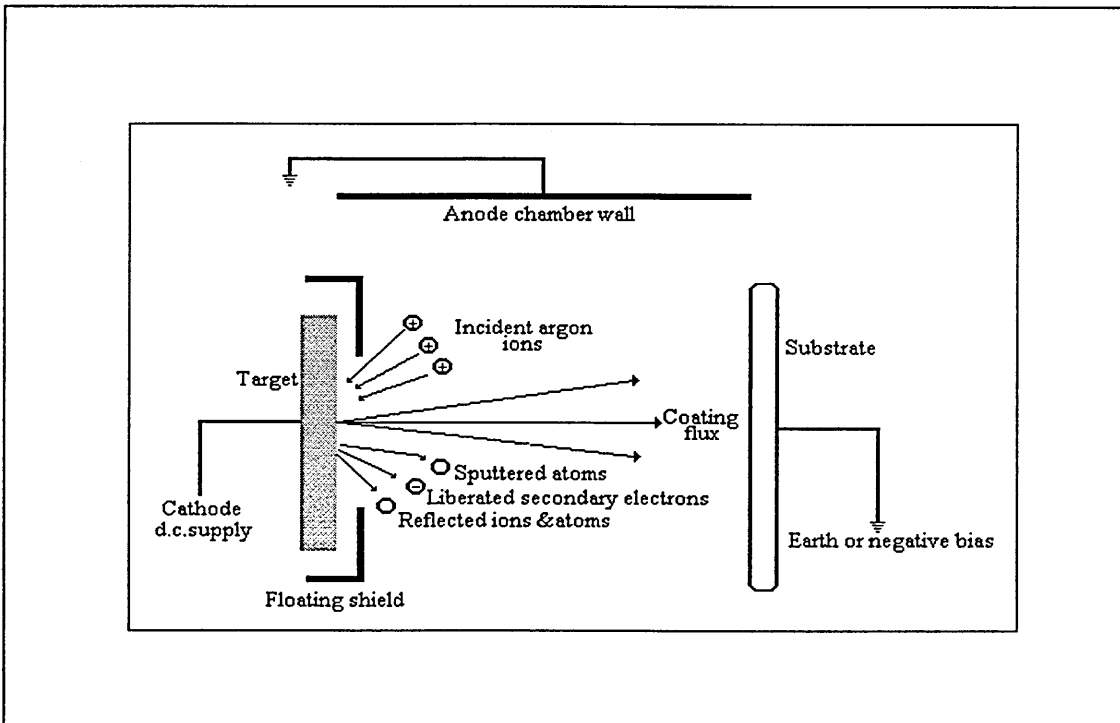
A number of important processes utilising sputtering and secondary electron emission mechanisms have evolved to deposit thin films and these will be described in greater detail.

### 2.1.2. D.C.Diode sputtering - The self sustained glow discharge.

The direct current diode sputtering arrangement is the oldest and most common of the sputtering techniques (17,18). The diode plasma, known as a "glow discharge" (19), can be formed in a vacuum chamber when a sufficiently large potential (~300-5000V) is applied between an anode / cathode pair of electrodes in the presence of an inert gas (figure 2.2). A small proportion of the gas will be naturally ionised and accelerated towards the cathode (comprising a solid "target" of the material to be deposited) and electrons towards the anode (vacuum chamber wall) .

When the accelerated ions reach the target they undergo charge-exchange collisions and lose most of their energy in the form of heat. Momentum is transferred to atoms in the near surface region of the target and creates collision cascades which can cause the ejection of target atoms.

Figure 2.2. Schematic of d.c.diode sputtering.



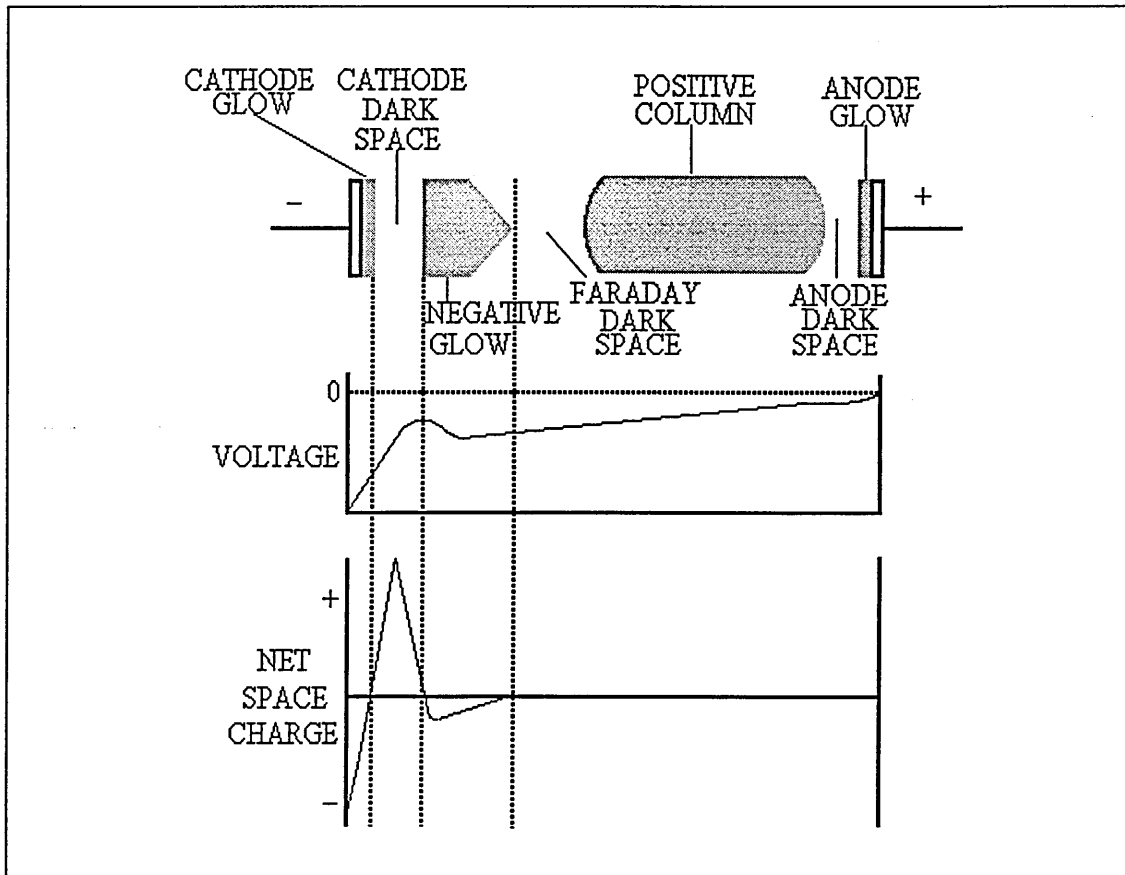
Another consequence of the ion bombardment is the liberation of secondary electrons from the target which are attracted towards the walls of the vacuum chamber, causing further ionisation events and dissociation and excitation of the argon atoms. Hence a closed circuit is formed and the glow discharge can be made to self-sustain.

The number of secondary electrons emitted per incident ion is termed the "secondary electron yield" and in sputtering processes is typically of the order of 0.1 (16). Combined with the low kinetic energy of sputtered particles (~5-20eV), the high percentage of neutrals created by sputtering (>90%) and the poor ratio of energy transferred by incident ions to the number of sputtered particles ejected (~1%) (20,21), the diode sputtering process is clearly very inefficient. However, a number of methods to improve the performance of sputtering, based on diode techniques, have recently been developed and will be discussed in sections 2.1.4 to 2.1.6.

### 2.1.3. Glow discharge characteristics.

Several distinct regions exist within a d.c.diode glow discharge plasma and their classical architecture is defined in figure 2.3. Directly next to the cathode is the cathode glow region which is highly luminous due to positive and negative ion neutralisation events occurring at the cathode surface. Adjacent to this is the cathode dark space or "cathode sheath" region, across which most of the potential is dropped, providing the accelerating force necessary to transport positively charged ions from the negative glow towards the target. The dark space region originates from plasma interactions with a surface which is electrically isolated. Initially, the electron flux will be greater than the positive ion flux due to higher random velocities, allowing the surface to acquire a negative potential relative to the plasma. This causes the formation of an electron depleted region adjacent to the cathode surface and creates an enhanced electric field which increases the positive ion flux density impinging on the target surface. The dark space region originates from plasma interactions with a surface which is electrically isolated. Initially, the electron flux will be greater than the positive ion flux due to higher random velocities, allowing the surface to acquire a negative potential relative to the plasma. This causes the formation of an electron depleted region adjacent to the cathode surface and creates an enhanced electric field which increases the positive ion flux density impinging on the target surface.

Figure 2.3. Plasma regions within the glow discharge



The thickness of the cathode sheath can be predicted for d.c. argon discharges from the free-fall version of the Child-Langmuir relationship (22) :

$$L = (4E_0/9J)^{1/2} (2q/m_i)^{1/4} V^{3/4} \dots\text{equation 2.4.}$$

where, L = Sheath thickness,  $E_0$  = Permittivity of free space,

J = Cathode current density, q = Ion charge.

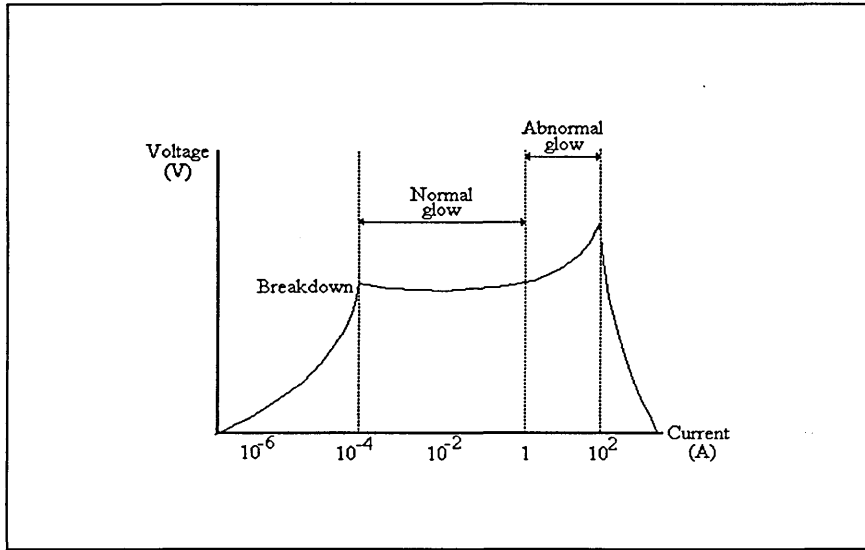
$m_i$  = Mass of ion, V = Potential drop across cathode sheath.

The cathode sheath is typically a few centimetres thick, and as the negative glow potential (plasma potential) is only a few volts positive with respect to earth, the voltage drop across the sheath is essentially the same as the bias applied to the cathode. However, the Child-Langmuir model treats the dark space in isolation and is not fully consistent due to incorrect assumptions on incoming ion velocities, collision theory within the dark space region and electric field suppositions at the dark space-plasma boundary (23).

In most PVD processes the negative glow region fills a considerable area within the chamber. When an ion strikes the target there is a possibility of secondary electron emission (5-10%) along with the generation of heat and the sputtering of atoms. These electrons are accelerated in the opposite direction to the  $\text{Ar}^+$  ions across the dark space and enter a region where they expend most of their energy in ionising and exciting collisions with argon neutral atoms, sustaining the discharge. Relaxation and de-excitation events generate photon emissions at wavelengths characteristic of the elements present, giving rise to a glow. Beyond the negative glow region is another dark space (Faraday dark space), the positive column (which most resembles a plasma), the anode dark space and the anode. For sputtering plasmas these regions are of lesser importance and are not considered further.

The current-voltage (IV) characteristic of the glow discharge is shown in figure 2.4. Sputter PVD systems aim to work with "abnormal" glow discharge properties, where an increase in power results in a sharp rise in voltage and an optimised increase in the target area carrying current.

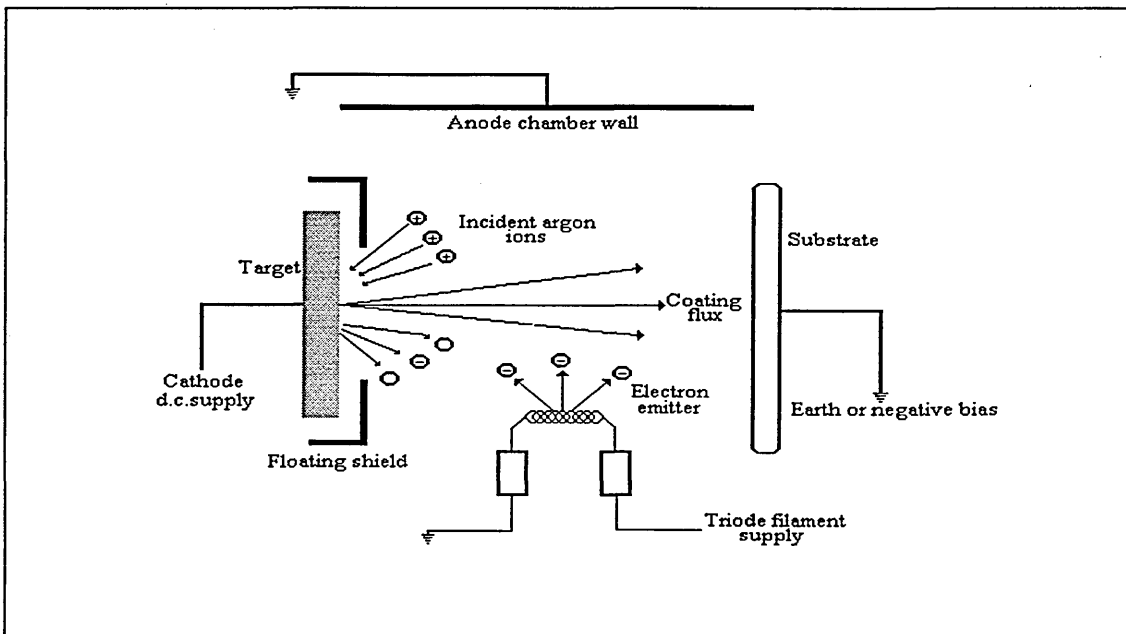
Figure 2.4. Glow discharge IV characteristics.



2.1.4. D.C triode sputtering

Improvements in the ionisation of a d.c. sputtering source can be made by the addition of a third electrode (thermionic emitting filament or a positively biased conductor) into the original diode arrangement. These type of systems are known as d.c. triode sputtering units (figure 2.5).

Figure 2.5. The d.c.triode sputtering arrangement.



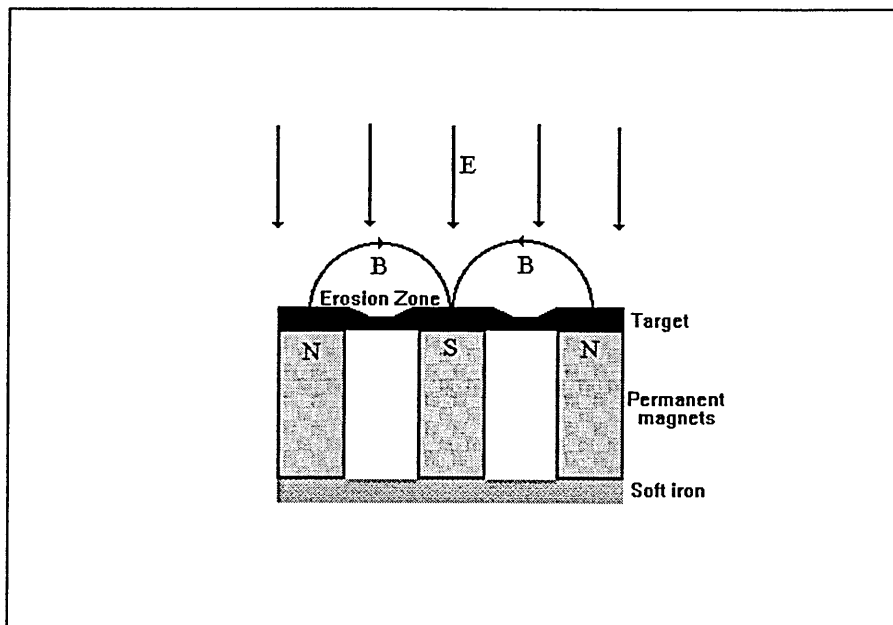
Triode sputtering allows independent variation of the discharge current and voltage, providing full control of increased ion densities impinging on both the substrate and the target (24) and allows deposition at lower pressures and higher rate. However these systems tend to be sensitive to contamination from the thermionic emission electrode and overheating from increased electron bombardment and radiation.

#### 2.1.5. Magnetron enhanced sputtering.

The application of a magnetic field in a glow discharge to trap emitted secondary electrons close to the target and enhance ionisation probability and deposition rate stems from original ideas by F.M.Penning in 1936 (25). However it was not until the 1970's (26,27) that the principle of crossing electric and magnetic fields was successfully applied to PVD sputtering systems.

The "magnetron" employs a magnetic arrangement positioned behind the target, to provide field lines which penetrate through the dark space and produce a magnetic field parallel to the cathode surface and an electric field perpendicular to the dark space (figure 2.6).

Figure 2.6. Magnetron configuration.



A particle of charge( $q$ ) travelling with velocity( $v$ ) interacts with a magnetic field( $B$ ), to produce a force perpendicular to both the magnetic field and the velocity. This may be expressed mathematically as:

$$F = q v \wedge B \quad \dots\text{equation 2.5.}$$

As electrons are much less massive ( $m_e$ ) than ions, only they are significantly affected by the weak magnetic fields applied in PVD systems. Under the application of an axial magnetic field, an electron travelling along the axis of the discharge will be unaffected since  $B$  and  $v$  will be parallel and their vector product will be zero. However, if the electron of mass  $m_e$  is travelling at angle  $\Theta$  to the magnetic field it will be subjected to a force  $Bev\sin\Theta$  perpendicular to the field. Thus, the electron will describe a circular motion of radius ( $r$ ) (assuming there are no collisions) such that:

$$\frac{m_e(v\sin\Theta)^2}{r} = Bev \sin\Theta \quad \dots\text{equation 2.6.}$$

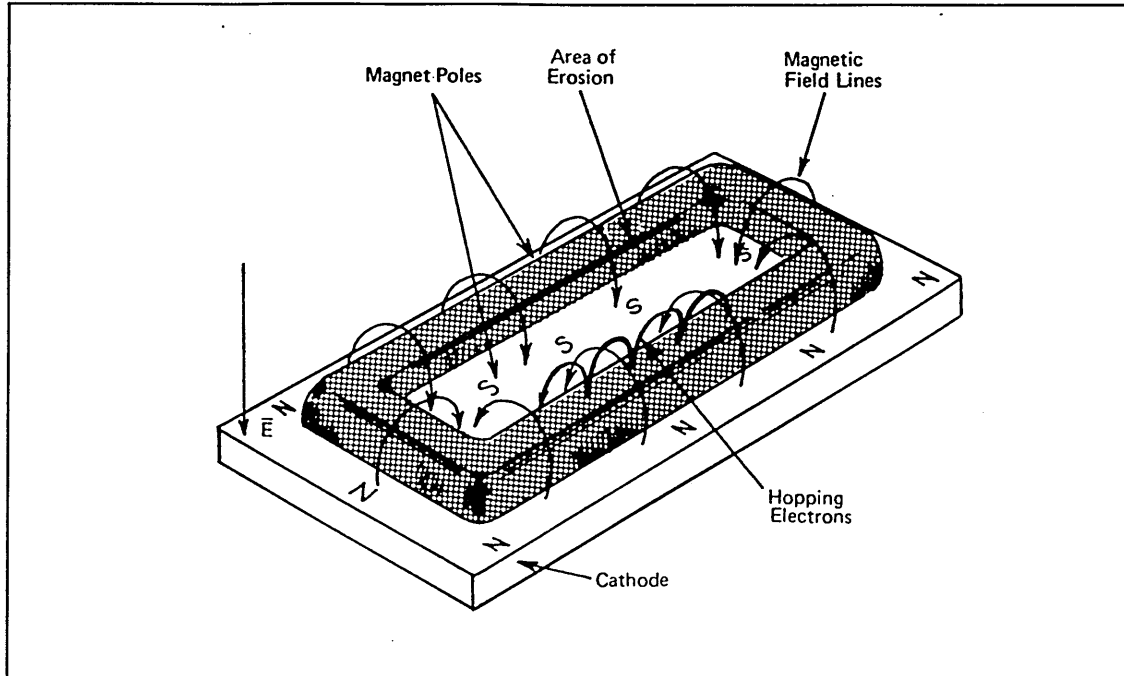
In magnetron systems this motion is coupled with a velocity  $v\cos\Theta$  parallel to  $B$ . Hence the general motion of the confined electrons in front of the target is helical, thereby extending their path lengths and the degree of interactions and ionisation events in the plasma. This increased ion density close to the target produces a considerably higher deposition rate ( $>500\text{nm/minute}$ ) when compared to diode sputtering systems and the electron trapping mechanism provides less free electrons to bombard the substrate surface and chamber walls, resulting in a cooler process capable of coating heat sensitive substrates (28-30).

Many different forms of magnetron configuration exist today, but common types include:

- (a) Cylindrical or post magnetrons (31).
- (b) Hollow cathodes (32).
- (c) S-guns (33).
- (d) Circular planar magnetrons (34).
- (e) Rectangular planar magnetrons (35).

The type which is practical for most applications is the rectangular planar magnetron (36) and will be described in greater detail (figure 2.7).

Figure 2.7. Schematic of the planar magnetron cathode.



The conventional planar magnetron has been designed such that a looping magnetic field around the inner and outer magnet pole pieces causes an ellipsoidal "racetrack" erosion area on the target surface. The magnetic field effectively concentrates the glow into a localised area to produce a stable line source which provides high plasma uniformity (37). Conventional magnetrons offer many advantages over diode and triode sputtering systems, however certain problems still remain inherent with this technique:

- (i) Decreases in ionisation at increasing target to substrate distances cause problems in deposited film quality (38,39).
- (ii) Three dimensional substrates may suffer from low degrees of ionisation and shadowing. (40).
- (iii) Uni-polar arcs may be established due to oxide patches or asperities on the surface of the target (41)
- (iv) Void formation at grain boundaries when the substrate current density is low (42).
- (v) The localised erosion track creates inefficient use of the target material (43).

Recently, a modification to the conventional magnetron arrangement has solved many of these problems.

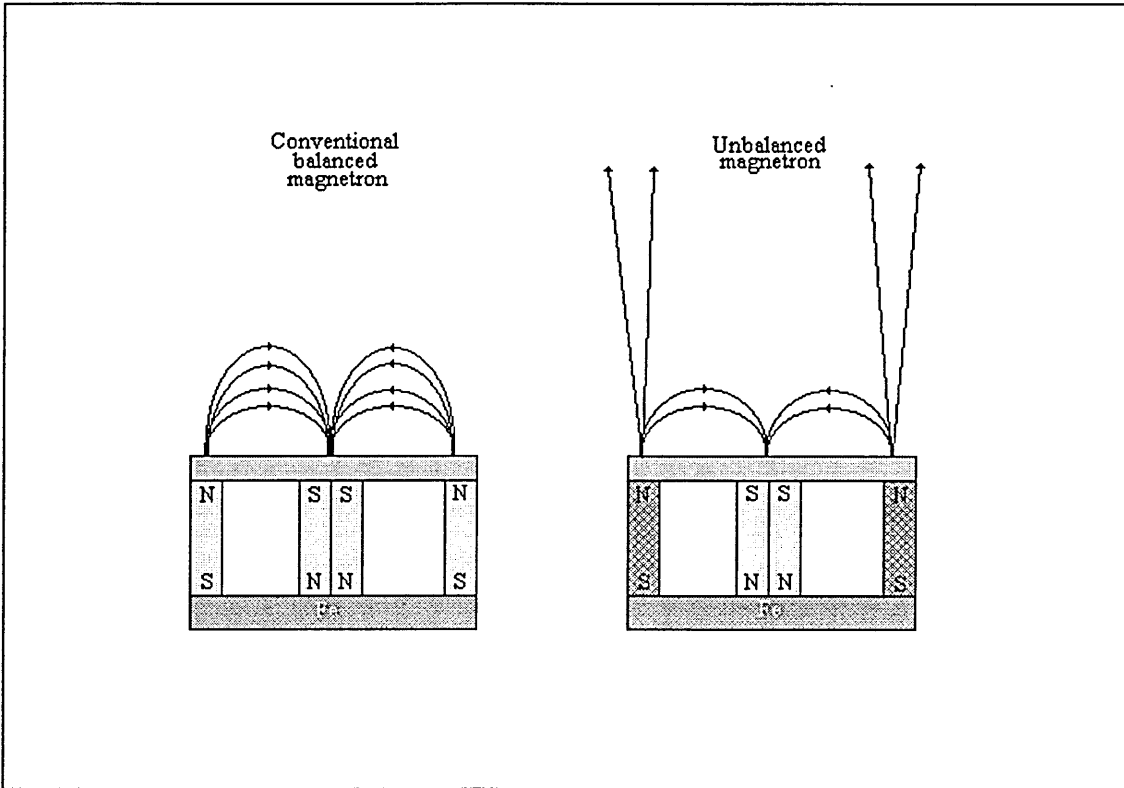
### 2.1.6. The unbalanced magnetron.

The amount of substrate ion bombardment in a conventional magnetron sputtering system is a function of the power to the cathode and the distance between the target and the substrate (44) and cannot be independently varied unless an auxiliary source of electrons is applied. This severely restricts the coating range and limits the geometries of substrates which can be accommodated. During the 1980's several research groups worked on modifications to the conventional magnetron to improve its ion bombardment properties and enhance plasma density at the substrate. In 1985-86 Window and co-workers published several reports on novel magnetron developments (45-48) which became the pre-cursor to the "unbalanced" magnetron sputtering cathode.

A conventional magnetron, in an idealised situation has all of its magnetic field lines looping between the inner and outer magnet pole pieces, and the return field lines contained by the steel yoke on which the magnets are fixed. Generally the magnetic field strength of the inner magnet array is the same (approximately) as the outer array, and this condition is said to be "balanced".

When a conventional magnetron is unbalanced, the strength of one set of magnets, normally the outer set (type II), is increased with respect to the other (49). The result is that the plasma formed is not confined close to the target surface but expands away due to the formation of a trumpet shaped magnetic field profile (figure 2.8), considerably increasing the substrate ion bombardment intensity such that it is comparable to other high deposition rate techniques (20). Experimental measurement and computer modelling of magnetic field and plasma profiles has been undertaken (50,51), confirming theoretical calculations on field shapes and throwing distances and revealing ion to deposited atom ratios greater than the order of 2:1 even at low substrate bias potentials.

Figure 2.8. Conventional and unbalanced magnetron configurations



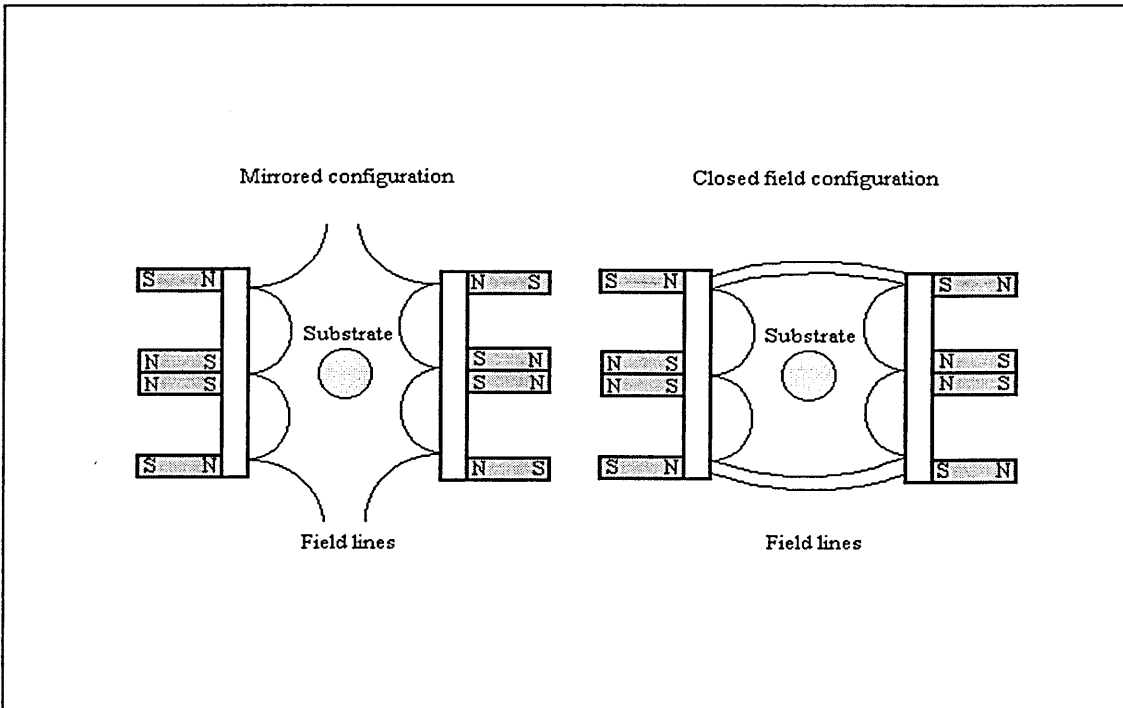
Since 1986 various research groups throughout Europe and the USA directed by Musil and Kadlec (52-54), Münz (55,56), Teer (57) and Sproul (58) have made contributions to advance unbalanced magnetron technology. Today, unbalanced magnetron sputtering systems can produce high quality coatings at target to substrate distances in excess of 200mm with bias current densities greater than  $2\text{mAcm}^{-2}$  and high deposition rate. However, the single unbalanced magnetron coating system has not solved all of the problems which conventional balanced magnetrons suffer from (section 2.1.5). The line of sight nature of the sputtering process means that variation in coating thickness uniformity and shadowing of complex 3-dimensional geometry can still occur. These problems have now largely been eradicated with the development of multi-cathode deposition systems using planetary substrate rotation mechanisms.

2.1.7. Multi-cathode systems and closed field geometry.

When a pair of unbalanced magnetron cathodes are mounted in a vacuum chamber, the spatial arrangement of the magnet arrays has a large effect on the plasma confinement characteristics (59). Generally two geometrical positions are possible (figure 2.9) :

- (a) Mirrored - where like poles face each other.
- (b) Closed field - where opposite poles face each other.

Figure 2.9. Schematic diagram of mirrored and closed field geometry.



Investigations on mirrored configuration sputtering have shown that the plasma ion densities were generally very low and substrate bias current densities were typically less than  $1\text{mAcm}^{-2}$  (60) resulting in a porous coating microstructure and poor adhesion. If the magnets were arranged in the closed field configuration, where the field lines from one set of magnets are directly coupled to the opposing magnet array, large increases in bias current density ( $>6\text{mAcm}^{-2}$ ) and ionisation at the substrate could be achieved. The linking of the magnetic field lines also provides a high degree of plasma confinement and exact control of the deposition region (61).

Before 1991 most reported work used single or dual unbalanced magnetron systems (62,63), but industrial scale equipment quickly moved to multi-cathode arrangements where more than two sources are used. The bi-polar nature of the magnet arrays meant that chambers comprising an odd number of cathodes suffered from the inability to completely link and close the magnetic field, allowing secondary electrons to escape and a subsequent decrease in plasma density at the substrate. Even number (usually four) cathode systems have been found to offer the best field linkage arrangement for large scale deposition systems.

Most PVD systems now also utilise 2-fold or 3-fold planetary substrate rotation systems to provide high coating uniformity and the suppression of shadowing effects (64). Here each individual substrate, its holder and the entire rotation assembly circulates at different angular velocities due to a complex gearing mechanism.

#### 2.1.8. Reactive sputtering.

Reactive sputtering involves the introduction of a reactive gas into the plasma during deposition to activate dissociation and ionisation of the gas molecules and allow combination with the metal vapour flux to produce compound formation at the substrate surface (65-68). Many reactive gases can be used to deposit a wide range of desired compounds, for example nitrogen to form nitrides, methane or acetylene to produce carbides or mixtures of both nitrogen and methane to yield carbo-nitride films. However, the reactive sputtering process is normally non-linear where often it is not possible to change one parameter without affecting others.

When a high reactive gas partial pressure is applied to a sputtering system, reaction can take place not only at the substrate but also the target surface due to chemisorption until, if a sufficient partial pressure is available, the target itself becomes completely covered with the depositing compound and the compound is sputtered instead of the pure metal. This phenomenon is known as "poisoning" (69). As the compounds often have much lower sputtering and secondary electron yields than the pure metals (70), the result is usually a drastic reduction in the deposition rate and ionisation within the plasma. Conversely, if the partial pressure of the reactive gas is too low, an insufficient quantity of gas atoms are available to react with the metal vapour flux and a sub-stoichiometric film is produced. The critical partial pressure required to produce a stoichiometric film without poisoning the target can be found by plotting the reactive gas partial pressure or the deposition rate against the reactive gas flow.

Figure 2.10 The reactive sputtering hysteresis effect.

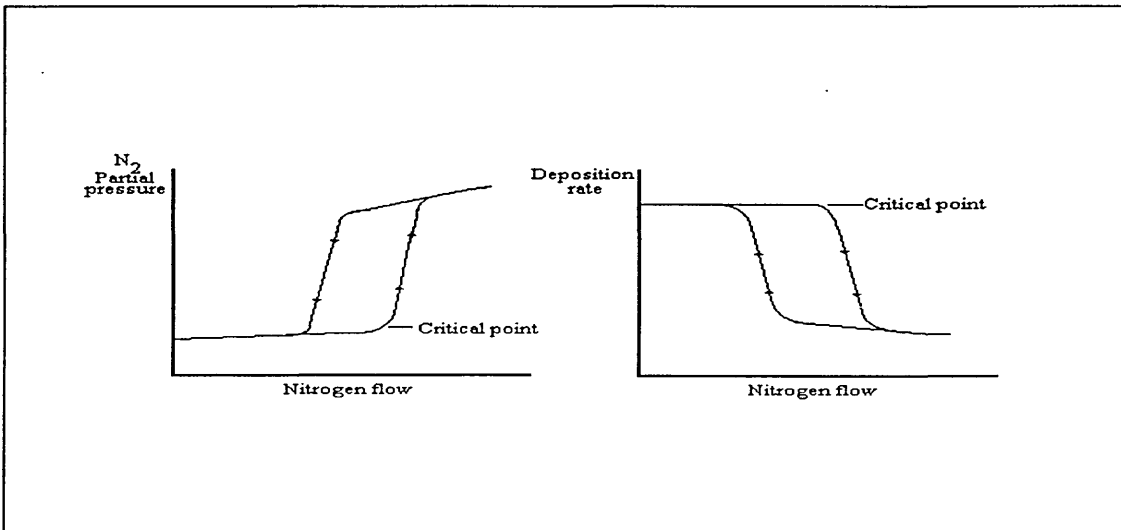


Figure 2.10 illustrates the unstable region in which the critical partial pressure point lies and the hysteresis effect common to all reactive sputtering systems. A substantial drop in metal vapour at the onset of target poisoning is clearly visible, resulting in a further excess of reactive gas (in this case  $N_2$ ) which serves to rapidly stabilise the process at a rate minimum. If the reactive gas partial pressure is subsequently lowered, the sputter yield only gradually recovers back to that of the pure metal due to the removal of the target surface compound, providing the evident mis-alignment of the upward and downward reaction behaviours. Many techniques to accurately control the reactive gas partial pressures have been developed. During the early 1980's Aronson et al (71) demonstrated a reactive gas pulsing method capable of producing non-homogeneous nitride films of deposition rates at around 70% of the pure metal rates. However, a major development in composition control came in 1984 with the use of automated flow control using fast feedback loops (72). Today, even more sophisticated methods are commonly available including:

- (i) Plasma emission monitors (73).
- (ii) Optical gas controllers (74).
- (iii) Mass spectrometer controllers (75).

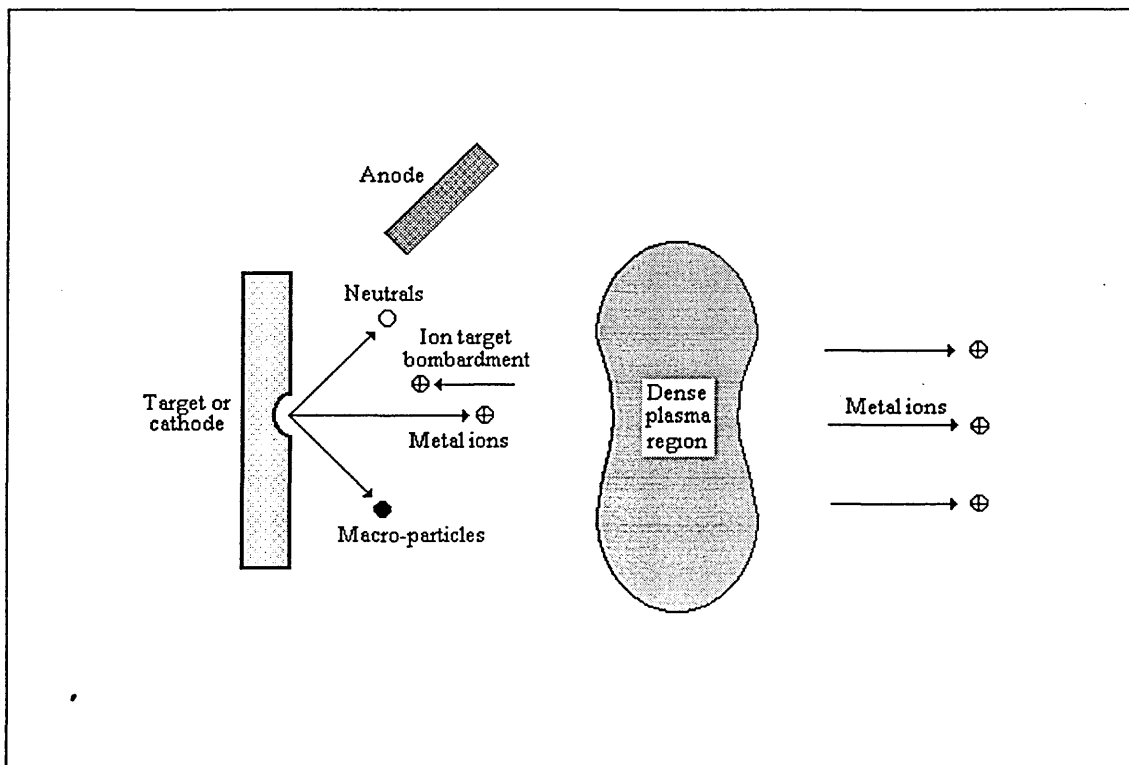
Some of these techniques require differential pumping and sensors located in close proximity to the target for accurate control (76), however a simple way to reduce or totally remove the hysteresis behaviour is to increase the pumping speed of the system (77,78). Unfortunately in practise this has proved expensive and inefficient in gas utilisation.

## 2.2. Arc evaporation techniques.

### 2.2.1. The random cathodic arc

An arc may be defined as a discharge of electricity, between two electrodes in the presence of a gas or vapour, that has a voltage drop at the cathode of the order of the minimum ionising or exciting potential of the gas or vapour (79). The process is characterised by the striking of a high current, low voltage arc on a cathode (target) which gives rise to a small, but highly active emitting area (cathode spot) which produces a high velocity jet of vapourised cathode material. The plasma jet intensity peaks in a direction normal to the cathode surface and contains a high proportion of multiply charged ions (80,81), neutral particles, clusters and macro-particles (82-84). Theoretically, the arc is a self-sustained discharge capable of supporting large currents by its own mechanism of electron emission from the cathode and positive ion re-bombardment under high vacuum conditions (figure 2.11). If a suitable reactive gas is introduced into the chamber, dissociation, ionisation and excitation can occur during interaction with the ion flux and compound film deposition results.

Figure 2.11. Cathodic arc vapour flux.



Without the influence of an external magnetic field, the cathode spot moves rapidly across the surface of the cathode in a random manner and evaporates microscopic points and protrusions to cause craters. However, if the cathode spot stays at an evaporative point for too long, it can generate a minute liquid pool of molten cathode material. This can become vigorously evaporated to a point where micro-explosions can eject relatively large masses of molten material which condense during vacuum transportation and land on the surface of the substrate to form macro-particles which can be detrimental to the coating performance.

Original work on random arc evaporation appears as early as 1939 by Burkhardt (85) and was further modified into arc evaporative PVD technology by workers in both the USA (86) and USSR (87,88) in the 1970's. Since this time the parameters and physical properties of the cathodic arc discharge have been intensively studied. Some of these parameters can be easily measured and are not the subject of any great contention, however, others are the subject of a great deal of dispute and are highly significant. The following sub-sections of this thesis will review in more detail the properties of the cathodic arc by experimental and theoretical analysis from literature on the following:

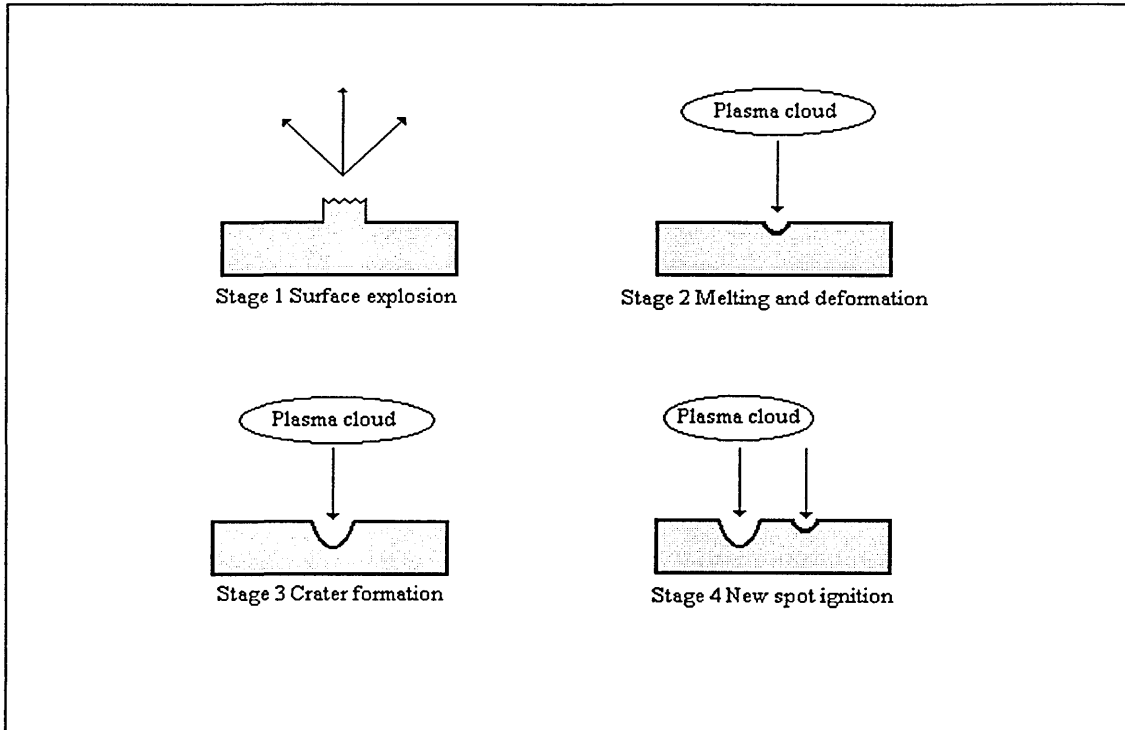
- (a) The spot life cycle.
- (b) The types of cathode spot.
- (c) The spot diameter and current density.
- (d) Spot splitting.
- (e) The types of erosion
- (f). The random spot motion.

### 2.2.2. The cathode spot life cycle.

Guile and Jüttner (89) have demonstrated that the cathode spot life cycle can be described by a four stage process consisting of surface explosion, melting and deformation of liquid, crater formation and quasi-steady state, followed by new spot ignition (figure 2.12). In the first stage, surface explosion, the application of a high voltage between anode and cathode leads to the rapid heating and evaporation of the cathode material, formation of a vapour cloud and electrical breakdown via the development of a field emission mechanism (90-92) from the tips of micro-protrusions on the surface of the cathode. This leads to localised resistive heating, high thermal loading and eventually explosive evaporation resulting in a rapidly expanding plasma plume which evolves into a dense cloud above the cathode spot. In the second stage, complete or explosive destruction of the micro-protrusion occurs (93) and pressure from

the plasma cloud combined with field rupture or surface tension on the molten liquid pool formed serves to produce hemispherical crater deformation. Stage three involves the main life-time ( $\sim 10^{-7}$ S) of the spot which is spent constantly evaporating material from within the crater with high spatial distribution and high kinetic energy ( $\sim 100$ eV).

Figure 2.12. The cathode spot life cycle.



After some time it is believed that the spot extinguishes and a new one ignites to take its place, completing stage four and the entire life cycle. Ecker (94) has suggested a model to describe stage four, where heating from the cathode spot gives rise to a localised increase in cathode resistance and the formation of lower voltage sites at locations near the original spot position. A balance must be achieved between the level of heating required to start a new spot and the unfavourable conditions offered by the rise in local resistance. The result is the formation of energetically more favourable spot positions at which the new spot ignites causing the old spot to extinguish.

### 2.2.3. The types of cathode spot.

Rakhovskii first identified that two different types of cathode spot generally exist, types I and II (95), which have distinct differences in their evaporative behaviour (96,97).

Type I spots only occur on contaminated cathodes with some degree of surface roughness and are characterised by:

- (i) Field emission of electrons from micro-protrusions below the spot plasma.
- (ii) Spot movement occurs by jumping from protrusion to protrusion.
- (iii) The mean distance jumped by the spot is greater than the mean crater radius.
- (iv) Velocity of the spot motion is governed by the plasma expansion.
- (v) Non-characteristic arc colour due to weak interaction with the bulk material.

Type II spots may exist in tandem with type I spots and are generally found on clean or conditioned cathodes. During the initial stages of the arcing process a change from type I to type II spot normally occurs and the type II spots are characterised by:

- (i) Thermal emission of electrons from the crater to sustain the arc.
- (ii) The active evaporation area has a lower velocity than in type I.
- (iii) The mean distance jumped by the spot is of the order of the mean crater radius.
- (iv) The colour of the arc is characteristic of the cathode material.

#### 2.2.4. The spot diameter and current density.

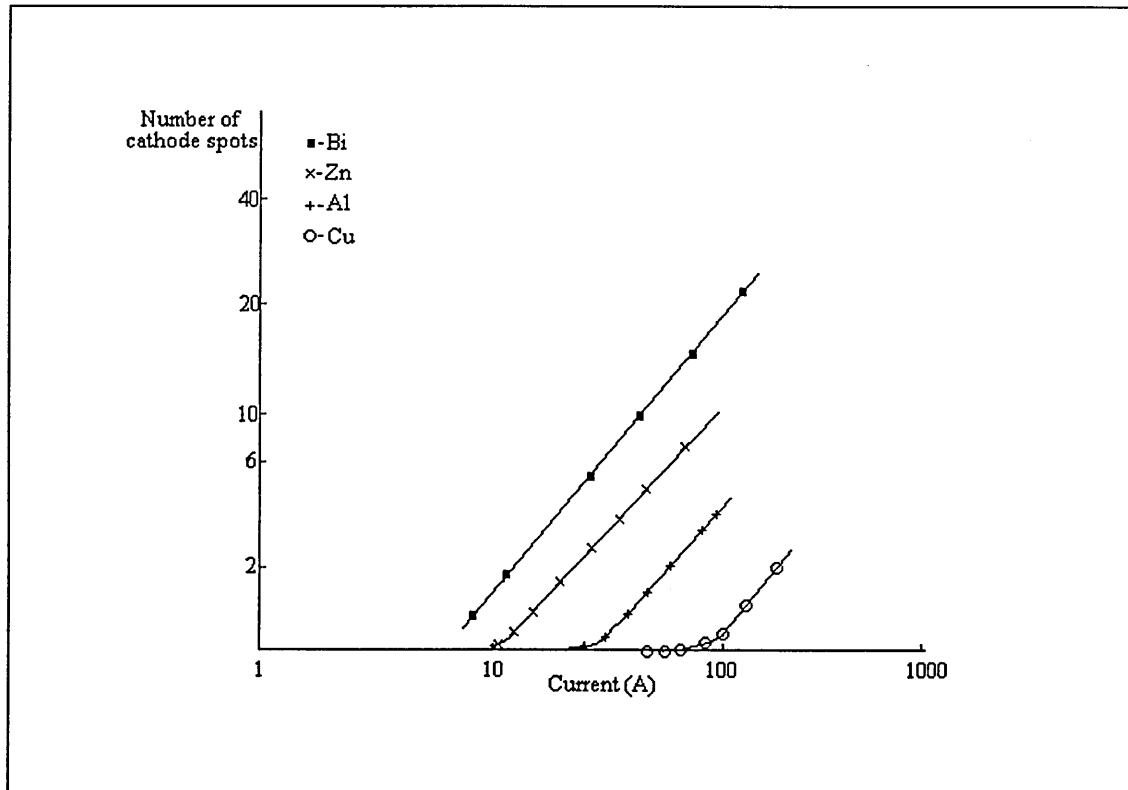
The measurement of the spot size and subsequent evaluation of the current density has proved very problematic due to the microscopic nature of the sub-spots (98) which make up the cathode spot and the plasma cloud obscuring optical evaluation. Two different methods to determine the dimensions of the spot are currently used - "autograph" methods (95) which analyse the craters left on the cathode and "fast registry" methods (99) which use high speed photographic techniques to examine the luminous plasma cloud region over the spot. Each evaluation method produces slightly different data due to the limitations of each technique, however typically the cathode spot diameter is of the order of  $10^{-6}\text{m}$  (100) and the current densities used in current random arc PVD equipment are approximately  $10^8\text{-}10^{12}\text{Am}^{-2}$  (90,101).

#### 2.2.5. Spot splitting.

As mentioned in section 2.4.4, the cathode spot consists of a sub-structure composed of sub-spots or cells. When the arc current is increased the number of cells increases accordingly until at a certain current limit another large spot begins to form (102). Eventually the spots split and the highly dynamic behaviour of multiple spot motion, ignition and extinction occurs on a continuous basis (figure 2.13).

In many materials the number of spots which can be formed at high arc currents can be as high as 2-20 and various models to predict and understand this phenomenon have been developed. The most consistent models treat sub-spot fission by considering the repulsive electrostatic forces between two dipoles in competition with the attractive magnetic forces between two current carrying conductors (102) and obtain good agreement with experiment.

Figure 2.13. The number of cathode spots as a function of arc current.



### 2.2.6. The types of erosion.

The erosion rate of a random arc on a cathode is a function of the following variables: (i) arc current, (ii) erosion time, (iii) cathode dimension, (iv) gas pressure. However, the parameter which influences the erosion most is the type of cathode spot.

Type I spots have been found to leave craters of  $10^{-7}$ m typical radius and depth with a constant erosion rate per coulomb (electric transfer factor) for degassed cathodes (103). Type II spots exhibit quite different behaviour, with average crater depths of the order of  $2.5 \times 10^{-5}$ m and groups of spots producing trails with depths of  $10^{-5}$ m, indicating the electric transfer factor is substantially dependent upon arc current.

The erosion rate reaches a minimum when arcing occurs under conditions which only allow the type I spot to exist, whilst operation when only type II spots can exist results in a substantial increase in the erosion rate. This can be explained by the different spot electron emission mechanisms.

### 2.2.7. The random spot motion.

A prominent feature of the cathode spot in the absence of external magnetic fields is its rapid, dynamic and random motion over the surface of the target material. The most consistent models consider the cathode spot movement as a random walk and describe a probability density function for the spot's location.

Daalder (104) assumed that the cathode spot starts to move from the origin of an x-y coordinate system such that during each time interval (T), the spot displacement was a step +s or -s along the x-axis and +s or -s along the y-axis. There is an equal probability that the step is +s or -s in each direction and movement along the x and y axis is stochastically independent. After n sets of displacements the spot position is (x,y) at time t, hence we take  $t = nT$ . Thus the probability that after n steps at time (t) the spot position in x (i.e one dimensional random walk) is given by the normal density function:-

$$p(x) = \frac{1}{(2\pi\alpha t)^{1/2}} \exp\left(-\frac{x^2}{2\alpha t}\right) \quad \text{.....equation 2.7}$$

where  $\alpha$ , the diffusion constant =  $(s^2/T)$ , provided n is large and in two independent random walk processes:-

$$p(x,y) = p(x)p(y) \quad \text{.....equation 2.8}$$

Thus;

$$p(x,y) = \frac{1}{2\pi\alpha t} \exp\left(-\frac{x^2 + y^2}{2\alpha t}\right) \quad \text{.....equation 2.9}$$

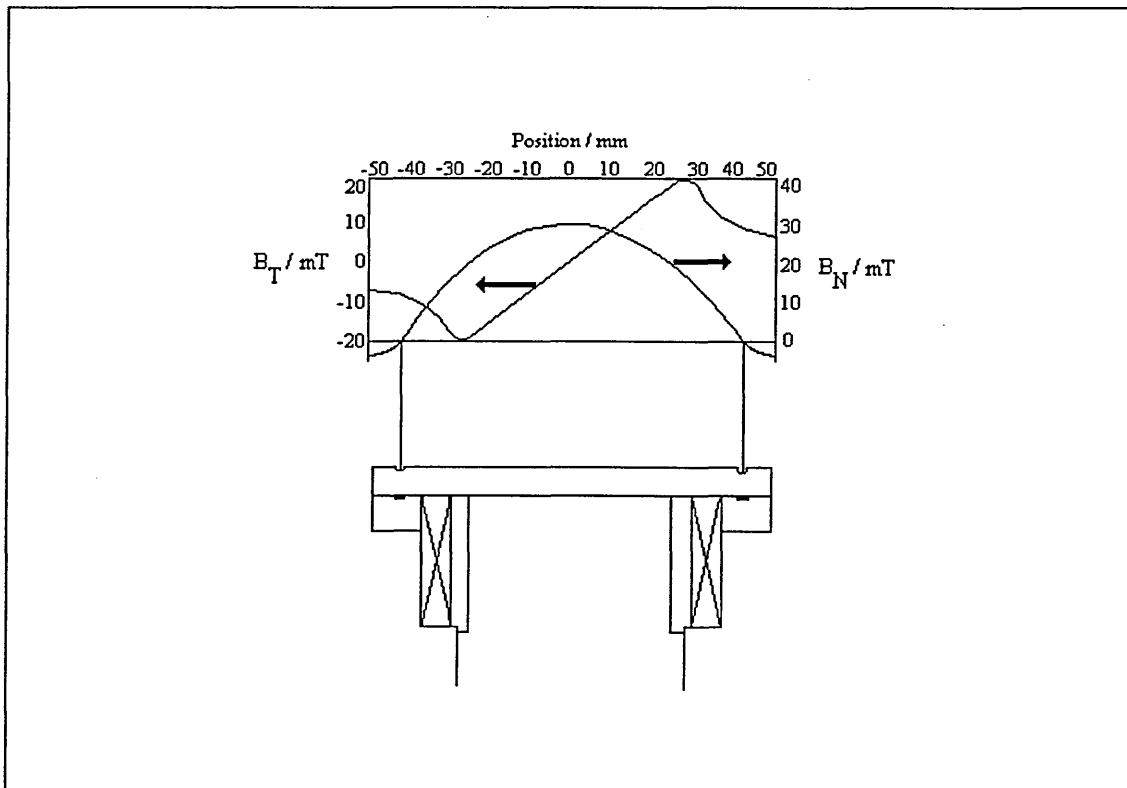
Which may be transformed from Cartesian to cylindrical coordinates such that the probability density function p(R), of distance R from the origin, where  $R = (x^2 + y^2)^{1/2}$ , is given by:-

$$p(R) = \frac{R}{\alpha t} \exp\left(-\frac{R^2}{2\alpha t}\right) \dots \text{equation 2.10}$$

### 2.2.8. The steered cathodic arc

The random arc evaporation technique suffers from the serious disadvantage that in addition to the plasma jet, the arc produces a spray of liquid droplets or macro-particles which can be tens of microns in diameter (82) and detrimental to surface quality and film adhesion. One method to decrease macro-particle incorporation in the coating is to increase the velocity at which the cathode spot moves and hence decrease the spot dwell time and molten pool dimensions. The steered arc system uses a magnetic field to control the motion of the cathodic arc (figure 2.14), which is essentially a current carrying conductor, and force the cathode spot along a pre-determined closed path defined by the position of the normal field component zero (105).

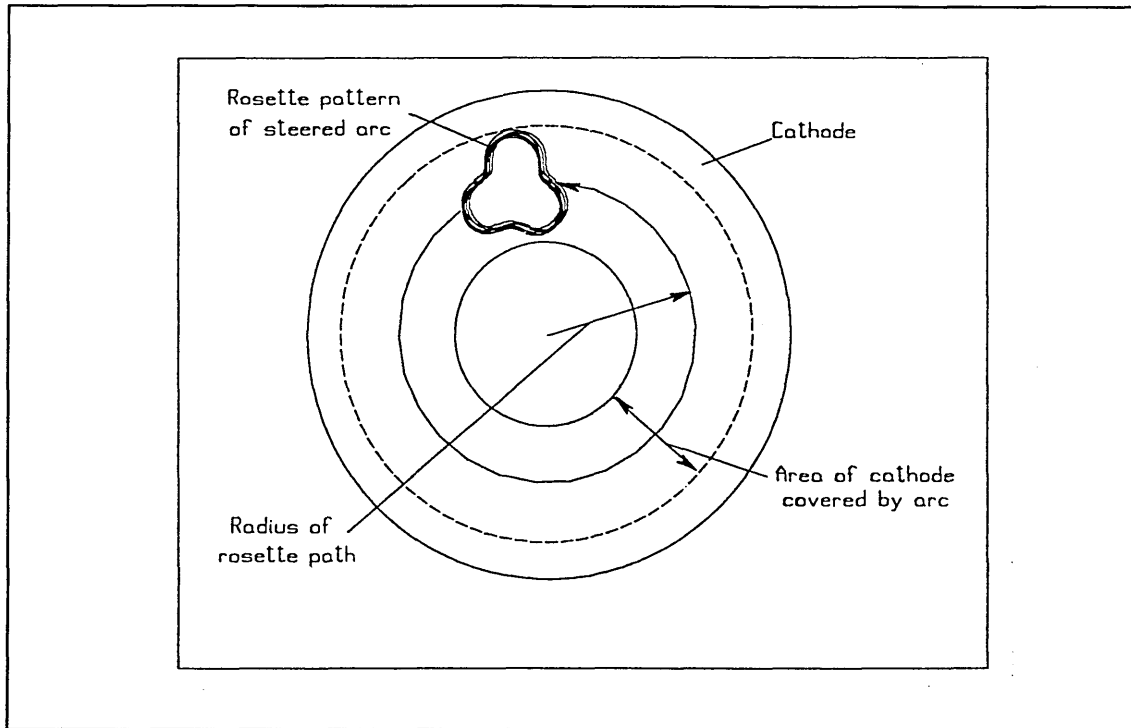
Figure 2.14 The transverse and normal field profiles from a single coil steering system



The first commercial PVD systems used a fixed permanent magnet array to steer the arc in a circular orbit (106). However, further developments to enhance cathode usage were

made by Interatom GmbH to provide rosette shaped arc paths by means of various motorised rotating magnets (figure 2.15). More recently Morrison (107) has utilised transient steering fields generated by electromagnetic coils to bounce the arc back and forth along a channel and Walke et al (108) have produced a two coil system which allows pre-selection of the arc track radius and highly efficient utilisation of the entire cathode material.

Figure 2.15. Schematic of Interatom permanent steered arc path.



All magnetic steered arc systems rely on the physical phenomenon that if a transverse magnetic field is applied from behind an arc evaporation cathode, a "Lorentz force" will be exerted on the arc such that:

$$v \sim -j \wedge B \dots \text{equation 2.11}$$

or,

$$F \sim q[ |B|^2 j - (B \cdot j) B ] \dots \text{equation 2.12}$$

where; F = Force.

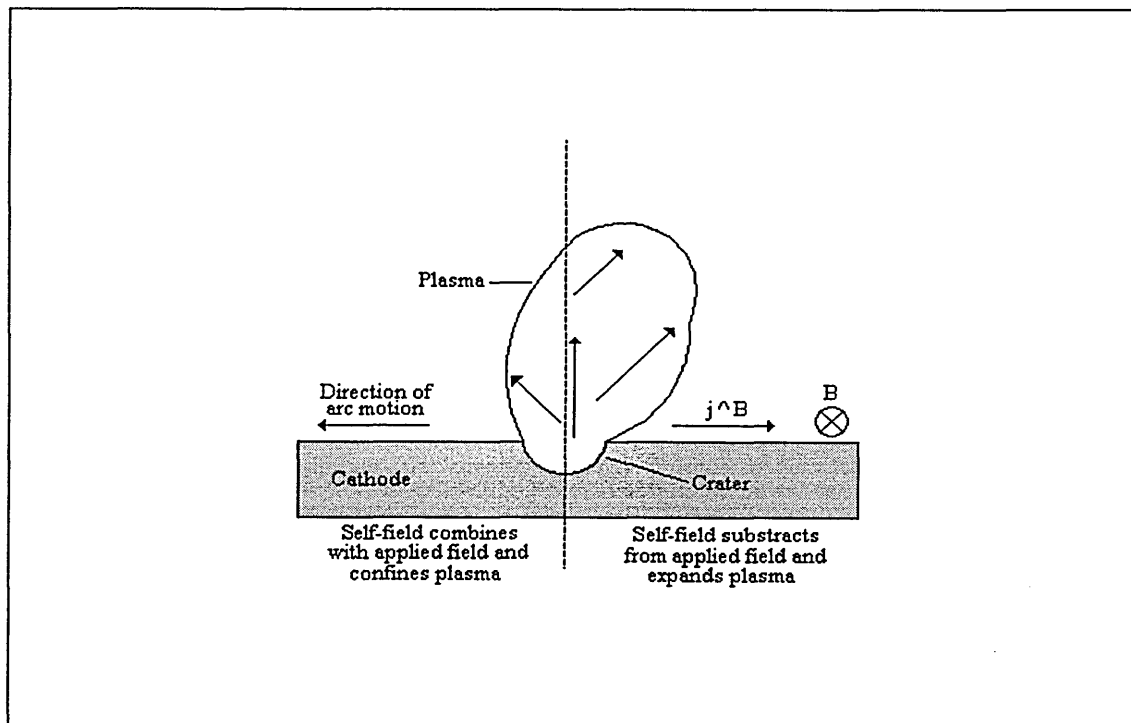
q = Moving charge.

j = Current.

$v \wedge B$  = Vector product of the particle velocity(v) and magnetic flux density(B).

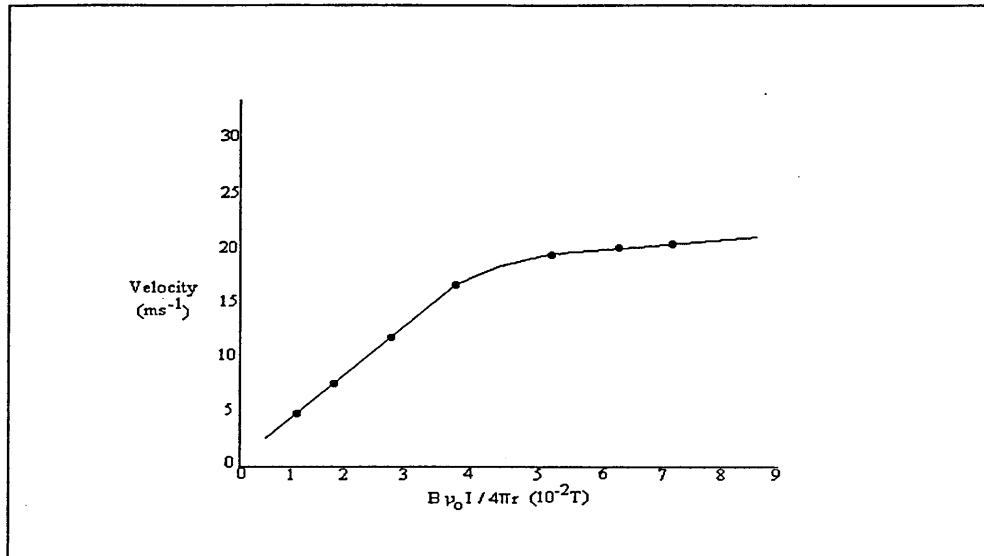
However, rather surprisingly at magnetic field strengths of up to one Tesla and chamber pressures below a critical value (1-60 Torr, depending upon working gas ) the arc moves in the non-amperian ( $-j \wedge B$ ) or retrograde direction (105,109,110). The most consistent models which have been developed to explain this, consider the superposition of self fields (generated by the electron current from the spot) and applied transverse fields which combine favourably on the retrograde side of the cathode spot to cause asymmetric plasma confinement (figure 2.16), more intense ion bombardment and the production of more favourable electron emission sites (111). Several other authors have used the movement of space charge (112), movement of the spot plasma (113) or bending of the plasma column (114) to explain the non-amperian behaviour.

Figure 2.16. Asymmetric confinement of the cathode spot.



The velocity dependence of a high current arc (2.7-6.9KA) as a function of the magnetic self-field strength is shown in figure 2.17 (115). Investigations have revealed an almost linear dependence with inherent field strength up to a velocity threshold of  $\sim 30\text{ms}^{-1}$  (for copper cathodes) for fields up to  $4 \times 10^{-2}\text{T}$ . If strong external transverse fields are applied ( $1 \times 10^{-1}-1\text{T}$ ) significant increases in arc velocity up to  $500-1000\text{ms}^{-1}$  have been recorded until at around 1 Tesla, a sharp transition from retrograde to amperian motion has been observed (114). The arc velocity decreases with increasing cathode temperature (116), thus creating more macro-particles and has also been found to have a complex dependence with arc voltage, thermal conductivity and cathode material.

Figure 2.17. Arc velocity as a function of self-magnetic field strength.



Most steered arc systems provide secondary confinement of the arc on the cathode surface by means of a passive border with predetermined electrical characteristics. The primary requirements of the border material is that it should have a very low secondary electron yield which promotes new spot ignition sites back on the cathode surface and that it provides high arc stability for operation over long periods of time. The material which is generally chosen for passive confinement is boron nitride.

Reactive steered arc evaporation processes are generally less sensitive to poisoning and require less complex gas partial pressure control than in sputtering systems. However, if high partial pressures of gas are applied cathode poisoning can occur and for certain modified processes is actively used to provide lower levels of macro-particle formation from the compound (117).

Mechanical or electrical changes to the magnetic field profiles allows precise movement and selection of the radius of the arc track (in circular geometry) on the surface of the cathode and provides various advantages over random arc systems:-

- (i) Exact control over the emission area.
- (ii) Elimination of periodic extinguishing or "quenching" at low current densities.
- (iii) Significant reduction in the production of macro-particles generally giving better coating surface finish combined with excellent adhesion.
- (iv) A capability to use multi-elemental segmented targets.

### 2.2.9. The filtered cathodic arc.

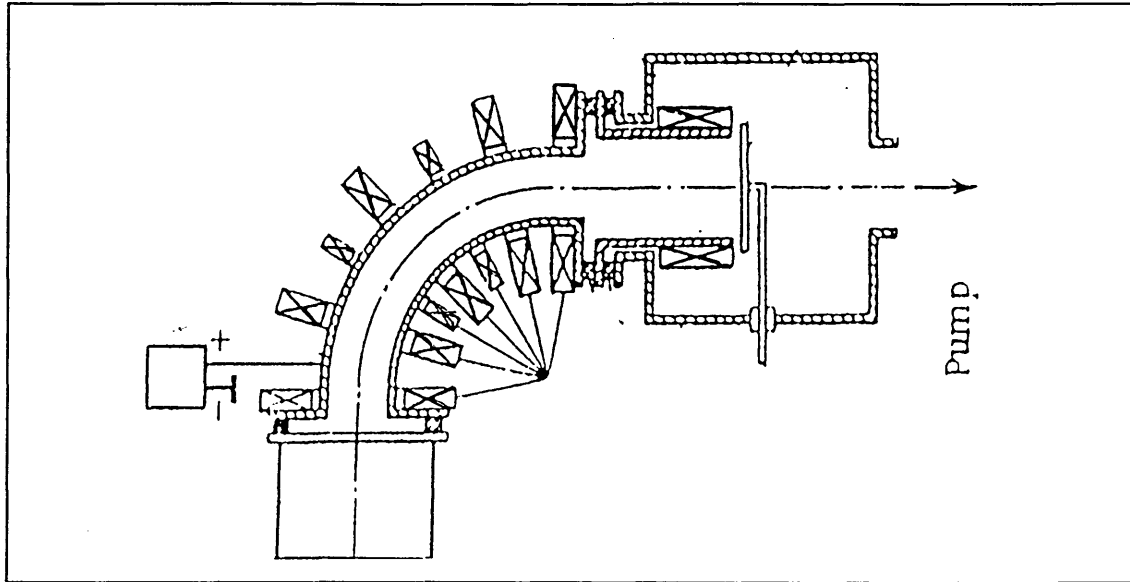
In an effort to alleviate the macro-particle incorporation problems which significantly affect random arc deposition techniques and to a lesser extent steered arc systems, a number of processes employing various "filtering" arrangements to remove droplets or extraneous particles from the coating flux have been developed.

(i) *Shielding* (118). This is the simplest and cheapest of the filtering methods, in which a screen or shutter (at floating potential with respect to the plasma) is brought directly into the vapour stream to block the path of the macro-particles. The substrate and shields are negatively biased to attract only the positive ions from the plasma, however this technique suffers from large reductions in deposition rates.

(ii) *Magnetic filtering* (119,120). A number of magnetic filtering devices have been developed which employ ring cathodes with the arc surface on the outside circumference. In this case the arc plasma is reflected by a series of solenoids which set up an electric field due to the insulating properties of the magnetic field lines running parallel to the coil surface.

(iii) *Magnetic plasma duct filtering* (121). This type of filtering device generally consists of a quarter torus in which a magnetic field can be developed with field lines parallel to the torus walls. The positive ions of the plasma stream are transported along the duct to the negative-biased substrate which is positioned directly in front of the exit orifice (figure 2.18). The macro-particles, which are massive, remain unaffected by the magnetic field and follow their normal trajectories. This technique has provided excellent reductions in macro-particle formation within various coatings but still suffers from problems in coating substrates of variable geometry (3-D) and industrial scale-up.

Figure 2.18 Magnetic plasma duct filtering.



#### 2.2.10. Arc evaporation of multi-elemental targets.

The deposition of complex, multi-component coatings by steered arc evaporation is generally carried out by one of two different techniques either:

- (i) Directly from evaporation of homogeneous alloy targets or hot isostatic pressed / sintered powder metallurgical targets (122).
- (ii) Co-evaporation of several pure metallic targets (123).

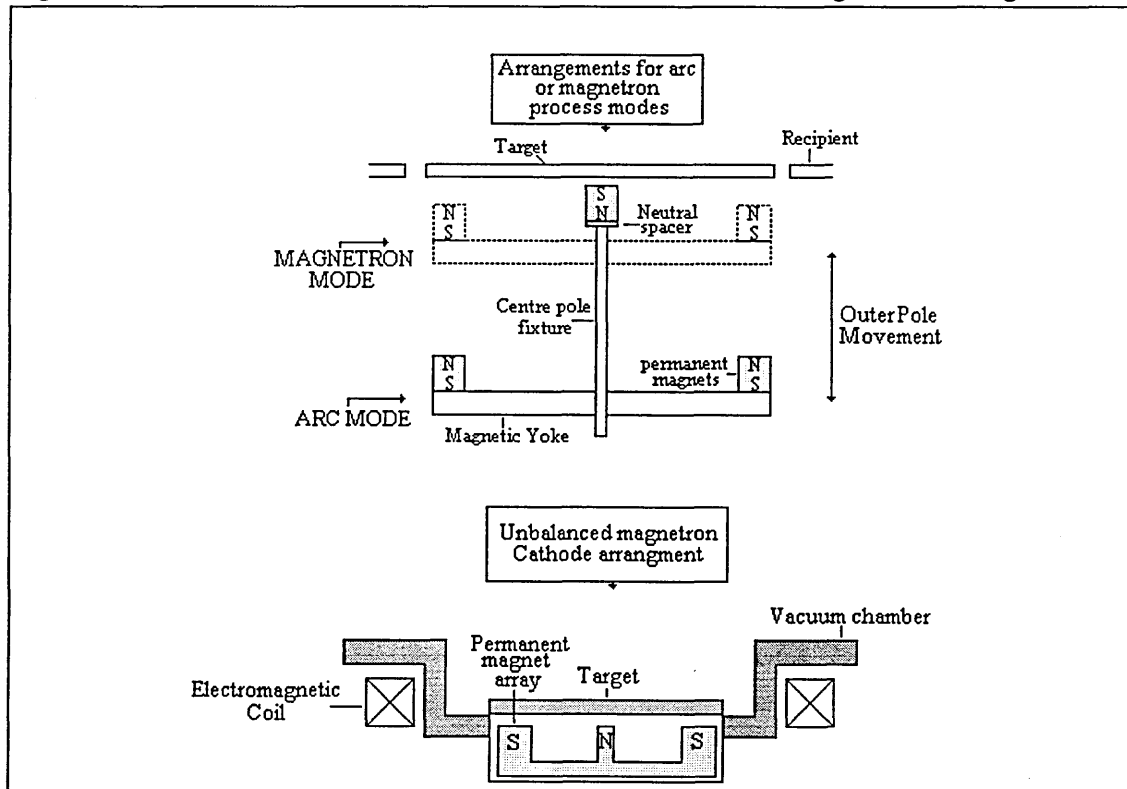
The common problem with the alloy deposition technique is that the various constituent elements of the cathode may have widely varying evaporation rates and melting points. This can rapidly result in the depletion of the more volatile components within the source (124,125) after a time, the production of a non-repeatable process causing variation in metal ratio within the coating flux and an inconsistent coating thickness (126), and inefficient utilisation of the cathode providing a shortened working lifetime. However, the co-evaporation methods also have serious disadvantages including cross-contamination problems, differing evaporation rates, inaccurate control and inflexibility of the metal ratio within the coating flux, the expense of using full size cathodes of certain materials and the line-of-sight nature of each source creating a lack of plasma mixing.

These fundamental and complex problems have in many cases still to be solved despite large scale efforts by many establishments, both academic and commercial.

### 2.3. The Arc-Bond Sputter technique

During the early 1990's, the concept of Arc-Bond Sputter™ technology (127) was developed to combine the excellent adhesion properties provided by steered arc processing with the highly flexible unbalanced magnetron coating technique. This was achieved by integrating the functions of both a steered cathodic arc evaporator and an electromagnetic unbalanced magnetron into a single cathode unit (figure 2.19).

Figure 2.19. The ABS cathode unit and the ABS unbalanced magnetron configuration.

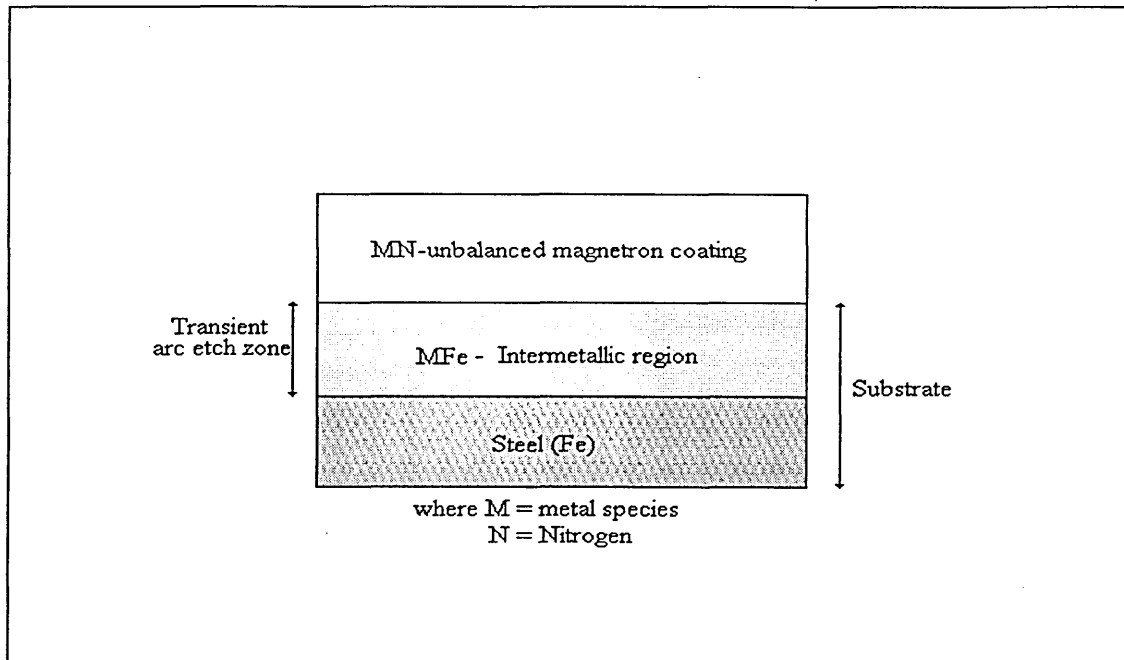


The technique relies on a key processing step which involves the initiation of a cyclic steered arc metal ion ( $M^{+1}$ ,  $M^{+2}$ ,  $M^{+3}$ ) etching treatment at high substrate bias voltages (-1000-1200V) prior to unbalanced magnetron coating.

Processing step number	Process step
1	Pump down
2	Heating & glow discharge cleaning
3	<b>Steered arc metal ion etching</b>
4	Unbalanced magnetron coating
5	Cool down

Several research groups (128,129) have claimed that the steered arc etching stage can provide low level implantation and diffusion of metal species into steel substrates, causing the formation of an adhesion promoting inter-metallic region (130) of thickness  $\sim 1200-1500\text{\AA}$  (figure 2.20). However, other workers (131) have shown that ions undergoing accelerating potentials of 1-2KeV will have insufficient momentum to provide significant implantation ( $20-50\text{\AA}$ ), thus diffusion, increased surface defect densities and additional heat input mechanisms are now thought to dominate. Ives (132) has also examined the role of keying mechanisms from the protrusion of carbides in underlying etched high speed steel substrates as an explanation for improved coating adhesion.

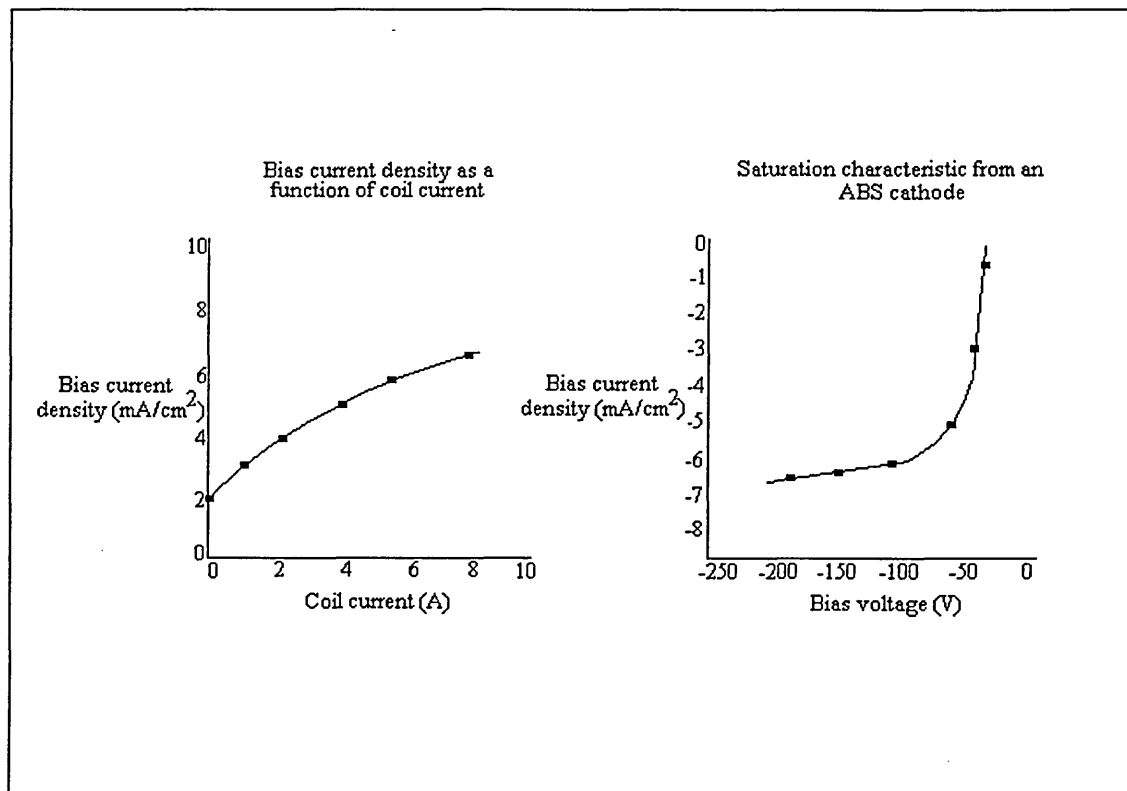
Figure 2.20. The effect of ABS steered arc metal ion etching.



The ABS technique has the unique property that the "degree of unbalance" is adjustable by means of the electromagnetic coil arrangement disposed concentrically with respect to the magnetron. This allows the bias current density to be controlled (through alteration of the coil current) independently of the bias voltage, discharge voltage or cathode power and within certain limits (bias voltage and temperature) gives a possibility to adapt the bias current density to the required coating properties (figure 2.21). If the unbalancing coils are applied during steered arc evaporation, significant alteration of the normal field component zero position and hence the arc track radius can be achieved to provide greater efficiency in target utilisation.

Various comparative trials have been carried out to examine binary and ternary coating adhesion and other physical properties when deposited by ABS against steered arc or unbalanced magnetron sputtering (133,134). Most reports have found ABS coatings show increased scratch adhesion critical load values when compared against unbalanced magnetron films of the same composition and near parity with steered arc films.

Figure 2.21. The effect of coil current and bias voltage on ABS bias current density



Recently, the flexibility of the ABS technique has also been demonstrated with reports on simultaneous steered arc evaporation and unbalanced magnetron sputtering trials within a single process (135).

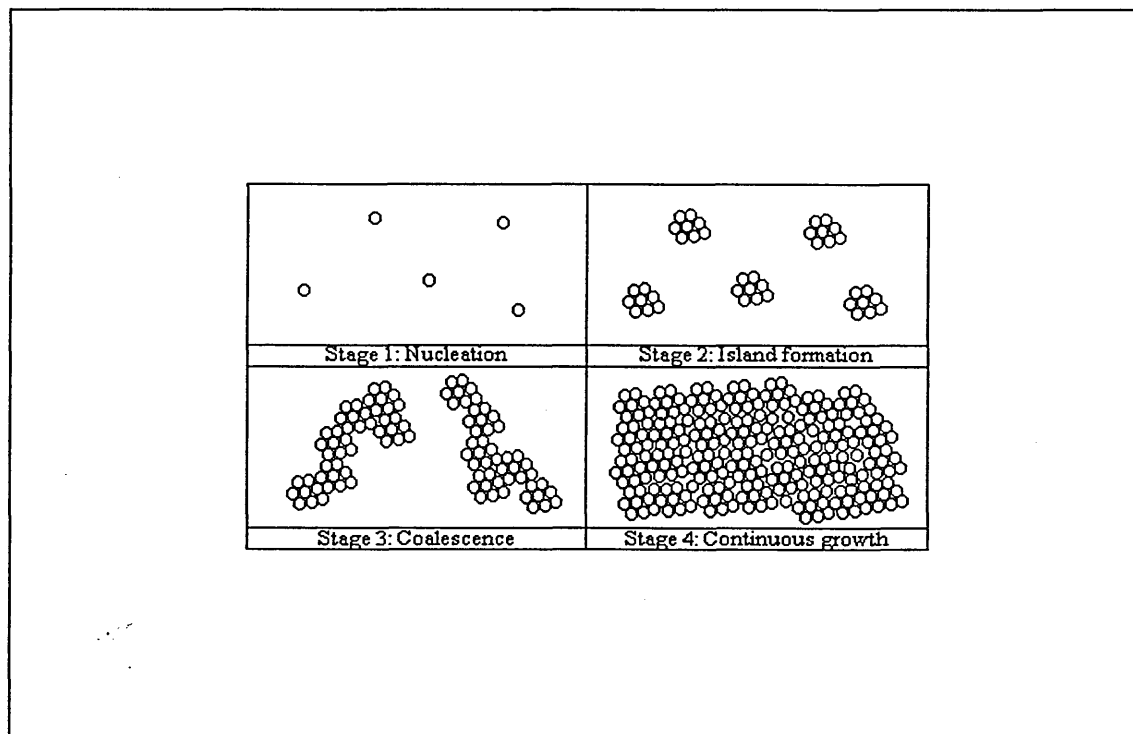
## 2.4. Film Deposition.

### 2.4.1 Nucleation and growth mechanisms.

During PVD coating, the film material is usually deposited atom by atom on a substrate by condensation from the vapour phase to the solid phase. The condensation step cannot be considered as a random impingement of atoms which stick on the growing surface at the point of impact, due to the development of interatomic attractive forces, thermal mobility considerations and surface defects. Normally the coating atoms arrive with low kinetic energy (few eV) and produce a film by the following simplified growth route.

Generally, a four stage dynamic process occurs consisting of nucleation, island growth, coalescence or competitive growth and finally continuous growth (figure 2.22).

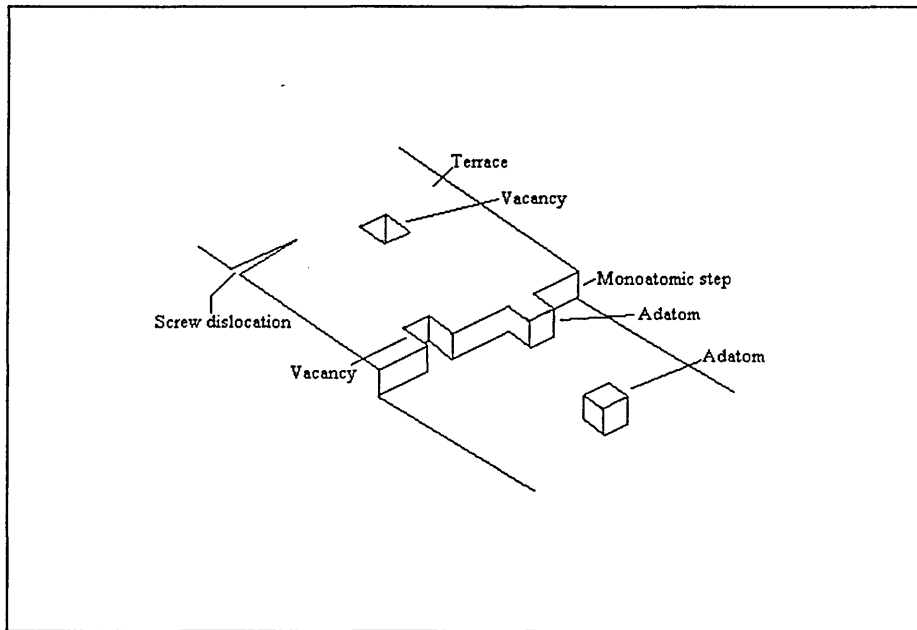
Figure 2.22. A simplified model of coating nucleation and growth.



Stage 1, nucleation, is one of the most important steps in PVD since it strongly affects coating adhesion, grain size, orientation and density. It is believed that the probability of coating atoms to nucleate on a substrate is highest at sites where defects exist to provide localised changes in the electronic states of the surface, a lack of adjacent neighbouring atoms and a subsequent availability of chemical bonds for possible reaction (136).

A polycrystalline solid surface normally exhibits many defect structures, such as dislocations, vacancies, and steps or barriers (on an atomic scale) formed by new atomic layers building up on layers below (137). It is at these steps and defects where the strongest adsorption sites occurs (figure 2.23).

Figure 2.23. Schematic of defects and atomic step adsorption sites on a substrate.



If the atoms are deposited at low substrate temperatures, thermodynamic considerations lead to the condensed atoms having insufficient kinetic energy and surface mobility to cross the steps and reach positions of lower potential energy (stable nucleation sites). A similar effect can also be observed at high deposition rates where adatoms have insufficient time to find low energy sites before being buried by subsequent depositing layers (figure 2.24), and this can eventually result in extensive self-shadowing (138), low density and high coating porosity (139).

If the substrate temperature is increased (by radiant heating or low energy ion bombardment) to a critical level, normally around  $0.3 T_m$  (melting temperature), the atoms receive sufficient energy to overcome the potential barrier which holds them in their initial site positions (figure 2.25) and they can become migrating or surface diffusing adatoms which actively seek neighbouring positions at lower potential energies (140).

Figure 2.24. The effect of increasing energetic ion bombardment and adatom mobility.

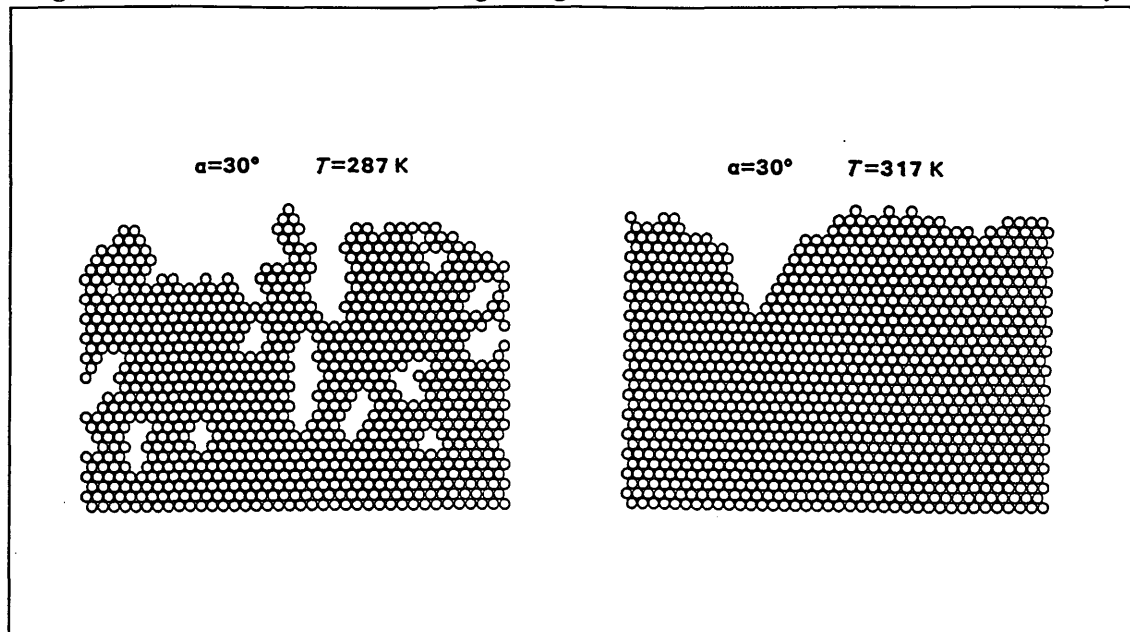
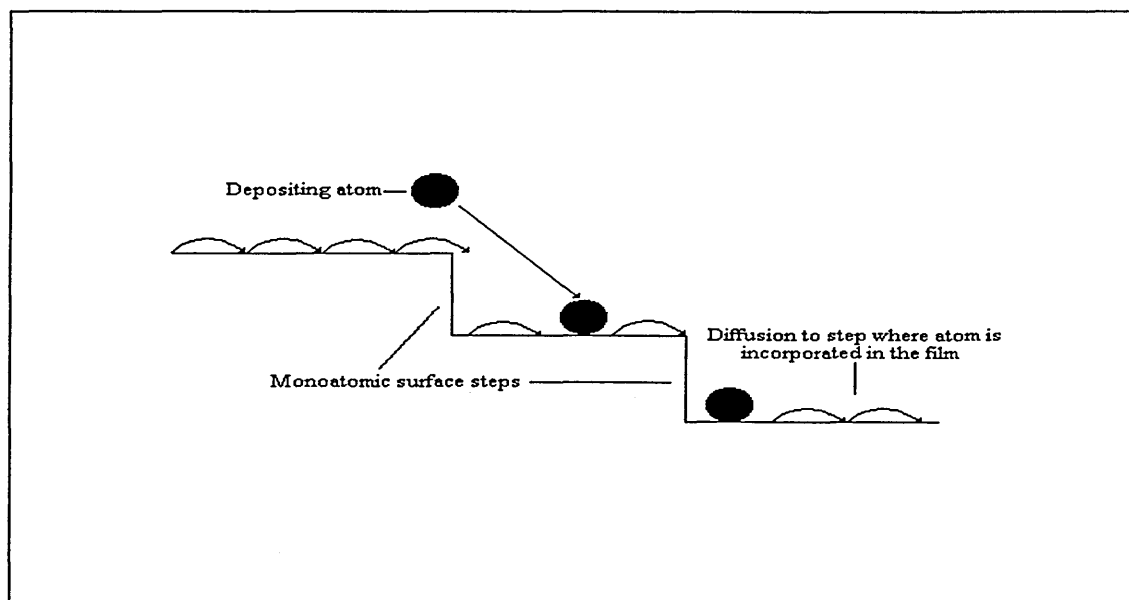


Figure 2.25. Surface diffusion of adatoms on heated substrates.



Once nucleation sites have been established the film starts to grow vertically and horizontally as expanding "islands" until their growth fronts meet other islands growing similarly. The effect of this is to provide a grain boundary defect and promote island growth only in the vertical direction.

In stage three, large scale coalescence of the growing islands occurs across many regions of the substrate. Each cluster of islands contains grains which were orientated so as to closely match the underlying substrate surface grain orientation at its original adsorption site. Competitive growth occurs with the most favoured (due to the incident ion energy, anisotropy in the surface energy for different crystallographic planes and gas pressure) taking precedence to give a preferred orientation.

Finally the entire substrate becomes coated, the film thickens and columns cluster tightly together to form large features with a dominant preferred orientation commonly observed as a columnar structure (141). Recently a more formal understanding of early growth modes in PVD thin films has been established through three mechanisms (142):

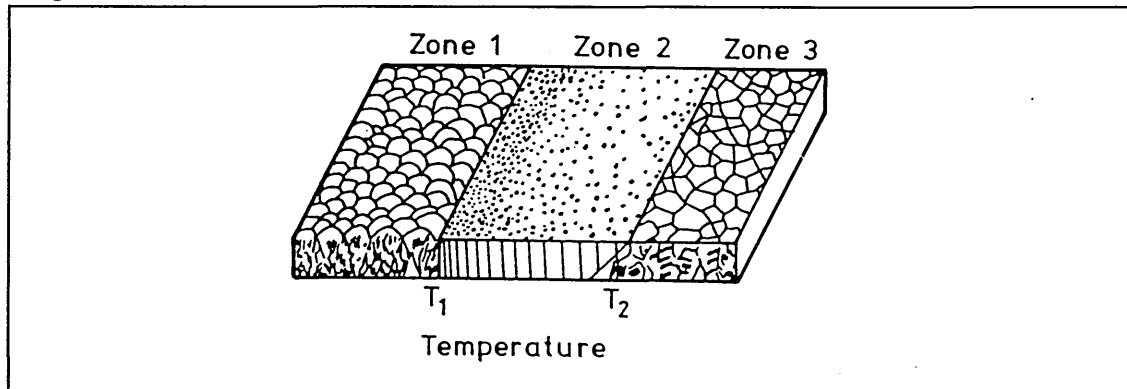
- (i) Layer-by-layer growth (Frank-van-der-Merwe) - When the binding energy of the film atoms ( $E_{f-f}$ ) is equal or less than the binding energy between the film and substrate atoms ( $E_{f-s}$ ).
- (ii) Three dimensional island growth (Volmer-Weber) - When ( $E_{f-f}$ ) > ( $E_{f-s}$ ) resulting in an immediate nucleation of small clusters of film atoms on the substrate surface (common mode for metals on insulators).
- (iii) Combined layer-by-layer and three dimensional island growth (Stranski-Krastanov) - this is still not completely understood but is believed to be partly due to a release of elastic energy from the coating / substrate interface.

#### 2.4.2 Structure zone models and film microstructure.

The exact nature of the columnar morphology generally observed in PVD thin films is thought to be dependent on the interrelated parameters of the incident ion energy of the bombarding species, the accelerating voltage applied to the substrate, the pressure within the chamber (effects of gas scattering) and the substrate temperature. Many different microstructures have been observed ranging from porous, open columns through to more fibrous and dense packed re-crystallised grains. Movchan and Demchishin (143) were the first to classify these observations (figure 2.26) with a three zone model which identified structures as a function of the ratio of substrate temperature to melting point ( $T_s / T_m$ ). The characteristics of each zone were:

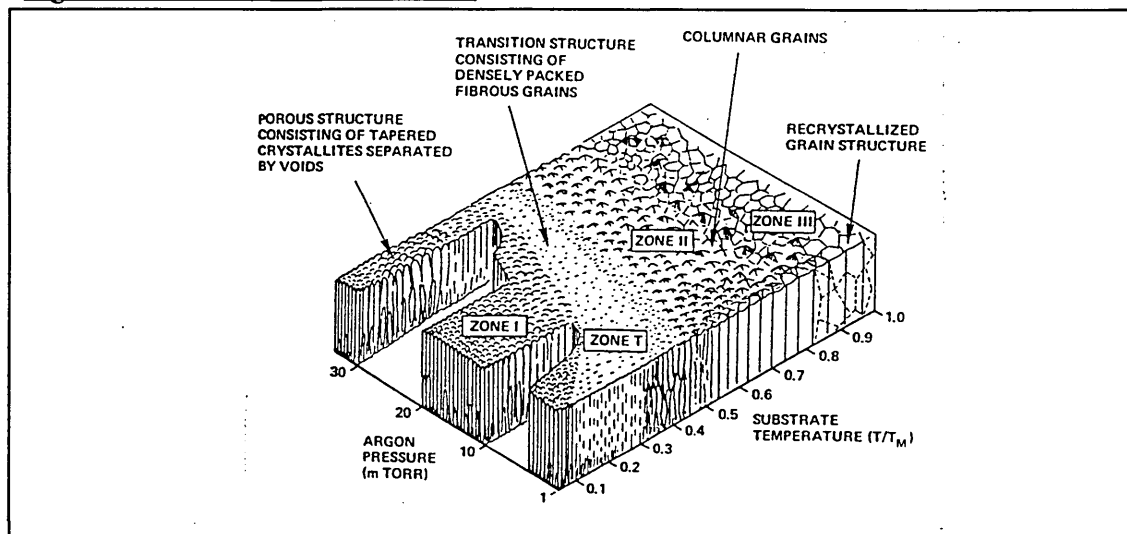
- Zone 1** : Low temperature ( $0-0.3T_S / T_M$ ) zone in which low adatom mobility produced porous films with widely spaced columns and domed or angular tops.
- Zone 2** : Medium temperature ( $0.3-0.45T_S / T_M$ ) zone in which increased adatom mobility and surface diffusion effects caused significant densification of the columns and smooth tops.
- Zone 3** : High temperature ( $0.45-1T_S / T_M$ ) zone in which bulk diffusion and re-crystallisation effects dominate and the structure becomes more equiaxed.

Figure 2.26. Movchan and Demchishin zone model.



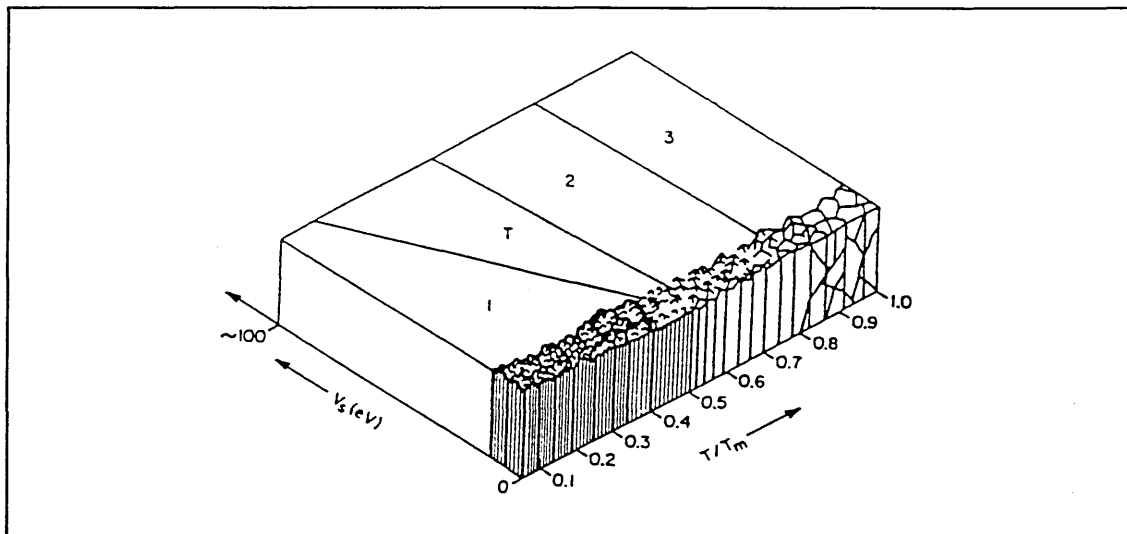
During 1974 this zone model was adapted to take account of the influence of pressure and substrate temperature by Thornton (144) (figure 2.27). Analysis showed that with increasing substrate temperature, a dense transition zone (zone-T) could be formed between the zone 1 open columnar arrangement and the dense columnar morphology of zone 2. This model also demonstrates that the minimum temperature to a grow a dense film (zone-T) increases with higher pressures.

Figure 2.27. Thornton zone model.



The final revision of the zone model was made by Messier (145) in 1984 to take account of the increase in substrate temperature, adatom mobility and point defect generation with the application of a negative substrate bias voltage (figure 2.28). Messier's examinations revealed a movement of the dense zone-T region towards lower temperatures with increasing negative bias (confirmed experimentally by Mattox (146)) and that only through precise control of the bias voltage, pressure and temperature could a desired and reproducible film micro-structure be possible.

Figure 2.28. Messier zone model.



#### 2.4.3. $Ar^+$ Sputter etching and metallic interlayers.

Sputter etching is usually one of the preliminary stages prior to the deposition process, undertaken after a suitable vacuum pressure has been reached in the system and the targets have been sputter cleaned. Generally an argon glow discharge is initiated and a high negative bias voltage (typically -1KV) is applied to the substrate which will behave in a manner similar to the cathode. The accelerated  $Ar^+$  ions will impinge on the substrate surface with sufficient momentum to create primary recoil atoms in the surface layers and set up collision cascades which cause sputtering. The effect of this is :

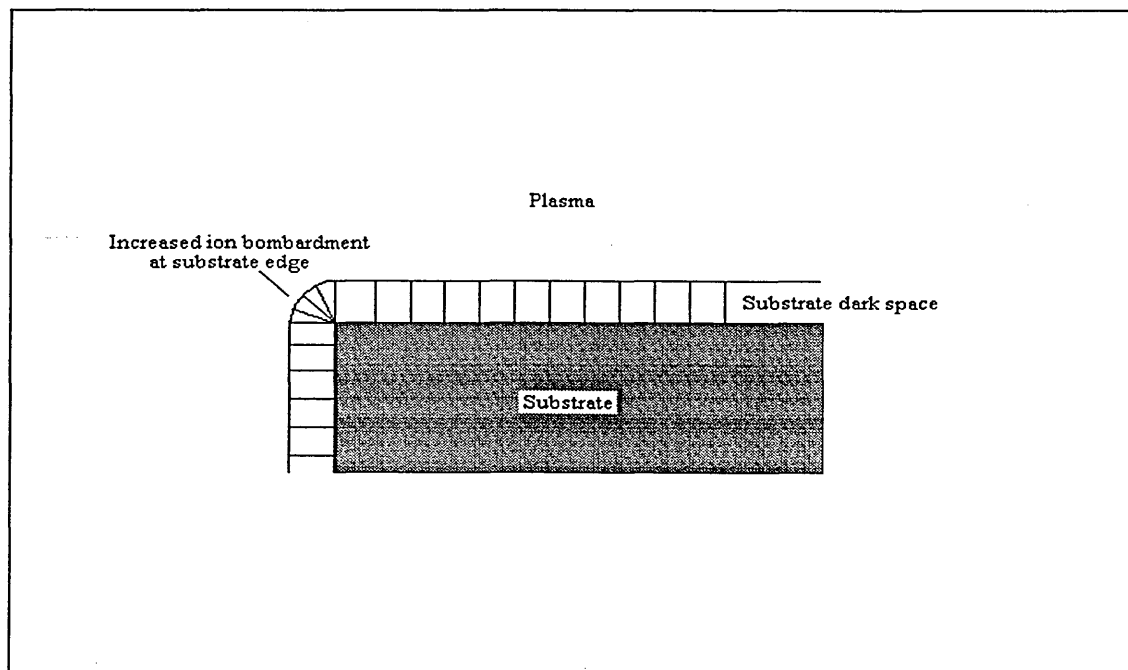
- (a) The sputtering of surface contaminants and general cleaning of the substrate.
- (b) Substrate heating and the removal of surface oxides.
- (c) A general roughening of the surface and the introduction of higher defect density.
- (d) The possibility of preferential sputtering and the development of protrusions to allow "mechanical keying"(147).
- (e) An improvement in coating adhesion.

For many operations (e.g. decorative) the increase in surface roughness and decrease in surface lustre effects through sputter etching cannot be tolerated. Another possible method to improve adhesion (148,149) in this situation is the use of a metallic interlayer (a layer of pure metal which lies between the substrate and working film). The adhesion enhancement is thought to result from a combination of chemical gettering and mechanical effects. Many pure metals, such as titanium, can dissolve weak surface oxide layers, whilst a soft and ductile layer can reduce shear stresses at the coating / substrate interface and hinder crack propagation. Generally these layers are of optimised thickness (0.1-0.4 $\mu\text{m}$ ) to provide an improved adhesive performance without affecting the mechanical properties of the working layer.

#### 2.4.4 Biasing edge effects.

Most PVD techniques utilise low energy ion irradiation of the growing film (30-250eV) to create higher packing density, an increase in surface temperature and adatom mobility, the generation of point defects and smaller grain size (150-152). However, these so-called "ion plating" (153) technologies can encounter difficulties in ensuring uniform ion bombardment when substrates are of complex 3-dimensional geometry.

Figure 2.29. Edge effects through low energy ion bombardment.



Since the substrate material acts as a cathode with respect to the plasma, it will obtain a dark space region across which most of the bias potential is dropped (section 2.1.3). At the edge regions or corners of the substrate, the ratio of dark space area to substrate will be largest, causing an increase in the ion current density drawn at these points (figure 2.29). If the bias current density is too large, re-sputtering of the growing film, ion bombardment damage and overheating of the film (annealing) and temperature sensitive substrates can occur.

#### 2.4.5. Residual stress.

Coatings deposited by PVD ion plating techniques commonly exhibit compressive residual stress which dictates to an extent the levels of coating thickness which can be applied prior to spallation (154), the coating adhesion to the substrate and the hardness of the film. It is generally accepted that this residual or internal stress consists of a combination of two components (155), intrinsic stress and thermal stress which can sum to levels as high as several gigapascals (GPa) in both reactive evaporated or sputtered films.

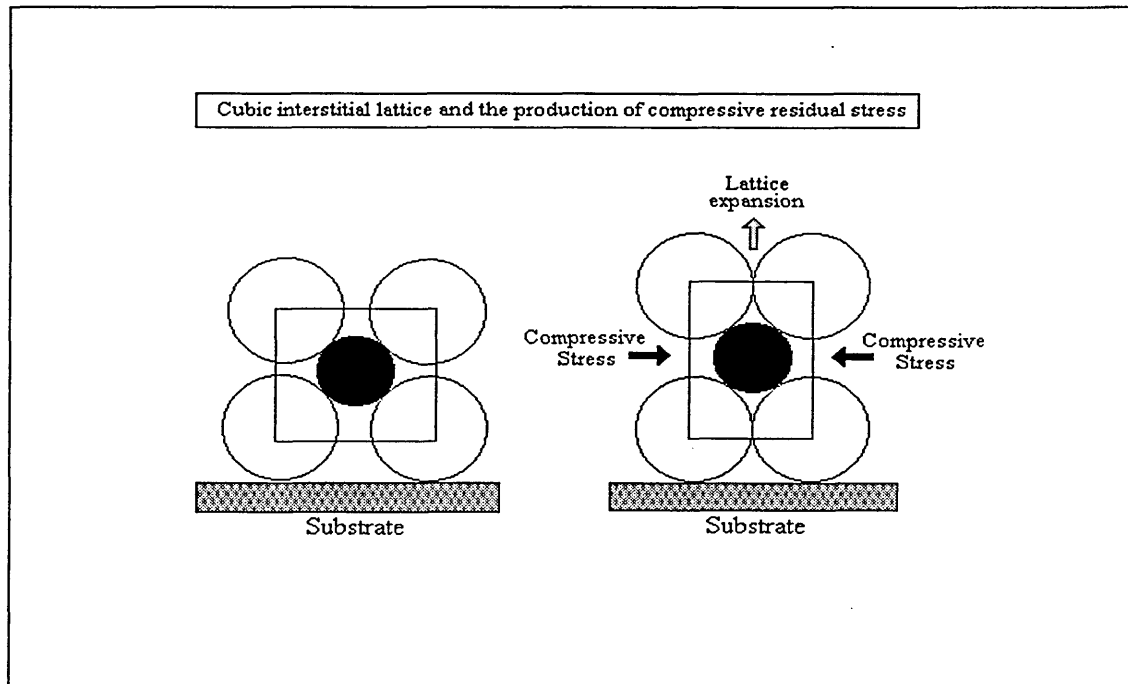
The intrinsic stress originates from the growth process as a result of in-grown defects and structural mismatch between the coating and substrate lattices. These growth induced stresses are a function of the microstructure, the ion density and the level of ion energy during bombardment of the growing film and can be calculated using;

$$\sigma = K R I_e^{1/2} \quad \dots\text{equation 2.12.}$$

where; K = material dependant constant,  $I_e$  = Ion energy, R = Ion to atom arrival rate.

Ion bombardment tends to generate compressive stress by an "ion-peening" mechanism in which the surface region of the growing film undergoes plastic deformation to accommodate defects. The extent of columnar packing also contributes to the level of stress, as pressing at tight columnar boundaries (Zone-T structures) creates more stress than in open columnar structures where relaxation into expanded voids is possible (so-called Zone-1). Clearly, any forced expansion or trapping of the depositing film lattice (interstitial atoms such as  $N_2$  or bombarding ions such as  $Ar^+$ ) will also make a significant contribution (156) (figure 2.30).

Figure 2.30. Interstitial distortion of a cubic lattice and the generation of compressive residual stress.



The thermal stress originates from the difference in the thermal expansion coefficients of the film and the substrate lattices. Hence, any fluctuation in the deposition temperature or cooling rate during the process will cause changes in the thermal induced stress of the system. This can be calculated using;

$$\sigma = \frac{E\Delta\alpha\Delta T}{1-\nu} \text{ .....equation 2.13.}$$

where; E = Young's modulus of the coating

$\Delta\alpha$  = Difference in thermal expansion coefficients.

$\Delta T$  = Difference between room temperature and deposition temperature.

$\nu$  = Poisson's ratio.

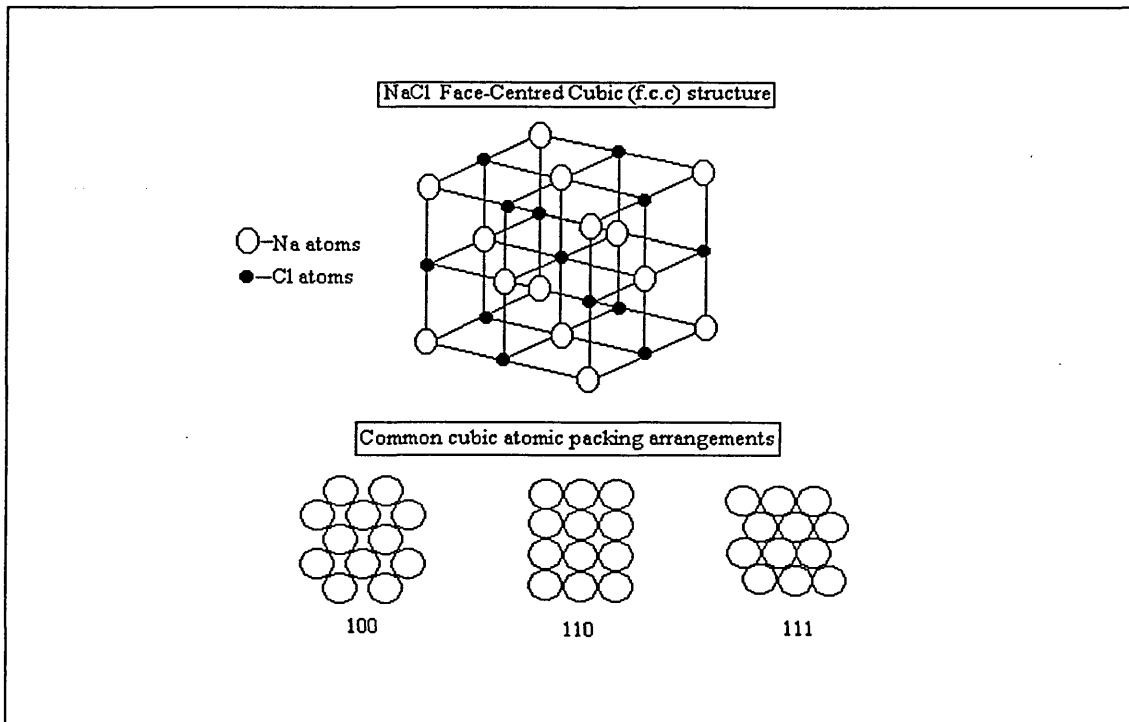
## 2.5 Coating systems.

This section of the literature review will describe the historical development of the three generations of PVD hard coatings. However due to the enormous number and complexity of coating systems which have been or are currently under investigation, only the principal coating systems and their general mechanical and physical properties will be illustrated and references will be given if the reader requires further information.

### 2.5.1. The first generation of PVD hard coatings.

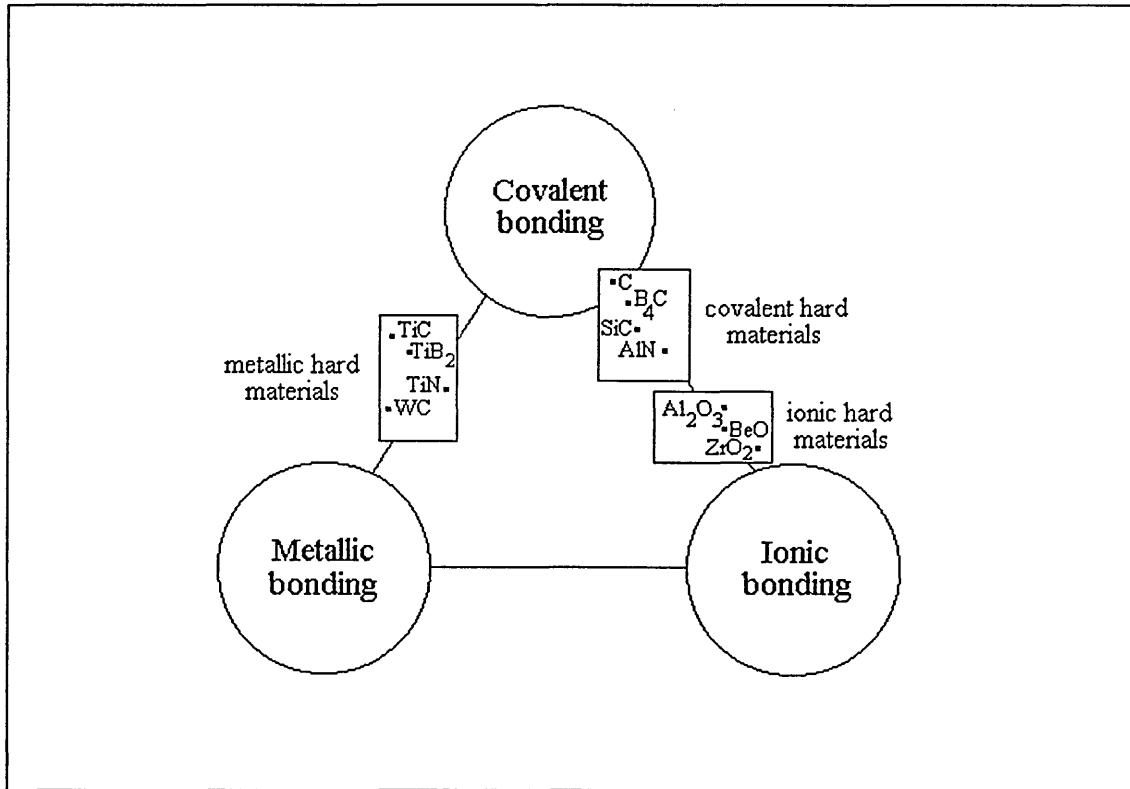
The first generation of PVD hard coatings, developed during the early 1980's, is considered to be the binary pseudo-ceramic materials which are characterised by single metal-non-metal compounds. The most frequently studied compounds have been the transition and refractory metal nitride, carbide and boride films, many of which crystallise into interstitial solid solutions with a face-centred cubic structure (figure 2.31). A variety of dense packing arrangements are possible with unit cells constructed of large cubic metallic lattices into which the non-metal atoms are positioned in the octahedral sites (interstices) and joined by a combination of covalent and heteropolar (metallic and ionic) bonding fractions.

Figure 2.31. The NaCl face centred cubic unit cell and common packing arrangements.



The vast majority of this early fundamental research centred on TiN due to its high hardness, gold colour, relative inexpense and availability as a target material and its position in the centre of the bonding triangle (figure 2.32) (157).

Figure 2.32. Schematic representation of the pseudo-ceramic material bonding types.



Numerous excellent reports on the properties of TiN exist in literature today, but the perhaps the most revealing on the reactive deposition and growth were by Musil, Kadlec and Vyskocil (158,159), Hedenqvist et al (160) and Sproul et al (161), whilst the most important analysis of the film micro-structure and properties was undertaken by Håkansson et al (162), Hultman et al (163), Petrov et al (164) and Rickerby et al (165). Today, the TiN coating system is still the most widely used of all PVD coatings for a variety of tribological (166), decorative (167) and industrial applications, has widespread commercial availability and is often used as a standard against which improvements in coating properties and substrate performance may be judged.

Interest in deposition with other elements from group IVA-VIa in the periodic table quickly occurred, with important works by Perry (168) on the examination of fundamental structural properties of ZrN and Jehn (169) and Sue (170) on the reactivity and behaviour of ZrN. Perry(171), Rudnik (172), Savvides (173) and Sproul (174) have

investigated the various phases of less reactive metal compounds such as Mo<sub>2</sub>N for wear resistance and super-conductivity, Aubert studied CrN for corrosion and wear resistance (175), Perry and Sproul analysed HfN for wear resistance and Hotovy (176) examined NbN films for micro-electronics applications. Some of their typical mechanical and physical properties are shown in table 2.1.

Table 2.1. The properties of some first generation metal nitride films.

	TiN	ZrN	CrN	HfN	Mo <sub>2</sub> N
Thickness (µm)	2.8-3.4	3.0-4.0	3.0-5.0	2.0-4.0	3.0-5.0
Micro-hardness on HSS (H <sub>v</sub> 25gf)	2200-2500	2000-2400	1700-1900	2500-2700	1700-2300
Roughness R <sub>a</sub> (µm)	0.02-0.13	0.02-0.11	0.03-0.09	0.02-0.12	0.02-0.11
Critical load (N)	60-80	50-60	50-80	50-60	50-60
Adhesion judgement (Class)	1-2	1-2	1-2	1-2	1-2
Colour L*	70-75	80-88	70-75		
a*	3.0-6.0	-1.0-0.0	-0.20-0.15	N/A	N/A
b*	30-40	14-28	0.10-1.80		

The interstices available in the metals detailed previously are of dimensions which allow other interstitial atoms such as C, B, H and O to be accommodated within the metal lattice (table 2.2) without large scale distortion (when a solvent accepts one of these interstitials there is generally a lattice expansion of the unit cell).

Table 2.2. The atomic radii of common constituents of reactive gases.

Element	H	B	C	N	O
Atomic radius (Å)	0.46	0.97	0.77	0.71	0.60

Steinmann and Hintermann (177) have studied the deposition and compared the properties of TiC films, Brückner et al (178) have examined the role of different Ar/CH<sub>4</sub> mixtures in ZrC films and Sella (179) investigated the interfaces and properties

of sputtered NiC, CoC and FeC films on glass and Si substrates. Studies on wear resistant TiB<sub>2</sub> coatings have also been undertaken by various groups including Knotek et al (180).

Research has shown that metal oxide films are intrinsically more heteropolar materials than the carbide or nitride systems and their unit cell arrangements are the opposite, i.e. the small metal cations are distributed regularly over the relatively simple sublattices of large oxygen anions. Many oxides form MO compounds (where M=a metal element) with NaCl structures, however other common oxide forms include MO<sub>2</sub> (SiO<sub>2</sub> and TiO<sub>2</sub>) or multi-phase M<sub>2</sub>O<sub>3</sub> arrangements (e.g. Al<sub>2</sub>O<sub>3</sub>). Most of these oxide systems are strongly insulating and are difficult to form by conventional steered arc evaporation PVD due to metallic macro-particle formation. The oxide systems are generally highly reactive and exhibit extreme hysteresis behaviour in reactive sputtering such that conventional gas flow control systems are unable to deposit stable, stoichiometric films and their poor electrical conductivity properties causes problems with standard d.c. biasing configurations. Schiller et al (181) and Scholl (182) have recently demonstrated pulse biasing, plasma emission monitoring and a.c. cathode power supply techniques can alleviate these problems. The use of PVD oxide films is growing steadily and they have found industrial applications in fields as varied as optical filtering on lenses through to hygienic barrier films in the food packaging industry.

#### 2.5.2. The second generation of PVD hard coatings.

The mid 1980's saw the development of the second generation of PVD hard coatings which are considered to be the multi-component materials. These can be formed in two distinct ways:

- (i) The substitution of further metal elements into a binary pseudo-ceramic film to form solid solutions in either an equilibrium or metastable super-saturated state generally resulting in strengthening, an increase in hardness and more favourable performance.
- (ii) The mixing of reactive gases (e.g. N<sub>2</sub> & CH<sub>4</sub>) to utilise extended formation of interstitial solid solutions such as TiCN.

In case (i), metastable materials are produced by the quenching of a multi-elemental pseudo-ceramic from the vapour phase which serves to synthesise a stable solid solution even when equilibrium conditions are not possible. This generally occurs when the desired coating is comprised of a combination of metallic bonding and covalent bonding

hard materials. A classical example of this metastable behaviour is titanium aluminium nitride ( $Ti+Al+N=TiAlN$ ) which when deposited by PVD techniques exists at room temperature in its high temperature f.c.c. phase instead of the h.c.p (hexagonal close packed) structure predicted by the phase diagram. However if the desired coating is comprised of a combination of similar bonding hard materials, stable solid solutions under equilibrium conditions are possible, i.e.  $Ti+Zr+N = TiZrN$  f.c.c phase. Here the Zr atoms can substitute at sites on the TiN lattice where Ti atoms would normally sit to atomic compositions from 0-100%.

It is has been established in many operations that no one binary film exhibits the maximum mechanical and physical properties required to achieve optimum component performance, however comparison of their individual properties based on bonding type and the requirements of the coating operation allows selection of an appropriate ternary or quaternary film to be deposited (table 2.3).

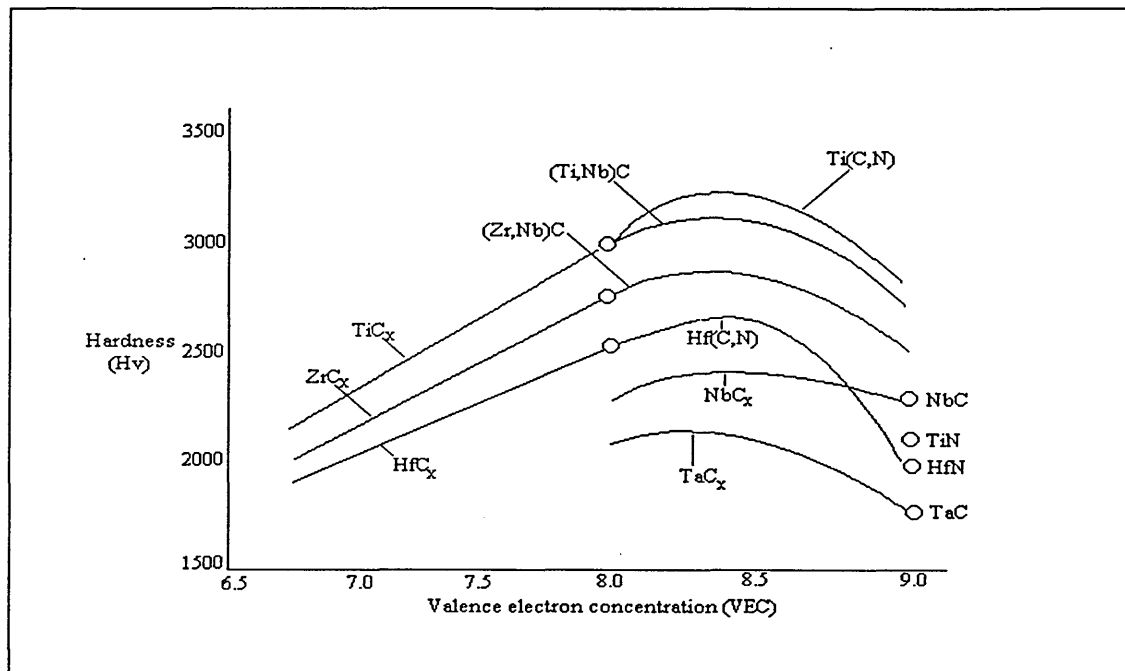
Table 2.3. Properties and behaviour of various hard coating groups.

Level	Hardness	Brittleness	Melting point	Stability ( $\Delta G$ )	Thermal expansion	Adherence	Inter-action
High	C	I	M	I	I	M	M
Med	M	C	C	M	M	I	C
Low	I	M	I	C	C	C	I

where C= Covalent bonding tendency, I=Ionic, M=Metallic.

In case (ii), variation in the relative concentrations of the mixed reactive gases, thereby changing the valence electron concentration (VEC), makes substantial changes in the mechanical and physical properties of the film. Investigations have shown that the maximum hardness of carbide and carbo-nitride systems (figure 2.33) occurs when the VEC is approximately 8.4 (183) and similar diagrams have been found for toughness, chemical stability and wear resistance.

Figure 2.33. The microhardness of various pseudo-ceramic materials as a function of valence electron concentration.



The past ten years have seen an expansion in the diversity of alloy nitride, carbide and carbo-nitride second generation coatings developed for a wide range of industrial applications. The most important developments for tribological use are TiAlN films (184-186) for increased oxidation resistance, TiCN(187), TiZrN (188-190) and TiBN(191) for significantly increased film micro-hardness and tribological properties and TiCrN(192) for combined corrosion and wear resistance. Today, both the number and combinations of elements in the films being studied and utilised by specialist end-users (e.g. aerospace & MCrAlY, Ti6Al4V based coatings) is increasing. Some of the standard second generation coating properties which are becoming commercially available are illustrated in table 2.4.

Table 2.4. Typical properties of various second generation PVD films.

	TiCN	TiAlN	TiZrN	CrAlN	TiNbN
Thickness ( $\mu\text{m}$ )	2.5-3.0	2.7-3.0	2.5-4.0	2.5-3.3	2.5-3.3
Micro-hardness ( $H_V25\text{gf}$ )	2300-2500	2350-2400	2400-3600	2000-2150	2200-2440
Roughness $R_a$ ( $\mu\text{m}$ )	0.04-0.21	0.06-0.28	0.02-0.15	0.04-0.17	0.10-0.18

	TiCN	TiAlN	TiZrN	CrAlN	TiNbN
Critical load (N)	40-60	60-70	45-60	50-70	60-70
Adhesion judgement (Class)	1-2	1-2	1-2	1-2	1-2
Colour L*	51-59	42-45	75-85	60-64	72-75
a*	7-12	2.1-2.3	0-2.0	0.5-0.6	4.7-7.4
b*	5-11	-0.4--0.6	20-30	3.0-3.6	32-34

### 2.5.3 The third generation of PVD hard coatings.

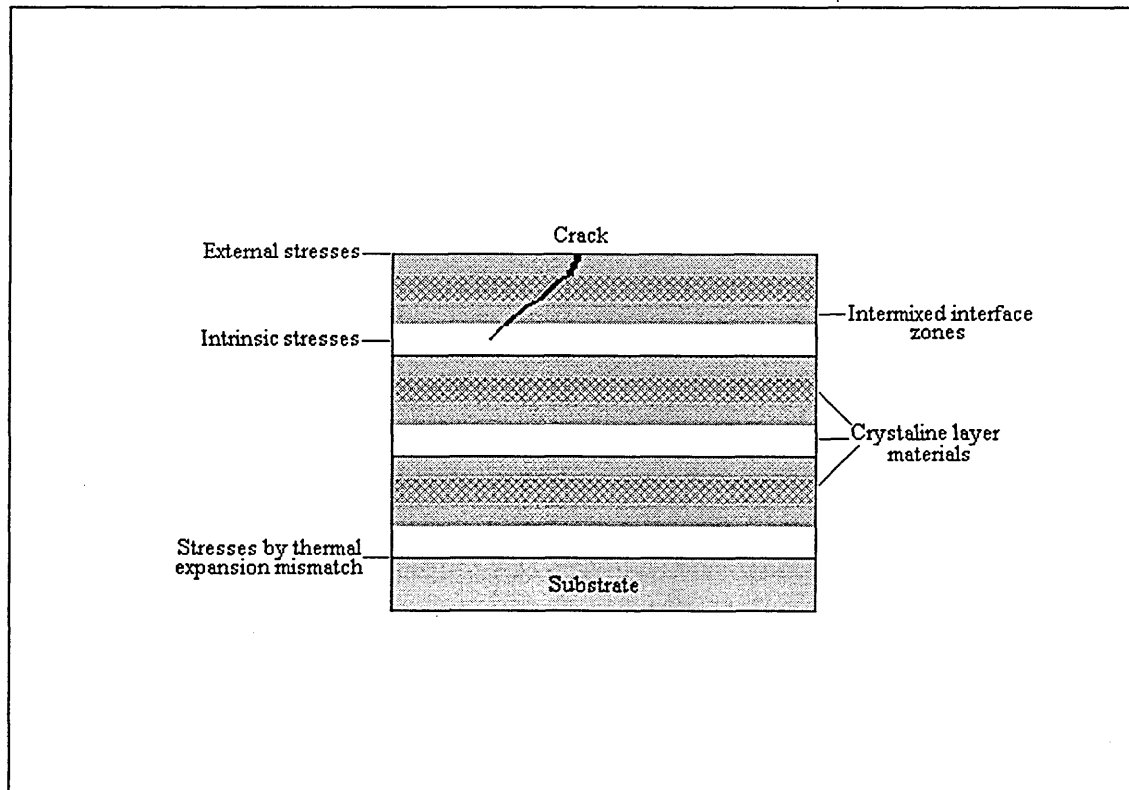
The third generation of PVD hard coatings is considered to be the multi-layered and superlattice pseudo-ceramic materials. These can generally be defined by two classes;

(i) Metal / ceramic multi-layers - where variation in the reactive gas partial pressure occurs during deposition to form alternating metal / pseudo-ceramic layers (i.e. M / MN film structure such as Ti / TiN).

(ii) Ceramic / ceramic multi-layers - where variation in the elemental composition of the metal coating flux or periodic changes of the reactive gas species occurs during deposition to form alternating pseudo-ceramic layers (i.e.  $M_1N / M_2N$  or  $MN / MC$  film structures such as TiN / NbN or TiN / TiC).

PVD technology, using either evaporation or sputtering techniques, has been successfully applied to produce many different types of multi-layer coatings on a wide variety of substrates (193-196). Holleck and his co-workers (197) along with Freller and Haessler (198) have broadly studied the production, properties and performance of magnetron sputtered multi-layer coatings to enhance tribological and crack deflection mechanisms (figure 2.34).

Figure 2.34. Schematic diagram of a possible multi-layer film crack deflection mechanism.



Knotek and Leyendecker (199) have successfully applied 30 layers of TiN / Al<sub>2</sub>O<sub>3</sub> to cemented carbide substrates and Keem (200) has reported improved performance of HfC / HfN multi-layer coatings on drill bits when compared against TiN. During the early 1990's the breadth of research into the mechanical and physical properties of multi-layers increased at a pace with excellent works on their characteristics published by Strafford et al (201), their architecture and deposition by Vetter et al (202) and Sproul (203) and their performance by Knotek et al (204).

If the period of the multi-layer is reduced to a level below 10-15nm (100-150Å) whilst maintaining the alternating arrangement and long range periodic order, the system can attain a unique reciprocal lattice different to the two layer materials which form it - characteristic of a "superlattice". This generally causes a grain size refining effect from the continual breaks in the growth and re-nucleation processes consistent with Wulff's law (205) (equation 2.14) and is partly attributable to substantial increases in the hardness of superlattice films due to the Hall-Petch effect (206,207)(equation 2.15).

$$\gamma / h = \text{constant} \quad \dots \text{equation 2.14}$$

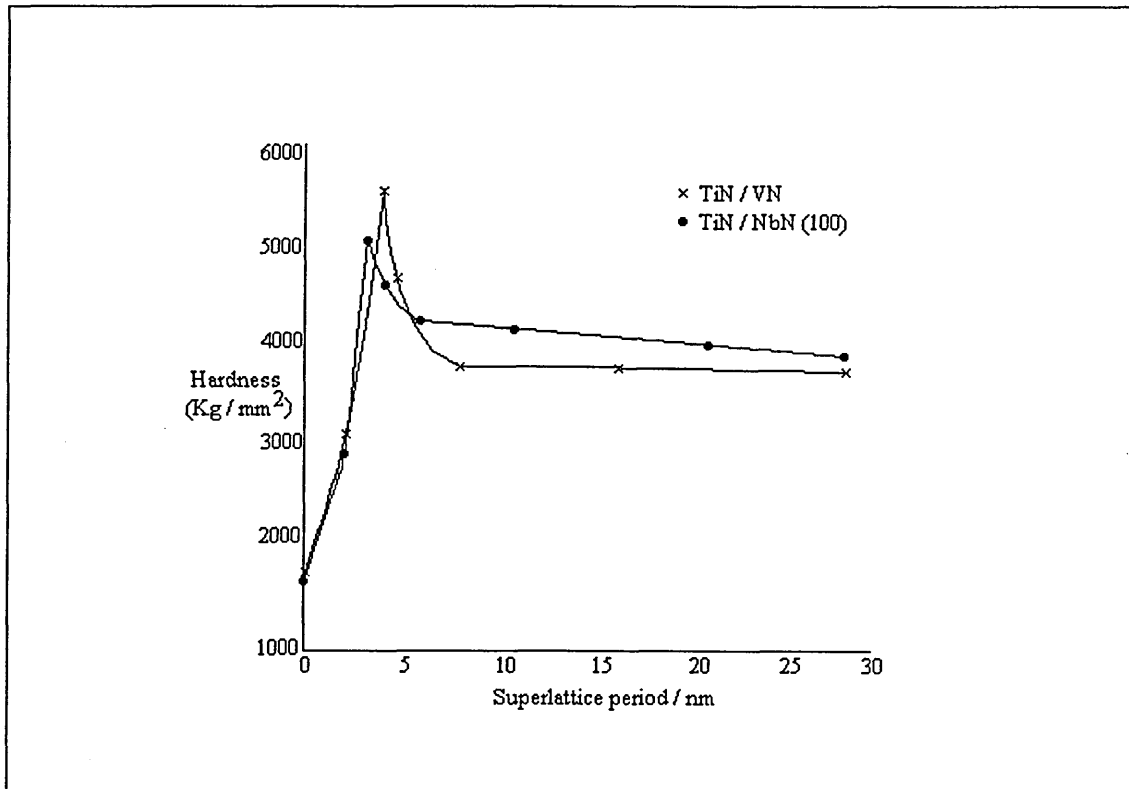
where;  $\gamma$  = The special free surface energy of the crystallographic plane considered.  
 $h$  = The spacing between the above mentioned crystallographic plane and its adjacent identical plane.

$$\sigma_{LY} = \sigma_0 + Kd^{-1/2} \quad \dots \text{equation 2.15}$$

where;  $\sigma_{LY}$  = lower yield strength,  $d$  = grain size,  $\sigma_0$  &  $K$  = constants.

Recent work by Shinn et al (208) has shown that for TiN / VN and TiN / NbN based layered systems with near equal layer thickness, there was a gradual increase in hardness to levels around 4000 Kgmm<sup>-2</sup> until at periods of approximately 40Å a sharp maxima occurred rising to values over 5000Kg/mm<sup>2</sup> (figure 2.35).

Figure 2.35. Hardness as a function of TiN based multi-layer period.



Lehoczky (209) and Koehler (210) have also made theoretical predictions on the strong influence of the difference in dislocation line energies and shear modulus of layer materials to explain high superlattice yield strength and hardness data.

The influence of substrate bias voltage (low energy ion irradiation) and deposition temperature on superlattice film coherency, interfacial mixing (figure 2.36) and layer thickness when produced by an ion plating technique has been studied by Håkansson et al (211). Generally the level of interfacial mixing and layer roughness increased with increasing temperature and bias voltage (figure 2.37), whilst the layer thickness decreased as a function of increasing negative substrate bias (-50 to -250V).

Figure 2.36. The effect of deposition temperature and bias voltage on interfacial mixing.

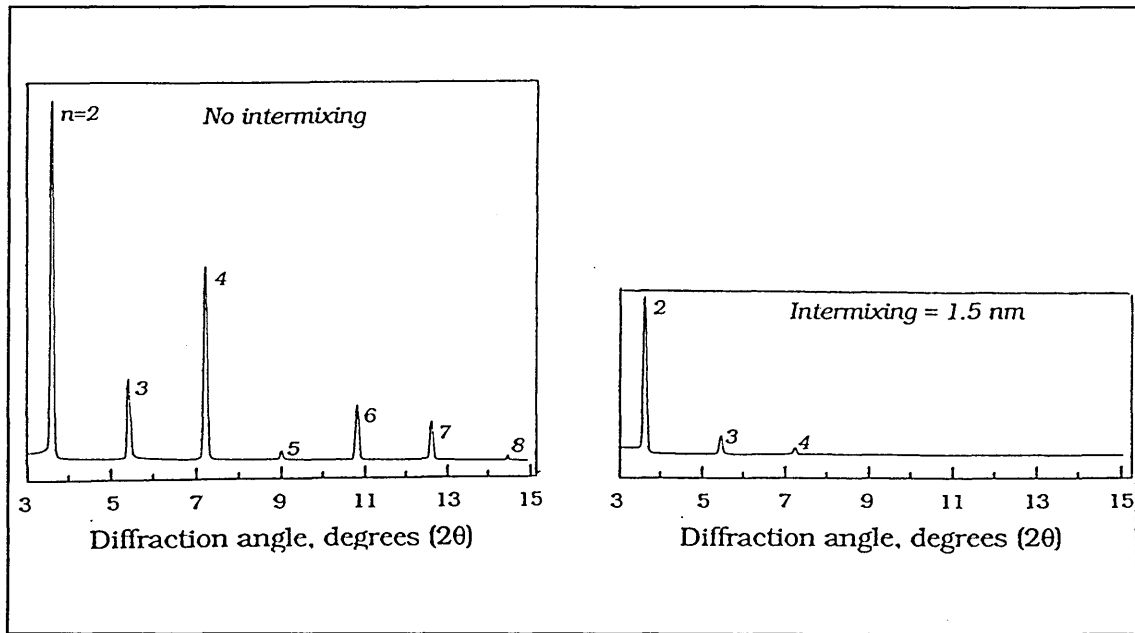
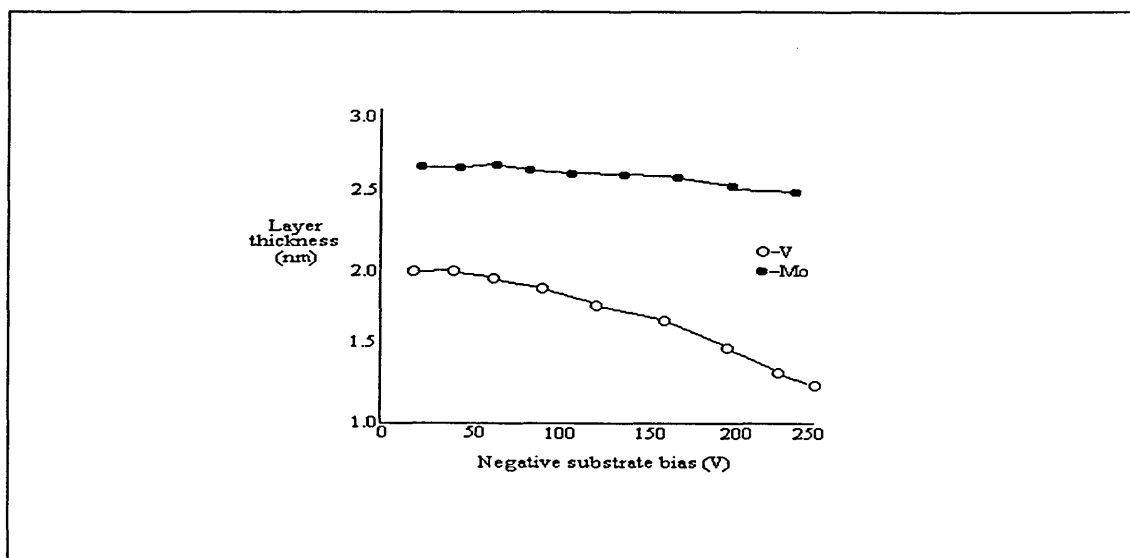


Figure 2.37 Influence of substrate bias voltage on layer thickness.



However, most superlattice coatings have only been fabricated on a small experimental scale, usually requiring complex reactive gas partial pressure control, atmospheric separation and shuttering mechanisms, and optimised commercial coating at industrial scale is currently unavailable. For a more detailed review of the theories, properties and deposition of a variety of superlattice systems the reader is directed to an article by Barnett (212).

## 2.6. Summary.

Some of the fundamental properties and principles involved in steered arc evaporation, unbalanced magnetron sputtering and arc-bond sputter technology have been discussed in this chapter. The effects of low energy ion irradiation during deposition, glow discharge and cathodic arc plasma characteristics and the influence of substrate ion etching prior to deposition has been reviewed. Also, the historical utilisation of all three techniques to reactively deposit advanced PVD hard coatings for improved mechanical, decorative, optical and tribological performance has been demonstrated.

The literature survey has highlighted deficiencies in current knowledge and production capabilities in the following areas:-

- (i) The ability of the steered arc technique to reproducibly produce ternary, quaternary and multi-layer/superlattice thin films with reasonable target utilisation.
- (ii) The ability to produce multi-layer/superlattice films at industrial scale by a simple PVD technique.
- (iii) A deeper understanding of the metallurgical and physical properties of multi-elemental films to allow optimisation of mechanical and physical properties such as hardness, oxidation and wear resistance and composition.

## References.

1. R.Behrisch, P.Sigmund, M.T.Robinson, H.H.Andersen, H.L.Bay, H.E.Roosendaal - "*Sputtering by particle bombardment*", Springer-Verlag Berlin press, 1981.
2. W.R.Grove - *Phil.Trans.Roy.Soc.London*, 1842, 142, 87.
3. E.Goldstein - *Verh.Dtsch.Phys.Ges*, 1902, 4, 228-237.
4. J.Stark - *Z.Elektrochem*, 1908, 14, 752.
5. G.Granquist - *Öfvers.Svenska Vet.Akad.Förh*, 1897, 54, 575.
6. K.H.Kingdon, I.Langmuir - *Phys.Rev*, 1922, 20,107.
7. O.Almen, G.Bruce - *Nucl.Instrum.Methods*, 1961, 11, 257-279.
8. P.Sigmund - *Phys.Rev*, 1969, 184, 383.
9. J.Plücker - *Ann.Phys.Chem*, 1858, 103, 88.
10. G.K.Wechner - Report No.2309, 1962, General Mills, Minneapolis, USA.
11. J.L.Vossen, W.Kern - "*Thin Film Processes*", Academic Press, 1978.
12. L.I.Maissel, R.Glang - "*Handbook of thin film technology*", McGraw-Hill Press, 1970.
13. J.J.Cuomo, S.M.Rossnagel, H.R.Kaufman - "*Handbook of ion beam processing technology*", Noyes Publication Press, 1989.
14. S.M.Rossnagel, J.J.Cuomo, W.D.Westwood - "*Handbook of plasma processing technology*", Noyes Publication Press, 1990.
15. D.S.Rickerby, A.Matthews - "*Advanced surface coatings*", Blackie / Chapman-Hall Press, 1991.
16. B.N.Chapman - "*Glow discharge processes*", Wiley New York Press, 1980.
17. G.Mohan Rao, S.Mohan - *J.Appl.Phys*, 1991, 69(9), 6652.
18. L.I.Maissel - "*Physics of Thin Films*", 1966, 3, 61.
19. E.Nasser - "*Fundamentals of gaseous ionisation and plasma electronics*", Wiley New York Press, 1971.
20. R.P.Howson, H.A.J'afar, A.G.Spencer - *Thin Solid Films*, 1990, 193/194, 127.
21. G.N.Jackson - *Thin Solid Films*, 1970, 5, 209.
22. K.S.Fancey, A.Matthews - *Surf.Coat.Tech*, 1987, 33, 17.
23. R.T.Farouki, M.Dalvie - *J.Appl.Phys*, 1990, 68(12), 6106.
24. J.M.Molarius, A.S.Korhonen, E.O.Ristolainen - *J.Vac.Sci.Technol*, 1985, A3(6), 2419.
25. F.M.Penning - *Physica III*, 1936, 9-10, 873-894.
26. P.J.Clarke - *U.S.Patent # 3711398*, 1973.
27. P.S.McLeod, L.D.Hartsough - *J.Vac.Sci.Technol*, 1977, 14, 263.
28. M.Y.Al-Jaroudi, H.T.G.Hentzell, S.E.Hornstrom, A.Bengston - *Thin Solid Films*, 1989, 182, 153.

29. M.Ahern - *Surf.Coat.Tech*, 1990, 43/44, 1-3, 279.
30. O.Knotek, M.Atzor, F.Jungblut - *Plasma.Surf.Eng*, 1989, 1, 579.
31. J.A.Thornton - *SAE report #730544*, 1973, SAE, New York, USA.
32. J.A.Thornton - *J.Vac.Sci.Technol*, 1974, 11(4), 666-670.
33. J.A.Thornton, A.S.Penfold - "*Thin Film Processes*", Academic New York Press, 1978.
34. P.J.Clarke - *U.S.Patent #3616450*, 1971.
35. J.S.Chapin - *Research / Development*, 1974, Jan, 37.
36. J.Almeida - *Vacuum*, 1989, 39, 7-8, 717-721.
37. B.N.Chapman - "*Glow discharge processes*", Wiley New York Press, 1980, 268.
38. S.Schiller - *J.Vac.Sci.Techol*, 1987, A5, 2188
39. W-D.Münz - *Vakuum Technik*, 1981, 30, 78.
40. J.Vyskocil, J.Musil, S.Kadlec, W-D.Münz - *Plasma.Surf.Eng.88*, 1989, Garmisch-Partenkirchen, DGM Informationsgesellschaft Verlag, 665.
41. J.Szczyrbowski, G.Tescher - *Proc.38th Annual Technical Conf. Society of Vacuum Coaters*, 1995, Chicago, USA, 389-394.
42. I.Petrov, L.Hultman, U.Helmersson, J-E.Sundgren, J.E.Greene - *Thin Solid Films*, 1989, 169, 299.
43. W.Yao, S.Tung, W.Shi, Z.Qi - *Plasma.Surf.Eng*, 1989, 1, 633.
44. W.D.Sproul - *Surf.Coat.Tech*, 1991, 49, 284-289.
45. B.Window - *J.Vac.Sci.Technol*, 1985, A3(6), 2368.
46. B.Window, N.Savvides - *J.Vac.Sci.Technol*, 1986, A4(2), 196.
47. B.Window, N.Savvides - *J.Vac.Sci.Technol*, 1986, A4(3), 453.
48. N.Savvides, B.Window - *J.Vac.Sci.Technol*, 1986, A4(3), 504.
49. Airco Temescal - *U.S Patent #4166018*.
50. S.L.Rohde - *Ph.D Thesis*, 1991, NorthWestern University, Illinois, USA.
51. M.S.Wong, W.D.Sproul, S.L.Rohde - *Surf.Coat.Tech*, 1991, 49, 121.
52. J.Musil, S.Kadlec, J.Vyskocil, V.Poulek - *Surf.Coat.Tech*, 1989, 39-40, 301-314.
53. S.Kadlec, J.Musil, V.Valvoda, W-D.Münz - *Vacuum*, 1990, 41(7-9), 2233.
54. S.Kadlec - *J.Vac.Sci.Technol*, 1990, A8(3), 1318.
55. W-D.Münz - *Surf.Coat.Tech*, 1989, 39-40, 487.
56. W-D.Münz - *Conf.Proc.IPAT*, 1989, Geneva, Switzerland, CEP consultants, 100.
57. D.G.Teer - *Surf.Coat.Tech*, 1988, 35, 901.
58. W.D.Sproul - *Proc.35th Annual.Tech.Conf.Soc.Vac.Coat*, 1992, Baltimore, USA, 236-238.
- 59 M.J.Murphy, D.C.Cameron, M.Z.Karim, M.S.J.Hashmi - *Surf.Coat.Tech*, 1993, 57,1.

60. W.D.Sproul, P.J.Rudnik, M.E.Graham, S.L.Rohde - *Surf.Coat.Tech*,1990, 43/44, 270-278.
61. I.Efeoglu, R.D.Arnell, S.F.Tinston, D.G.Teer - *Surf.Coat.Tech*, 1993, 57, 61.
62. J.Musil, S.Kadlec - *Vacuum*, 1990, 40, 435.
63. S.L.Rohde, I.Petrov, W.D.Sproul, S.A.Barnett, P.J.Rudnik, M.E.Graham - *Thin Solid Films*, 1990, 193/194, 117-126.
64. W.D.Sproul - *Surf.Coat.Tech*, 1991, 49, 284-289.
65. W.Fleischer, D.Schulze, R.Wilberg, A.Lunk, F.Schrade - *Thin Solid Films*, 1979, 63, 347.
66. J.Vyskocil, J.Musil, S.Kadlec, W-D.Münz - *Plasma.Surf.Eng*, 1989, 1, 661.
67. U.König - *Surf.Coat.Tech*, 1987, 33, 91-103
68. L.Hultman, W-D.Münz, J.Musil, S.Kadlec, I.Petrov, J.E.Greene - *J.Vac.Sci.Technol*, 1991, A9(3), 434-438.
69. W.D.Sproul - *Surf.Coat.Tech*, 1987, 33, 73.
70. J-E.Sundgren, B.O.Johansson, S.E.Karlsson - *Thin Solid Films*, 1983, 105, 353.
71. A.J.Aronson, D.Chen, W.H.Class - *Thin Solid Films*, 1980, 72, 535.
72. J.Affinito, R.R.Parsons - *J.Vac.Sci.Technol*, 1984, A2, 1275.
73. S.Schiller, U.Heisig, C.Korndörfer, G.Beister, J.Reschke, K.Steinfeldler, J.Strümpfel - *Surf.Coat.Tech*, 1987, 33, 405.
74. C.A.Gogol - *U.S.Patent #4692630*, 1987.
75. W.D.Sproul, J.A.Tomashek - *U.S.Patent #4428811*, 1984.
76. W.D.Sproul, P.J.Rudnik, C.A.Gogol - *Thin Solid Films*, 1989, 171, 171.
77. S.Berg, T.Larsson, C.Nender, H-O.Bolm - *J.Appl.Phys*, 1988, 63, 887.
78. S.Kadlec, J.Musil, J.Vyskocil - *Vacuum*, 1987, 37(10), 729.
79. J.M.Lafferty, J.D.Cobine, G.Ecker, G.A.Farrell, A.N.Greenwood, L.P.Harris - *"Vacuum Arcs - theory and application"*, J.Wiley-Interscience Press, 1980.
80. I.G.Brown, X.Godechot - *IEEE Trans.Plasma.Sci*, 1991, 19(5), 715.
81. I.I.Aksenov, S.I.Vaukula, V.Stel'nitskii, V.M.Khoroshikh - *Sov.Phys-Tech.Phys*, 1980, 25, 1164.
82. R.L.Boxman, S.Goldsmith - *Surf.Coat.Tech*, 1992, 52, 39.
83. J.E.Daalder - *J.Phys.D: Appl.Phys*, 1976, 9, 2379.
84. C.N.Tai, E.S.Koh, K.Ahari - *Surf.Coat.Tech*, 1990, 43/44, 324.
85. A.Burkhardt - *U.S.Patent #2157478*, 1939.
86. A.A.Snaper - *U.S.Patent #3836451* 1974.
87. L.P.Sablev - *U.S.Patent #3783231*, 1974.
88. L.P.Sablev - *U.S.Patent #3793179*, 1974.
89. A.E.Guile, B.Jüttner - *IEEE Trans.Plasma.Sci*, 1980, PS8(3), 259.

90. J.Mitterauer, P.Till, E.Fraunschiel, M.Haider - *7<sup>th</sup> Intl.Symp.on Discharges and Electrical insulation in vacuum*, 1976, Novosibirsk, USSR, 83.
91. F.R.Schwirzke - *IEEE Trans.Plasma.Sci*, 1991, 19(5), 690.
92. V.V.Kanzel, V.I.Rakhovskii - *Proc.6<sup>th</sup>. Intl.Symp.on Discharges and Electrical insulation in vacuum*, 1974, Swansea, 265.
93. B.Jüttner - *Beitr.Plasma.Physik*, 1982, 22, 453.
94. G.Ecker - "*Vacuum Arcs - theory and application*", J.Wiley-Interscience Press, 1980.
95. V.I.Rakhovskii - *IEEE Trans.Plasma.Sci*, 1976, PS4(2), 81.
96. Y.H.Fu, R.P.P.Smeets - *IEEE Trans.Plasma.Sci*, 1989, 17(5), 727.
97. A.I.Bushik, B.Jüttner, H.Pursch - *Beitr.Plasma.Physik*, 1979, 19, 177.
98. L.P.Harris - *8<sup>th</sup> Intl.Symp.on Discharges and Electrical insulation in vacuum*, Albuquerque, 1978, F1, 106.
99. E.Hantzche, B.Jüttner - *IEEE Trans.Plasma.Sci*, 1985, PS13(5), 231.
100. J.E.Daalder - *IEEE Trans.Pow.App.Sys*, 1974, PAS93, 1747.
101. B.E.Djakov, R.Holmes - *J.Phys.D.Appl.Phys*, 1974, 7, 569.
102. L.A.Sena - *Sov.Phys.Tech.Phys*, 1971, 15(9), 1513.
103. V.I.Rakhovskii - *IEEE Trans.Plasma.Sci*, 1990, 18(3), 677.
104. J.E.Daalder - *J.Phys.D.Appl.Phys*, 1983, 16, 17.
105. P.D.Swift, D.R.Mckenzie, I.S.Falconer - *J.Appl.Phys*, 1989, 66(2), 505.
106. S.Ramalingam - *U.S.Patent # 4763477*, 1987.
107. J.R.Morrison - *U.S.Patent # 4724058*, 1988.
108. P.J.Walke - *Ph.D Thesis*, 1994, Sheffield Hallam University, United Kingdom.
109. J.Vyskocil, J.Musil - *Surf.Coat.Tech*, 1990, 43-44, 299.
110. D.Y.Fang - *J.Appl.Phys*, 1982, 15, 833.
111. M.G.Drouet - *Jap.J.Appl.Phys*, 1981, 20(6), 1027.
112. L.P.Harris - *10<sup>th</sup> Intl.Symp.on Discharges and Electrical insulation in vacuum*, 1981, 106.
113. A.P.Nevskii - *Sov.Phys.Tech.Phys*, 1969, 14(6), 803.
114. A.E.Robson, A.von Engel - *Phys.Rev*, 1954, 93a, 653.
115. J.C.Sherman, R.Webster, J.E.Jenkins, R.Holmes - *J.Phys.D.Appl.Phys*, 1972, 8, 249.
116. D.Y.Fang, A.Nurnberg, U.H.Bauder - *J.Nucl.Mat*, 1982, 111-112, 517.
117. H.D.Steffens, M.Mack, K.Moehwald, K.Reichel - *Surf.Coat.Tech*, 1991, 46, 65.
118. H.Brandolf - *U.S.Patent #4511593*, 1985.
119. D.M.Sanders, D.B.Boercker, S.Falabella - *IEEE Trans.Plasma.Sci*, 1990, 18(6), 883-892.

120. G.V.Kljuchko, V.G.Padalka, L.P.Sablev, R.I.Stupak - *U.S.Patent # 4492845*, 1985.
121. P.J.Martin, R.P.Netterfield, A.Bendavid, T.J.Kinder - *Surf.Coat.Tech*, 1992, 54-55,136.
122. O.Knotek, W.D.Münz, T.Leyendecker - *J.Vac.Sci.Technol*, 1987, A5(4), 2173-2179.
123. J.Vetter, H.J.Scholl, O.Knotek - *Surf.Coat.Tech*, 1995, 74-75, 286-291.
124. O.Knotek, F.Löffler, M.Böhmer, R.Breidenbach, C.Stöbel - *Surf.Coat.Tech*, 1991, 49, 263-267.
125. A.Leyland, A.S.James - "*Advanced Surface Coatings*", edited by D.S.Rickerby & A.Matthews, Blackie / Chapman-Hall Press, 1991.
126. B.F.Coll, R.Fontana, A.Gates, P.Sathrum - *Mat.Sci.Eng*, 1991, A140, 816-824.
127. W-D.Münz, D.Schulze, F.J.M.Hauzer - *Surf.Coat.Tech*, 1992, 50, 169.
128. W-D.Münz - *Surf.Coat.Tech*, 1991, 48, 93.
129. T.Weber, J.Verhoeven, F.W.Saris, T.Osipowicz, W-D.Münz - *Proc.Intl.Conf.IBBM-95*, In Press Instr.Meth.B.
130. P.C.Johnson - *Physics of Thin Films*, 1989, 14, 129.
131. S.Kadlec, J.Musil, J.Vyskocil - *Surf.Coat.Tech*, 1992, 54-55, 287.
132. M.R.Ives - *Ph.D thesis*, 1994, Sheffield Hallam University, U.K.
133. W-D.Münz, T.Hurkmans, G.Keiren, T.Trinh - *J.Vac.Sci.Technol*, 1993, 11(5), 2583-2589.
134. W.D.Sproul, P.J.Rudnik, K.O.Legg, W-D.Münz, I.Petrov, J.E.Greene - *Surf.Coat.Tech*, 1993, 56, 179.
135. W-D.Münz, I.Petrov, J.E.Greene, T.Hurkmans, T.Trinh - *Proc.Intl.Conf ICMCTF-1994*, San Diego, USA, to be published.
136. M.Prutton - "*Surface Physics*", 1983, Oxford University Press, United Kingdom.
137. A.Zangwill - "*Physics at Surfaces*", 1988, Cambridge University Press.
138. A.G.Dirks, H.J.Leamy- *Thin Solid Films*, 1977, 47, 219-233.
139. K.-H.Müller - *J.Appl.Phys*, 1985, 58(7), 2573-2576.
140. P.G.Shewmon - "*Diffusion in Solids*", 1963, McGraw-Hill Press.
141. P.Ding, Z.Ni, S.Zhou, F.Pan - *Surf.Coat.Tech*, 1991, 49, 203.
142. J.A.Venables, G.D.T.Spiller, M.Hanbucker - *Rep.Prog.Phys*, 1984, 47, 399.
143. B.A.Movchan, A.V.Demchishin - *Fiz.Met.Metalloved*, 1969, 28, 653.
144. J.A.Thornton - *J.Vac.Sci.Technol*, 1974, 11, 666.
145. R.Messier, A.P.Giri, R.A.Roy - *J.Vac.Sci.Technol*, 1984, A2(2), 500.
146. D.M.Mattox - *J.Vac.Sci.Technol*, 1973, 10, 74.
147. J.A.Thornton - *Metal Finishing*, 1979, 5, 83.

148. K.A.Pischow, L.Eriksson, E.Harju, A.S.Korhonen, E.O.Ristolainen - *Surf.Coat.Tech*, 1993, 58, 163.
149. D.S.Rickerby, P.J.Burnett - *Thin Solid Films*, 1988, 157, 195.
150. R.P.Howson, H.A.Ja'fer, A.G.Spencer - *Vacuum*, 1993, 44, 3-4, 191-195.
151. L.Hultman, G.Håkansson, U.Wahlström, J.E.Sundgren, I.Petrov, F.Abidi, J.E.Greene - *Thin Solid Films*, 1991, 205, 153-164.
152. K.-H.Müller - *J.Appl.Phys*, 1986, 59(8), 2803-2807.
153. D.M.Mattox - *U.S.Patent # 3329601*, 1967.
154. D.S.Rickerby, G.Eckold, K.T.Scott, I.M.Buckley-Golder - *Thin Solid Films*, 1987, 154, 125.
155. D.S.Rickerby - *J.Vac.Sci.Technol*, 1986, A4(6), 2809-2814.
156. O.Knotek, R.Elsing, G.Krämer, F.Jungblut - *Surf.Coat.Tech*, 1991, 46, 265-274.
157. H.Holleck - *Vacuum*, 1990, 41, 7-9, 2220-2222.
158. J.Musil, S.Kadlec, J.Vyskocil, V.Poulek - *Surf.Coat.Tech*, 1989, 39/40, 301-314.
159. S.Kadlec, J.Musil, V.Valvoda, W-D.Münz, H.Petersein, J.Schroeder - *Vacuum*, 1990, 41, 7-9, 2233-2238.
160. P.Hedenqvist, M.Olsson, P.Wallen, A.Kassman, S.Hogmark, S.Jacobson - *Surf.Coat.Tech*, 1990, 41, 243-256.
161. W.D.Sproul, P.J.Rudnik, M.E.Graham - *Surf.Coat.Tech*, 1989, 39/40, 355-363.
162. G.Håkansson, L.Hultman, J-E.Sundgren, J.E.Greene, W-D.Munz - *Surf.Coat.Tech*, 1991, 48, 51-67.
163. L.Hultman, W-D.Münz, J.Musil, S.Kadlec, I.Petrov, J.E.Greene - *J.Vac.Sci.Technol*, 1991, A9(3), 434-438.
164. I.Petrov, L.Hultman, U.Helmersson, J-E.Sundgren, J.E.Greene - *Thin Solid Films*, 1989, 169, 299-314.
165. D.S.Rickerby - *J.Vac.Sci.Technol*, 1986, A4(6), 2809-2814.
166. E.J.Lee, R.F.Hochman, A.Erdemir - *Proc.ASM.Conf. Ion Plating and Implantation*, 1986, 157-160.
167. B.Zega - *Surf.Coat.Tech*, 1989, 39/40, 507-520.
168. A.J.Perry, J.P.Schaffer, J.Brunner, W.D.Sproul - *Surf.Coat.Tech*, 1991, 49, 188-193.
169. H.A.Jehn, J-H.Kim, S.Hofmann - *Surf.Coat.Tech*, 1988, 36, 715-727.
170. J.A.Sue, H.H.Troue - *Surf.Coat.Tech*, 1991, 49, 31-39.
171. A.J.Perry, A.W.Baouchi, J.H.Petersen, S.D.Pozder - *Surf.Coat.Tech*, 1992, 54/55, 261-265.
172. P.J.Rudnik, M.E.Graham, W.D.Sproul - *Surf.Coat.Tech*, 1991, 49, 293-297.
173. N.Savvides - *J.Appl.Phys*, 1987, 62, 600.

174. W.D.Sproul, M.E.Graham, M-S. Wong, P.J.Rudnik - *Surf.Coat.Tech*, 1993, 61, 139-143..
175. A.Aubert, R.Gillet, A.Gaucher, J.P.Terrat - *Thin Solid Films*, 1983, 108, 165-172.
176. I.Hotovy, J.Huran - *Phys.Stat.Sol.A* - 1993, 137, 25-28.
177. P.A.Steinmann, H.E.Hintermann - *J.Vac.Sci.Technol*, 1985, A3(6), 2394-2400.
178. J.Brückner, T.Mäntylä - *Surf.Coat.Tech*, 1993, 59, 166-170.
179. C.Sella, M.Maaza, M.Miloché, M.Kaabouchi, R.Krishnan - *Surf.Coat.Tech*, 1993, 60, 379-384.
180. O.Knotek, F.Löffler, M.Böhmer, R.Breidenbach, C.Stöbel - *Surf.Coat.Tech*, 1991, 49, 263-267.
181. S.Schiller, K.Goedicke, V.Kirchhoff, T.Kopte - *Proc.38th Annual Technical Conf. Society of Vacuum Coaters*, 1995, Chicago, USA, 293-297.
182. R.A.Scholl - *Proc.3rd European Workshop on Plasma and Ion Surface Engineering*, 1995, Würzburg, Germany.
183. H.Holleck - *J.Vac.Sci.Technol*, 1986, A4, 266.
184. W.D.Münz - *J.Vac.Sci.Technol*, 1986, A4(6), 2717-2725.
185. J.R.Roos, J.P.Celis, E.Vancoile, H.Veltrop, S.Boelens, F.Jungblut, J.Ebberink, H.Homberg - *Thin Solid Films*, 1990, 193/194, 1-2, 547-556.
186. M.Kerkhofs, M.Van Stappen, M.D'Olieslaeger, C.Quaeyhaegens, L.M.Stals - *Surf.Coat.Tech*, 1994, 68/69, 741-746.
187. E.Ertürk, O.Knotek, W.Burgmer, H.-G.Prenzel, H.-J.Heuvel, H.G.Dederichs, C.Stössel - *Surf.Coat.Tech*, 1991, 46, 1, 39-46.
188. H.Randhawa, P.C.Johnson, R.Cunningham - *J.Vac.Sci.Technol*, 1988, A6(3), 2136-2139.
189. O.Knotek, A.Barimani - *Thin Solid Films*, 1989, 174, 51-56.
190. O.Knotek, W-D.Münz, T.Leyendecker - *J.Vac.Sci.Technol*, 1987, A5(4), 2173.
191. W.Gissler - *Surf.Coat.Tech*, 1994, 68, 556-563.
192. H.A.Jehn, F.Thiergarten, E.Ebersbach, D.Fabian - *Surf.Coat.Tech*, 1991, 50, 45-52.
193. T.Freisen, J.Haupt, W.Gissler, A.Barna, P.B.Barna - *Surf.Coat.Tech*, 1991, 48, 169-174.
194. J.Markowski, A.Prajzner, J.Zdanowski, K.Masseli - *Surf.Coat.Tech*, 1993, 60, 1-3, 450-453.
195. U.Helmerson, S.Todorova, S.A.Barnett, J.-E.Sundgren, L.C.Markert, J.E.Greene - *J.Appl.Phys*, 1987, 62, 481.
196. X.Chu, M.S.Wong, W.D.Sproul, S.L.Rohde, S.A.Barnett - *J.Vac.Sci.Technol*, 1992, A10(4), 1604-1609.
197. H.Holleck, M.Lahres, P.Woll - *Surf.Coat.Tech*, 1990, 41, 179.
198. H.Freller, H.Haessler - *Surf.Coat.Tech*, 1988, 36, 219.

199. O.Knotek, T.Leyendecker - "*High Tech.Ceramics*", 1987, Mater.Sci.Monograph 38C, Elsevier Press.
200. J.Keem - "*Surface Modification Technologies : An Engineers Guide*", 1990, Marcel Dekker Press.
201. K.N.Strafford, C.Subramanian, T.P.Wilks - *J.Mater.Process.Tech*, 1993, 38, 1-2, 431-448.
202. J.Vetter, W.Burgmer, H.G.Dederichs, A.J.Perry - *Surf.Coat.Tech*, 1993, 61, 1-3, 209-214.
203. W.D.Sproul - *J.Vac.Sci.Technol*, 1994, 12(4), 1595-1601.
204. O.Knotek, F.Löffler, G.Krämer - *Surf.Coat.Tech*, 1992, 54/55, 241-248.
205. R.Huang, L.S.Wen, L.P.Guo, J.Gong, B.H.Yu, H.Bangert - *Surf.Coat.Tech*, 1992, 50, 97-101.
206. E.O.Hall - *Proc.Phys.Soc.London*, 1951, 643, 747.
207. N.J.Petch - *J.Iron.Steel.Inst.London*, 1953, 173, 25.
208. M.Shinn, L.Hultman, S.A.Barnett - *J.Mater.Res*, 1992, 7, 901.
209. S.L.Lehoczky - *J.Appl.Phys*, 1978, 49, 5479.
210. J.S.Koehler - *Phys.Rev.B*, 1970, B2, 547.
211. G.Håkansson - *Ph.D thesis*, 1991, 255, Linköping University, Sweden.
212. S.A.Barnett - "*Physics of Thin films*", 1993, 17, 1-77, Academic Press.

## CHAPTER THREE

### EXPERIMENTAL

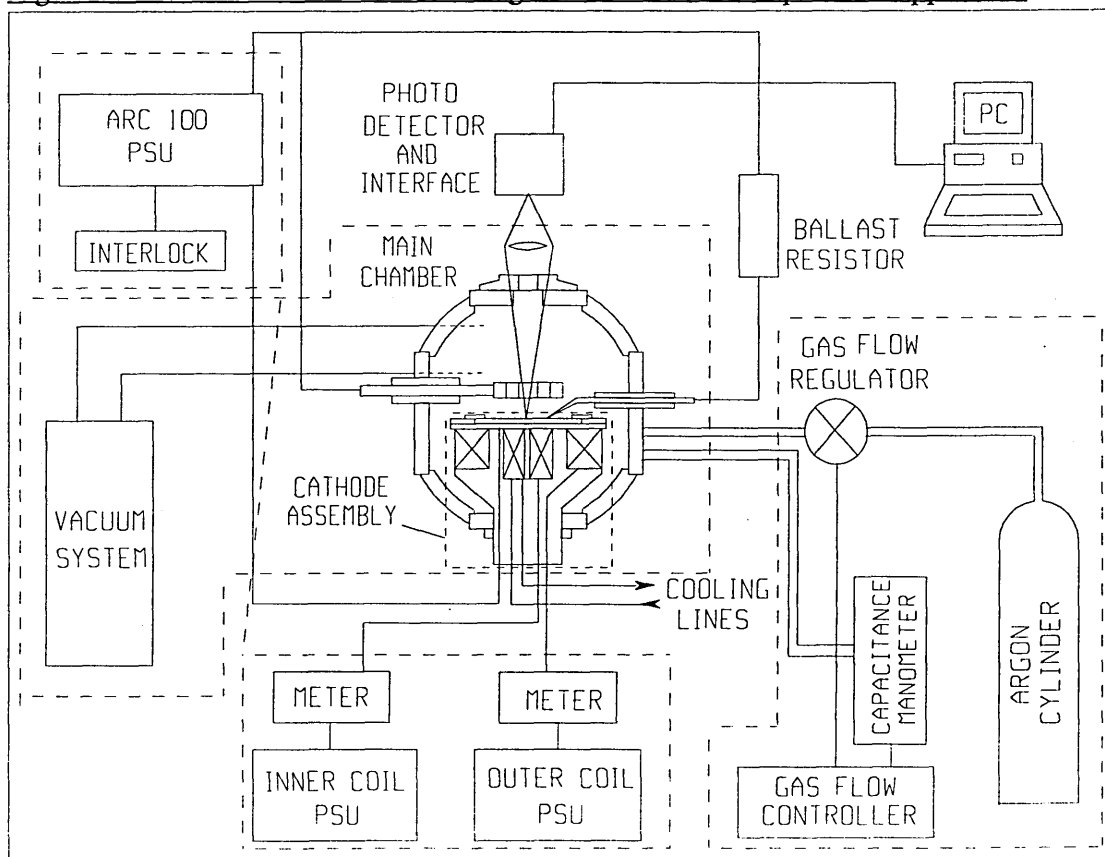
This chapter describes the physical vapour deposition equipment, target manufacturing techniques and the bulk and surface characterisation methods employed during analysis of the advanced coating systems and the investigation of steered arc motion on segmented targets.

#### 3.1. The physical vapour deposition equipment.

##### 3.1.1. The electromagnetic steered arc evaporation PVD unit.

This sub-section outlines the design and construction of the experimental electromagnetic steered arc facility at the MRI, Sheffield Hallam University and the nature of its associated control systems and power supplies. The unit was principally designed and built by Dr P.J.Walke during a Ph.D study on the fundamental motion of steered arcs (1) with contributions on the cathode assembly design by Dr R.New and its manufacture by Messrs R.Day and G.Robinson.

Figure 3.1. Schematic of the electromagnetic steered arc evaporation apparatus.



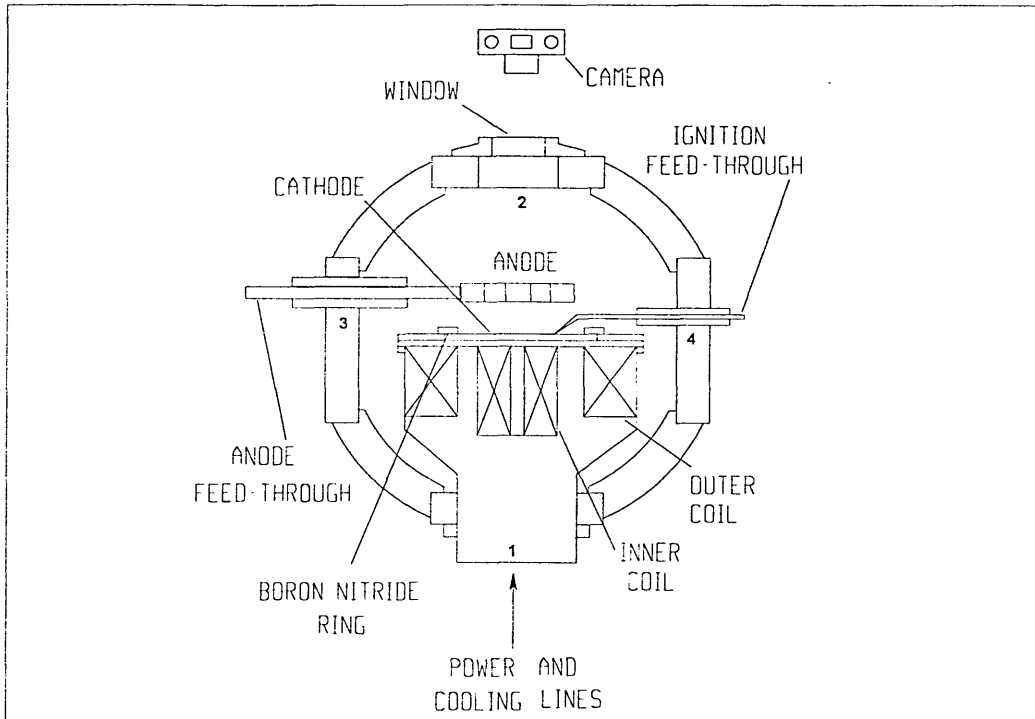
The apparatus (figure 3.1) consists of a central cylindrical aluminium PVD chamber mounted upon a modified base plate of an existing Genevac evaporation system. Vacuum pressure is attained by means of a 20cm throat diffusion pump backed by a rotary vane pump, together capable of a pumping capacity of approximately  $1300\text{ls}^{-1}$  and a typical base pressure below  $1 \times 10^{-5}$  mbar. Entrance to the chamber can be achieved through a circular top plate by which the chamber is also earthed. Four orthogonal ports were positioned on the sides of the chamber each consisting of a square plate through which a number of feed-throughs were mounted (figure 3.2).

- Port 1 - Provided an access to the cathode assembly.
- Port 2 - Provided a circular viewing port allowing photographic or optical analysis.
- Port 3 - Provided a water cooled electrical feed-through that supplies current and supports a circular anode positioned in front of the cathode.
- Port 4 - Provided electrical and gas feed-throughs and a connection to a pressure transducer.

The electrical feed-through in port four was designed to accommodate a rotating motion and a connection to anode potential through a ballast resistor. This allowed a high current cathodic arc to be struck by making a momentary short between the supply voltage and the earth via the rotary movement of a Monel spike. The main arc current was generated using an "ARC-100" commercial supply manufactured by ELMA Technik GmbH, capable of delivering fixed current outputs between 0 and 100A at potentials of up to 100 Volt.

The magnetic steering of the arc upon a path of continuously variable radius (in circular geometry) was achieved by two sets of water cooled electro-magnetic coils mounted behind the cathode. The inner coil was driven by a constant current power supply (currents up to 20A) with feedback stabilisation, whilst the outer set was supplied by a similar unit capable of current up to approximately 10A. Independent control of the inner and outer coil current meant that substantial movement of the position of the normal field component zero and consequently the arc radius (usage of nearly the entire cathode area) could be achieved .

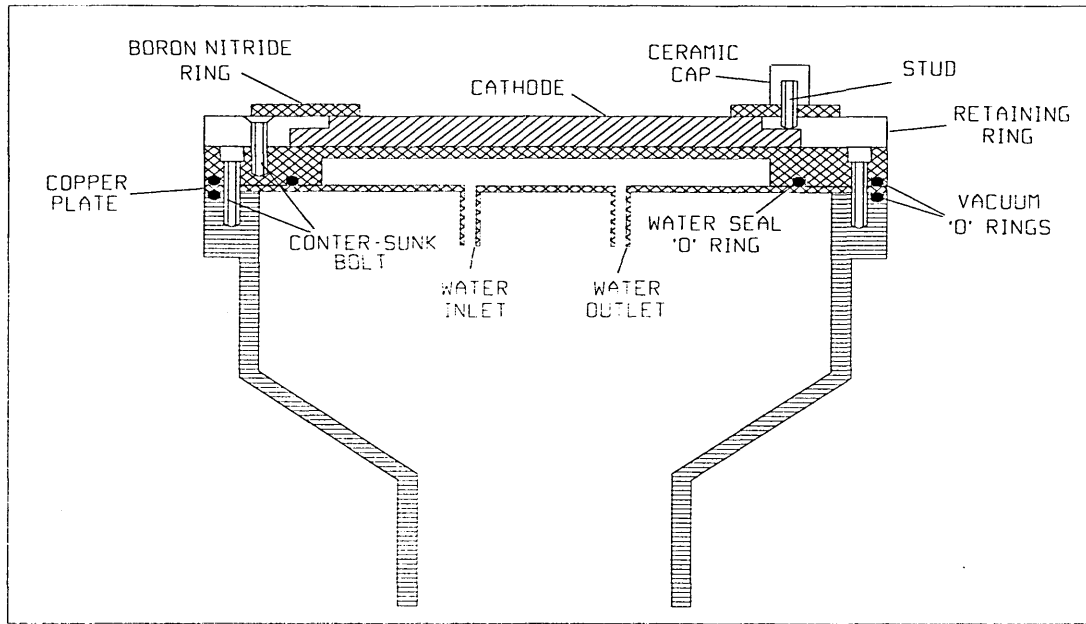
**Figure 3.2. Primary feedthroughs on electromagnetic steered arc PVD chamber.**



The cathodes consisted of  $\text{Ø}45\text{mm}$  or  $\text{Ø}150\text{mm}$  diameter x 5mm thick discs of the material under investigation, secured into an assembly by means of an aluminium ring fixed by a number of counter-sunk bolts around its circumference (figure 3.3). The joint between the cathode material and the retaining ring was covered by a boron nitride disc which acted as a passive arc barrier and prevented arc burrowing at the cathode / ring interface. The cathode and retaining ring were mounted on a copper cooling plate (thermocouple monitored) which also served as a vacuum seal between the main body of the assembly and the cathode mounting. Power was applied to the cathode by direct connection to the cooling plate.

During evaporation trials, argon (99.999% purity) was generally introduced into the system to obtain a working pressure of the order of  $3 \times 10^{-2}$  mbar and aid arc initiation and an increase in arc stability. This was achieved by an MKS Instruments 250 gas pressure controller combined with a MKS Baratron 122A pressure transducer and a MKS 248 solenoid gas flow control valve. Prior to steered arc evaporation, a random arc conditioning of the cathode for a duration of 2-3 minutes at 100 A arc current was always initiated to remove surface oxides and obtain reproducible type II cathode spot (2) data.

**Figure 3.3. Steered arc cathode assembly.**

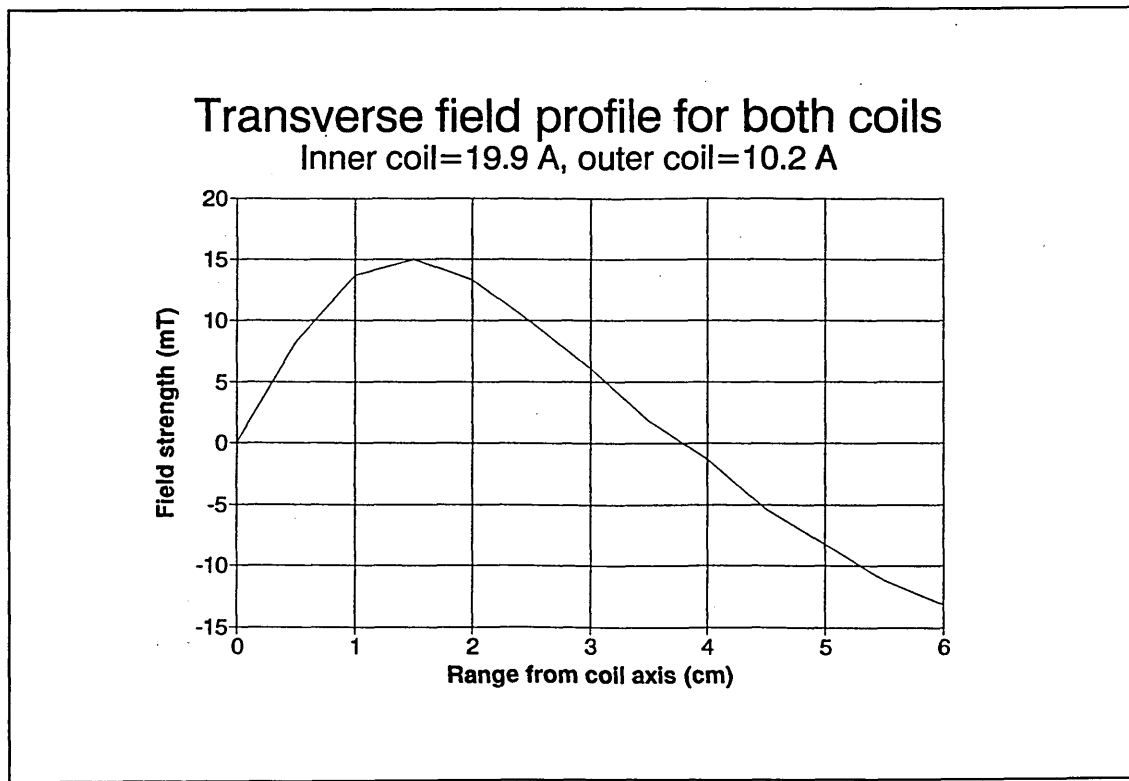
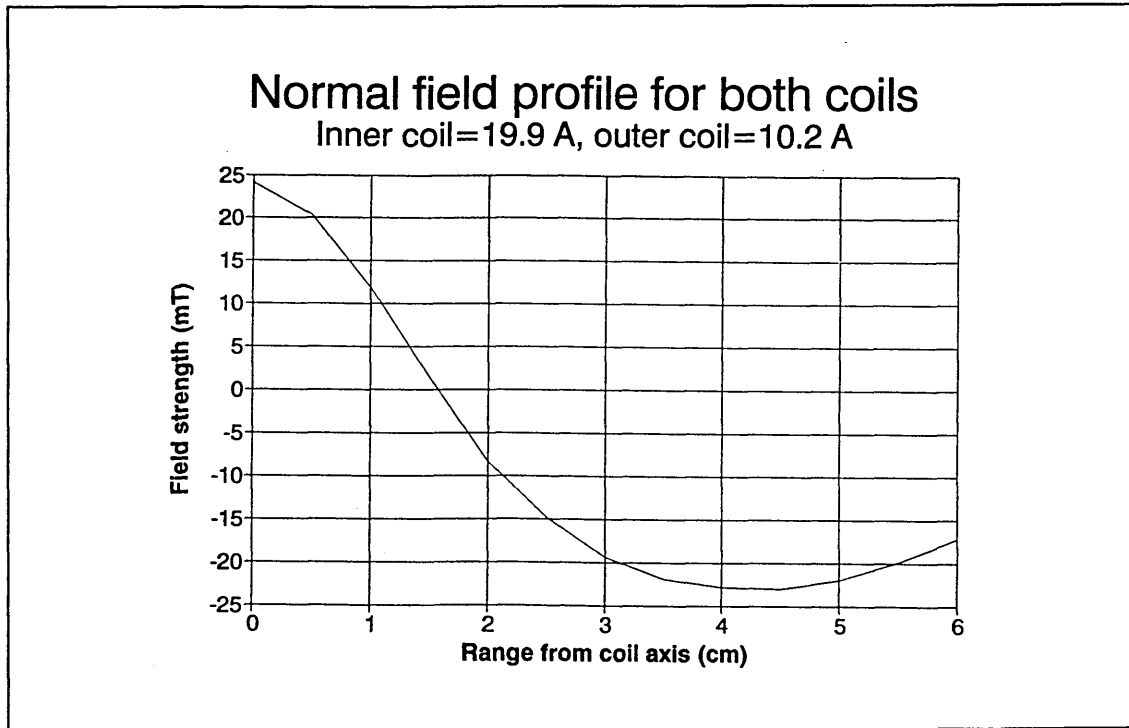


The typical process parameters and field profiles used during evaporation trials are shown in table 3.1. and figure 3.4.

**Table 3.1. Segmented target steered arc evaporation trial parameters**

Process parameters	Ø 45mm TiZr targets central & offset interfaces	Ø150mm TiZr, TiMo & ZrMo targets central interfaces
Base pressure	$< 1 \times 10^{-5}$ mbar	$< 1 \times 10^{-5}$ mbar
Working pressure	$3 \times 10^{-2}$ mbar	$3 \times 10^{-2}$ mbar
Working gas	Argon	Argon
Inner coil current	19.9 Amp	15.0 Amp
Outer coil current	10.2 Amp	6.0 Amp
Arc current	85 Amp	85 Amp
Arc radius	15mm	20mm
Normal field gradient	$18.2 \text{ mTcm}^{-1}$	$12.1 \text{ mTcm}^{-1}$
Transverse field strength	11.6 mT	11.2 mT
Start temperature	25°C	25°C
Cathode conditioning	5 mins random arc	5 mins random arc

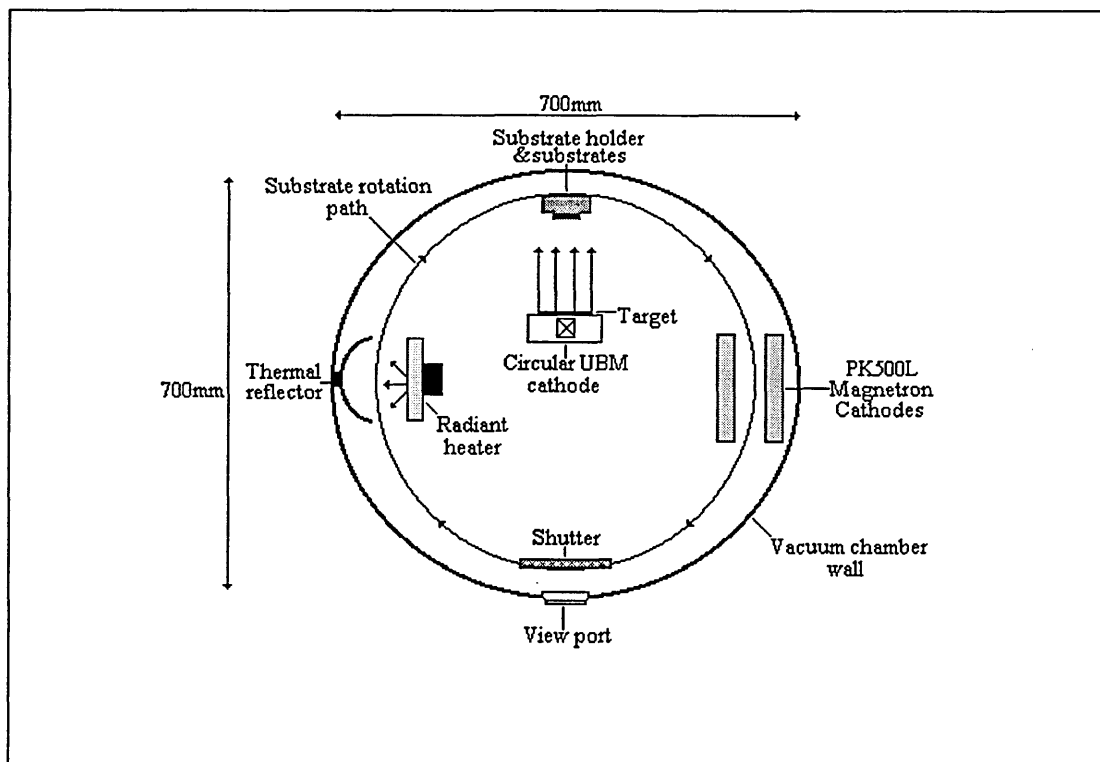
Figure 3.4. Typical steered arc evaporation magnetic field profiles.



### 3.1.2. The unbalanced magnetron sputtering PVD unit.

Various unbalanced magnetron sputtering trials have been carried out using a Z-700 Leybold A.G. PVD unit at the Forschungsinstitut für Edelmetalle und Metallchemie, Schwäbisch Gmünd, F.R.G. The system consists of a  $\text{Ø}700\text{mm}$  diameter x  $700\text{mm}$  high cylindrical vacuum chamber pumped by a Turbovac 1500 turbomolecular pump (nominal pumping speed  $1500\text{ls}^{-1}$ ) and backed by a Trivac D65B rotary vane pump ( $75\text{m}^3\text{h}^{-1}$ ) and a Ruvac WS151 roots pump ( $153\text{m}^3\text{h}^{-1}$ ) to provide a typical base pressure of  $2 \times 10^{-5}\text{mbar}$ . Deposition was conducted in a stationary mode with substrates positioned directly in front of a US Gun II d.c supplied, circular permanently unbalanced magnetron sputtering cathode with a target to substrate distance of  $80\text{mm}$ . The targets were of  $\text{Ø}150\text{mm}$  diameter x  $12\text{mm}$  thick dimensions and mounted into the cathode assembly, ensuring a good thermal contact against a copper cooling jacket, by means of an aluminium ring fixed by a number of counter-sunk bolts around its circumference (figure 3.5).

Figure 3.5. Schematic of the Leybold Z-700 unbalanced magnetron sputtering unit.



Substrate heating prior to coating could be undertaken utilising a radiant heating element positioned at approximately  $90^\circ$  to the target capable of raising the substrate to a maximum temperature of  $350^\circ\text{C}$  (thermocouple monitored) prior to deposition.

The substrates could be rotated around different areas of the chamber at a maximum velocity of 2 r.p.m along a circular perimeter path and stopped in front of various components. This allowed direct control of the substrate position at various pre-deposition stages including a target sputter cleaning step (1.1KW power for 5 minutes) in which a shutter was brought between the target and substrate, and an argon ion etching process step where the substrates were highly negative biased (-1000V) and introduced in close proximity between two PK500L cathodes operating with a glow discharge. Entrance to the chamber was achieved through a large door, vacuum sealed by a rectangular O-ring, which contained a viewing port for observation of the coating process.

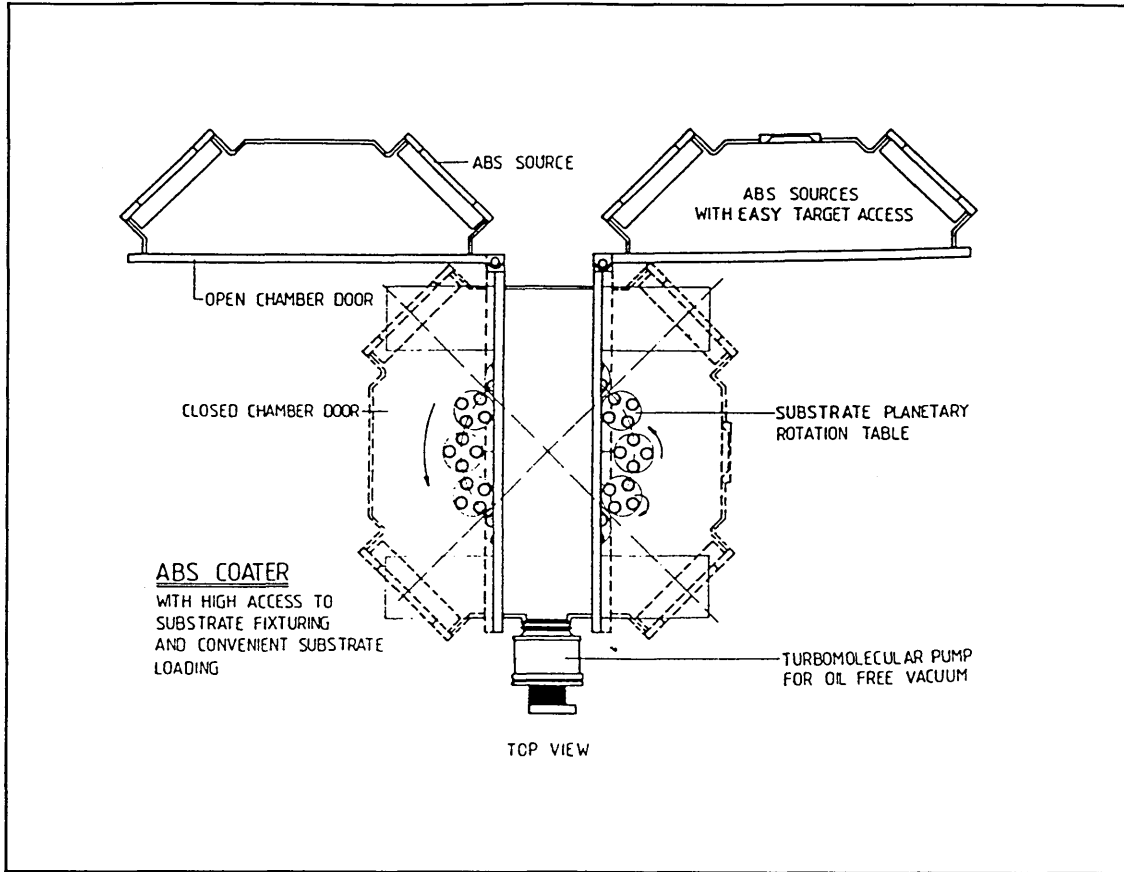
The system was controlled and monitored by a iSBC 83/05A computer unit and Leybold Decocontrol 1.0 software capable of guiding all of the important system switching, rotation, interlocking and processing sequences automatically. In reactive deposition the system incorporated a quadrupole mass spectrometer partial pressure control technique using a Leybold Quadruvac PGA100 residual gas analyser. The working gas used was argon (purity 99.999%) and the reactive gas was nitrogen (purity 99.999%) regulated by means of a piezo-electric control valve. The chamber pressure was determined from Pirani and Penning gauges.

### 3.1.3. The arc-bond sputter PVD unit.

The industrial scale HTC 1000-4 arc-bond sputter (ABS) deposition unit at Sheffield Hallam University essentially consists of a 25mm thick stainless steel octagonal cross-section vacuum chamber (figure 3.6). Access to the chamber is achieved through two large chamber doors in which the four cathode assemblies at 90° to one another. The diagonal distance between each orthogonal cathode is 1m which combines with a similar clear vessel height to give a total chamber volume of approximately 1m<sup>3</sup>. Each cathode houses a target of dimensions 600 x 190 x 12mm, fixed to a water cooled copper jacket by recessed high tensile bolts and a retaining ring covered by boron nitride strips.

The system is equipped with two viewing ports and openings for pumps and rotary motion feed-throughs, as well as another 10 openings for additional instrumentation. Welded cooling coils and three large internal radiant heaters permit substrate heating and sensitive chamber area cooling during operation, and high quality ferro-fluidic rotary feed-throughs allows the use of a 3-fold planetary rotation substrate turntable capable of holding 6 (for research purposes) or 12 (for commercial production) rotating satellites and approximately 800 6mm drills.

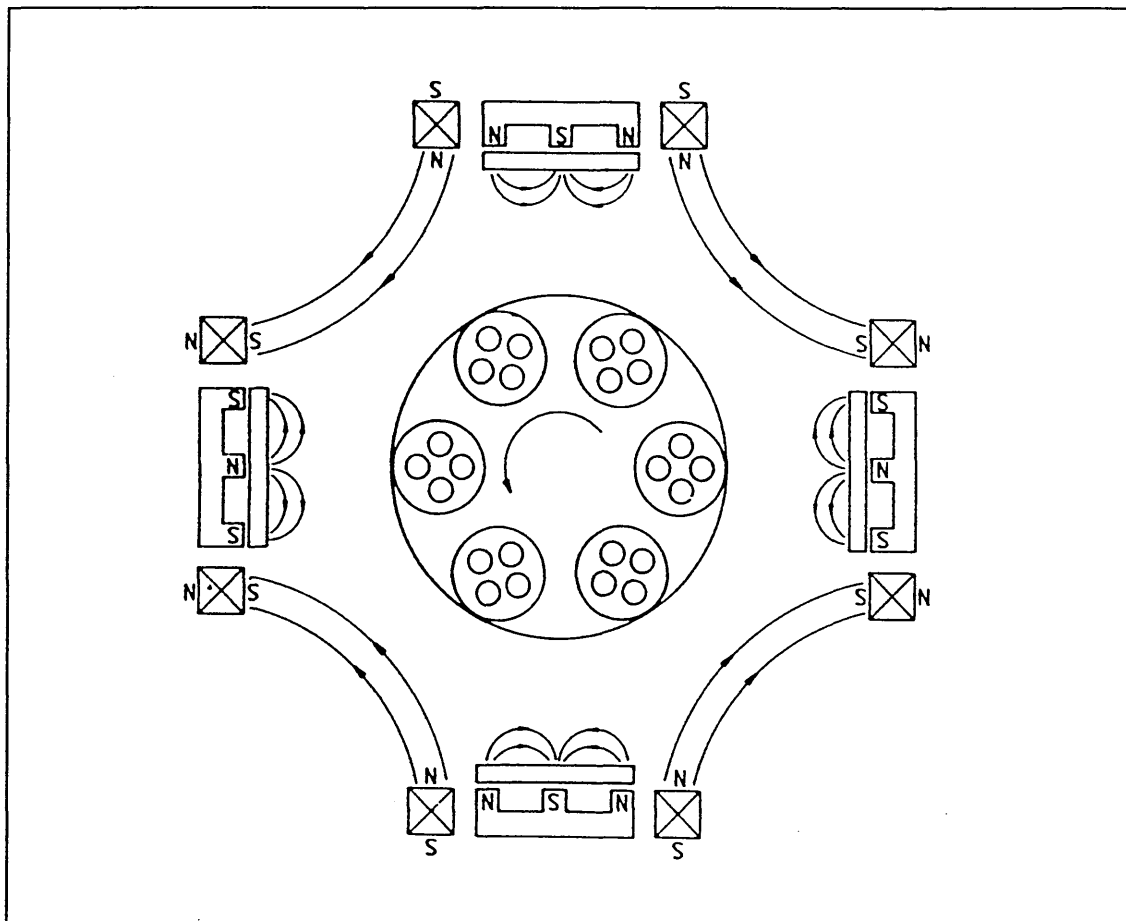
Figure 3.6. Arc-Bond Sputter PVD unit.



The turntable and its substrates are directly linked to the bias voltage supply which can deliver typically -1200V for high voltage etching process steps and 0V to -200V for coating steps. Adequate vacuum pressure is assured by means of two Balzers TPH 2200 turbomolecular pumps with oil lubricated bearings and inert gas sealing, in combination with a large Pfeiffer-Balzers rotary vane pump (speed 250 m<sup>3</sup>/h) and a roots pump with a pumping speed of 500m<sup>3</sup>/h. The turbomolecular pumps are flanged to the chamber by two 250mm VAT high vacuum gate valves, allowing the pumps to be kept at full speed despite times when the system is open. This provides a nominal pumping capacity of 4400l.s<sup>-1</sup> and typical base pressures of 2x10<sup>-5</sup>mbar with leak rates better than 5x10<sup>-2</sup>Pa.l.s<sup>-1</sup>. The cathodes are capable of accepting powers greater than 10Wcm<sup>-2</sup> and utilise SmCo fixed magnet arrays. In magnetron mode the array is brought directly behind the target and unbalancing (reinforcing of the outer magnet poles) is achieved by varying the current to a rectangular toroidal electromagnet disposed concentrically around each target outside the vacuum chamber (figure 3.7), capable of generating a magnetic field of up to 1x10<sup>4</sup> ampere turns. This allows closed field magnetic linkage and typical mean bias current densities at target to probe distances of 30cm of

$\sim 5\text{mAcm}^{-2}$  (3) with all four magnetrons operating. The unbalanced magnetron cathode is converted into arc mode by a suitable movement of the magnet array directly away from the target by means of compressed air. The power supply is capable of operating in arc mode (high current-low voltage) with current / voltage values of typically 80V / 100A and may be switched by a relay network into magnetron mode (high voltage-low current) to deliver 750V / 40A and maximum power of 10KW per target.

Figure 3.7. Schematic of closed magnetic field profile within the ABS chamber.



The system is controlled and monitored by a Mitsubishi SPS control unit capable of guiding all of the important system switching, interlocking and processing sequences automatically. In reactive deposition the control unit incorporates a P.I.D. (proportional integrating differential) control technique with feedback to total pressure measured by a Leybold Viscovac system. The chamber pressure was also monitored in the region atmospheric-  $1 \times 10^{-1}$  mbar by a pirani gauge and from  $1 \times 10^{-1}$ - $1 \times 10^{-5}$  mbar by a Balzers ion gauge. The gas flow is controlled by fast feedback piezo-electric valves and the gas purities (Ar as the working gas and  $\text{N}_2$  as the reactive gas) were 99.999%. The deposition temperature was monitored by two thermocouples placed on the rotating

turntable in dummy test-pieces positioned directly adjacent to the actual substrates and any contamination of the chamber and coating plasma was assessed by a Hiden quadrupole residual gas analyser.

### **3.2. The target manufacturing techniques.**

The multi-elemental targets used in this thesis were manufactured by two distinct processing techniques which have the common feature of fabrication via a hot isostatic pressing (HIPping) process.

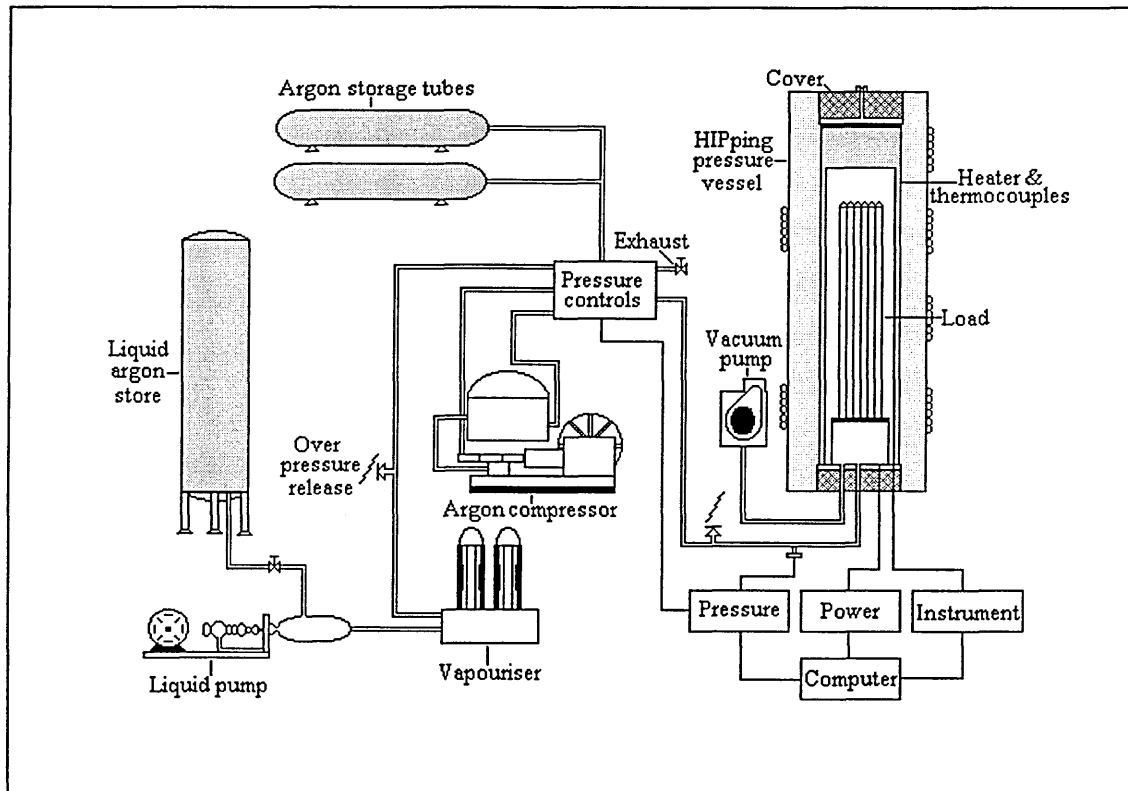
Segmented targets for use in fundamental studies of electro-magnetic steered arc motion, ABS and unbalanced magnetron sputtering trials were produced by a HIP diffusion bonding method. This may be defined as the process of joining two or more components by atomic movement, where the relative numbers of atoms crossing the interfaces in both directions is controlled by the activation energies of diffusion for the various species (4,5). Hot isostatic pressing involves subjecting the materials to be bonded, encased in an appropriate evacuated capsule, to a simultaneous elevated temperature and high isostatic argon gas pressure for a controlled period of time. The technique relies on the yield strength of the material at the elevated temperature, normally approximately  $2/3^{\text{rd}}$  of the melting temperature, to be lower than that at the surrounding gas pressure. If this criterion is achieved then non-surface fracturing or discrete voids within the component will decrease in size by plastic flow induced by the net external stresses. At further densification stages, internal surfaces of pores are squeezed allowing diffusion across the prior pore surfaces. A diffusion bond is formed and the defect is completely removed from the material. Thus the process is limited only by the size of the HIPping vessel and the combination of materials chosen, and it is also important to reflect that diffusion bonding occurs in the solid state and therefore offers many advantages over conventional techniques for the manufacture of segmented targets such as fusion bonding or welding such as;

- HIPping does not produce heat affected zones.
- HIPping does not produce cast structures.
- The strength of the bond will be at least the same as the weaker of the two materials being joined.

For this study all segmented targets were produced using either a National Forge HIP vessel capable of operation with charge dimensions of  $\text{Ø}250\text{mm}$  diameter x 760mm (figure 3.8) or an Autoclave Engineering Isohipper research and development HIP

vessel of dimensions  $\text{Ø}75\text{mm}$  diameter x 120mm in collaboration with the Hot Isostatic Processing Centre at H.I.P. Ltd, Chesterfield, U.K.

Figure 3.8. Schematic of the Hot Isostatic Pressing (HIP) apparatus.



The manufacturing trials produced the following set of targets (figure 3.10) by an encapsulation, evacuation and processing route illustrated in table 3.2 and figure 3.9.

- TiZr circular segmented targets of dimensions  $\text{Ø} 45\text{mm}$  diameter x 5mm with central and offset diffusion bond interfaces.
- TiMo, TiZr and ZrMo circular segmented targets of dimensions  $\text{Ø} 150\text{mm}$  diameter x 5mm thickness for electromagnetic steered arc evaporation trials.
- TiMo, TiZr and ZrMo circular segmented targets of dimensions  $\text{Ø} 150\text{mm}$  diameter x 12mm thickness for unbalanced magnetron sputtering trials.
- 80 atomic% Ti (18 strips of 25x200x12mm), 20 atomic% Zr (18 strips of 15x200x12mm) planar rectangular ABS segmented target of dimensions 600mm x 200mm x 12mm.

Figure 3.9. Plot of hot isostatic pressing parameters.

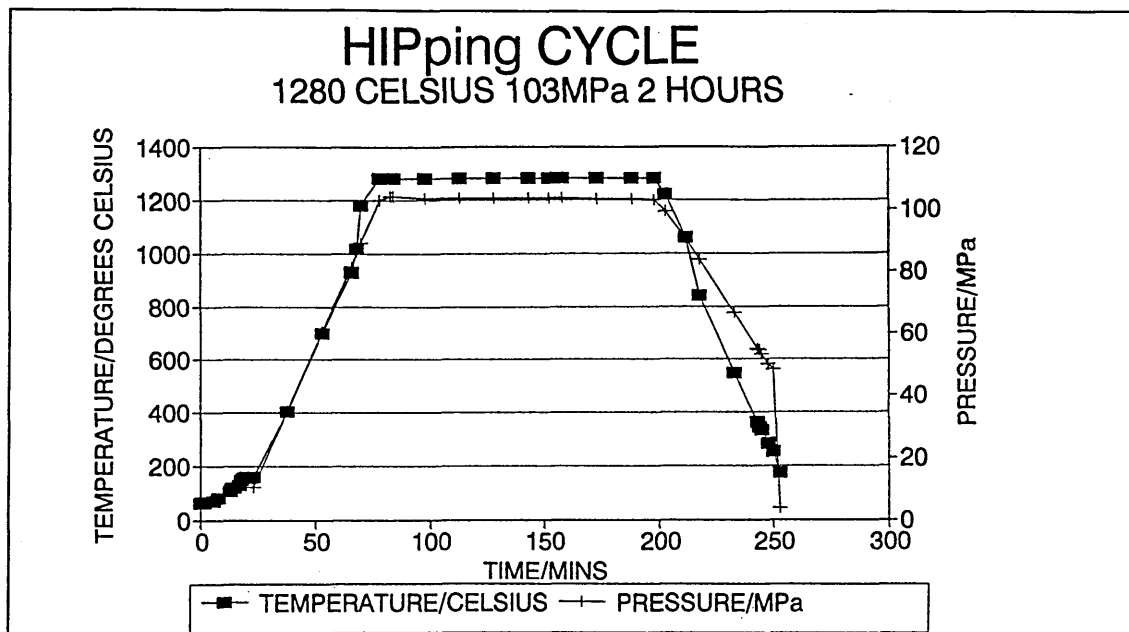


Table 3.2. Segmented target processing route.

Encapsulation material	MIG welded titanium canister
Encapsulation pressure	2Pa
Temperature monitoring	Thermocouples
Purging	0.34MPa Argon 3 times
Furnace heating	Convection & radiation
HIPping pressure	103MPa
HIPping temperature	1280°C
HIPping duration	2 hours
Initial pressure let-down	2.07MPa
Final pressure let-down	Atmospheric

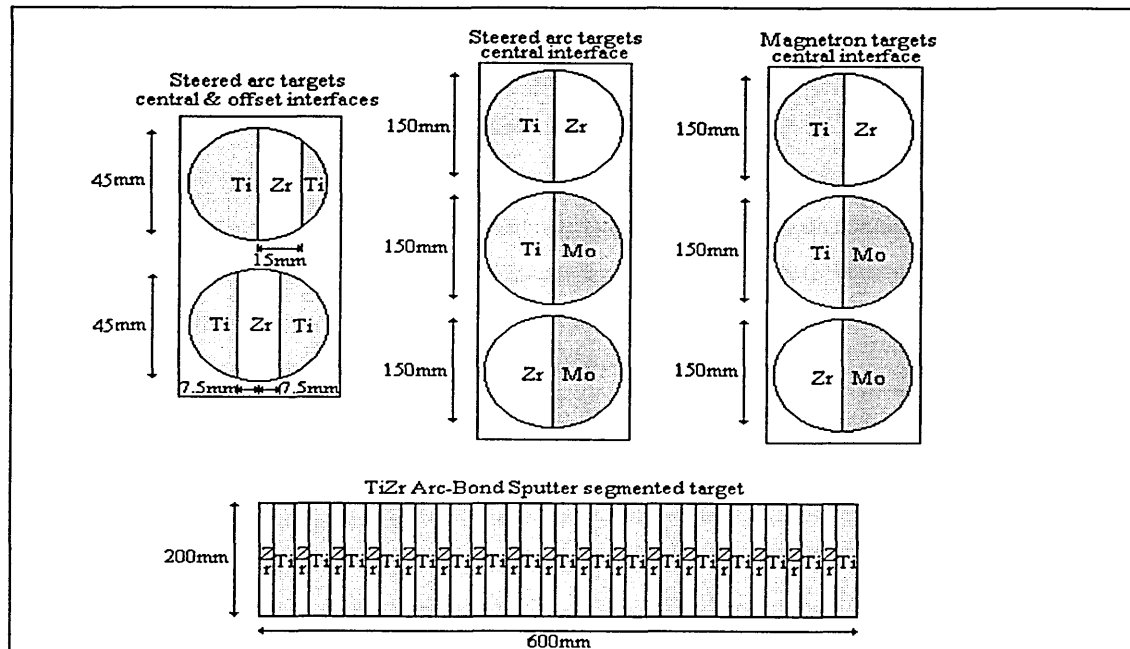
The targets were comprised of solid strips or semi-circular sections with bonding edges in intimate contact, cleaned in tri-chloroethane ultrasonic and distilled water baths, of combinations of the following materials:-

ASTM B265-79 grade 2 titanium (purity >99.7%)

ASTM B551-85 grade 702 zirconium (purity >99.6%).

SGR 4571 commercial grade molybdenum (purity >99.6%).

**Figure 3.10. Schematic of the range of segmented targets manufactured by HIP diffusion bonding.**



The industrial scale homogeneous TiAl alloy targets for use in arc-bond sputter PVD advanced coating trials were manufactured via a powder metallurgical HIPping route by Heraeus GmbH. Here, mixed titanium and aluminium powders of 300 $\mu$ m particle size were encapsulated in mild steel and HIPped at a temperature of approximately 550 $^{\circ}$ C and pressures in excess of 100MPa.

The pure metallic Ti and Zr targets (600x190x12mm) also used in ABS technology were produced by a vacuum melting and casting technique performed by Titanium International Ltd.

### **3.3. Sample preparation for coating.**

The substrates chosen for use in the coating trials were as follows:-

- M2 high speed steel (HSS) cylindrical stubs ( $\varnothing$ 30mm x 10mm) mechanically polished to a 1 $\mu$ m diamond finish ( $R_c$ 64,  $R_a$ 0.01 $\mu$ m,  $R_z$ 0.05 $\mu$ m,  $R_t$ 0.06 $\mu$ m).
- 304 bright annealed stainless steel rectangular coupons (20mm x 50mm x 1.5mm).
- 6mm Presto tools HSS drill blanks.

The substrates were cleaned in a commercially available cleaning line according to the following procedure:-

1. Degreasing in hot NaOH based strong alkali solution (70°C) with ultrasonic agitation.
2. Immersion rinsing in distilled water.
3. Degreasing in 1% "Borer HT017" acid solution with ultrasonic agitation.
4. Immersion rinsing in distilled water.
5. Degreasing in hot 2% "Bannerclean 16" alkali solution (70°C) with ultrasonic agitation.
6. Immersion rinsing in distilled water.
7. Degreasing in hot 2% "Bannerclean 13" alkali solution (70°C) with ultrasonic agitation.
8. Immersion rinsing in distilled water with ultrasonic agitation.
9. Water displacement and spot-free drying in acetone and its vapour.
10. Hot-air drying.

The alkaline steps were used for the removal of inorganic contaminants from the substrate surface and the acid cleaning step was carefully monitored to prevent over-activation of the metal surface and pitting corrosion of the high speed steel. After cleaning, all substrates were handled with clean cotton gloves to prevent re-contamination from the oils and salts present in human skin.

### **3.4. Sample preparation techniques for analysis.**

Most of the analytical techniques utilised did not require any form of sample preparation other than surface cleaning with an air jet or solvent (acetone or analar methanol) to remove dust and possibly fingerprints. An analysis strategy was adopted such that distortion and contamination of the samples by mechanical polishing, sectioning or thinning was minimised. However, some analytical instruments (e.g. X-ray diffraction) could only accept samples of limited size, therefore specimens were sectioned from the coated samples using an Accutom II metallurgical rotary saw using an Al<sub>2</sub>O<sub>3</sub> cutting wheel. The electron microscopy techniques were the most demanding in terms of sample preparation, particularly during the examination of cross-sections (6).

### 3.4.1. Scanning Electron Microscope fracture cross-sections.

This technique was used to examine the columnar morphology and grain structure of the coatings and was always performed on HSS 6mm drills blanks. The procedure involved the following steps:-

- The cutting of a deep slit ( $\sim 2/5^{\text{th}}$  of diameter of drill blank) into the side of the sample opposite to that to be examined using an Accutom II rotary saw.
- The quenching of the sample in liquid nitrogen for 2-3 minutes.
- The clamping of the bottom of the sample in a vice and the application of a uniformly distributed load to the upper exposed half causing fracture to occur evenly along the length of the slit.
- Vertical cold mounting of the fracture section via a conductive paste to an aluminium sample stub.

### 3.4.2. Transmission Electron Microscope coating cross-sections.

- Specimens were prepared by bonding (using Gatan G1 low viscosity epoxy resin) two sections of coated steel face-to-face and coring out (or spark eroding) 2.8mm cylinders.
- Cylinders were then inserted and bonded into stainless steel tubes (outside diameter = 3mm) from which 200 $\mu\text{m}$  slices were cut using a diamond impregnated wire saw (substrate/coating interface was parallel to the cut or scratches generated) .
- The sectioned discs were mechanically ground and polished on one face to a thickness of 50 $\mu\text{m}$  and to a finish of 0.25 $\mu\text{m}$ .
- The reverse face was further thinned by dimple grinding (14 $\mu\text{m}$  diamond paste followed by 1 $\mu\text{m}$  felt polisher) - generating a central thickness of 10 $\mu\text{m}$  and to a finish of 0.25 $\mu\text{m}$ .
- Final thinning to electron translucency was accomplished by argon ion beam thinning at an incident beam angle of  $4^\circ$ , an accelerating voltage of 5KV and a current of 7 $\mu\text{A}$ . In order to preserve the coating and interface, the ion beam was only operated at  $\pm 15^\circ$  to the coating growth axis.

### 3.5 The characterisation techniques

#### 3.5.1. X-ray diffraction.

X-ray diffraction is a tool for the investigation of the structure of matter which had its beginnings with the discovery of X-rays by Röntgen in 1895, Von Laue's discovery in 1912 that crystalline solids can diffract X-rays and the further development of its physical equations by W.H and W.L.Bragg . Von Laue realised that, if crystals were composed of regularly spaced atoms which might act as scattering centres for X-rays, and if the X-rays were electro-magnetic waves of wavelength about equal to the crystal interatomic distance, then it is possible to diffract X-rays by means of the crystal. The diffraction process is due essentially to the existence of certain phase relations between two or more waves from an incident X-ray source that have been scattered by a periodically repeating array of atoms in a lattice. If the path lengths of the waves are exactly equal or differ by a whole number of wavelengths, so-called "in-phase", constructive interference will occur. However, if the waves are out of phase, differences in the path lengths leads to a change in phase and produces modification of the wave amplitude and destructive interference may occur.

Bragg showed that if an X-ray beam is incident on atomic array of interplanar spacing  $d$  and is diffracted at an angle  $\Theta$  by atoms K and L lying in parallel planes (figure 3.11), then the path difference between the diffracted rays may be given by equation 3.1.

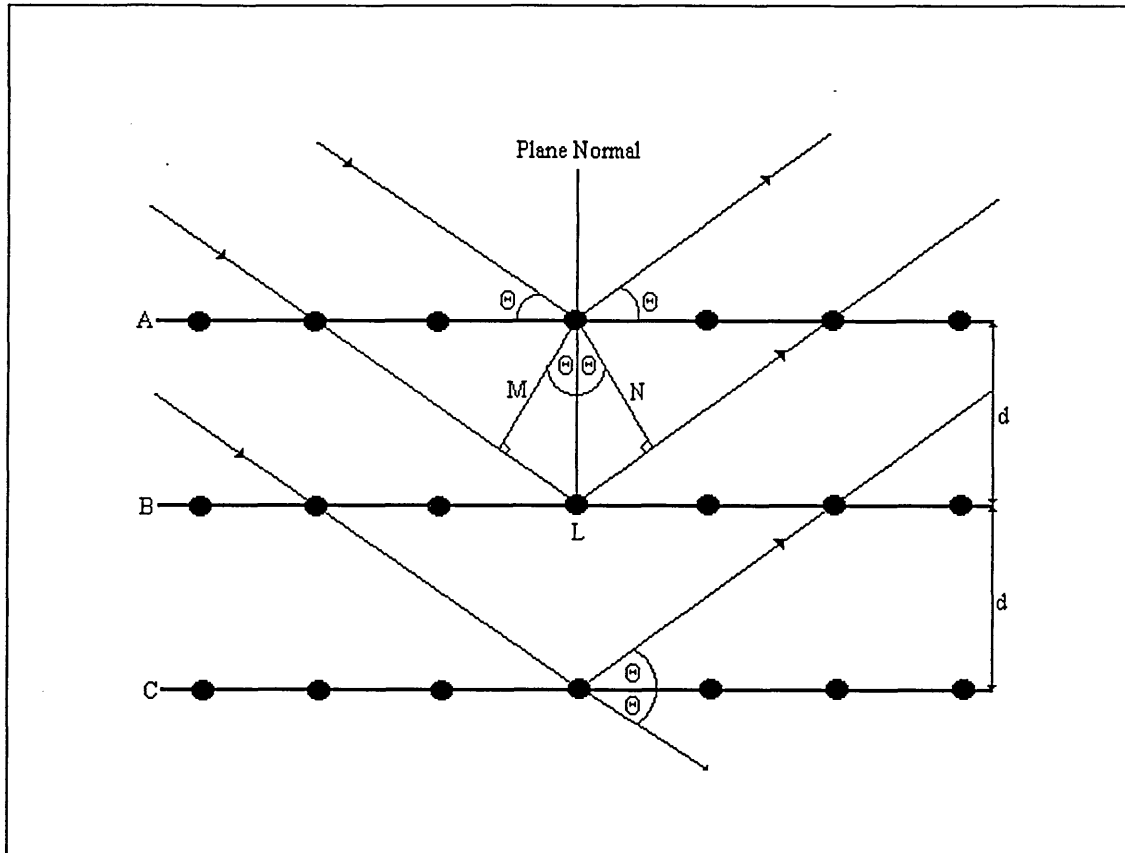
$$ML + LN = d\sin\Theta + d\sin\Theta \quad \text{.....equation 3.1.}$$

Hence the two rays will be completely in phase if the path difference is equal to a whole number  $n$  of wavelengths  $\lambda$ , or if the Bragg condition (the essential condition for diffraction to occur) is satisfied in equation 3.2 where:-

$$n\lambda = 2d\sin\Theta \quad \text{.....equation 3.2.}$$

Therefore, the incident beam, the normal to the reflecting plane and the diffracted beam are always co-planar, and the angle between the diffracted beam and the transmitted beam is always  $2\Theta$ .

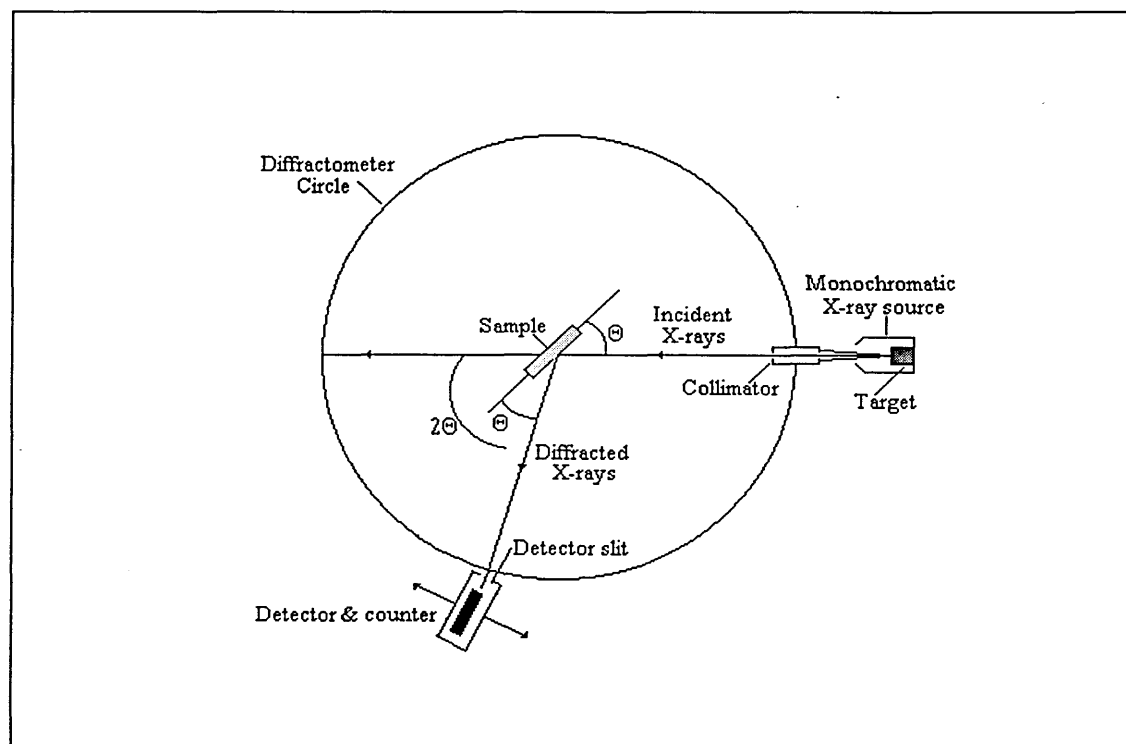
Figure 3.11. Schematic of the diffraction of X-rays by a crystal.



Many systems have been developed to take advantage of the above relationships for the examination of crystal structure including Laue, Debye-Scherrer, Seeman-Bohlin and Guinier cameras (7). However the technique which is best suited and the most flexible for the examination of thin PVD films is the X-ray diffractometer method and will be discussed in further detail.

Diffractometer techniques essentially measure the intensity of a diffracted beam directly by means of a movable X-ray detector and electronic counter and its main features are shown in figure 3.12.

Figure 3.12. Schematic diagram of a X-ray diffractometer.



Monochromatic X-rays of a known wavelength are generated and allowed to diverge from the source and irradiate a flat plate sample supported in the centre of the apparatus on a table which can rotate about its axis through an angle  $\Theta$ . The X-rays are diffracted by the sample to form a convergent diffracted beam which comes to a focus at a collimation slit at the front of the motor driven, constant angular velocity counter which is mechanically coupled to the specimen to cause rotation about the same axis through an angle  $2\Theta$  (to maintain the Bragg condition). The detector senses a succession of current pulses at a given angle of  $2\Theta$  and outputs the number of counts or X-ray intensity over a selected scan period. The result is a plot of the number of X-ray counts as a function of diffraction angle  $2\Theta$  and is represented as a series of peaks at positions and intensities characteristic of the unit cell of each phase present in the crystalline solid.

Analysis of the full width at half maximum (FWHM) of the individual x-ray peaks can also yield information on the film grain size, lattice strain and the extent of peak shift (8). Examination of the peak position and intensity provides data on the film preferred orientation, unit cell dimensions and the atomic arrangement within the crystalline lattice (9). The crystallographic texture,  $P^*$  can also be calculated from an X-ray trace using the inverse pole figure technique (equation 3.3).

$$P^* = \frac{\frac{I_{hkl}}{R_{hkl}}}{\frac{1}{n} \sum_0^n \frac{I_{hkl}}{R_{hkl}}} \quad \text{.....equation 3.3.}$$

Where I(hkl) and R(hkl) are the intensities from the (hkl) reflections in the specimen and a random powder respectively and n is the number of reflections considered. Thus, a P\* value of 1 signifies a random orientation of the plane, whilst for P\* values greater than 1, the plane is considered to have a preferred orientation.

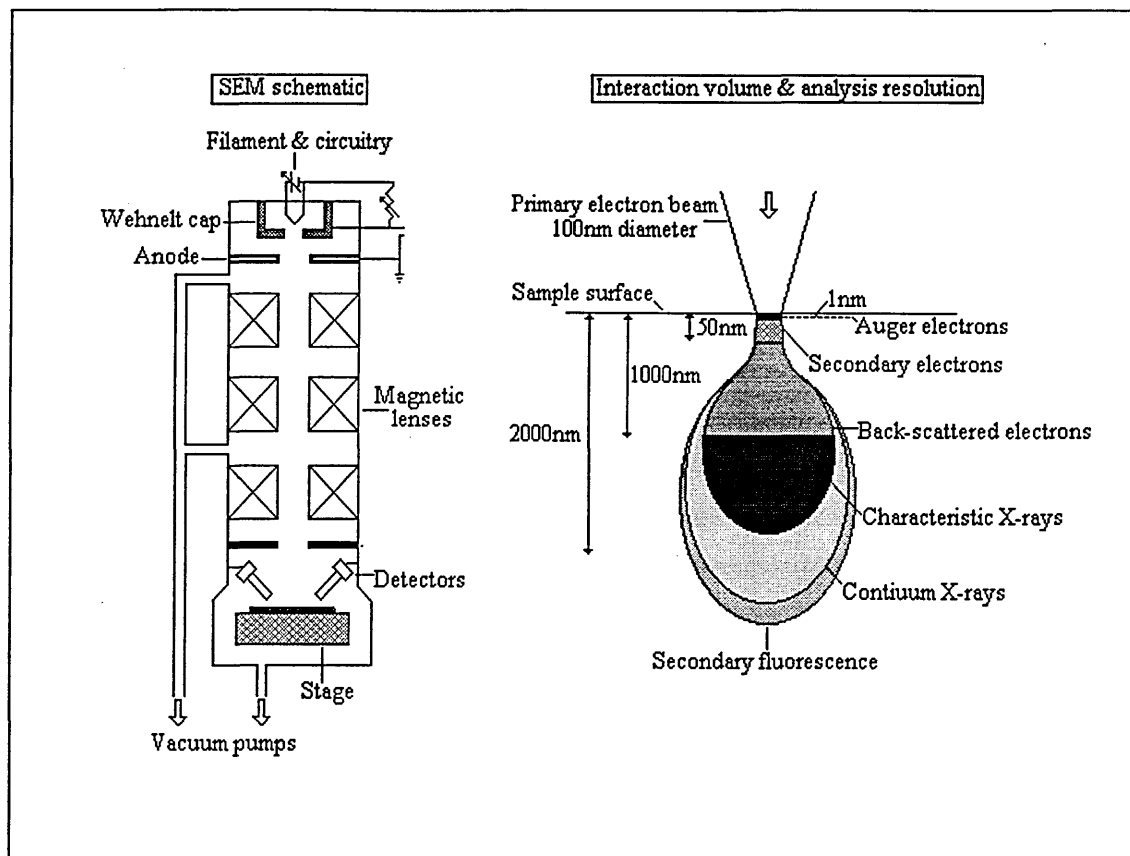
All X-ray diffraction analysis performed during this thesis was carried out on a PW1710 Philips horizontal axis powder diffractometer (counter movement arranged in the vertical plane), computer controlled via automated powder diffraction software, utilising monochromatic Cu K $\alpha$  radiation ( $\lambda=1.542\text{\AA}$ ) and Bragg-Brentano geometry.

### 3.5.2. Scanning electron microscopy.

Electrons are generated by a gun positioned above the microscope column which consists of a filament (usually W or LaB<sub>6</sub>) heated to incandescence at around 2850K to become a thermionic electron emitter which operates most efficiently at the point of saturation (10). The electrons on emission are affected by an electrostatic field provided by a wehnelt grid which has a small negative bias applied to it. This has the effect of deflecting the electrons in such a way as to focus them at a point just before an anode with a cross-over diameter of ~50 $\mu\text{m}$ .

The electron beam is then passed through the microscope column (figure 3.13) under a vacuum pressure of the order of 10<sup>-6</sup>mbar, whose function is to produce a beam of coherent electrons focused to a very fine probe at the specimen surface (11). Disposed at various positions along the column are several electromagnetic condenser lenses and scanning coils to cause collimation, deflection, de-magnification, focusing and synchronous rastering of the electron beam in two orthogonal directions.

Figure 3.13. Schematic of the SEM and its typical interaction volume.



At every point on the scanned sample a signal is generated, however since the surface will differ in its efficiency at producing the given signal, contrast is developed and an image may be derived. An aperture is located at the pivot of the beam and may also be used to vary the intensity of the signal and the depth of field. The signals generated during scanning are detected and converted into electrical pulses which can be used to synchronously control the intensity of output of the electron gun in a cathode ray tube (CRT).

The most common mode used for imaging utilises the secondary electron signal emanating from the sample surface. The secondary electron detector consists of a positively biased grid attached to a scintillator/photomultiplier and positioned at an acute angle to the specimen surface. Contrast in secondary electron images is derived from the fact that secondary electrons are not energetic and may be considered to "drift" from the specimen. Therefore they will only be accelerated towards the detector if they experience a field on the grid which is strongly affected by topographical effects on the specimen surface. Thus regions of the specimen which are in the "shadow" of the field are not attracted into the detector and signals from such areas are low and appear dark in

the image. Hence a secondary electron image provides information relating to surface topography.

Other interaction events which may take place when an electron beam impinges on the surface of a sample include back-scattering of energetic primary electrons and the liberation of characteristic X-rays. Back-scatter detectors are normally positioned above the sample encircling the final condenser lens, where contrast is developed from the fact that different elements have different back-scattering efficiencies. Therefore Back-scattered images are sensitive to elemental composition variations and fine scale topographical details.

If a high energy primary electron from the incident beam collides with an atom in the sample, an inner shell electron may be ejected causing excitation and the production of a vacancy. The atom can return to its ground state by an electron transition from a high energy shell to fill the vacancy, a process which generally occurs with the liberation of an X-ray photon. The X-ray energy is defined by the energy gap between the energy levels in the atom and hence is characteristic of the type of atom. The energy of the X-ray photon is element specific and provides information about the elemental composition of the sample. Thus energy dispersive X-ray detectors (EDX) are also mounted within the chamber to provide a capability for elemental analysis in tandem with imaging.

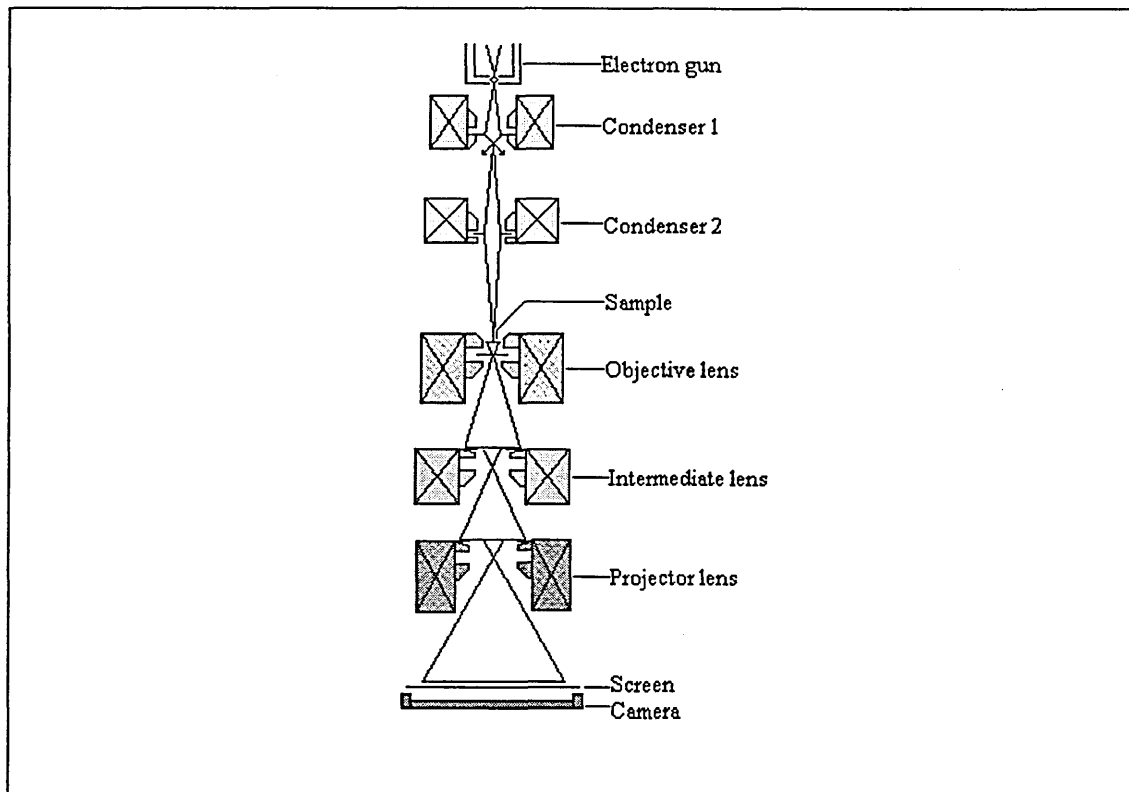
The equipment used for analytical scanning electron microscopy were either a Philips XL40 series ASEM comprising a Link eXL EDX and back-scatter facility or a Jeol 840A microprobe analyser and Link AN10000 EDX facility.

### 3.5.3. Transmission electron microscopy.

One of the most powerful instruments for investigating the microstructural features of thin films such as grain size, defect types, inclusions and micro-voids is the transmission electron microscope (TEM). The main features of the conventional TEM are shown in figure 3.14 and, by comparison, it is obvious that many of the aspects are similar to the SEM. The elevated column contains the electron source, again usually a tungsten filament or LaB<sub>6</sub> crystal, together with an assembly of condenser, objective and projector lenses. The electrons are emitted from the incandescent filament and accelerated by the application of a high negative potential typically 100-300KV which also acts as the first simple electrostatic lens which focuses the beam to a cross-over of about 10-50 $\mu$ m (12). The first condenser lens then acts to reduce the focus point by

approximately 100 times to form a de-magnified image of about  $1\mu\text{m}$  diameter whilst the second condenser (normally weaker  $\sim 2\times$ ) acts to project the reduced image of the filament on the sample. The sample to be analysed is mounted in a eucentric goniometer directly above the objective lens which projects a magnified image ( $\sim 20$  times) of a small part of the sample to the objective plane of an intermediate lens. Here, a magnification occurs (variable times) further into the objective plane of a final projection lens which again magnifies ( $\sim 10$  times) and projects the image on a fluorescent screen or photographic plate. The effective changes in magnification which can be brought about by changes in the magnetic lens currents is typically in the range from 500-1000000 times (13).

Figure 3.14. Schematic of a transmission electron microscope.

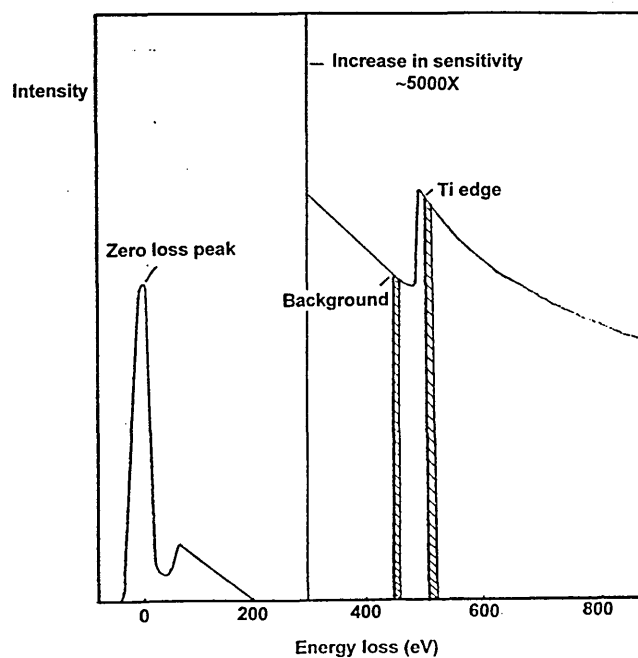


The sample to be analysed by the TEM technique must be electron transparent and provide a low level of inelastic scattering, criteria which limit its maximum thickness to approximately 200nm. For PVD films the sample is generally in the form of a 3mm disc obtained by a combined mechanical and ion beam polishing method which is illustrated in section 3.4.

Bright field and dark field images are the basic mode for viewing crystalline specimens in the transmission electron microscope. A bright field image is produced when an objective aperture, typically 25-200 $\mu\text{m}$  in diameter, is positioned to allow all of the direct beam to form the image. However, for a parallel incident electron beam, the diffracted beams leaving the specimen are focused in the back focal plane of the objective lens, thus the diffraction pattern may be imaged if the back focal plane is projected onto the viewing screen by reducing the excitation of the first projector lens. Using interchangeable apertures positioned close to the back focal plane of the objective lens, a single diffracted beam may be selected and a dark field image produced.

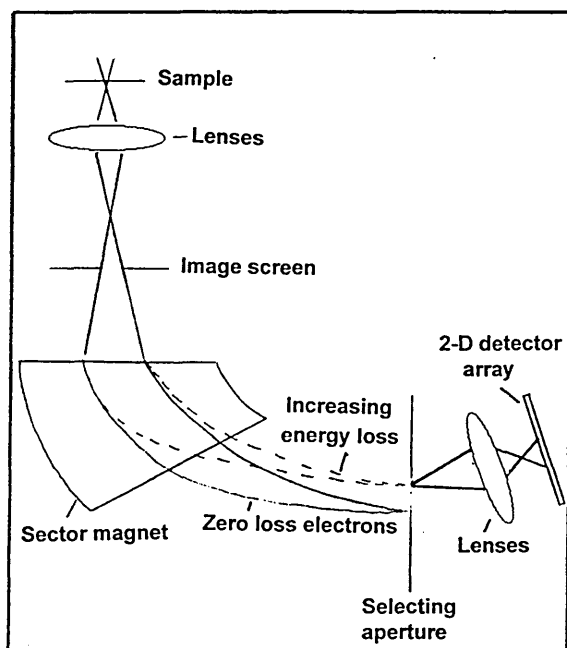
A recent development to high resolution transmission electron microscopy is parallel electron energy loss spectroscopy and image filtering. Here the high energy electrons in the beam of the TEM lose energy in passing through the sample by several mechanisms. One such mechanism, the ionisation and ejection of inner shell electrons within the sample atoms, causes losses which have energy minima which are characteristic of the elements in the sample. The energy distribution of the transmitted beam can be displayed as a spectrum of intensity versus energy (or energy loss) by analysing with a sector magnet fitted below the viewing chamber of the microscope. A typical spectrum is shown schematically in figure 3.15. The positions of the characteristic energy loss edges are manifest as sharp increases in signal on a falling background, as the energy loss increases.

Figure 3.15. Schematic of a typical energy loss spectra showing position of the energy windows to form jump ratio images.



A recent addition to the energy loss technique is the capability of selecting a narrow region of the spectrum and collecting an intensity map of the distribution of electrons across the sample from where the energy losses were incurred. This is known as "energy filtered imaging". Figure 3.16 shows schematically how this is achieved. The normal linear detector array is replaced by an aperture which is positioned to allow transmission only of the selected energy "window". Further lenses allow magnification control at a 2-dimensional solid state detector, which integrates the incident electron charge before being read into an index display/storage system.

Figure 3.16. Schematic of an electron energy loss image filter.



If two images are acquired, one having an energy window just above an edge which is characteristic of an element of interest and the other just below that edge, the two images can be subsequently ratioed to reveal local increases of concentration of the selected element. This procedure can be repeated for all elements of interest.

Alternatively, two images can be recorded using energy windows just below an edge, and a third just above the edge. The first two images are used to calculate an extrapolated background under the edge, which is then subtracted from the third image to leave an elemental map. Again, this is repeated for all elements of interest.

For this thesis a Philips CM20 series STEM instrument comprising a LaB<sub>6</sub> crystal and a 200KeV accelerating potential and a HP-501 TEM was used for high resolution analysis of coating cross-sections on stainless steel substrates.

### 3.5.4. Glow discharge optical emission spectroscopy.

The GDOES technique has been designed to utilise an argon glow discharge to cause removal and stable excitation of atoms from the test sample and allow qualitative and quantitative determination of the metal and non-metal elemental composition as a function of depth.

If sufficient energy is transferred to an atom from the sample by an argon atom from a glow discharge, an increase in electron energy can occur such that a higher energy level or orbital transition takes place to provide an excited state and a lower energy level vacancy. This state is unstable and the atom relaxes back to the ground state by the transition of an electron to fill the vacancy, normally accompanied by the liberation of the excess energy in the form of a photon of wavelength defined by equation 3.4.

$$\lambda = \frac{hc}{E_1 - E_2} \dots\dots\dots\text{equation 3.4.}$$

where;  $E_1$  &  $E_2$  = Energy states

$h$  = Planck's constant

$c$  = Speed of light,  $\lambda$  = Wavelength

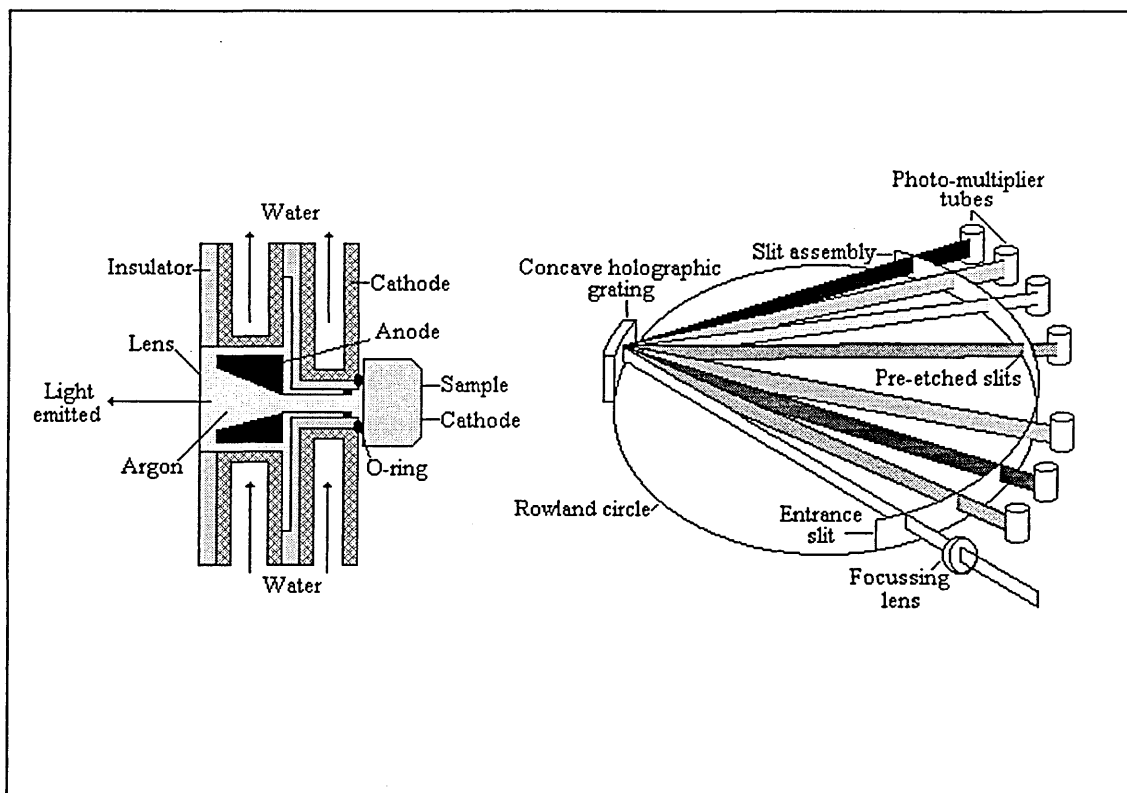
Because each element has different electron orbital energy levels, the wavelength of the photon emissions will be characteristic of the elements present within the sample and the intensities of the emission lines will be proportional to the number of emission quanta and hence elemental concentration (14).

To produce clean line spectra without significant contribution from continuum energy in the form of thermal radiation or lattice vibrations, the atoms must be in the form of a low pressure gas, volatilised from a solid within a vacuum chamber. The glow discharge is ideally suited to provide this process since it naturally separates atoms from the solid surface and from the subsequent excitation and ionisation of those atoms to reduce matrix effects and sample-to-sample inconsistencies.

The GDOES equipment used was a Leco 750-GDS which consisted of a water cooled Grimm type (15) glow discharge source with standard 4mm diameter aperture and a hollow cylindrical anode under vacuum. The cathodic sputtering process of the Grimm lamp is created by applying a voltage to the sample (which acts as the cathode) under a controlled argon pressure across the sample surface. Surface atoms are removed by the sputtering process and diffuse into the argon plasma where excitation and photon

emission occurs (figure 3.17). Separation of the atom removal and excitation provides spectra with a linear relationship between element concentration and spectral intensity.

Figure 3.17. The glow discharge lamp and polychromator



At one end of the glow discharge lamp is a focusing lens and entrance slit to the polychromator through which the emitted light passes. The spectrometer is of classical Paschen-Runge configuration where the polychromator, based on a Rowland circle containing a series of pre-etched slits, enables a range of spectral wavelengths to be focused on a surface simultaneously and allows detection of up to 44 elements through a series of photo-multiplier tubes accurately positioned around the spectrometer perimeter.

The system is generally operated in constant current or voltage mode (both are a function of emission line intensity) and quantification is performed against a range of certified standard reference materials of accurately known concentration. However the quantified depth profile results must be assessed with care as the following parameters can significantly affect accuracy:-

- All spectra have compositions normalised to 100%.
- Non-uniform crater shape.
- Inaccuracies in sputter rate data for compound PVD films
- Surface roughness effects.

### 3.5.5. Vickers hardness test.

The hardness of a material generally implies a resistance to deformation or penetration by another body under a load. This resistance, often an excellent guide to the coatings suitability for wear resistance, is generally measured by techniques based on a standardised indentation technique first proposed by Brinell in 1900 (16).

Today, one of the most common methods to measure the bulk hardness properties of a material is the Vickers hardness test which uses a square-base diamond pyramid as an indenter, where the included angle between opposite faces of the pyramid is  $136^\circ$  (17). Here the indenter is brought into close proximity with the test sample and a known force (typically 0.5-100Kg) is applied to the indenter for a specific period of time to cause an indentation. The Vickers hardness may be calculated using equation 3.5 and is simply defined as the load divided by the surface area of the indentation, however in practise this area is calculated from reflected light microscopic measurement of the length of the diagonals of the impression (figure 3.18).

$$\text{Vickers hardness (Kgmm}^{-2}\text{)} = \frac{2P\sin(\Theta/2)}{L^2} = \frac{1.854P}{L^2} \text{ .....equation 3.5.}$$

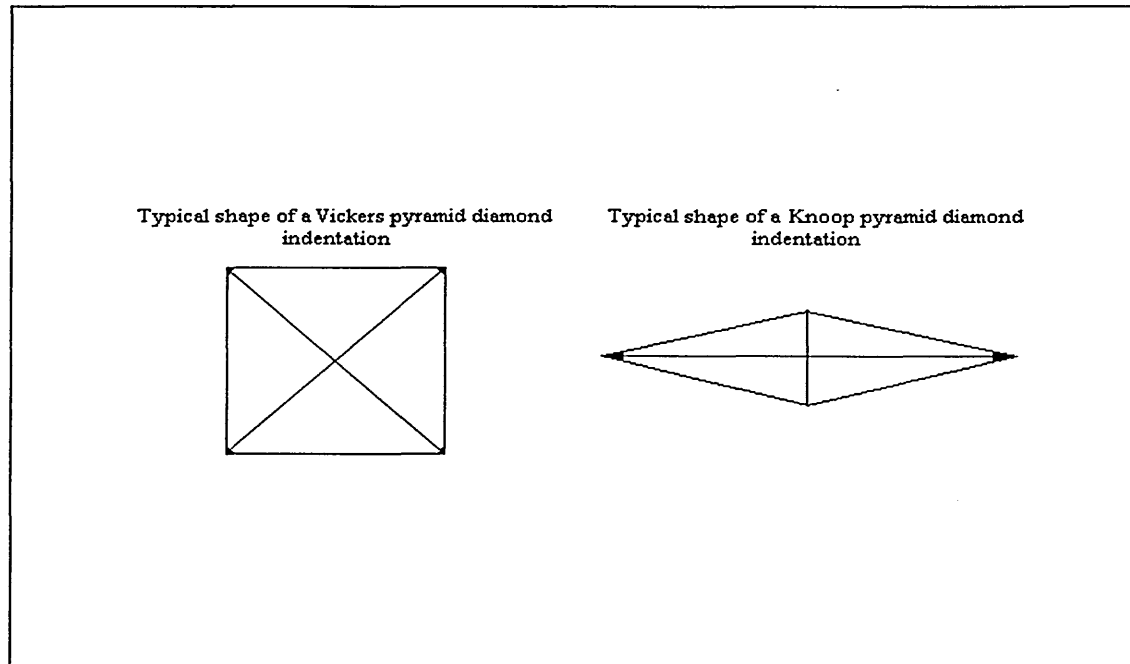
where: P = Applied load in Kg.

L = Average length of diagonals in mm.

$\Theta$  = Angle between opposite faces of diamond =  $136^\circ$

It should be noted that the deformation effect transmitted to the material by the indenter (known as the virtual indenter) extends to approximately 10 times the indentation depth, hence the thickness of the test material should be chosen accordingly.

Figure 3.18. Vickers and Knoop diamond indentation.



The Vickers hardness work carried out in this thesis was undertaken on a Vickers Armstrong tester using 20Kg standard loading and the mean of 10 measurements at separate sample locations was recorded.

### 3.5.6. Knoop microhardness test

The development of the Knoop indenter by the U.S. National Bureau of Standards combined with the introduction of mechanical equipment capable of delivering stable low loads (1-100g) has allowed micro-hardness measurement on thin materials such as PVD coatings without contribution from the substrate (18). The Knoop indenter consists of a diamond ground to a pyramidal form that produces a diamond-shaped indentation with the long and short diagonals in the approximate ratio of 7:1 (figure 3.18) where the depth of the indentation is about 1/30<sup>th</sup> of the length of the longer diagonal under an applied load.

The Knoop hardness can be defined as the load divided by the unrecovered projected area of the indentation (equation 3.6). In practise, the long diagonal is measured by vernier optical microscopy:-

$$\text{Knoop hardness} = \frac{P}{A_p} = \frac{P}{L^2 C} \quad \dots\dots\dots\text{equation 3.6.}$$

- where:-  
 P = Applied load in Kg  
 A<sub>p</sub> = Unrecovered projected area of indentation in mm.  
 L = Length of long diagonal in mm.  
 C = Indentor constant.

The low load used with the Knoop micro-hardness test requires extreme care when making measurements as changes in the level of surface asperities and roughness, elastic recovery of the sample, vibrations and operator error when viewing small indents can all significantly affect accuracy.

All Knoop micro-hardness values quoted in this thesis were recorded from the mean of 10 separate measurements per sample and were taken using either a Tukon MO or a Mitutoyo MVK-G1 tester under 10g, 25g or 50g loading.

3.5.7. Coating thickness Calotest.

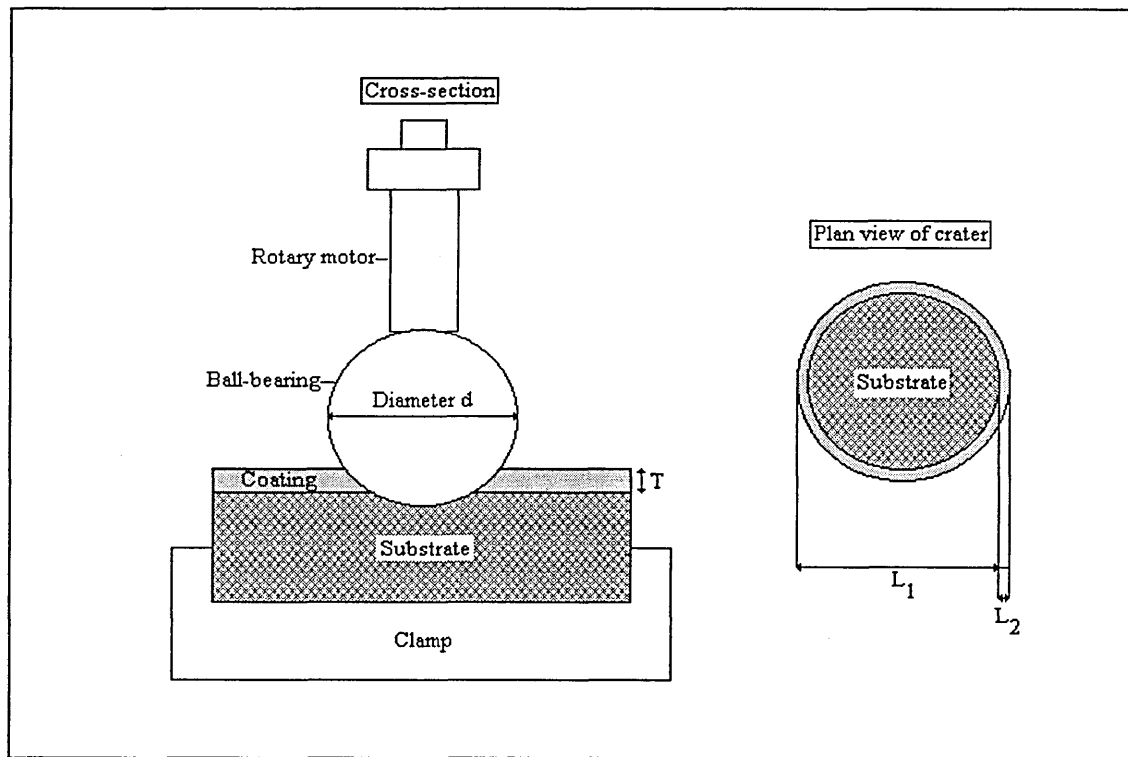
The thickness of the coating is clearly an important parameter in the optimisation of the coating process time and the mechanical properties of the film. An obvious method which can be utilised to obtain the coating thickness is cross-sectional investigation of coating-substrate fracture sections using the scanning electron microscope (sections 3.4 and 3.5.2), however this process can be time consuming, expensive and inflexible. A more rapid method to determine the coating thickness is known as the Calotest (19,20).

The technique utilises a rotating steel ball-bearing (figure 3.19) , typically of diameter ranging from 10-50mm, which is coupled to the coated substrate in the presence of a diamond lapping compound and spun at relatively high velocity to create a shallow hemispherical taper section or "ball-crater".

The ball-cratering process develops a ring pattern which is measurable for coatings of thickness above ~ 0.3µm, where the lengths L<sub>1</sub> and L<sub>2</sub> can be determined using a vernier optical microscope. A simple relationship (equation 3.7) exists between the crater lengths (L<sub>1</sub>&L<sub>2</sub>) and the ball diameter(d) which allows approximation of the coating thickness (T).

$$T = \frac{L_1 \cdot L_2}{d} \dots\dots\dots\text{equation 3.7.}$$

Figure 3.19. Schematic of the Calotest and a plan view of a ball-crater on a coated substrate.



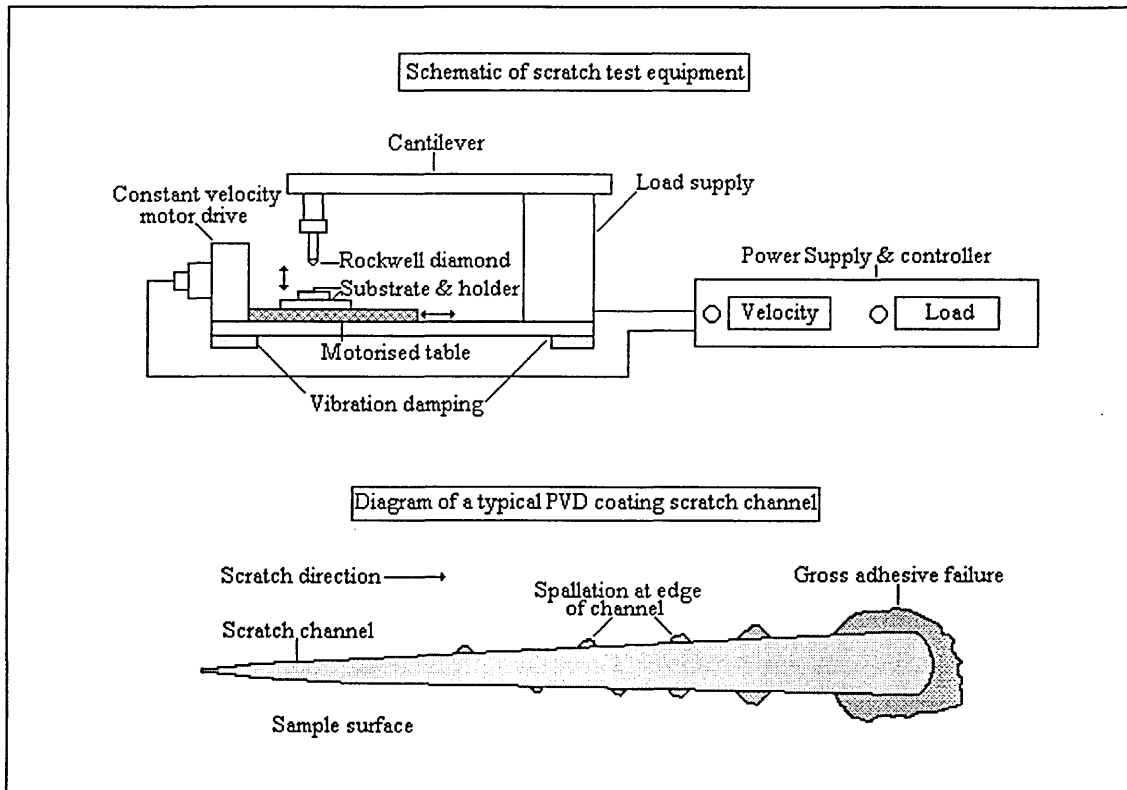
All calotest thickness measurements undertaken in this thesis were performed using a commercially available Eifeler Nord Calopräp tester using a stainless steel ball-bearing of 40mm diameter.

### 3.5.8. Scratch adhesion testing.

One of the primary requirements of a PVD coating is adequate adhesion of the coating to the substrate, a state which may be defined in which the two surfaces are held tightly together by interfacial forces throughout the systems working lifetime. Numerous evaluation techniques have been developed to examine coating adherence and failure modes, most of which induce adhesive failure of the coating-substrate composite by either scratching, indentation, particle erosion and shock-wave exposure (21,22). Of these methods, the mechanical scratch test is perhaps the most widely used and of greatest commercial availability. The test involves the drawing of a Rockwell-C diamond stylus over the coated surface of a substrate at a constant velocity whilst the applied normal force is increased continuously or stepwise until spallation of the coating occurs (figure 3.20). The critical normal force at which the adhesive failure is first

detected (the critical load  $L_c/N$ ), neglecting extreme low load film detachments due to isolated flaws in the coating surface, is used as the measure of adhesion. In practise the critical load is detected directly by vernier optical microscopy of the scratch channel.

Figure 3.20. Schematic of scratch testing equipment and a typical scratch channel



However, great care must be taken in the interpretation of scratch data due to the following variables (23-25):-

- Coating thickness and surface roughness.
- Substrate hardness.
- Indentor wear.
- Residual stress state.
- The subjective nature of  $L_c$  determination and operator error.

For this study a ST200 scratch tester manufactured by Teer Coating Services Ltd and Digiplan motor drive was used for all scratch adhesion trials. The system comprises a Rockwell-C diamond of tip radius  $200\mu\text{m}$  which was used to scratch clamped coated high speed steel coupons ( $R_c64$ ) in two different modes;

**Mode 1:** Continuous increasing load from 0-100N at a rate ( $dI/dx$ ) of  $10\text{Nmm}^{-1}$  to obtain an approximate critical load value measured by vernier optical microscopy (Olympus Vanox).

**Mode 2:** Several further scratch tests were then performed using stepwise loading at new positions on the sample surface for accurate  $L_C$  determination. Mode 2 scratch trials started at a load slightly below the approximate  $L_C$  found by mode 1 and were increased in increments of 5N. The arithmetic mean of several critical load values found by microscopic failure determination was recorded.

### 3.5.9. Rockwell indentation adhesion testing.

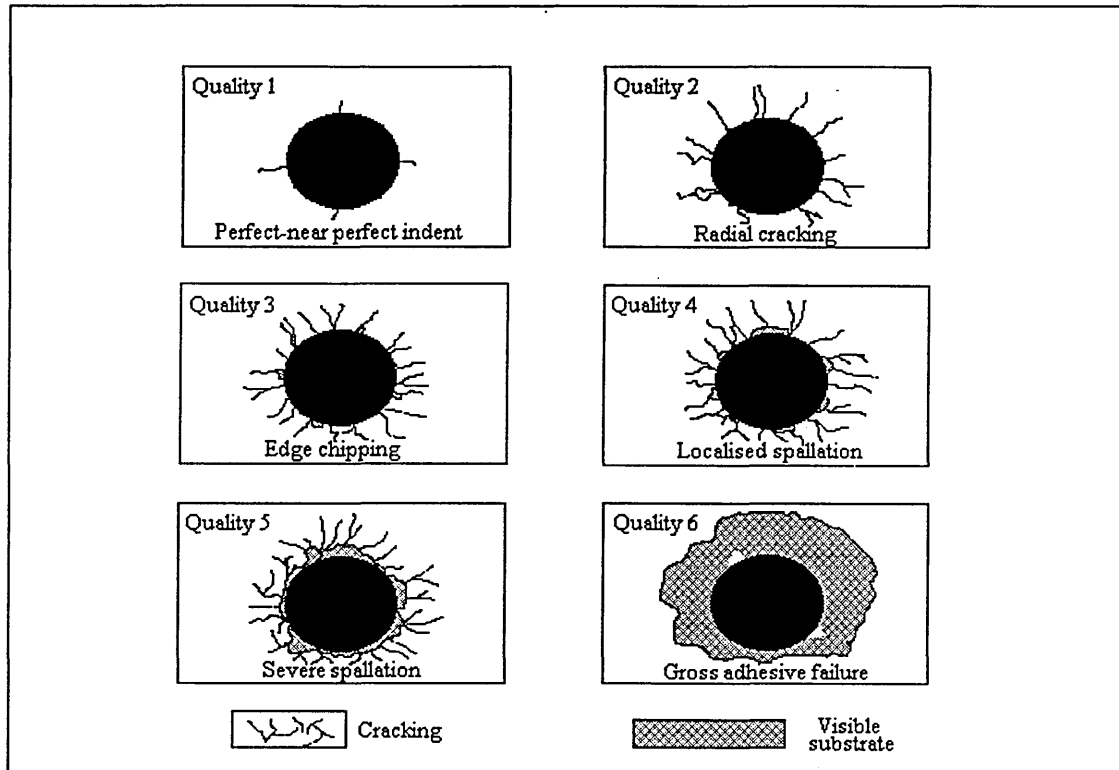
A second method to examine the adhesion of a PVD coating to a substrate is the application of an excessive point load (greater than would normally occur) to the composite system. Such a method is the Rockwell-C indentation test (26). This technique develops a mechanically stable crack through the coating and into the substrate by means of a Rockwell-C diamond indentation under the application of a 150Kg standard load. The resistance to propagation of the crack along the interface is then used as a measure of adhesion. Examination and comparison of the cracking profile against an adhesion criterion developed by Verein Deutscher Ingenieure (VDI) allows the classification of the cracking or spalling of the coating (figure 3.21) at the surface, subject to the following parameters:

- The coating thickness is less than  $5\mu\text{m}$ .
- The cracking profile is analysed using an optical microscope at magnification  $\times 100$ .
- The substrate hardness is in excess of  $R_C54$ .

The VDI criterion predicts indentation classes from 1-4 represent an acceptable level of coating adhesion and indentation classes 5-6 are not acceptable, but no specific adhesion value is normally assigned. Rockwell indenting also allows examination of the cohesion of the coating and may also be used to investigate any annealing of heat sensitive coated substrates if an excessive etching or deposition temperature has been utilised.

Hence, all Rockwell indentation investigations presented in this thesis were performed on HSS substrates of  $R_C64$  coated with films of 1- $5\mu\text{m}$  thickness using an Avery 1412 indenter.

Figure 3.21. The VDI Rockwell indentation adhesion criteria.



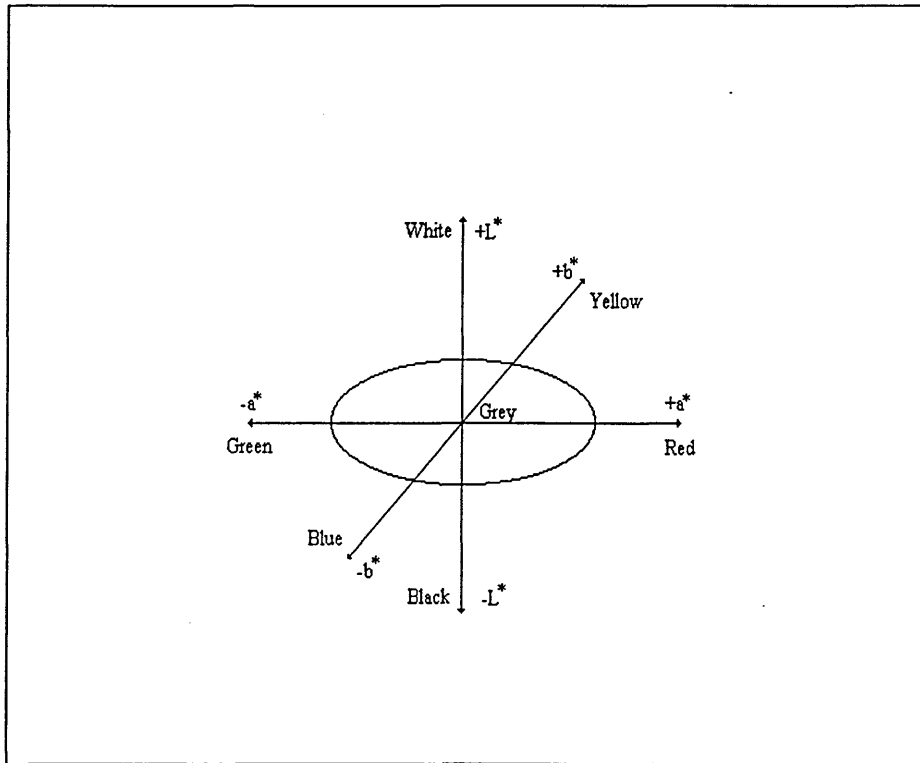
### 3.5.10. Colourimetry.

Colourimetry may be defined as the quantitative measurement of perceived colour, encompassing the illumination of the sample, its reflectance and the visual response of the observer. Determination of a sample's colour involves illuminating the sample surface with a standard source (normally from a xenon halogen discharge tube) and detecting the reflected light using a range of photocells, individually filtered to accept one of the primary colours. The colourimeter detects tristimulus values ( X,Y,Z - red, green, blue) over wavelengths ranging from 400-700nm, converts them into chromaticity components of colour (hue & intensity) and compares them against a reference calibration (white-black) where the deviation is calculated. The colour difference detected defines a position in CIELAB colour space based on human colour perception, established by the Commission Internationale de l'Eclairage in 1976 (27), which has 3 orthogonal axes (figure 3.22).

L\*- The difference in lightness or reflectance (black to white).

a\* - The difference in red to green , b\* - The difference in blue to yellow.

Figure 3.22. The CIELAB colour space.



The colourimeter is a useful instrument in PVD technology enabling:-

- Colour matching of decorative coatings.
- Indications of changes in stoichiometry and composition (28,29).
- Detection of changes in surface roughness produced by ion bombardment.
- A standard, non-visual method of accurately describing film colour.

During this research project two types of colourimeter were utilised, a Dr.Lange micro-colourimeter and an Applied Colour Systems Chroma Sensor-3.

### 3.5.11. Surface roughness profiling.

The measurement of surface roughness, a parameter which can critically affect the decorative, frictional and tribological properties of the coating-substrate composite, involves the movement of a fine stylus across the surface of a sample at a constant velocity. The small vertical displacements transmitted to the stylus contact as it traverses the sample are monitored to produce a surface profile output of vertical displacement as a function of trace distance. Modern instruments are interfaced to

computer control systems which allow various statistical analyses of the profile raw data.

$R_a$  - The average roughness - Defined as the arithmetical mean of the absolute values of the profile's departures within a measuring length  $L$ .

$$R_a = \frac{1}{L} \int_0^L |y(x)| dx \quad \text{.....equation 3.8.}$$

$R_z$  - Defined as the average value of the absolute values of the heights of the five highest profile peaks ( $p$ ) and the depths of the five deepest profile valleys ( $v$ ) within a measuring length  $L$ .

$$R_z = \frac{\sum |y_{pi}| + \sum |y_{vi}|}{5} \quad \text{.....equation 3.9.}$$

$R_t$  - Defined as the distance between the highest peak and the lowest valley within a measuring length  $L$ .

The surface profiler is a useful tool for the surface engineer to assess not only the coating roughness and hence its coefficient of friction, but also the extent of defects or voids within the film, the uniformity of coating coverage and macro-particle incorporation from arc etching or deposition techniques.

The surface roughness equipment used were Rank Taylor Hobson 120-L and Mitutoyo 211 form talysurfs.

### **3.6. Summary of equipment and techniques.**

#### Evaporation and sputtering equipment.

- Experimental electromagnetic steered arc evaporation facility at S.H.U, U.K.
- Industrial scale unbalanced magnetron sputtering facility at F.E.M, F.R.G.
- Industrial scale Arc-Bond Sputter combined arc / magnetron facility at S.H.U, U.K.

#### Target manufacturing apparatus.

- Segmented targets- Autoclave Isohipper and National Forge HIP vessels.
- TiAl ABS targets- Powder metallurgical HIP route manufactured by Heraeus GmbH.
- Ti and Zr ABS targets- Melting and casting route manufactured by Titanium Intl Ltd.

#### Characterisation techniques.

- X-ray diffraction - Philips PW1710 CuK $\alpha$  powder diffractometer.
- Scanning electron microscopy - Philips XL40 and Jeol 840A.
- Transmission electron microscopy - Philips CM20 STEM.
- Optical microscopy - Olympus Vanox-T.
- Glow discharge optical emission spectroscopy - LECO GDS-750.
- Vickers hardness test - Vickers Armstrong engineering tester.
- Knoop micro-hardness test - Tukon MO and Mitutoyo MVK-G1.
- Calotest - Eifeler Nord Calopräp.
- Scratch adhesion test - ST200 Teer Coating Services Ltd.
- Rockwell-C indentation test - Avery 1412.
- Colourimetry - Dr.Lange micro-colourimeter and Applied Colour Systems Chroma Sensor-3.
- Surface roughness profile - Rank Taylor Hobson Form 120-L and Mitutoyo 211 talysurfs.

## References.

1. P.J.Walke - *Ph.D thesis*, 1994, Sheffield Hallam University, United Kingdom.
2. V.I.Rakhovskii - *IEEE Trans.Plasma.Sci*, 1976, PS-4, 2, 81-102.
3. W-D.Münz, D.Schulze, F.J.M.Hauzer - *Surf.Coat.Tech*, 1992, 50, 169.
4. R.M.Walker, D.J.Roberts, B.A.Rickinson - "*Component assembly using HIP diffusion bonding*", 1990, Infutech Ltd Publication, H.I.P, Chesterfield, U.K.
5. I.J.Mellanby - *Metal Powder Report*, 1989, 44, 6.
6. P.J.Goodhew - "*Specimen Preparation in Materials Science*", 1972, North-Holland Press.
7. B.D.Cullity - "*Elements of X-ray Diffraction*", 1978, Addison-Wesley Press.
8. D.S.Rickerby, A.M.Jones, B.A.Bellamy - *Surf.Coat.Tech*, 1989, 37, 111-137.
9. J.A.Sue - *Surf.Coat.Tech*, 1992, 54-55, 154.
10. A.R.Gabriel - "*SEM-A Users Manual for Materials Science*", 1972, North-Holland Press.
11. D.K.Bowen, C.R.Hall - "*Microscopy of Materials*", 1975, Macmillan Press.
12. M.H.Loretto - "*Electron Beam analyses of Materials*", 1984, Chapman & Hall Press.
13. P.E.J.Flewitt, R.K.Wild - "*Physical Methods for Materials Characterisation*", 1994, IOP Press.
14. H.A.Strobel - "*Chemical Instrumentation*", 1977, Addison-Wesley Press.
15. W.Grimm - *Spectrochimica Acta*, 1968, 23B, 443.
16. J.A.Brinell - *Congr.Int.Methods d'Essai*, 1900, Paris.
17. H.E.Boyer - "*Hardness testing*", 1987, ASM International Press.
18. B.W.Mott - "*Micro-indentation hardness testing*", 1956, Butterworth Press.
19. H.Schwarz - *Pract.Met*, 1987, 24, 257.
20. A.Schulz, H.R.Stock, P.Mayr - *Mat.Sci.Eng*, 1991, A140, 639.
21. J.Valli, U.Mäkela, A.Matthews - *Surf.Eng*, 1986, 2(1), 49.
22. D.S.Rickerby - *Surf.Coat.Tech*, 1988, 36, 541.
23. M.Olsson - *Ph.D thesis*, 1989, 200, Uppsala University, Sweden.
24. P.A.Steinmann, H.E.Hintermann - *J.Vac.Sci.Technol*, 1985, A3(6), 2394.
25. S.J.Bull - *Surf.Coat.Tech*, 1991, 50, 25-32.
26. Verein Deutscher Ingenieure - *Richtlinie 3198*, 1992, Dusseldorf, F.R.G.
27. G.J.Chamberlin, D.G.Chamberlin - "*Colour - Its Measurement, Computation and Application*", 1980, Heydon & Son Press.
28. B.Zega - *Surf.Coat.Tech*, 1989, 39-40, 507.
29. G.Reiners, H.Hantsche, H.A.Jehn, U.Kopacz, A.Rack - *Surf.Coat.Tech*, 1992, 54-55, 273.

## **CHAPTER FOUR**

### **INVESTIGATION OF TiZr, TiMo AND ZrMo SEGMENTED TARGETS.**

This chapter presents the results of metallurgical and physical investigations on various vacuum arc melted TiZr alloys and TiZr, TiMo and ZrMo segmented targets manufactured by a Hot Isostatic Pressing (HIP) diffusion bonding process for use in steered arc, unbalanced magnetron and arc-bond sputter PVD trials. Prior to the manufacture of the segmented targets, a detailed examination of the alloy properties was undertaken which also provided some of the appropriate parameters used in HIPping. After target fabrication, fundamental characterisation of the target properties and performance in evaporative and sputtering trials was evaluated.

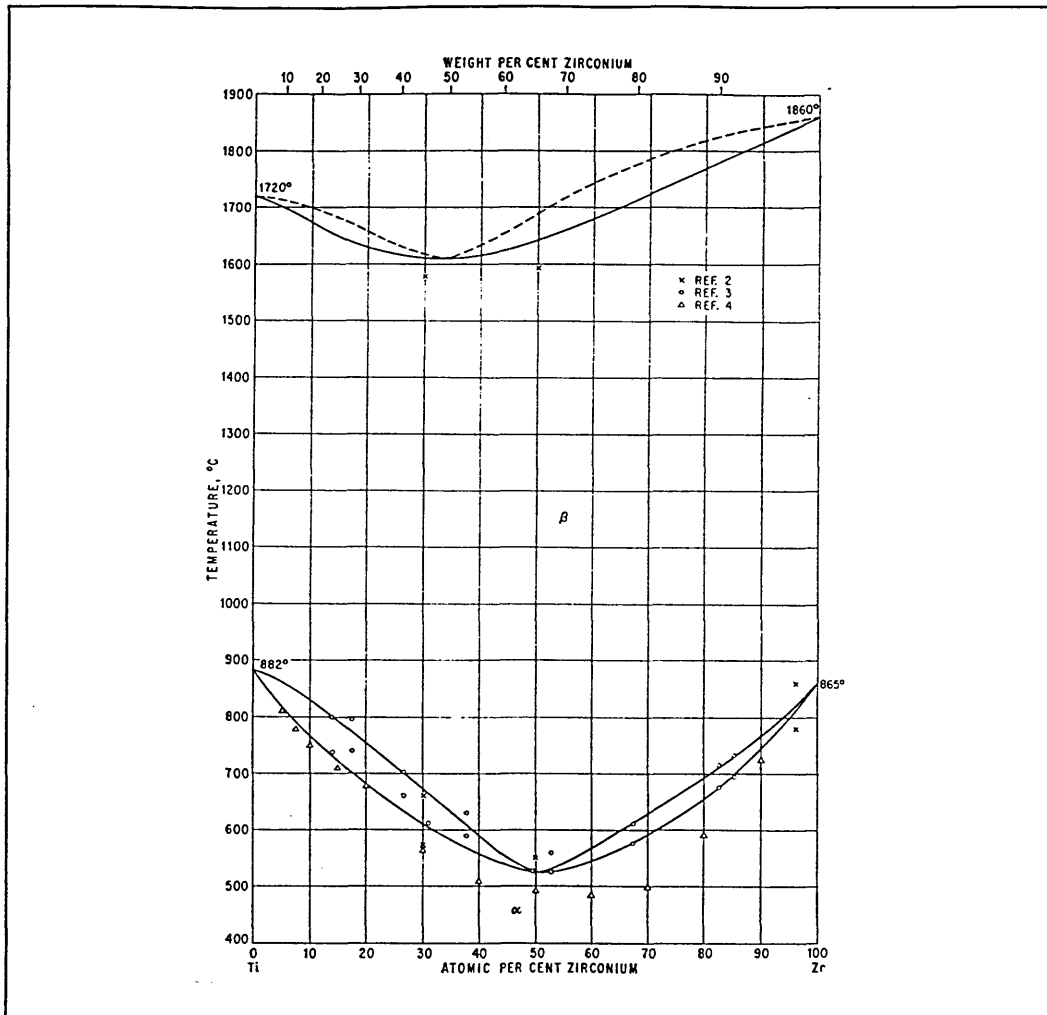
#### **4.1. TiZr model alloy investigations.**

##### **4.1.1. Alloy manufacture, sample preparation and equilibrium studies**

Phase equilibrium investigations by Fast (1) & Duwez (2) identified that the TiZr system can exhibit two series of complete solid solutions (figure 4.1) comprising a low temperature alpha phase (close packed hexagonal structure) and an elevated temperature beta phase (body centred cubic structure). The  $\alpha$ - $\beta$  transformation was found to have been depressed to a minimum in 50/50at % alloys at a temperature of 535°C and the liquidus reached a minimum at 67at% Zr at 1610°C.

Metallurgical and physical property investigations on the TiZr system were performed using a series of 50g button melts of compositions 20Ti / 80Zr, 50Ti / 50Zr and 80Ti / 20Zr atomic % (Ti purity >99.7% , Zr purity >99.6%) manufactured in vacuum arc melting facilities at Hallam University and the University of Sheffield. The homogeneous melts were sectioned for analysis using a Struers Accutom II metallurgical rotary saw comprising an alumina ( $\text{Al}_2\text{O}_3$ ) cutting wheel to provide samples of dimensions 25mm x 15mm x 5mm and examined by a range of bulk and micro-analysis techniques including SEM, optical reflective microscopy, XRD, X-ray fluorescence spectroscopy (XRF) and Vickers hardness testing (20Kgf).

Figure 4.1. TiZr binary alloy equilibrium phase diagram.



For determination of alloy thermal stability, variation in mechanical properties and confirmation of phase equilibrium, two types of elevated temperature trials were initiated:-

(i) Samples of the three compositions were evacuated, purged and sealed in a pure argon atmosphere before temperature elevation to constant 450°C (just below the  $\alpha$ - $\beta$  transus) for a period of 72 hours prior to analysis.

(ii) Samples of the three compositions were evacuated, purged and sealed in a pure argon atmosphere before thermal cycling above and below the  $\alpha$ - $\beta$  transus using the regime:-

**(a) 20°C -(b) 300°C & 2 hours -(c) 900°C & 2 hours -(d) 300°C & 2 hours -(e) 20°C**

#### 4.1.2. Results of 20%Ti / 80%Zr alloy investigations.

In the as cast condition, the 50g button melt appeared metallic silver in colour and smooth in texture under initial visual examination. Microstructural investigation using a standard electro-polishing technique (Struers A3 electrolyte) revealed a complex cross-networking of fine needle crystals characteristic of a martensitic transformation (figure 4.2), i.e. a rapid transformation involving a shear process but without diffusion. X-ray diffraction studies confirmed the alloy had a hexagonal close packed (hcp) crystal structure with the  $(10\bar{1}1)$  reflection as the major intensity peak and lattice parameters  $a = 3.17\text{\AA} \pm 0.01\text{\AA}$  and  $c = 5.06\text{\AA} \pm 0.01\text{\AA}$  providing an axial ratio of 1.59 (figure 4.3). A series of Vickers hardness indentations showed that the alloy was relatively soft at  $244H_V \pm 40H_V$ .

Figure 4.2. 20/80 TiZr alloy microstructure (as-cast condition).



Figure 4.3. X-ray diffraction traces from 20/80 TiZr alloy.

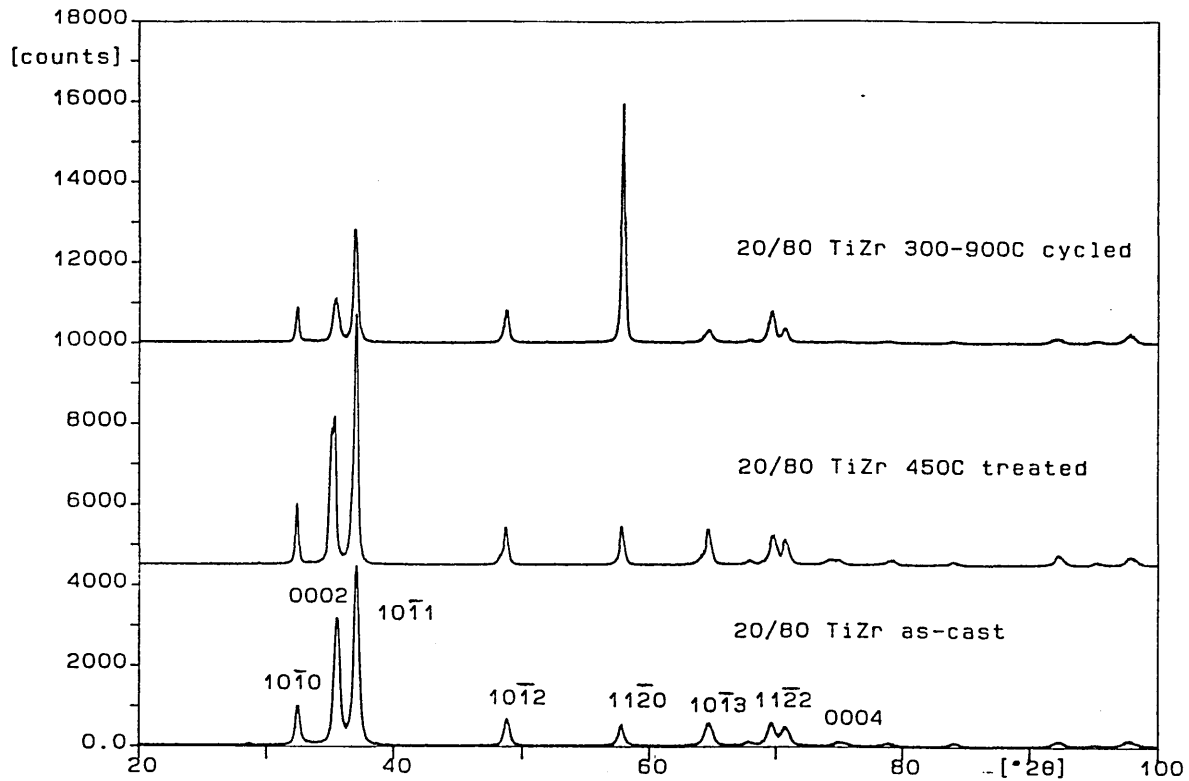
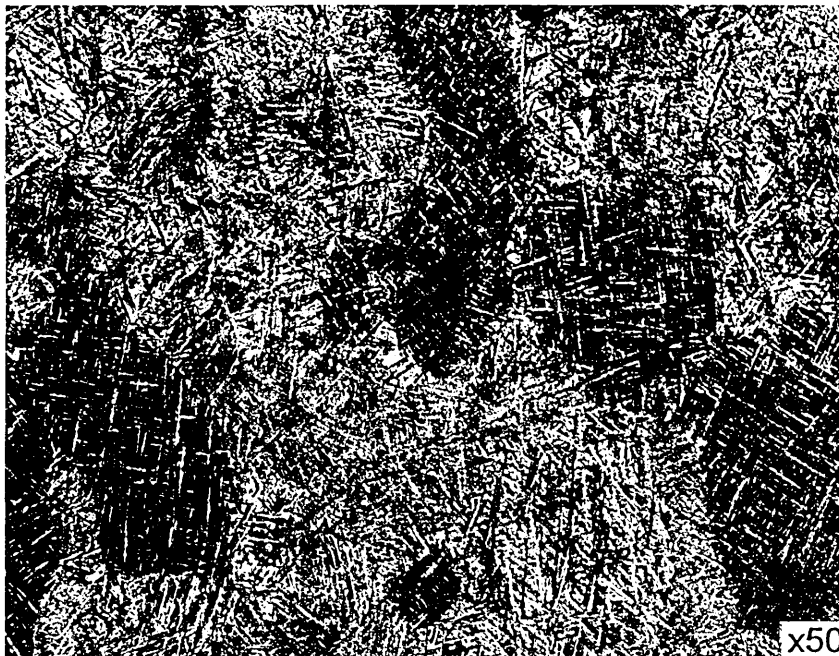


Figure 4.4. 20/80 TiZr alloy microstructure (450°C treated condition).



X-ray diffraction analysis of the specimen elevated to 450°C for 72 hours (figure 4.3) indicated that the crystal structure remained hexagonal close packed although small peak shifts were observed due to annealing and stress relaxation effects. An increase in major peak ( $10\bar{1}1$ ) intensity was noted, whilst calculation of the lattice parameters showed that the extent of the peak shifts were sufficient to cause only slight changes in unit cell dimensions. SEM and OM analysis of electro-polished samples showed that the microstructure remained dominated by the martensite networks with no evidence of secondary component or phase generation (figure 4.4). Vickers indentation measurements revealed that the increase in temperature had also caused a modest reduction in hardness to  $233H_V \pm 40H_V$ .

Elevation and depression of the temperature forcing allotropic transformation of the 20/80 alloy provided several significant property changes. X-ray diffraction revealed that the crystal structure remained single phase hexagonal close packed but recrystallisation effects had provided a change in texture such that the  $(11\bar{2}0)$  plane produced the major intensity reflection (figure 4.3). Negligible variation in lattice parameters was recorded. Microstructural assessment showed that the alloy had adopted a more acicular, pseudo-Widmanstätten morphology caused by a series of martensitic transformations during the cooling phases of the thermal cycling regime (figure 4.5). Vickers hardness analysis demonstrated that thermal cycling of the alloy had further reduced the hardness to  $200H_V \pm 40H_V$ .

Figure 4.5. 20/80 TiZr alloy microstructure (300-900°C cycled condition).



#### 4.1.3. Results of 50%Ti / 50%Zr alloy investigations.

As-cast 50%Ti / 50%Zr alloys revealed major structural and morphological differences between the individual Hallam University and University of Sheffield samples. X-ray diffraction analysis of the 50/50 button melt produced at Hallam University (where the arc melting unit was only rotary pumped to a pressure  $\sim 1 \times 10^{-2}$  mbar and did not comprise a Zr getter) indicated the presence of a two phase system, predominantly metastable body centred cubic ( $\beta$ -phase) with a lattice parameter of  $a = 3.45 \text{ \AA} \pm 0.01 \text{ \AA}$  with evidence of lower intensity h.c.p ( $\alpha$ -phase) reflections (figure 4.6). Similar analysis on the 50 /50 alloy produced at the University of Sheffield (where the arc melting unit was rotary and diffusion pumped to a pressure  $\sim 1 \times 10^{-4}$  mbar and comprised a Zr getter) indicated only a single phase hexagonal close packed structure was formed (figure 4.7), similar to the 20/80 alloy, where a reduction in lattice parameter occurred such that  $a = 3.08 \text{ \AA} \pm 0.01 \text{ \AA}$  and  $c = 4.91 \text{ \AA} \pm 0.01 \text{ \AA}$  giving an axial ratio of 1.59. Analysis revealed that the oxygen impurity concentration in the Hallam University sample (2600ppm) was significantly higher than the University of Sheffield sample (890ppm). Microstructural investigations revealed that the Hallam University sample had an equiaxed grain structure (figure 4.8) whilst the University of Sheffield alloy demonstrated a martensite grain structure. Vickers indentations showed that the bulk hardness of the Hallam University sample had significantly increased to  $566 H_V \pm 40 H_V$  whilst the University of Sheffield sample remained lower at  $290 H_V \pm 40 H_V$ .

**Figure 4.6. X-ray diffraction traces from 50/50 TiZr alloy (Hallam University)**

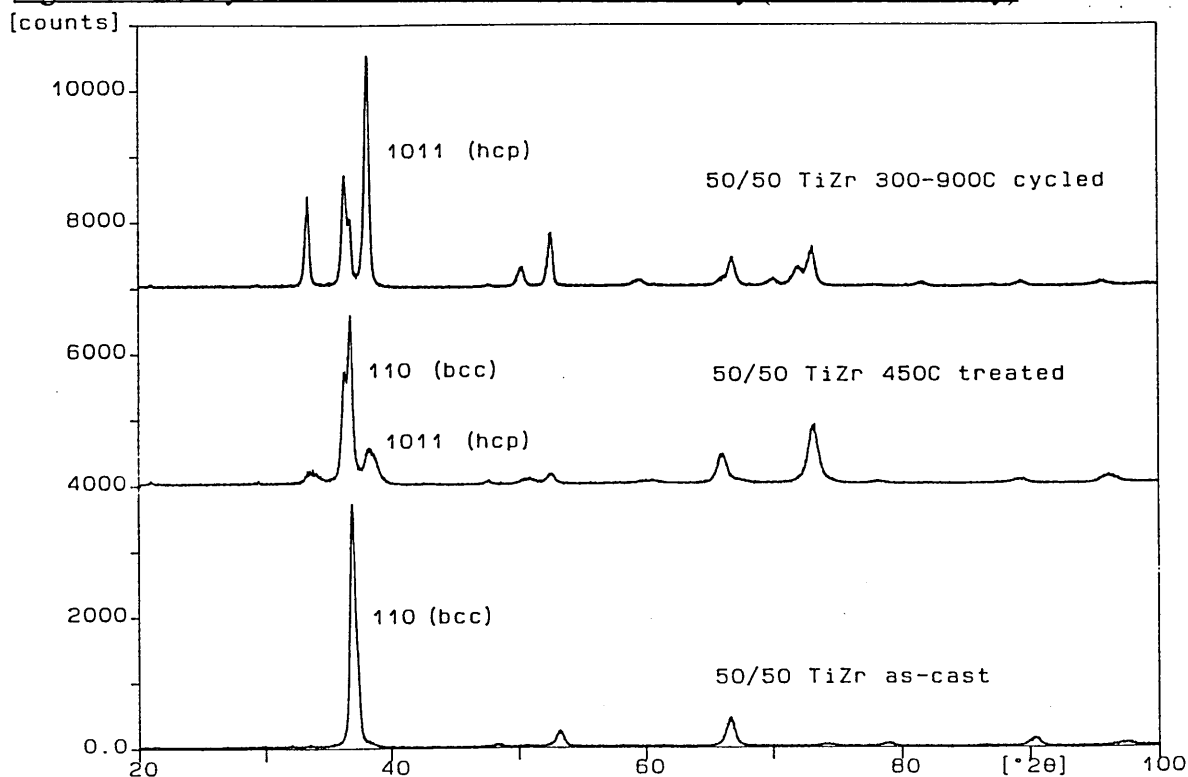


Figure 4.7. X-ray diffraction trace from as-cast 50/50 TiZr alloy (Sheffield University)

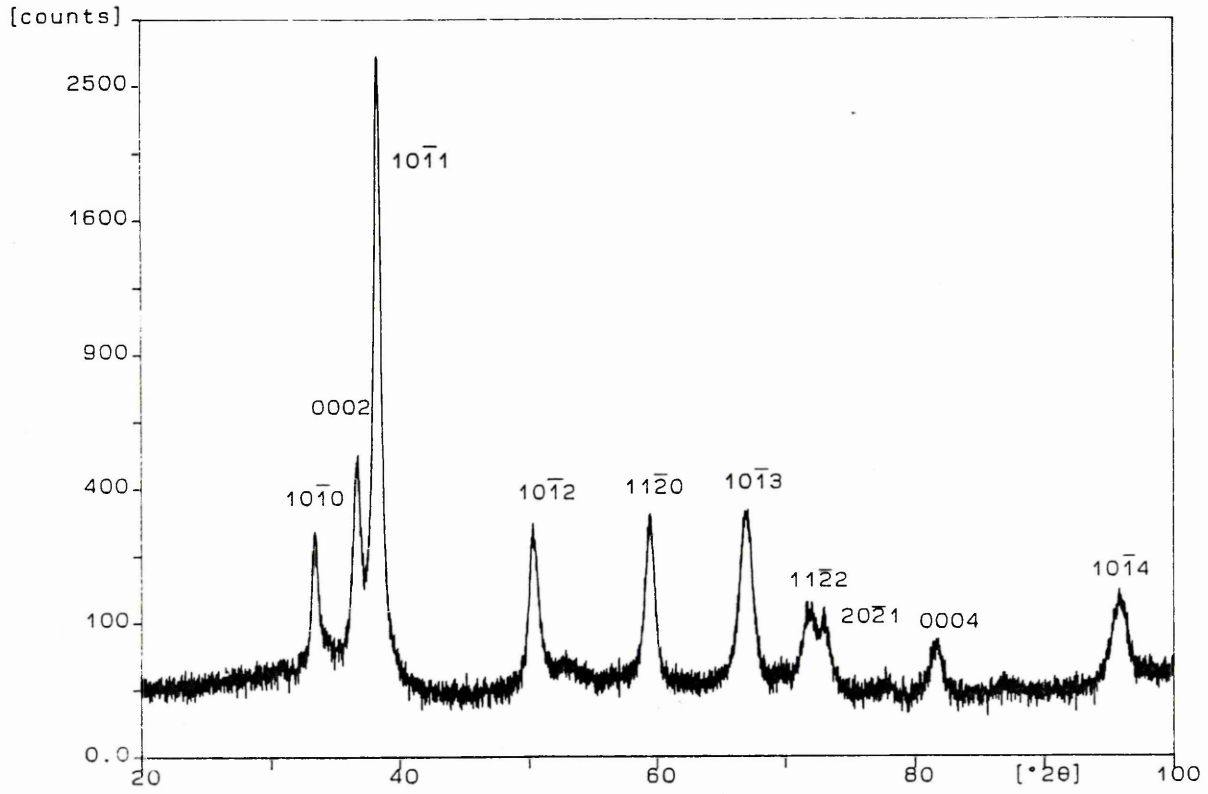
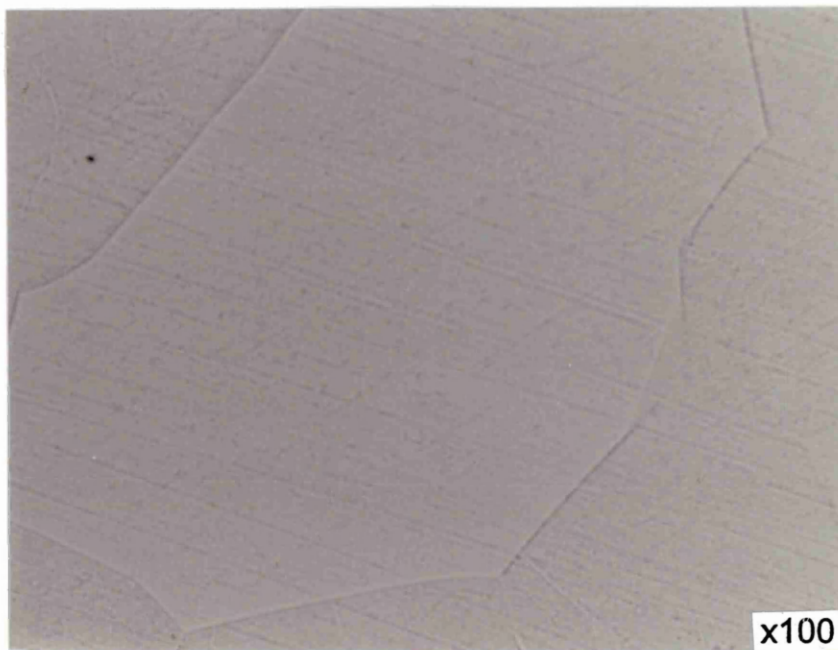
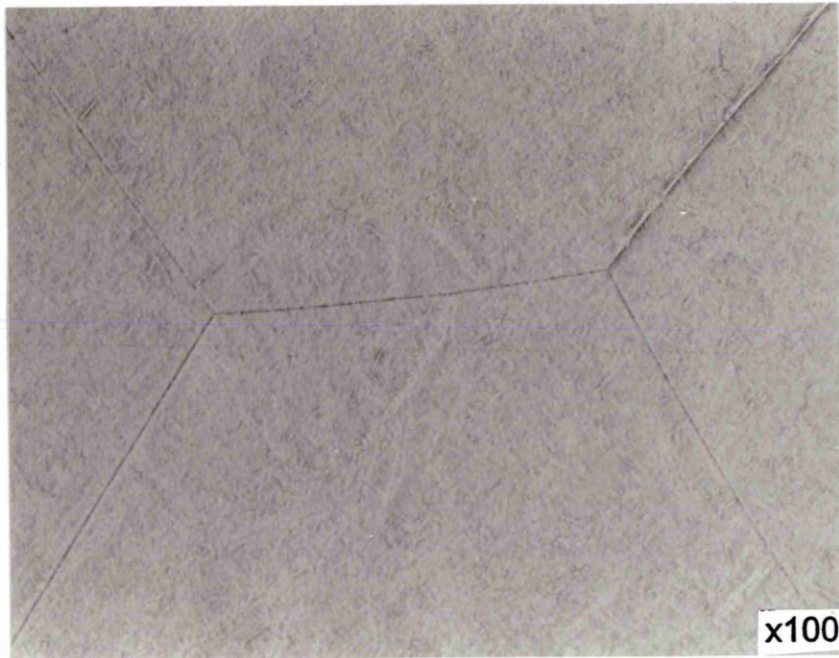


Figure 4.8. 50/50 TiZr alloy microstructure (as-cast condition).



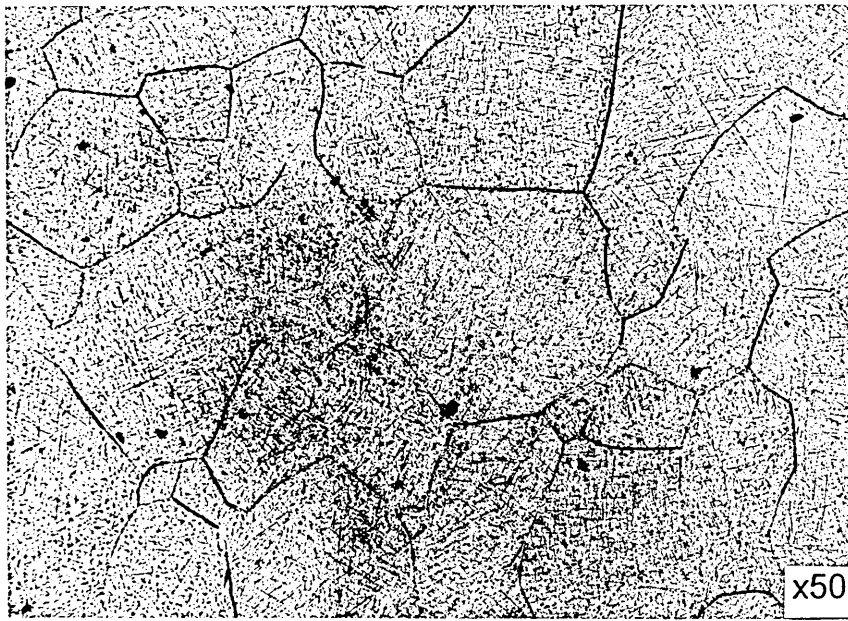
Constant thermal treatment at 450°C did not provide any major change in structure of both the Hallam University or University of Sheffield samples. The Hallam University alloy remained b.c.c structured and (110) textured (figure 4.6), however the intensity of the h.c.p reflections was found to have significantly increased. The University of Sheffield sample continued to exhibit a single phase h.c.p structure. SEM and OM investigations provided evidence of a granular equiaxed structure in the Hallam University sample (figure 4.9) whilst the University of Sheffield sample exhibited martensite. Vickers hardness measurements showed that the hardness of both alloys had reduced to  $535H_V \pm 40H_V$  and  $265H_V \pm 40H_V$  respectively.

Figure 4.9. 50/50 TiZr alloy microstructure (450°C treated condition).



Thermal cycling of the Hallam University alloy resulted in the hexagonal phase becoming dominant with the  $(10\bar{1}1)$  reflection becoming the major intensity peak (figure 4.6). No change in unit cell structure was detected for the h.c.p University of Sheffield alloy. Microstructural investigations revealed that the Hallam university sample had adopted a combined martensite and equiaxed morphology (figure 4.10) whilst the University of Sheffield grain structure remained unchanged. Vickers indentation testing showed that the hardness of both alloys had again decreased to  $507H_V \pm 40H_V$  and  $245H_V \pm 40H_V$  respectively.

Figure 4.10. 50/50 TiZr alloy microstructure (300-900°C cycled condition).



4.1.4. Results of 80%Ti / 20% Zr alloy investigations.

The 80Ti / 20Zr alloy properties were found to have many similarities with those of the 20Ti / 80Zr alloy. As-cast X-ray diffraction analysis revealed a hexagonal close packed crystal structure with lattice parameters  $a = 3.00\text{\AA} \pm 0.01\text{\AA}$  and  $c = 4.77\text{\AA} \pm 0.01\text{\AA}$  giving an axial ratio of 1.59 and major intensity peak due to the  $(10\bar{1}1)$  plane (figure 4.11). Microstructure assessment revealed a characteristic martensite needle cross network pattern (figure 4.12) and hardness measurements indicated values typically  $260H_V \pm 40H_V$ .

Figure 4.11. X-ray diffraction traces from 80/20 TiZr alloy.

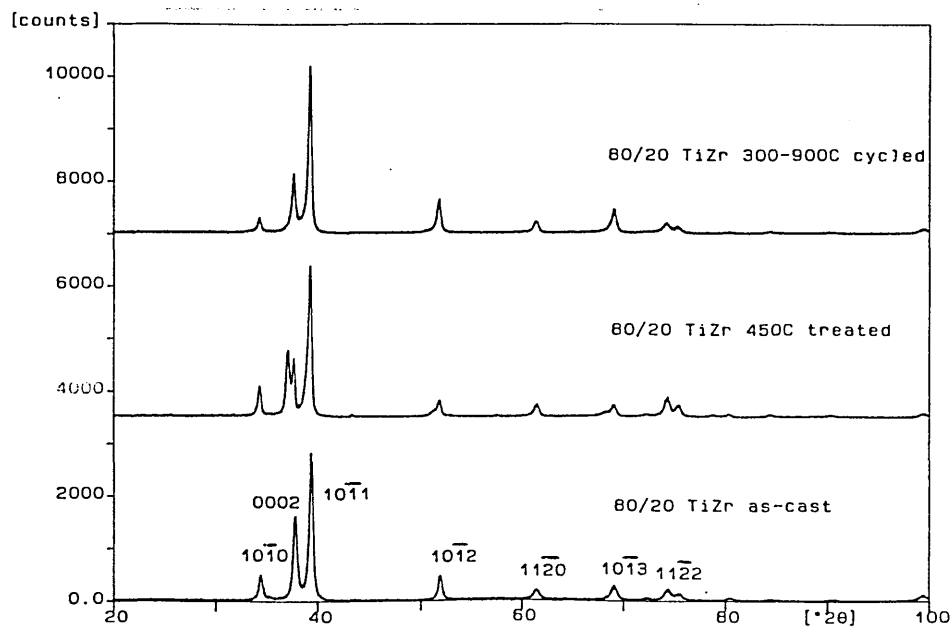
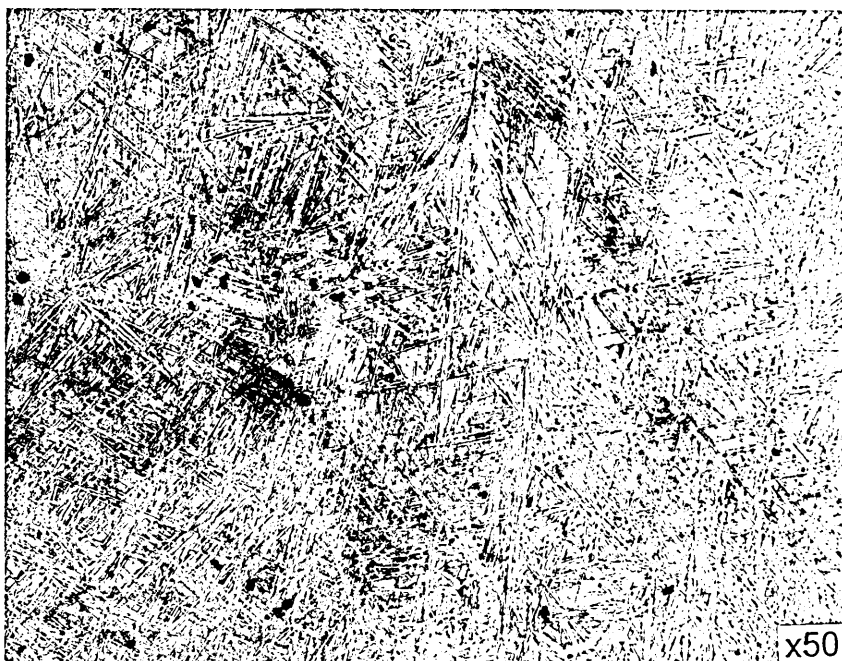


Figure 4.12. 80/20 TiZr alloy microstructure (as-cast condition).



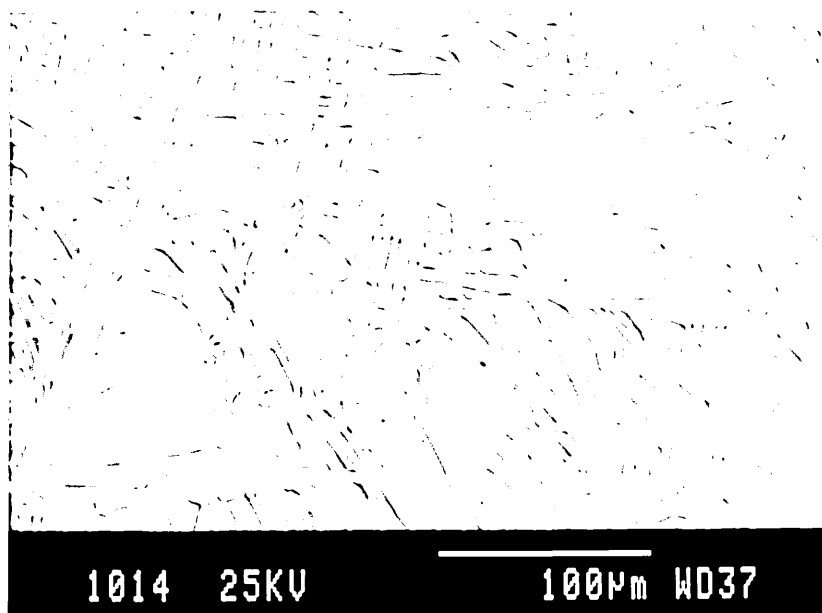
Thermal treatment at 450°C produced little change in the alloy mechanical and physical properties. The alloy crystal structure remained h.c.p (figure 4.11) with small amounts of peak shift due to stress relaxation effects. The major intensity peak was due to the  $(10\bar{1}1)$  plane whilst the microstructure remained the same as in the as-cast state (figure 4.13). A modest reduction in Vickers hardness was recorded ( $240H_V \pm 40H_V$ ) due to annealing effects.

Figure 4.13. 80/20 TiZr alloy microstructure (450°C treated condition).



Thermal cycling of the 80Ti / 20Zr alloy produced X-ray diffraction traces which fitted well to the 450°C trace with h.c.p. structure, peak positions remaining unaltered and comparable texturing and peak intensities (figure 4.11). Microstructural examinations showed a more expanded and regular martensite morphology (figure 4.14), whilst Vickers indents indicated a further reduction in hardness to  $213H_V \pm 40H_V$ .

Figure 4.14. 80/20 TiZr alloy microstructure (300-900°C cycled condition).



#### 4.2. Mechanical and Physical properties of TiZr, TiMo, ZrMo segmented targets.

Metallurgical investigation of the TiZr binary alloy system demonstrated its suitability for use as a target material in the production of PVD metal nitride hard coatings. Similar properties could also be found in certain stable regions of the TiMo and ZrMo phase diagrams. Thus a range of TiZr, TiMo and ZrMo segmented targets (section 3.2) were fabricated by a HIP diffusion bonding process at a temperature of 1280°C (above the Ti and Zr  $\alpha$ - $\beta$  transus) and pressure of 103MPa. Characterisation and comparison of the targets was initiated prior to use in steered arc evaporation and sputtering trials.

(i) Two Ø45mm diameter x 5mm thick TiZr targets were HIP diffusion bonded using 2 Ti and 2 Zr strips with roughened bonding faces in intimate contact. Target 1 contained Ti / Zr interfaces located centrally and 15mm offset. Target 2 contained Ti / Zr interfaces symmetrically offset 7.5mm either side of the centre (the purpose of the offset interfaces was to cause steered arc crossing angles  $\neq 90^\circ$ ).

(ii)  $\text{Ø}150\text{mm}$  diameter x  $5\text{mm}$  thick TiZr, TiMo and ZrMo targets were HIPped with mirror polished faces in intimate contact and a centrally located Ti / Zr interface.

(iii) A  $600\text{mm} \times 190\text{mm} \times 12\text{mm}$  thick TiZr ABS target was HIPped using 18 strips of Ti and 18 strips of Zr with mirror polished faces in intimate contact.

#### 4.2.1. X-ray diffraction results from TiZr, TiMo and ZrMo segmented targets.

The grade 2 titanium prior to HIPping exhibited a hexagonal close packed A3 crystal structure with lattice parameters  $a = 2.95\text{Å} \pm 0.01\text{Å}$  and  $c = 4.68\text{Å} \pm 0.01\text{Å}$  giving an axial ratio of 1.59 (figure 4.15). The major intensity peak was associated with the  $(10\bar{1}1)$  reflection. After HIPping the peaks remained closely aligned with the original interplanar spacings, the crystal structure remained hexagonal and the  $(10\bar{1}1)$  intensity increased (figure 4.16).

Figure 4.15. Titanium X-ray diffraction trace prior to HIP process.

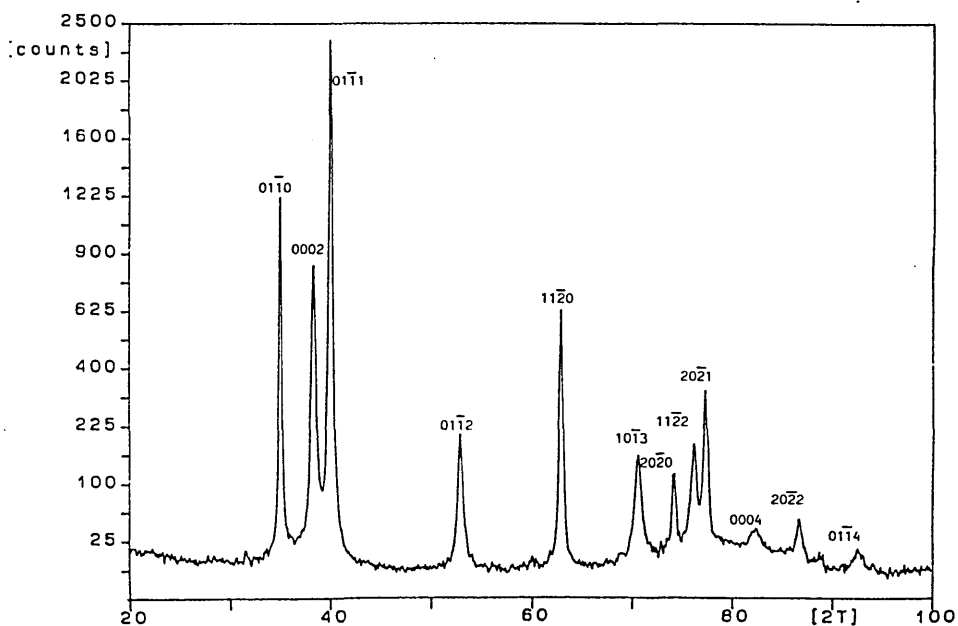
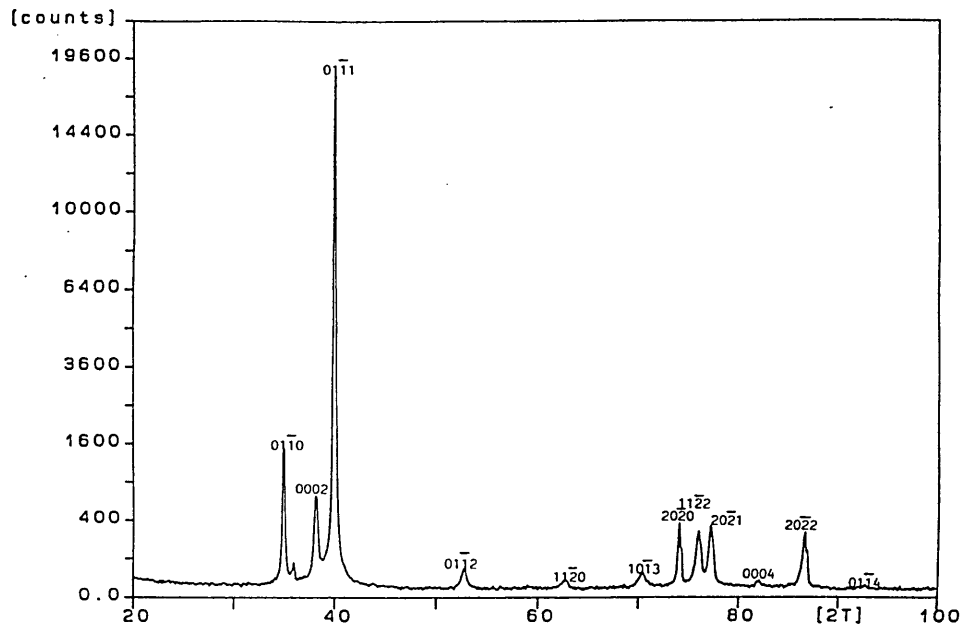


**Figure 4.16. Titanium X-ray diffraction trace after HIP process.**



Grade 702 zirconium similarly exhibited a hexagonal close packed A3 crystal structure prior to HIPping with lattice parameters  $a = 3.23\text{\AA} \pm 0.01\text{\AA}$  and  $c = 5.15\text{\AA} \pm 0.01\text{\AA}$  again giving an axial ratio of 1.59 and  $(10\bar{1}1)$  major intensity peak (figure 4.17). Post HIPping analysis revealed little change in crystal structure, stronger  $(10\bar{1}1)$  texturing and no change in lattice parameter (figure 4.18).

**Figure 4.17. Zirconium X-ray diffraction trace prior to HIP process.**

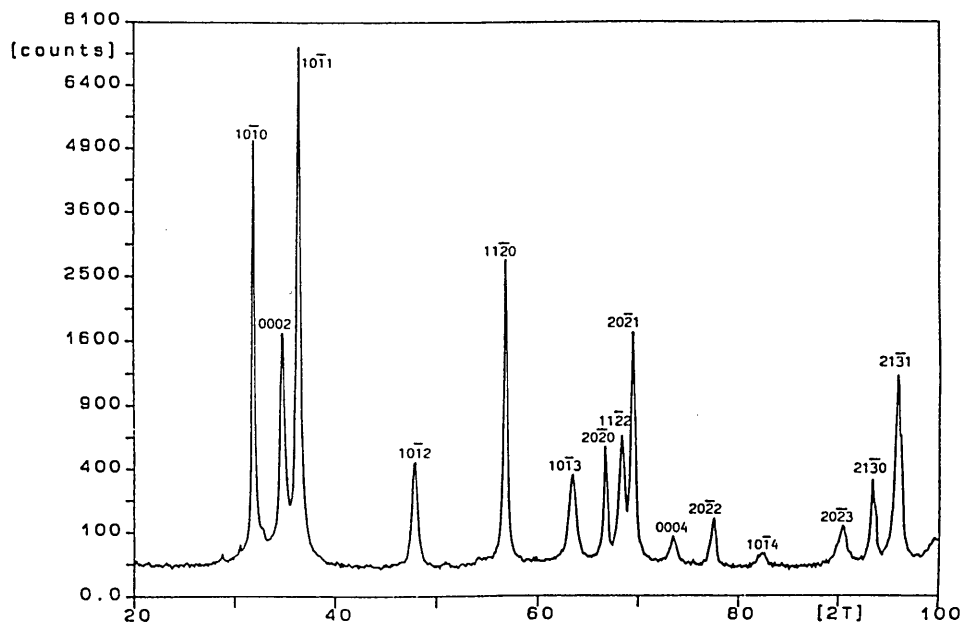
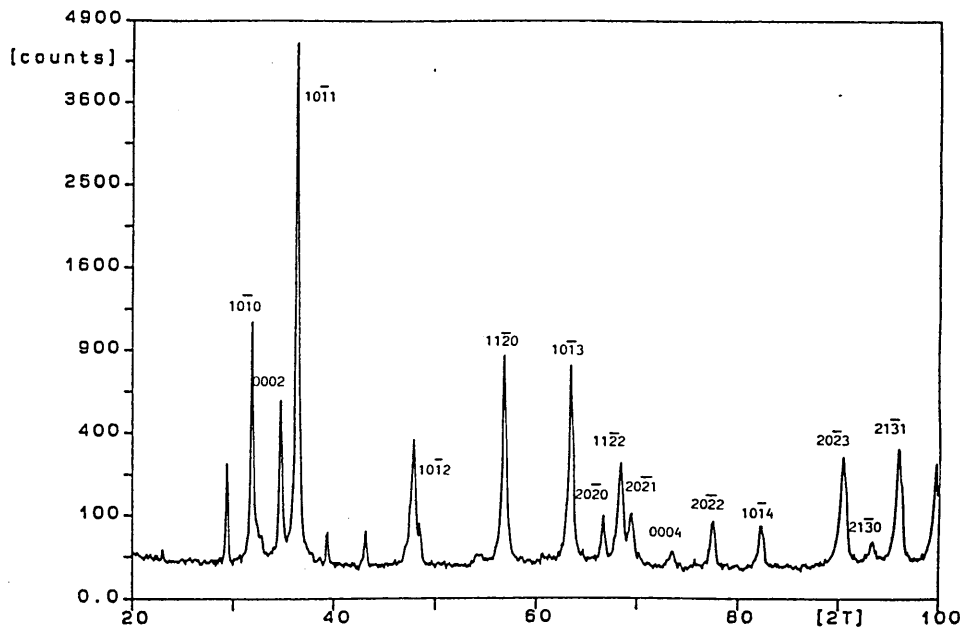


**Figure 4.18. Zirconium X-ray diffraction trace after HIP process.**



Molybdenum prior to HIPping exhibited a b.c.c crystal structure with lattice parameter  $a = 3.14\text{\AA} \pm 0.01\text{\AA}$  and  $(110)$  texturing (figure 4.19). After HIPping, the inter-planar spacings remained closely aligned to their original positions but a change in material texture led to the  $(211)$  reflection exhibiting the major peak intensity (figure 4.20).

**Figure 4.19. Molybdenum X-ray diffraction trace prior to HIP process.**

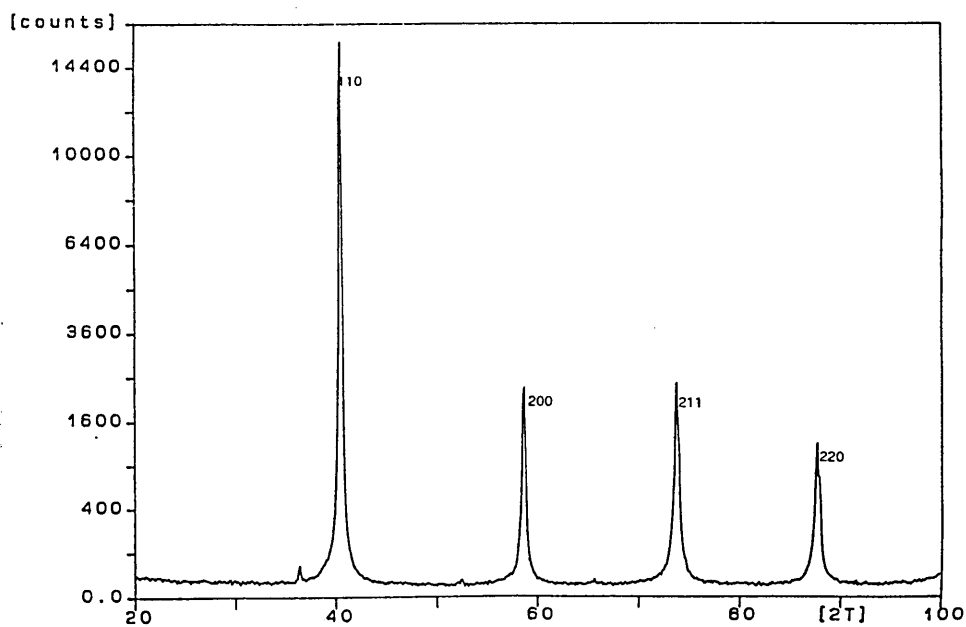
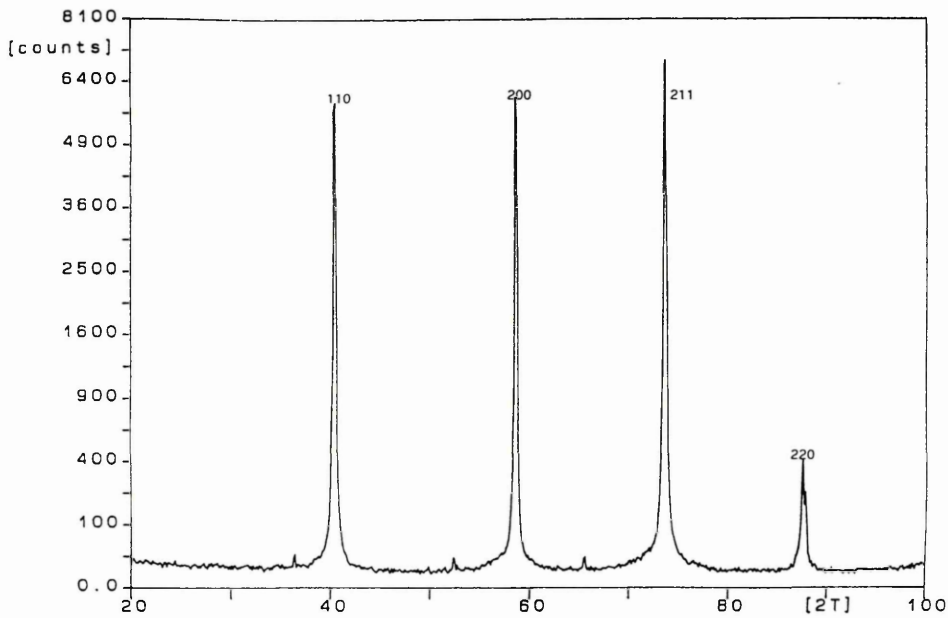


Figure 4.20. Molybdenum X-ray diffraction trace after HIP process.



4.2.2. Microstructural analysis of TiZr, TiMo and ZrMo segmented targets.

Prior to hot isostatic pressing the titanium segments exhibited an equiaxed grain structure which altered to a complex cross-needle network due to a martensitic transformation during the cooling phase of the HIPping cycle (figure 4.21a&b).

Figure 4.21a. Ti prior to HIP process.

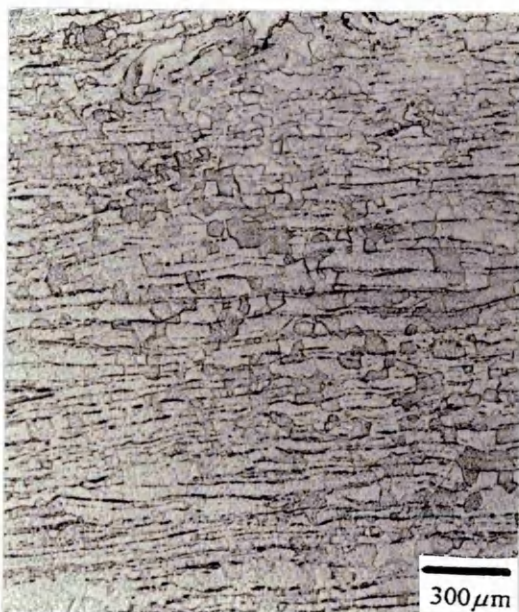
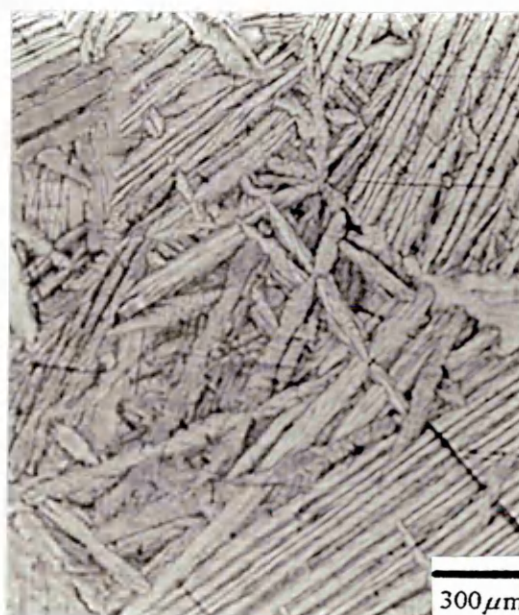


Figure 4.21b. Ti after HIP process



Before HIPping the zirconium also had a well defined equiaxed grain structure which altered to a pseudo-Widmanstatten morphology after the HIP process (4.22a&b).

Figure 4.22a. Zr prior to HIP process.



Figure 4.22b. Zr after HIP process



Molybdenum prior to HIPping exhibited an elongated grain structure due to rolling of the bulk metal during the manufacturing process (figure 4.23a). HIPping caused the development of a near equiaxed grain structure due to tempering effects (figure 4.23b).

Figure 4.23a. Mo prior to HIP process.

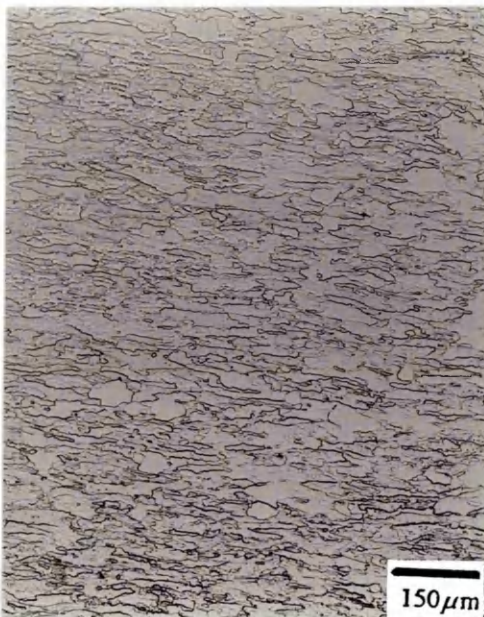
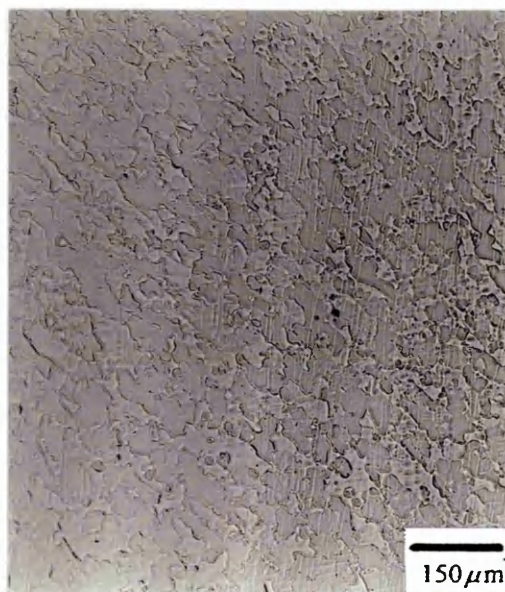


Figure 4.23b. Mo after HIP process



### 4.2.3. Interfacial microscopy of TiZr, TiMo and ZrMo segmented targets.

Microscopic examination of TiZr segmented target interfaces formed with mirror polished and rough (standard machined) bonding faces revealed extensive differences in their diffusion mechanisms. HIPped TiZr targets with smooth bonding faces exhibited a large intermixed diffusion zone which extended over a distance of approximately 250 $\mu\text{m}$  until the pure titanium and zirconium boundaries could be defined (figure 4.24). The intermetallic TiZr grain structure could be distinguished within the diffusion region and a martensitic transformation had been undertaken. Conversely, the TiZr target HIPped with rough bonding faces showed a surprisingly low level of diffusion had caused the formation of an abrupt TiZr intermetallic bonding zone which extended over a distance of approximately 5 $\mu\text{m}$  (figure 4.25).

Figure 4.24. TiZr inter-diffusion zone.

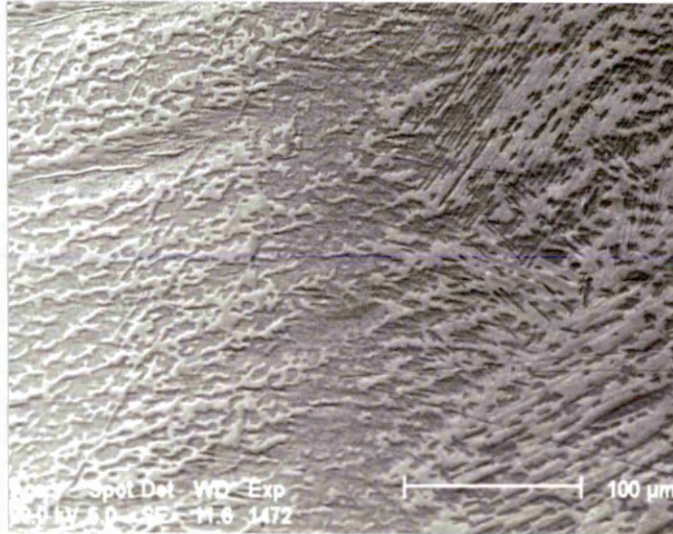
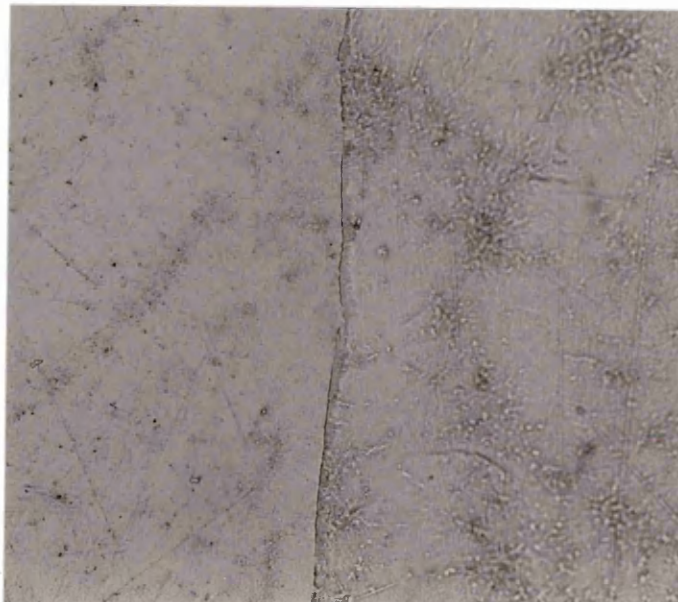
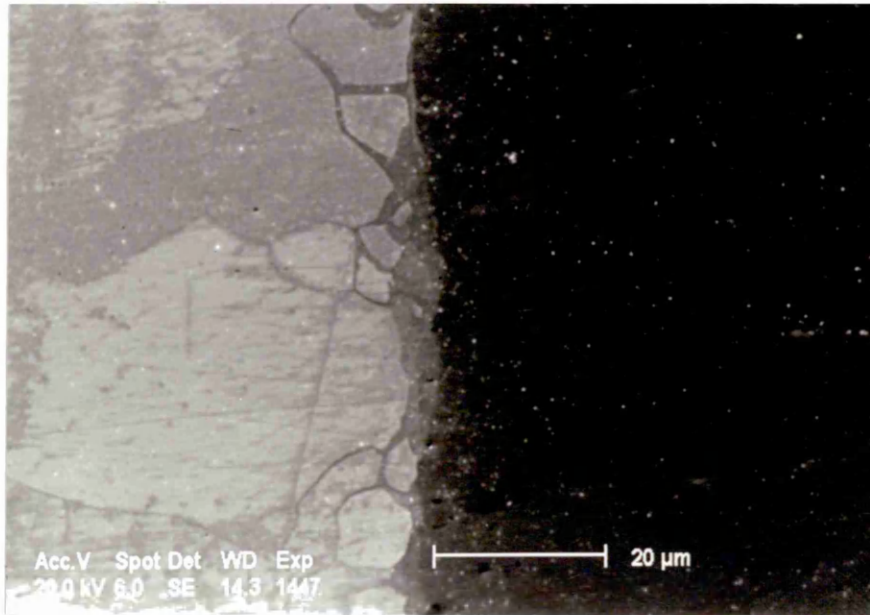


Figure 4.25. TiZr abrupt segment junction.



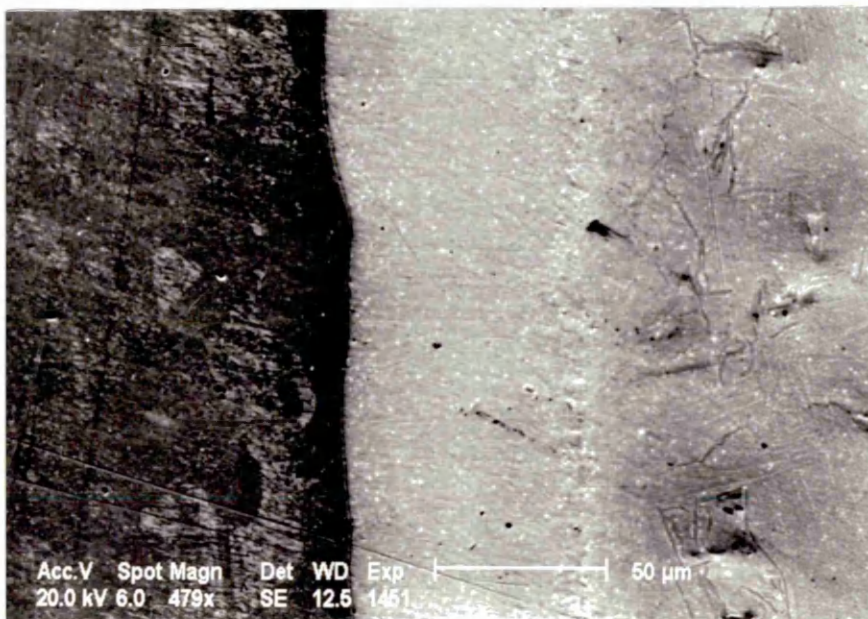
Investigation of TiMo HIPped junctions showed a relatively abrupt ( $\sim 30\mu\text{m}$ ), short range diffusion zone had been created. Inspection revealed that diffusion of titanium had occurred along grain boundary network of the molybdenum causing the formation of large TiMo intermetallic pockets at the junction (figure 4.26).

Figure 4.26. TiMo diffusion bonded interface.



Analysis of the ZrMo HIP bonded interface demonstrated a well defined, central diffusion zone, comprising the ZrMo intermetallic, had been produced over a region extending approximately  $70\text{-}80\mu\text{m}$  (figure 4.27). The pure Zr and Mo boundaries were clearly defined.

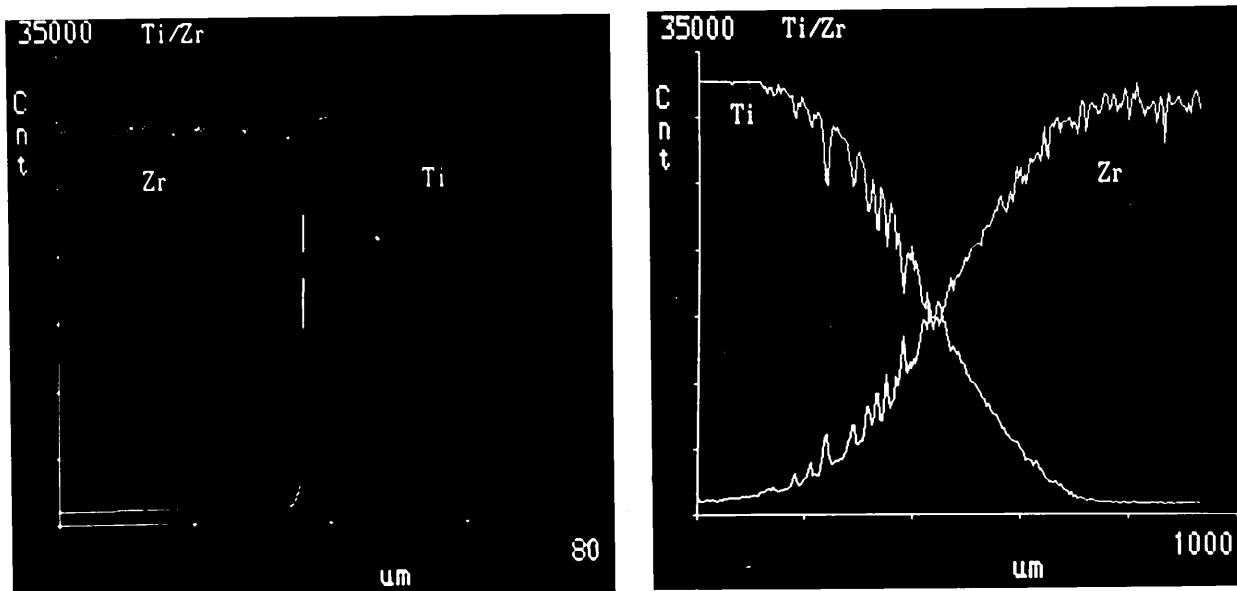
Figure 4.27. ZrMo diffusion bonded interface.



#### 4.2.4. Interfacial diffusion analysis by X-ray linescanning

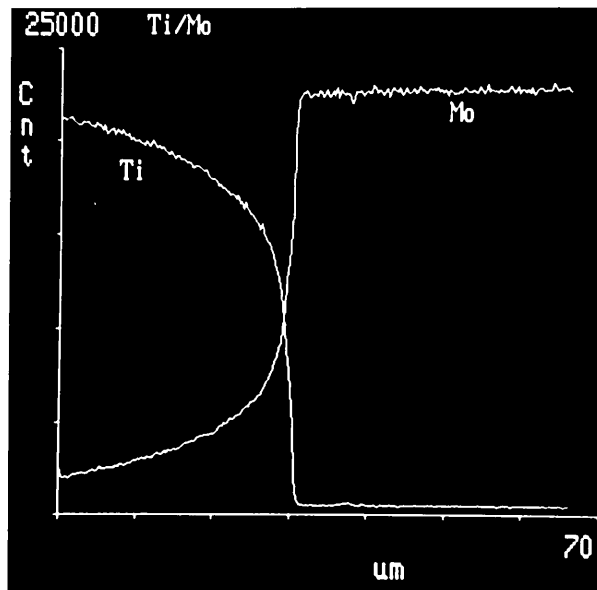
Energy dispersive X-ray linescans were performed across the interfacial regions of the TiZr, TiMo and ZrMo segmented targets to provide inter-diffusion data. Analysis on TiZr targets with rough bonding edges correlated well with microscopic evidence and revealed the formation of an abrupt interface (figure 4.28a) with little sign of inter-diffusion ( $\sim 5\mu\text{m}$ ). Improvements in the surface roughness of the bonding faces resulted in a significant diffusion profile in both the Zr and Ti segments (figure 4.28b). The line scan revealed that the extent of diffusion was even further than was observed during microscopic imaging ( $\sim 400\mu\text{m}$ ). Clearly, the more intimately the strips could be brought into contact during HIPping with high thermal energies and pressures, the greater the extent of diffusion.

Figure 4.28a. TiZr abrupt junction linescan. Figure 4.28b. TiZr inter-diffusion linescan.



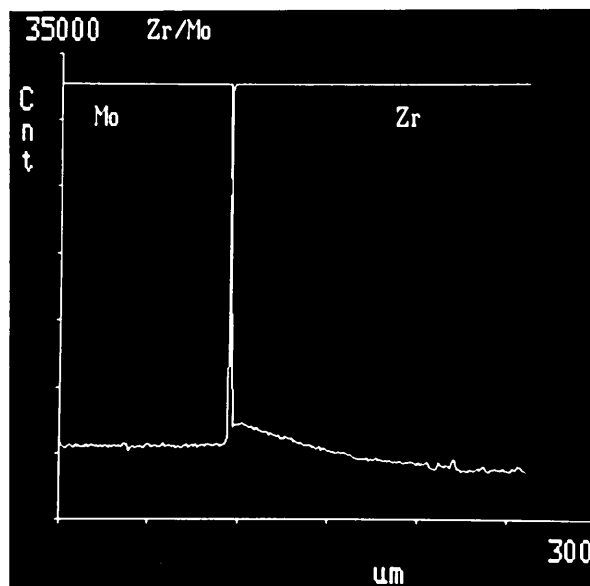
Linescan spectra obtained from the TiMo target identified that the range of diffusion was significantly less than in the equivalent TiZr target. The linescan plot confirmed that titanium had diffused into the molybdenum over a 40-50 $\mu\text{m}$  region (figure 4.29).

Figure 4.29. TiMo interface X-ray linescan.



Linescans from ZrMo targets indicated that the range of diffusion was less than in TiZr targets but greater than in TiMo. Spectra showed that the distinct, well defined diffusion zone indicated from the microscopy which was predominantly caused by zirconium inter-diffusion and extended over a distance of approximately 100 $\mu$ m (figure 4.30).

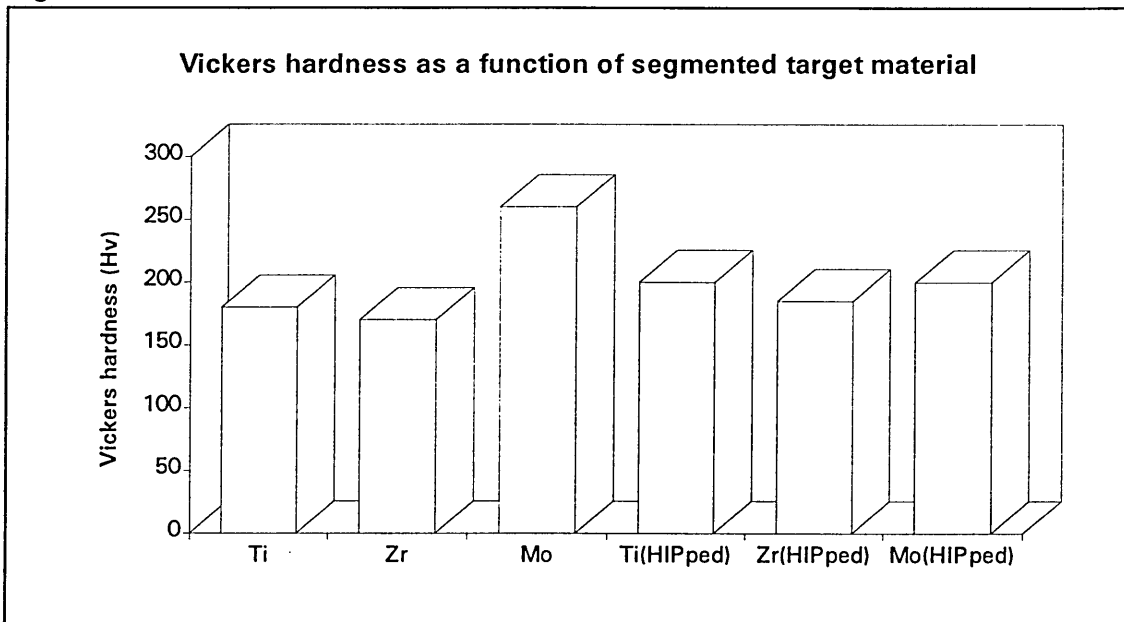
Figure 4.30. ZrMo interface X-ray linescan.



#### 4.2.5. Hardness measurements on TiZr, TiMo and ZrMo segmented targets.

Both titanium and zirconium showed modest increases in hardness (Vickers diamond at 20kgf) after hot isostatic pressing due to a combination of a reduction in porosity (a result of the encapsulation and the HIPping pressure) and a martensitic transformation (figure 4.31). In all cases the hardness values were lower than  $Ti_xZr_y$  values reported in section 4.1.2 - 4.1.4. However, molybdenum exhibited a significant decrease in hardness due to tempering effects.

Figure 4.31.



### 4.3. Target performance in steered arc evaporation trials.

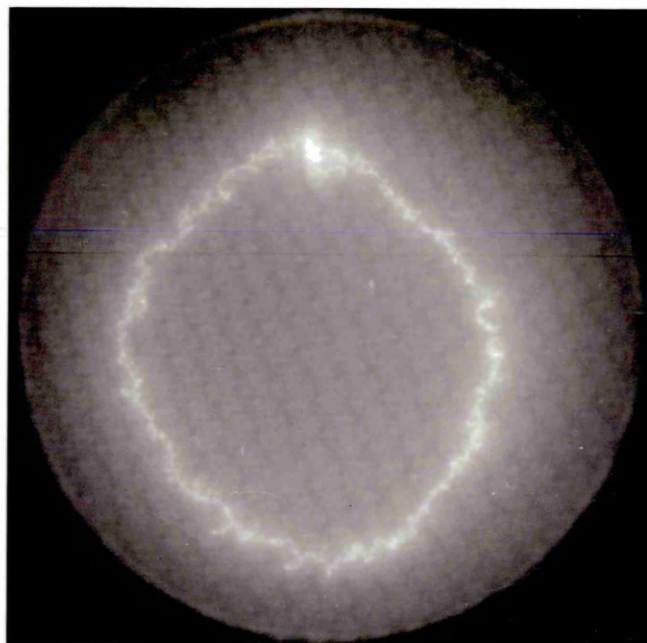
The experimental conditions and magnetic field profiles used during the electro-magnetic steered arc evaporation trials are described in section 3.1.1.

#### 4.3.1. TiZr target performance.

Cathode conditioning (using random arc evaporation) prior to all evaporation trials, ensured the use of a type II cathode spot, indicated by the characteristic discharge colour and erosion track. Despite the production of targets with significantly differing inter-diffusion profiles, little change in target performance was noted.

In both cases, a single cathode spot was observed to reduce in velocity and "stall" for a short period of time ( $\sim 0.4\text{ms}$  stall time out of  $\sim 10\text{ms}$  total time to make 1 revolution observed by 6000 frame per second high speed camera) when crossing the segment interface from titanium to zirconium (figure 4.32). As a result, a significant increase in the volume of cathode material evaporated at the junction region occurred and deleterious erosion trenches were formed at the near-interface region of the titanium segments. However, the cathode spot appeared to cross the junction in the opposite direction, from zirconium to titanium, without impediment or formation of an erosion trench.

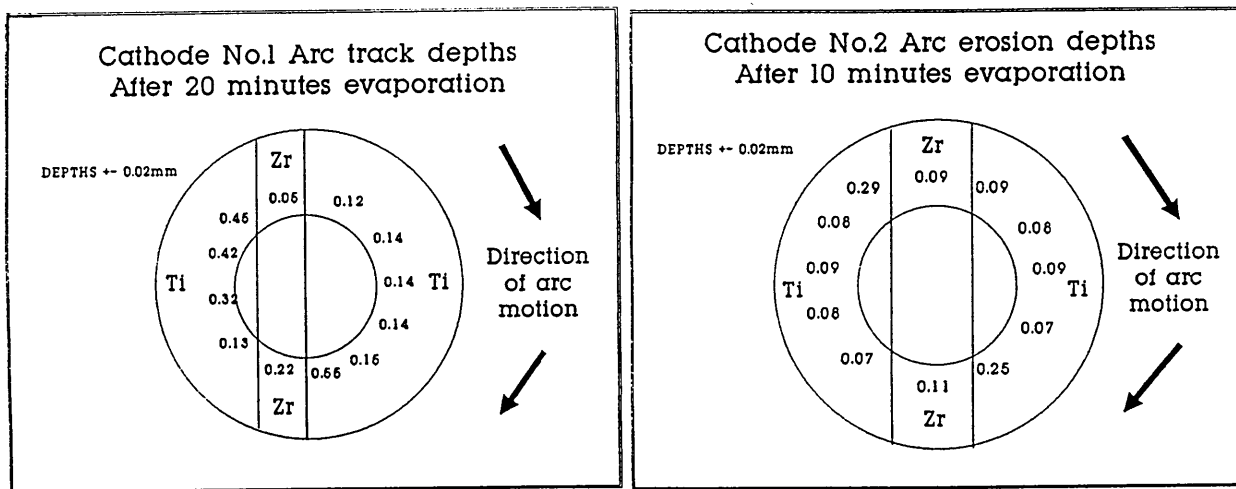
Figure 4.32. Steered arc evaporation of abrupt interface TiZr segmented target.



The highest degree of arc control was maintained on targets which allowed the cathode spot to cross segment interfaces perpendicular to the junction. Offset interfaces, which provided crossing angles less than  $90^\circ$ , occasionally allowed a phenomenon of cathode spot propagation along the segment interface towards the boron nitride passive barrier when traversing from titanium to zirconium. An increase in cathode spot intensity and multiple track formation was also observed.

The erosion depths at various positions on the Ti-Zr segmented target were assessed by high precision point micrometer measurements and talysurf profiling (figure 4.33). Generally, the erosion tracks were found to be deeper on the titanium segments than on the adjacent zirconium segments. The trench depths at segment crossing positions were typically a factor of three times larger than the normal arc track and clear evidence of enhanced interfacial erosion on offset junctions was also obtained.

Figure 4.33. Erosion track depth measurements.



The ABS TiZr segmented target showed an identical performance to the small steered arc targets used during the evaporation trials. However, the standard ABS technique generally utilised the steered arc evaporation process as a cyclic metal ion etch substrate pre-treatment prior to sputter coating. Hence the extent of deleterious erosion at the Ti to Zr interfaces was minimised and thus the longevity of the target was only slightly reduced.

#### 4.3.2. TiMo target performance.

The TiMo target, which had the largest mismatch of intrinsic vapour pressures (table 4.1), showed a similar cathode spot stalling phenomena when crossing from the titanium to molybdenum segment. This provided an excessive volume of cathode material evaporated at the junction region and formed more extensive deleterious erosion trenches (0.65mm maximum trench depth after 20 minutes) than in TiZr targets at the near-interface region of the titanium segments. Again, the cathode spot appeared to

cross the junction in the opposite direction, from molybdenum to titanium, without impediment or formation of an erosion trench.

#### 4.3.3. ZrMo target performance.

The ZrMo target, which had the smallest mismatch of intrinsic vapour pressures (table 4.1), also showed the least severe cathode spot stalling phenomena when crossing from the zirconium to molybdenum segment. This produced the lowest volume of cathode material evaporated at the junction region and formed the least deleterious erosion trenches (0.20mm maximum trench depth after 20 minutes) when compared to TiZr and TiMo targets at the near-interface region of the zirconium segment. The cathode spot appeared to cross the junction in the opposite direction, from molybdenum to zirconium, without impediment or formation of an erosion trench.

Table 4.1.

<b>Physical property</b>	<b>Titanium</b>	<b>Zirconium</b>	<b>Molybdenum</b>
Melting point (°C)	1667	1850	2607
Boiling point (°C)	3317	4507	5557
Temperature in °C at vapour pressure of $1 \times 10^{-2}$ mbar	1760	2370	2490
Electrical resistivity at 25°C ( $\mu\Omega\text{cm}$ )	42	40	98.4
Thermionic work function (eV)	3.95	4.16	4.20
Atomic number (Z)	22	40	42

#### 4.4. Computer simulation of segmented target sputter performance.

The "Trim95" (Transport of Ions in Matter) Monte-Carlo simulation code (3,4) allowed the rigorous treatment of elastic scattering, explicit consideration of surfaces and interfaces and the determination of energy and angular distributions of particles during interactions with matter. Computer simulations were undertaken to derive probable sputtering yields (Y), lateral ranges (ion penetration depths) and analyse the effects of high substrate bias voltage etching. Thus, the following constants and assumptions were applied:-

- (a) Bombarding ions - Ar, Ti, Zr, Mo.
- (b) Angle of ion incidence - 90°.
- (c) Target voltage - -400V.
- (d) Substrate voltage (typical coating condition) -100V.
- (e) Substrate voltage (arc etching condition) - -1200V.
- (f) Target materials - Ti, Zr, Mo.
- (g) Substrate material - Fe.
- (h) Mean density - Ti=4520Kgm<sup>-3</sup>, Zr=6470Kgm<sup>-3</sup>, Mo=10200Kgm<sup>-3</sup>.
- (i) The surface binding energy  $\approx$  Heat of sublimation.
- (j) Heat of sublimation:- Ti=4.88eV, Zr=6.32eV, Mo=6.82eV.
- (k) Number of interaction events = 500.
- (l) Arc etch mean ion charge states = Ti<sup>2.1+</sup>, Zr<sup>2.6+</sup>, Mo<sup>3.1+</sup>.
- (m) Glow discharge argon etch charge state = Ar<sup>+</sup>
- (n) Straggle, Skewness & Kurtosis values were related to the second, third and fourth moments of the ion distribution i.e.

where;

Straggle ( $\sigma$ ) is square root of variance:- $\sigma = \left[ \left( \sum_i x_i^2 \right) / N - R_p^2 \right]^{1/2} = \langle (\Delta x_i)^2 \rangle^{1/2}$ .

Skewness:-  $\gamma = \langle \Delta x^3 \rangle / \langle \Delta x^2 \rangle^{3/2}$  and Kurtosis:-  $\beta = \langle \Delta x^4 \rangle / \langle \Delta x^2 \rangle^2$ .

$\langle x \rangle$  = mean projected range of all ions.

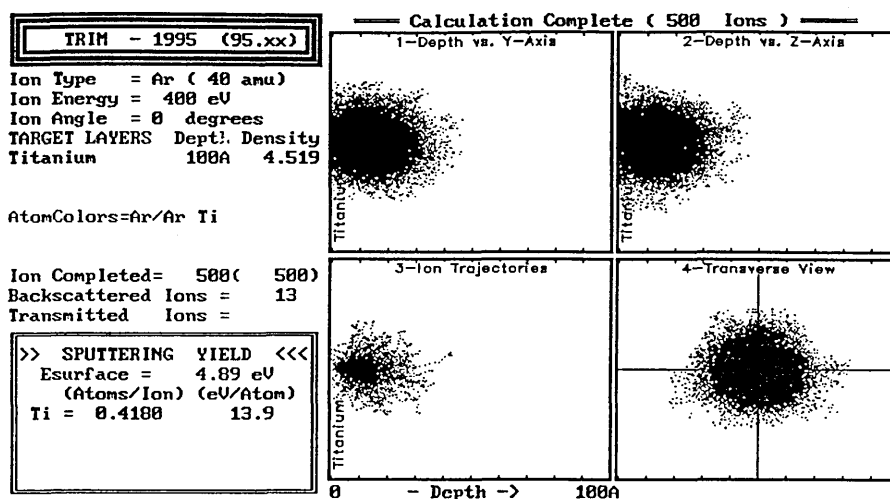
$\sum_i x_i / N$  = mean projected range of N ions.

$\sum_i x_i$  = sum of ion ranges and a Gaussian distribution has  $\beta=3$ .

#### 4.4.1. Sputter yields and ion ranges.

Monte-Carlo simulations were carried out to predict the sputter yields and typical ion ranges taking place during argon ion bombardment of the surface of Ti, Zr and Mo targets at a potential of -400V. A typical ion interaction analysis is shown in figure 4.34 and the simulation results are summarised in table 4.2.

Figure 4.34. TRIM-95 titanium sputter yield simulation.



The data indicated that the Mo target exhibited the highest sputter yield of the three materials examined and was typically a ratio of 1.81:1 greater than Ti and 1.41:1 larger than Zr.

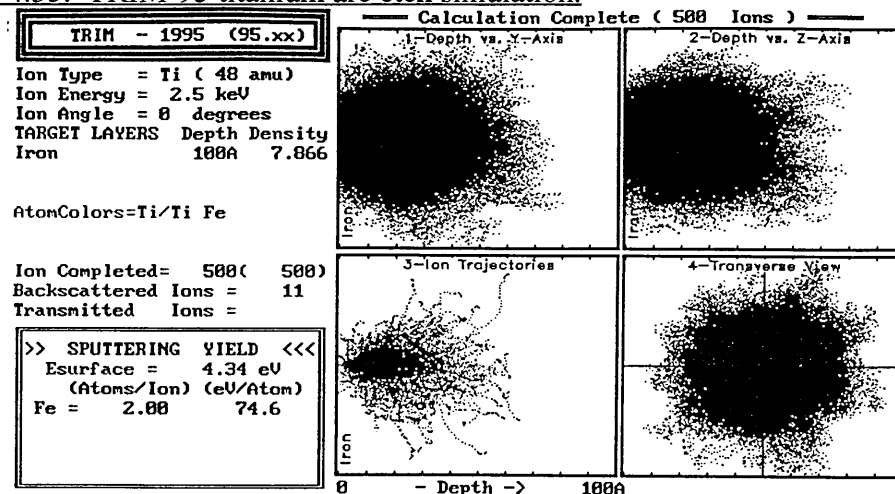
Table 4.2

	Ti sputter	Zr sputter	Mo sputter
Target	Ti	Zr	Mo
Ion	Ar <sup>+</sup>	Ar <sup>+</sup>	Ar <sup>+</sup>
Target potential	-400V	-400V	-400V
Sputter Yield (Y)	0.42	0.54	0.76
Number of backscattered ions	13	50	81
Mean ion range / Å	14	15	10
Maximum ion range / Å	45	45	35
Straggle / Å	7	8	6
Skewness	0.79	0.55	0.79
Kurtosis	3.72	2.87	3.63

#### 4.4.2. Simulation of substrate ion etching.

Monte-Carlo simulations were carried out to predict the typical levels of ion implantation and sputter etching undertaken during cathodic arc metal ion etching of iron substrates at a bias potential of -1200V. The mean charge state of the metal vapour flux was taken from earlier work by Brown and Godechot (5). A typical ion interaction plot is shown in figure 4.35 and the simulation results are summarised in table 4.3.

Figure 4.35. TRIM-95 titanium arc etch simulation.



The Trim-95 trials identified a significant level of metal ion implantation within the iron substrate with mean ion ranges of the order of 25Å and maximum ion ranges typically 65Å. Extensive collision cascades were formed within a 100Å sub-surface region of the substrate and high iron sputter yield values ( $Y > 1.50$ ) were recorded indicating a high degree of sputter etching.

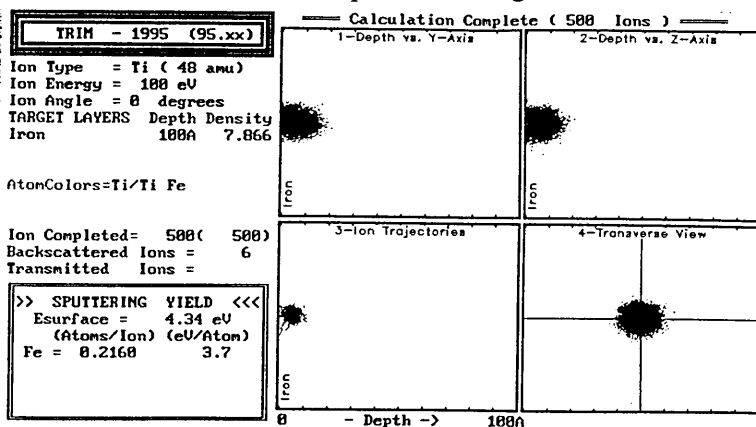
Table 4.3.

	Ti arc etch	Zr arc etch	Mo arc etch	Ar ion etch
Substrate bias potential	-1200V	-1200V	-1200V	-1200V
Substrate	Fe	Fe	Fe	Fe
Ion	Ti <sup>2.1+</sup>	Zr <sup>2.6+</sup>	Mo <sup>3.1+</sup>	Ar <sup>+</sup>
Sputter Yield (Y)	2.00	1.58	1.52	1.57
Number of backscattered ions	11	1	0	23
Mean ion range / Å	24	23	25	16
Maximum ion range / Å	67	67	65	45
Straggle / Å	13	10	10	9
Skewness	0.61	0.59	0.59	0.69
Kurtosis	3.01	3.56	3.46	3.11

#### 4.4.3. Simulation of substrate sputter coating.

Monte-Carlo simulations were undertaken to examine the levels of iron substrate sputtering and the ion interaction depths under typical unbalanced magnetron sputter coating conditions. For the purposes of Trim calculations, the metal vapour flux had to be at minimum in a 1+ charge state, however sputter processes will typically have a flux characteristic of ~1% ionised species. A typical result from the simulation trials is shown in figure 4.36 and analysis is provided in table 4.4.

Figure 4.36. TRIM-95 titanium sputter coating simulation.



The data indicated that the ion interaction range and the extent of the collision cascade volume was only in the near surface region of the iron substrate. The sputter yield values recorded for the iron substrate and hence the levels of sputter etching were also found to be very low.

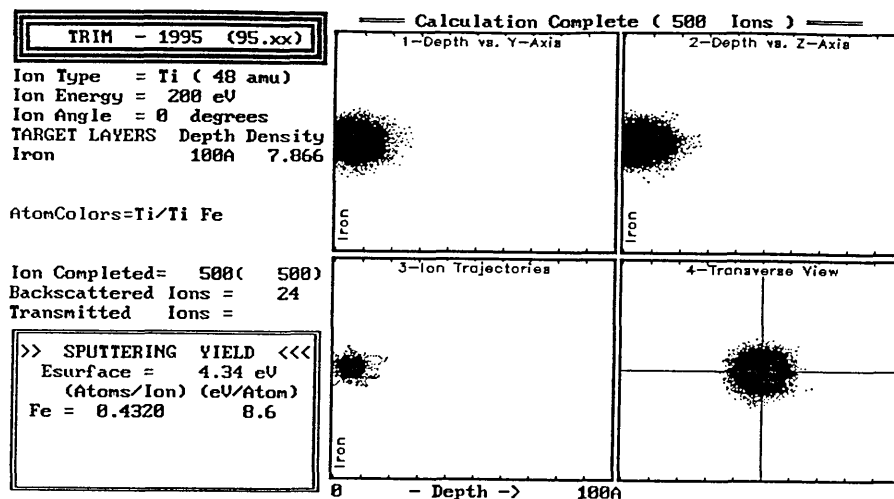
Table 4.4.

	Ti sputter coating	Zr sputter coating	Mo sputter coating
Substrate	Fe	Fe	Fe
Substrate bias voltage	-100V	-100V	-100V
Ion	Ti <sup>+</sup>	Zr <sup>+</sup>	Mo <sup>+</sup>
Sputter Yield (Y)	0.22	0.03	0.02
Number of backscattered ions	6	0	0
Mean ion range / Å	5	5	5
Maximum ion range / Å	12	12	12
Straggle / Å	2	1	1
Skewness	0.69	0.87	0.61
Kurtosis	3.48	3.98	3.20

#### 4.4.4. Simulation of substrate arc coating.

The final set of simulations were carried out to examine the levels of iron substrate sputtering and the ion interaction depths under typical cathodic arc evaporation coating conditions. The titanium arc coating plot is shown in figure 4.37 and a summary of the simulation data is illustrated in table 4.5.

Figure 4.37. TRIM-95 titanium arc coating simulation.



The data recorded were found to be similar to magnetron sputter coating in that the ion interaction range and the extent of the collision cascade volume was only in the near surface region of the iron substrate. The sputter yield values recorded for the iron substrate and hence the levels of sputter etching were also found to be higher than sputter coating but significantly lower than in etching trials.

Table 4.5.

	Ti arc coating	Zr arc coating	Mo arc coating
Substrate	Fe	Fe	Fe
Substrate bias voltage	-100V	-100V	-100V
Ion	Ti <sup>2.1+</sup>	Zr <sup>2.6+</sup>	Mo <sup>3.1+</sup>
Sputter Yield (Y)	0.43	0.17	0.15
Number of backscattered ions	24	0	0
Mean ion range / Å	6	7	8
Maximum ion range / Å	15	18	21
Straggle / Å	3	3	3
Skewness	0.78	0.52	0.88
Kurtosis	3.67	2.92	4.46

#### 4.5. Target performance in unbalanced magnetron sputtering trials.

The performance of segmented targets in unbalanced magnetron sputter processing, the effects of preferential target poisoning in co-sputter deposition and the composition and spatial distribution of the coating flux was investigated.

##### 4.5.1. The influence of preferential target poisoning.

The role of preferential poisoning on segmented targets was investigated using the TiMo and ZrMo segmented targets which exhibited strong differences in elemental reactivities with nitrogen. A series of constant power unbalanced magnetron deposition processes (table 4.7) were undertaken with increasing nitrogen partial pressures and nitrogen flow rates using quadrupole ion probe current increments of  $0.5 \times 10^{-10}$  Amp (for process control the frequency of the quadrupole ion mass separator was adjusted such that only  $N^+$  ions were allowed to pass to the ion registration probe).

**Table 4.6**

Coating (RGA current $\times 10^{-10}$ A)	Approximate $N_2$ flow rate (sccm)	Atomic composition $\pm 5\%$
TiMo (0)	0	Ti <sub>0.42</sub> Mo <sub>0.58</sub>
TiMoN (0.5)	4.5	Ti <sub>0.36</sub> Mo <sub>0.58</sub> N <sub>0.06</sub>
TiMoN (1.0)	8.5	Ti <sub>0.32</sub> Mo <sub>0.57</sub> N <sub>0.11</sub>
TiMoN (1.5)	11.1	Ti <sub>0.28</sub> Mo <sub>0.56</sub> N <sub>0.16</sub>
TiMoN (2.0)	15.0	Ti <sub>0.25</sub> Mo <sub>0.56</sub> N <sub>0.19</sub>
TiMoN (2.5)	17.0	Ti <sub>0.21</sub> Mo <sub>0.60</sub> N <sub>0.19</sub>
TiMoN (3.0)	21.0	Ti <sub>0.20</sub> Mo <sub>0.60</sub> N <sub>0.20</sub>
TiMoN (3.5)	22.4	Ti <sub>0.19</sub> Mo <sub>0.60</sub> N <sub>0.21</sub>
TiMoN (4.0)	24.1	Ti <sub>0.17</sub> Mo <sub>0.61</sub> N <sub>0.22</sub>
ZrMo (0)	0	Zr <sub>0.43</sub> Mo <sub>0.57</sub>
ZrMoN (0.5)	5.1	Zr <sub>0.37</sub> Mo <sub>0.58</sub> N <sub>0.05</sub>
ZrMoN (1.0)	9.0	Zr <sub>0.32</sub> Mo <sub>0.57</sub> N <sub>0.11</sub>
ZrMoN (1.5)	12.8	Zr <sub>0.30</sub> Mo <sub>0.57</sub> N <sub>0.13</sub>
ZrMoN (2.0)	16.4	Zr <sub>0.26</sub> Mo <sub>0.57</sub> N <sub>0.17</sub>
ZrMoN (2.5)	18.9	Zr <sub>0.22</sub> Mo <sub>0.56</sub> N <sub>0.22</sub>
ZrMoN (3.0)	23.0	Zr <sub>0.20</sub> Mo <sub>0.55</sub> N <sub>0.25</sub>
ZrMoN (3.5)	24.7	Zr <sub>0.18</sub> Mo <sub>0.55</sub> N <sub>0.27</sub>
ZrMoN (4.0)	29.8	Zr <sub>0.17</sub> Mo <sub>0.53</sub> N <sub>0.30</sub>

Table 4.7. TiMoN and ZrMoN process parameters.

<b>Static <math>Ti_xMo_yN</math> and <math>Zr_xMo_yN</math> unbalanced magnetron sputter process parameters (Z-700)</b>
<p><u>(1) Chamber pump down and radiant heating</u>  Substrates rotated directly in front of heaters  Time = 75 mins  Pressure = <math>&lt; 1 \times 10^{-5}</math> mbar  Temperature = 350°C</p>
<p><u>(2) Glow discharge target cleaning</u>  Substrates rotated through 270°  Shutter directly in front of target  Substrate bias voltage = 0V  Power = 1KW  Ar flow = 150sccm  Pressure = <math>\sim 4 \times 10^{-3}</math> mbar  Time = 5 mins  Temperature = 300°C</p>
<p><u>(3) Glow discharge substrate ion etching</u>  Substrates rotated through 270°  Substrates directly between double magnetron cathodes  Power = 0.15KW  Ar flow = 300sccm  Substrate bias voltage = -1000V  Time = 10mins  Pressure = <math>\sim 6 \times 10^{-3}</math> mbar  Temperature = 350-400°C</p>
<p><u>(4) Unbalanced magnetron sputtered metal interlayer deposition</u>  Substrates rotated through 270°  Substrates directly in front of circular unbalanced magnetron sputter source  Power = 1.1KW  Ar flow = 150sccm  Time = 2mins  Substrate bias voltage = -100V  Pressure = <math>\sim 4.5 \times 10^{-3}</math> mbar  Temperature = 350°C</p>
<p><u>(5) Unbalanced magnetron reactive sputter deposition</u>  Substrate position as in stage 4  Power = 1.1KW  Ar flow = 150sccm  Quadrupole RGA partial pressure control current = 0 - <math>4.0 \times 10^{-10}</math> A  RGA quadrupole ion probe current increments = <math>0.5 \times 10^{-10}</math> A  N<sub>2</sub> flow = 0-30sccm  Time = 30mins  Substrate bias voltage = -100V  Pressure = <math>\sim 4.5 \times 10^{-3}</math> mbar - <math>\sim 5 \times 10^{-3}</math> mbar  Temperature = 350°C</p>

GDOES analysis revealed that with increasing nitrogen composition, the highly reactive Ti and Zr segments rapidly became poisoned, resulting in a strong group IV transition metal depletion in the alloy. However, the molybdenum segment yield remained relatively constant leading to the formation of near  $\text{Mo}_2\text{N}$  films in high  $\text{N}_2$  partial pressure processes (table 4.6).

X-ray diffraction analysis confirmed the GDOES data and indicated that the TiMo ( $a_0 = 3.18\text{\AA}$ ) and ZrMo ( $a_0 = 3.30\text{\AA}$ ) metal alloys exhibited single phase body centred cubic structures (figure 4.38 and 4.39). As the nitrogen flow was increased ( $\sim 9\text{sccm}$ ), both systems showed significant increases in b.c.c lattice strain through peak broadening until transition to a  $\langle 100 \rangle$  orientated single phase face centred cubic structure occurred. As the nitrogen partial pressure was further increased (10-30sccm  $\text{N}_2$ ), a reduction in the lattice parameter of  $\text{TiMoN}_x$  and  $\text{ZrMoN}_x$  was recorded (figure 4.40) due to preferential poisoning of the Ti and Zr target segments and the system approached the unit cell dimensions of  $\gamma\text{-Mo}_2\text{N}$  ( $a_0 = 4.163\text{\AA}$ ).

**Figure 4.38.** X-ray diffraction analysis of TiMoN as a function of  $\text{N}_2$  flow.

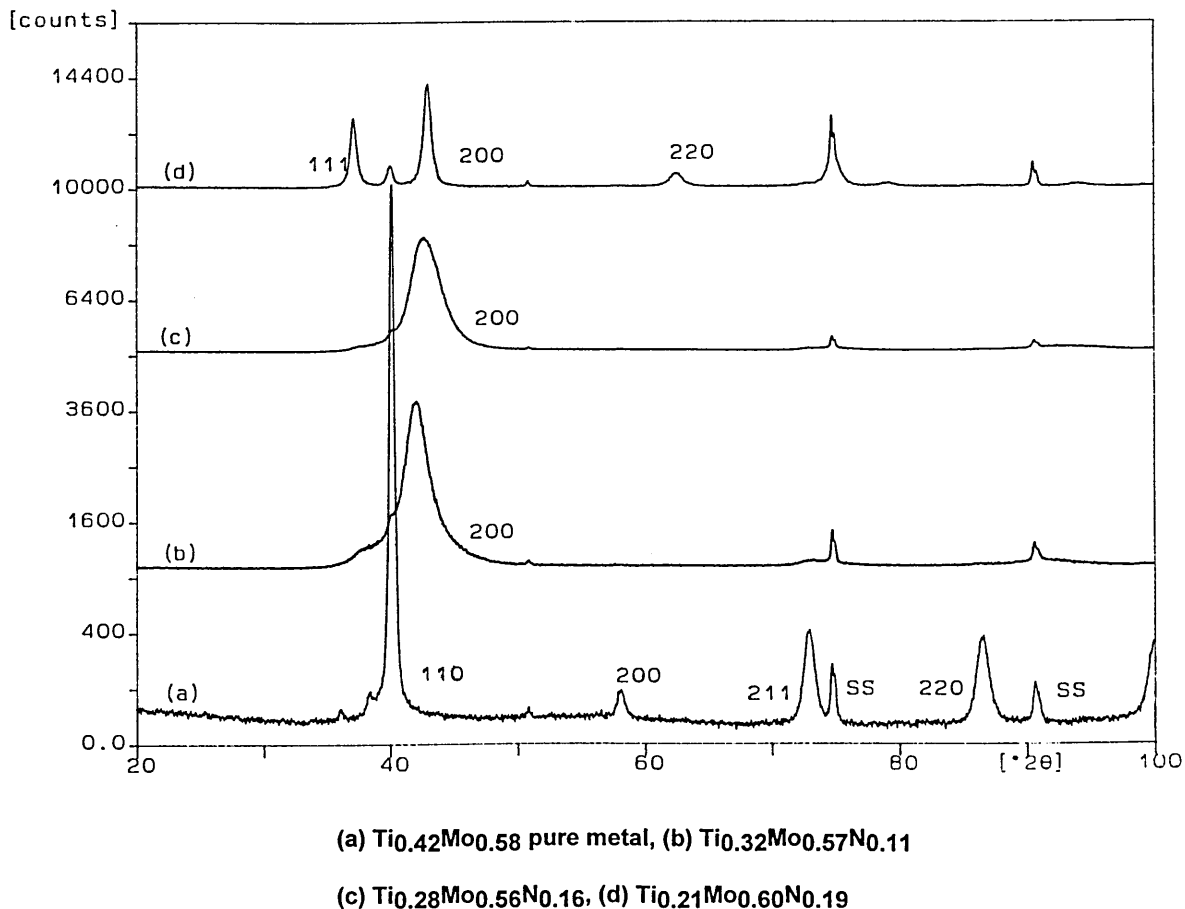


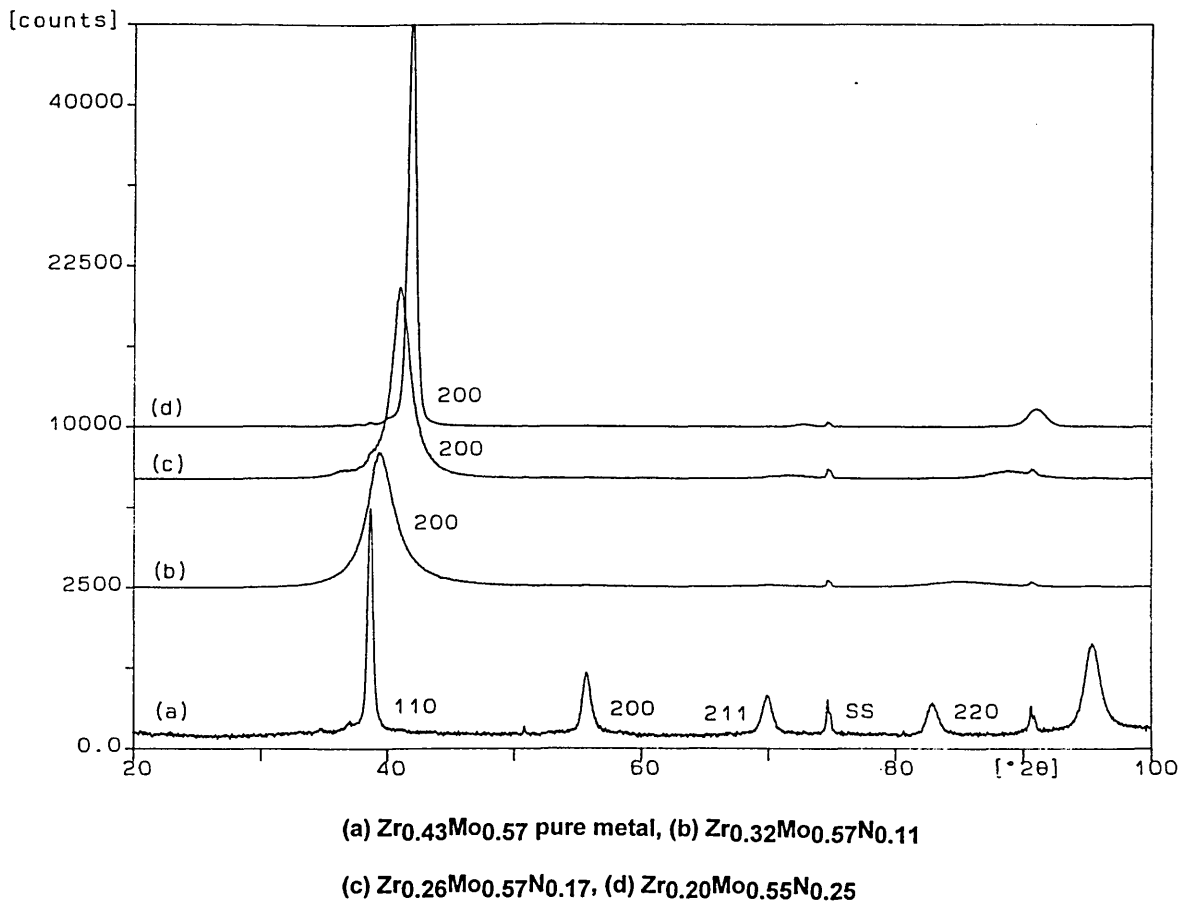
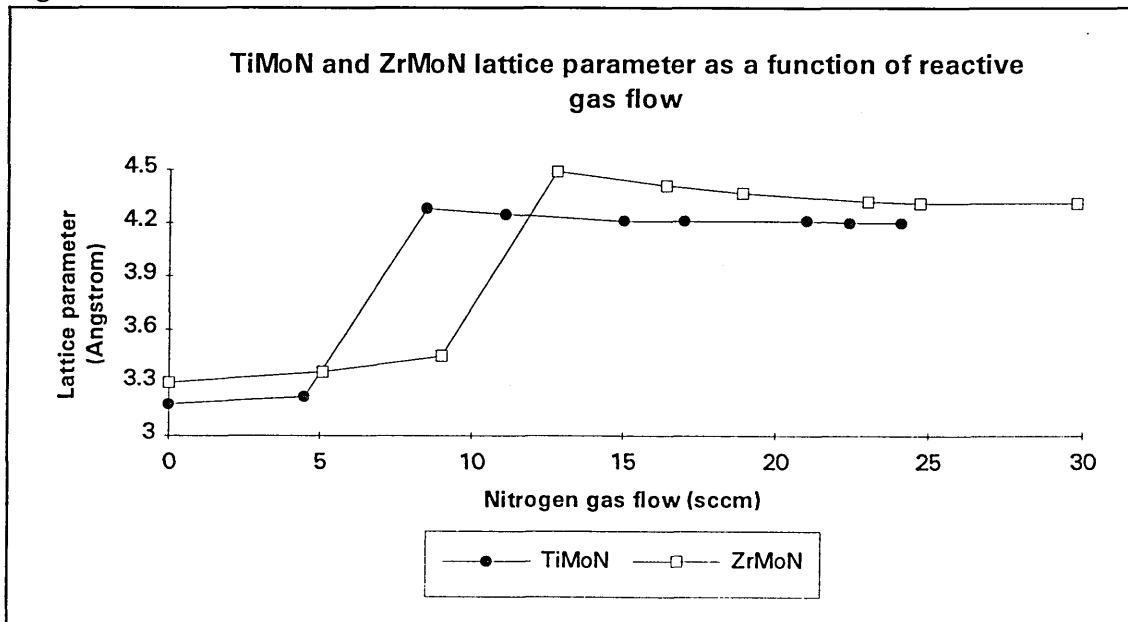
Figure 4.39. X-ray diffraction analysis of ZrMoN as a function of N<sub>2</sub> flow.

Figure 4.40.



#### 4.5.2. Mechanical and physical properties of TiMoN and ZrMoN ternary coatings

The mechanical and physical properties of TiMo and ZrMo alloys with increasing nitrogen content are shown in table 4.8. The film thickness, deposition rate and ductility was found to decrease as a function of increasing nitrogen partial pressure. In general all coatings exhibited excellent Rockwell adhesion, surface roughness ( $\sim 0.02\mu\text{m}$ ) and  $L^*$  values. Colour measurements showed a trend of decreasing  $L^*$  with increasing  $N_2$  partial pressure, whilst an opposing increasing / decreasing  $a^*$  trend was observed for TiMoN and ZrMoN. The hardness of the alloy generally increased as a function increasing nitrogen flow due to solid solution strengthening prior to preferential target poisoning. As the level of titanium or zirconium was significantly reduced at high nitrogen flow rates, the hardness of the films was steadily found to reduce.

Table 4.8.

Coating (N <sub>2</sub> flow rate) sccm	Thickness / $\mu\text{m}$ $\pm 0.1\mu\text{m}$	R <sub>c</sub> quality	Scratch Lc / N $\pm 2\text{N}$	Hardness (Hk <sub>0.025</sub> ) $\pm 200\text{Kgmm}^{-2}$	L* $\pm 0.1$	a* $\pm 0.1$	b* $\pm 0.1$
ZrMo (0)	6.00	1	10 d	820	80.54	0.46	3.89
ZrMoN (5.1)	5.79	1	20 d	1460	78.79	0.46	3.58
ZrMoN (9.0)	5.59	1-2	50	2400	78.05	0.34	2.89
ZrMoN (12.8)	5.36	1-2	55	3150	77.36	0.29	2.78
ZrMoN (16.4)	4.52	1-2	50	3050	75.88	0.25	2.86
ZrMoN (18.9)	4.20	1-2	50	2900	75.54	0.25	2.91
ZrMoN (23.0)	4.15	2	50	2770	75.43	0.25	2.91
ZrMoN (24.7)	4.07	2	45	2700	74.96	0.35	3.15
ZrMoN (29.8)	4.05	2	40	2600	74.57	0.46	3.77
TiMo (0)	5.71	1	10 d	780	79.41	0.95	3.69
TiMoN (4.5)	5.64	1	25 d	1600	79.30	0.73	2.56
TiMoN (8.5)	5.60	1-2	50	2600	78.99	0.63	2.77
TiMoN (11.1)	5.36	1-2	50	2780	77.77	0.63	3.22
TiMoN (15.0)	4.93	1-2	50	2900	77.39	0.66	3.29
TiMoN (17.0)	4.57	1-2	55	2860	77.13	0.68	3.38
TiMoN (21.0)	4.36	1-2	55	2750	76.89	0.74	3.58
TiMoN (22.4)	4.29	1-2	55	2650	76.78	0.79	3.83
TiMoN (24.1)	3.43	1-2	60	2500	76.66	0.81	3.85

d - ductile failure

Cross-sectional scanning electron microscopy revealed identical structural trends in both the TiMo and ZrMo films. Pure metal coatings were found to be the most columnar and exhibited a zone-1 structure (figure 4.41). As the quadrupole probe current was increased to  $2 \times 10^{-10} \text{A}$  ( $\text{N}_2$  flows 15-16.4sccm), the film densified, reduced in thickness, became smoother and grain size refining allowed a reduction in columnar size (figure 4.42). Coatings generated at high nitrogen partial pressures ( $4 \times 10^{-10} \text{A}$ ) were the least thick and exhibited a clearly visible, highly columnar pure metal interlayer below a highly dense zone-T pseudo-ceramic structure (figure 4.43).

Figure 4.41. SEM cross-section micrograph of TiMo alloy.

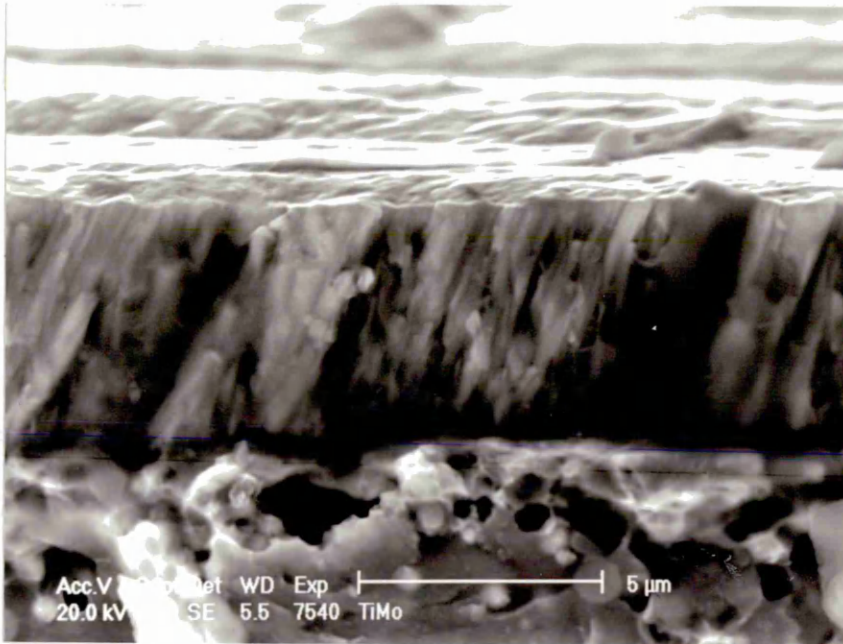


Figure 4.42. SEM cross-section micrograph of TiMoN ( $2 \times 10^{-10} \text{A}$  probe current).

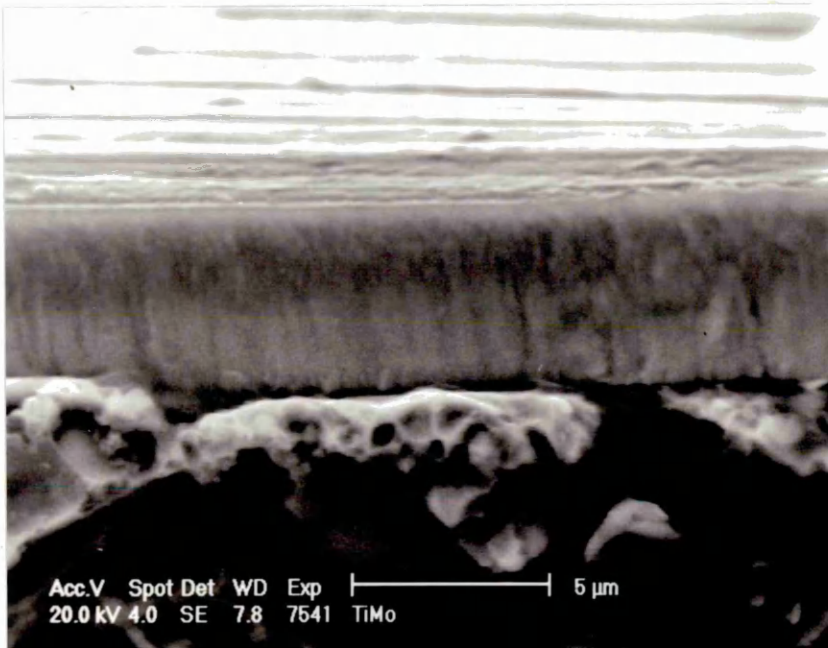
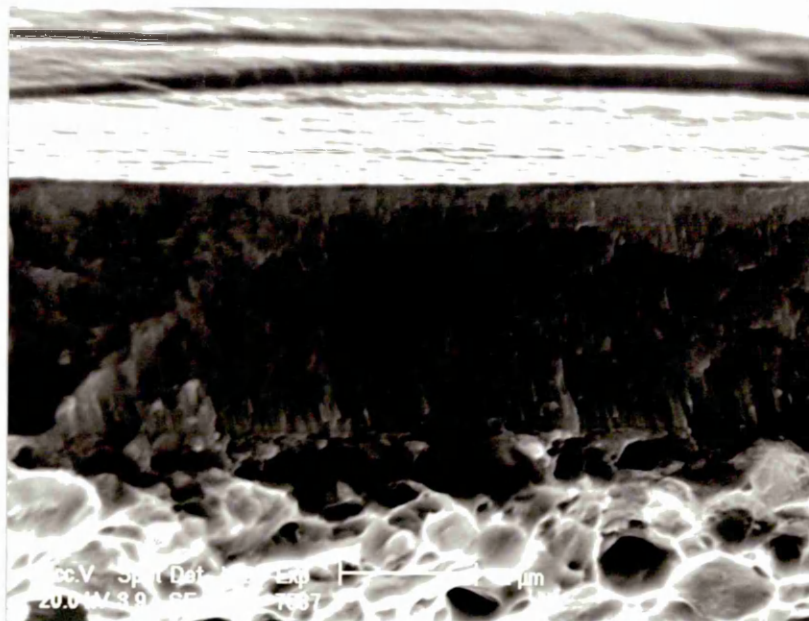


Figure 4.43. SEM cross-section micrograph of TiMoN ( $4 \times 10^{-10}$  A probe current).



#### 4.5.3. Flux distribution analysis.

A series of high speed steel substrates, which extended 90mm in total horizontal length and 30mm in height, were positioned directly in front of the TiZr, TiMo and ZrMo segmented targets (figure 4.44), at a fixed target to substrate distance of 80mm, such that the centre of the substrate was directly aligned with the centre of the target (where the segment interface ran in the vertical direction). After a series of non-reactive unbalanced magnetron deposition processes (table 4.7), the relative composition of the coating fluxes were assessed by quantitative GDOES analysis across the substrates in horizontal increments of 10mm from the centre. Figures 4.45, 4.47 & 4.49 show the flux composition distributions as a function of position in front of TiZr, TiMo and ZrMo targets and the typical variations in their associated GDOES spectra (figures 4.46a&b, 4.48a&b and 4.50a&b) .

Figure 4.44.

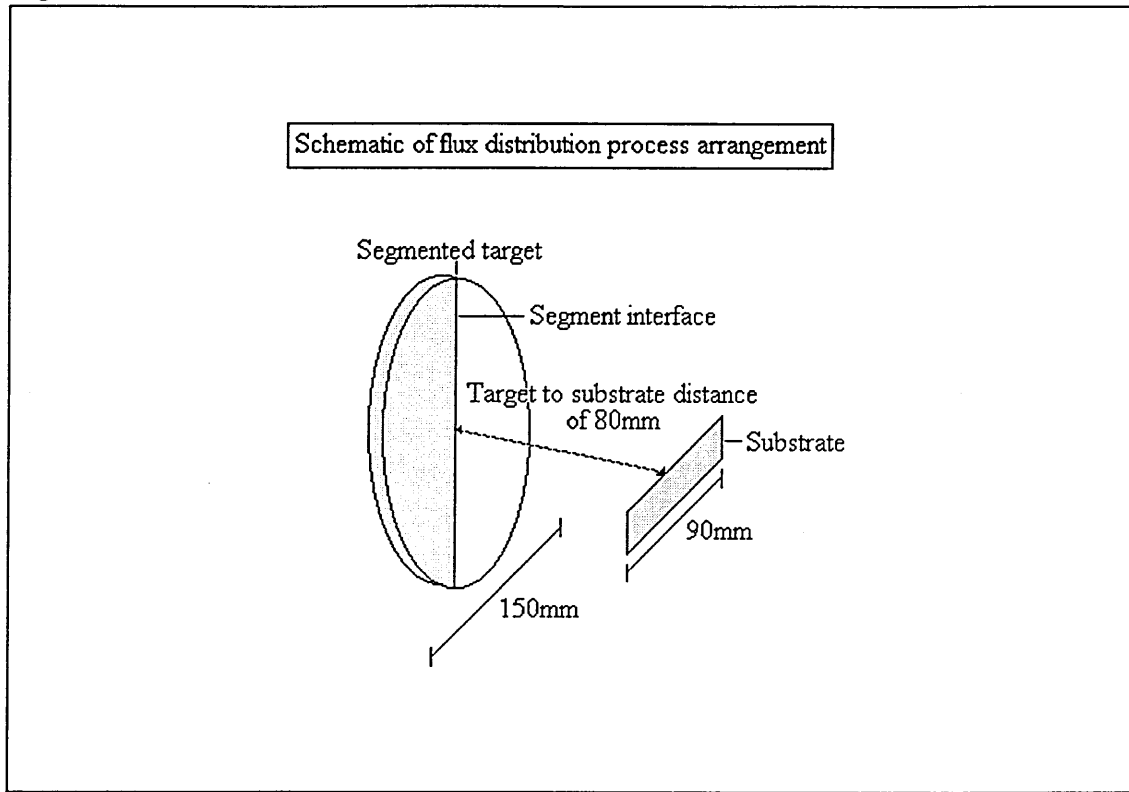


Figure 4.45. TiZr target

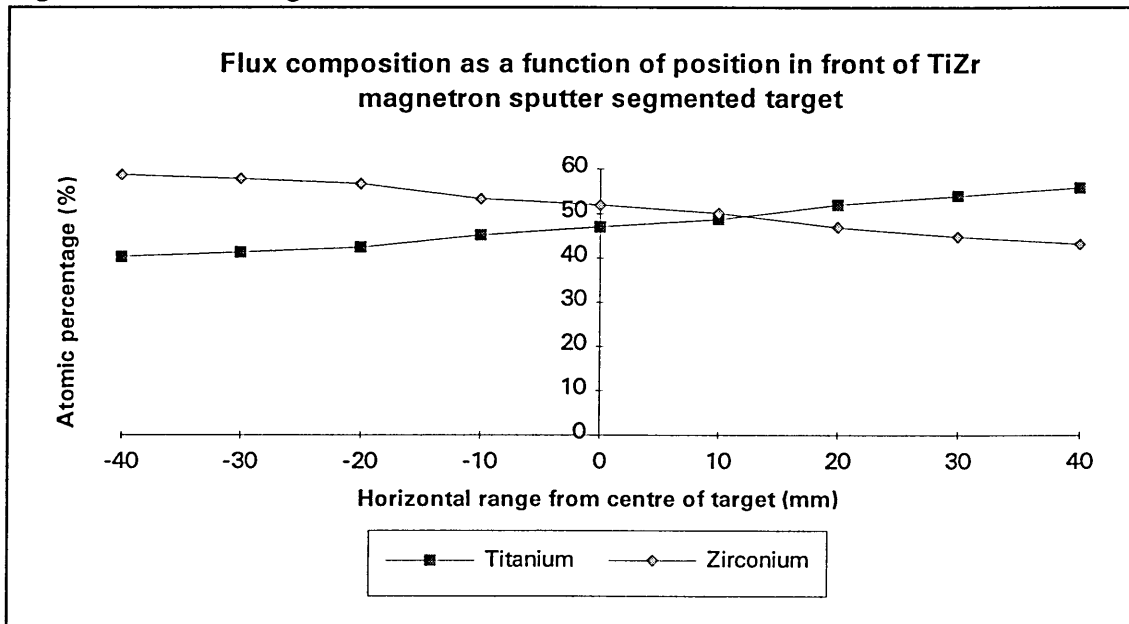


Figure 4.46a. TiZr GDOES depth profile.

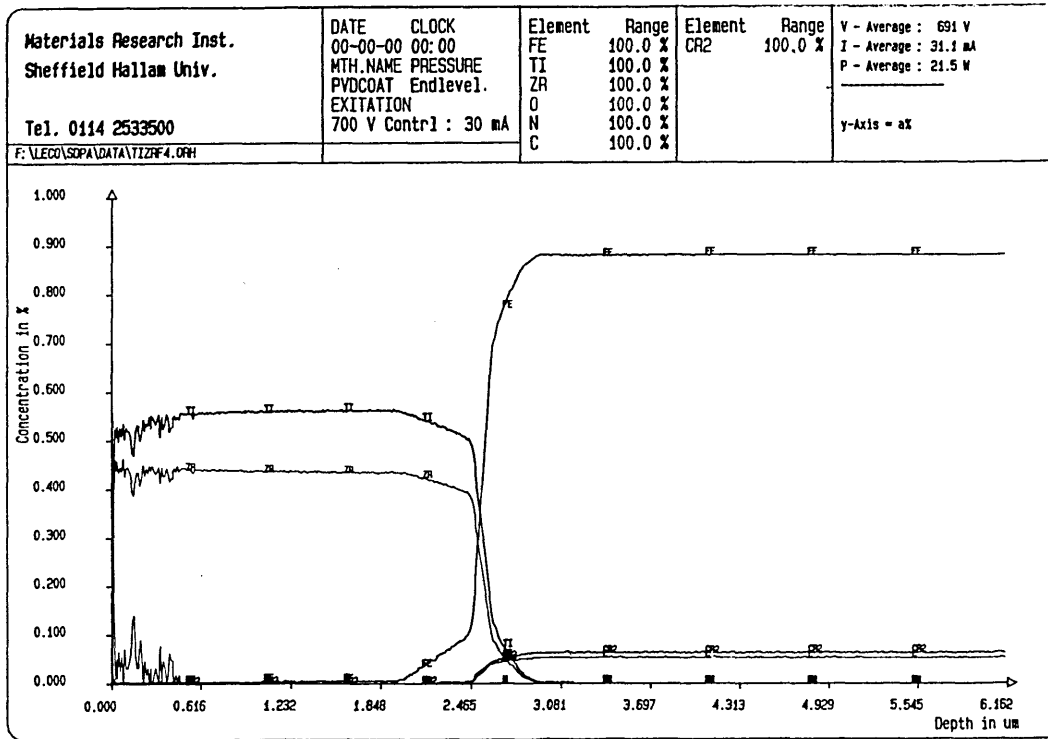


Figure 4.46b. TiZr GDOES depth profile.

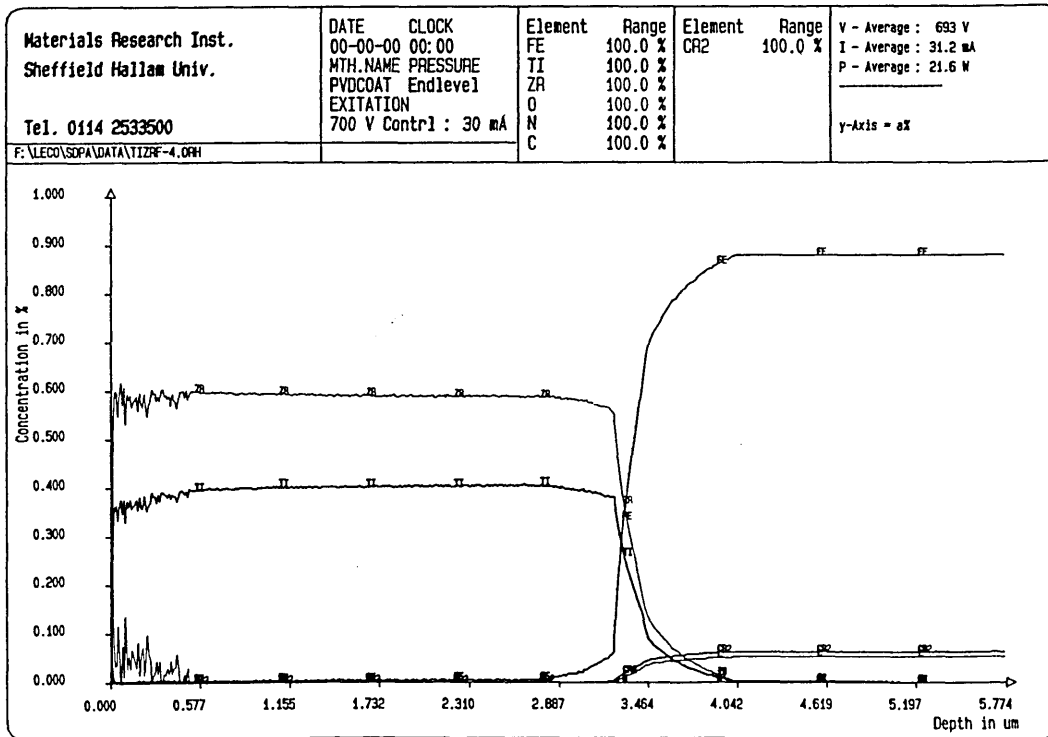


Figure 4.47. TiMo target.

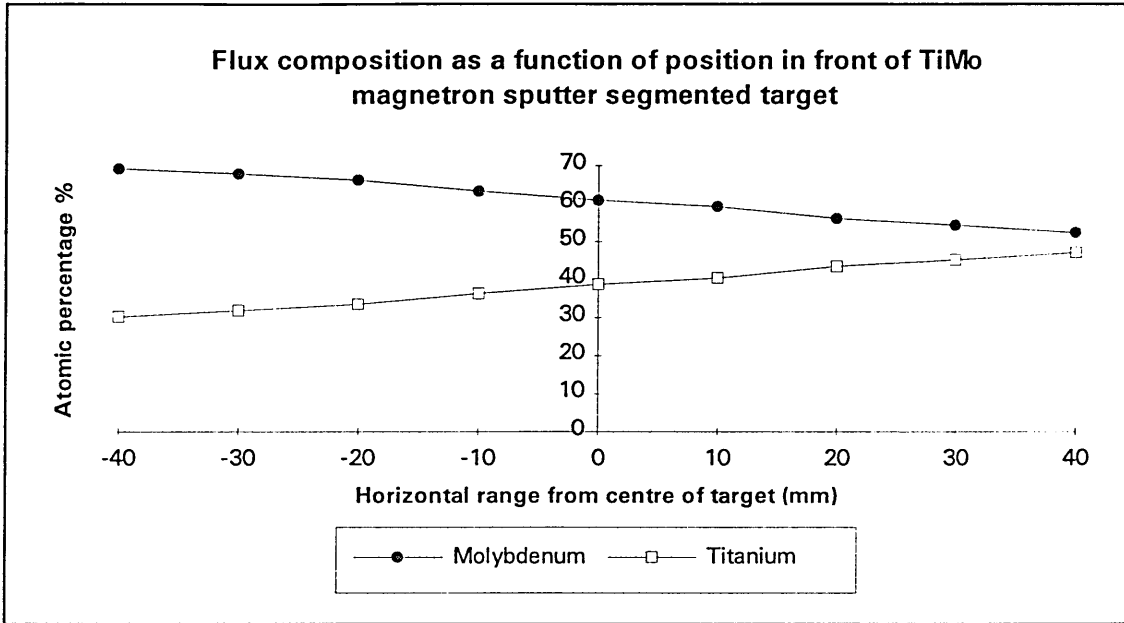


Figure 4.48a. TiMo GDOES depth profile.

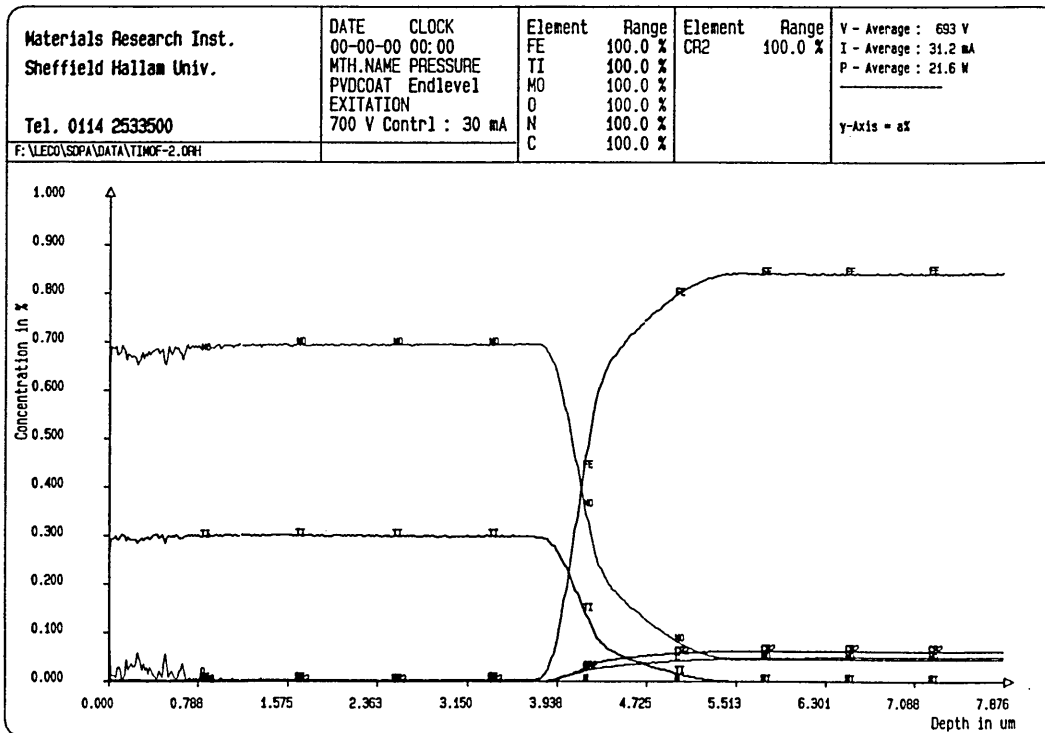


Figure 4.48b. TiMo GDOES depth profile.

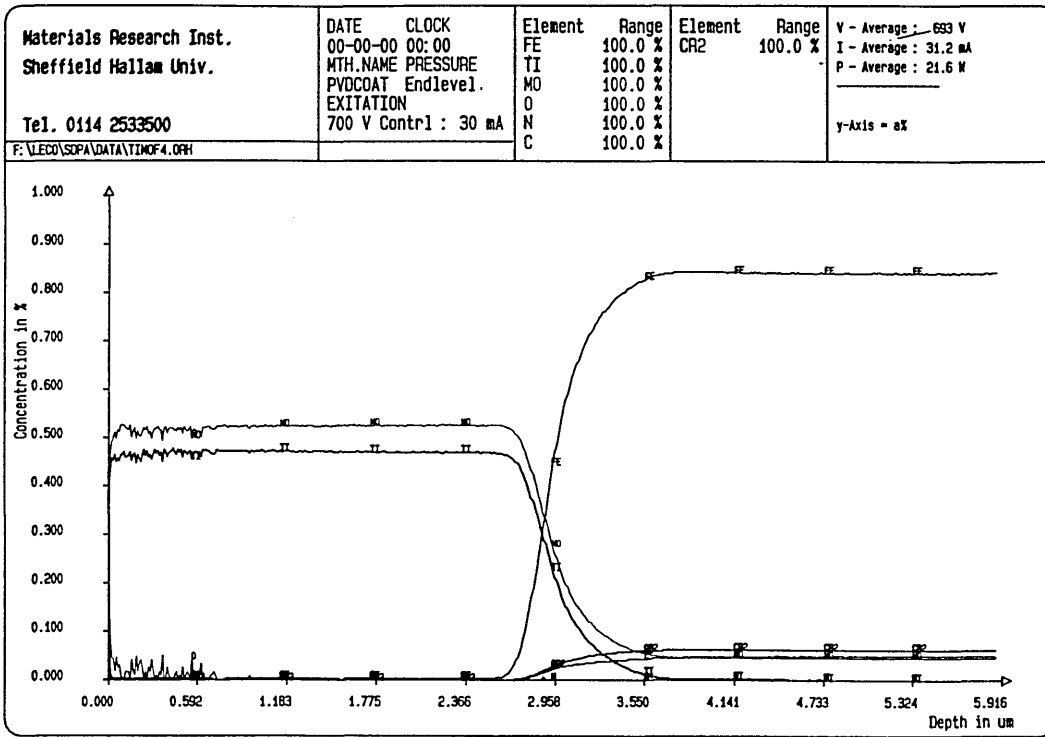


Figure 4.49. ZrMo target

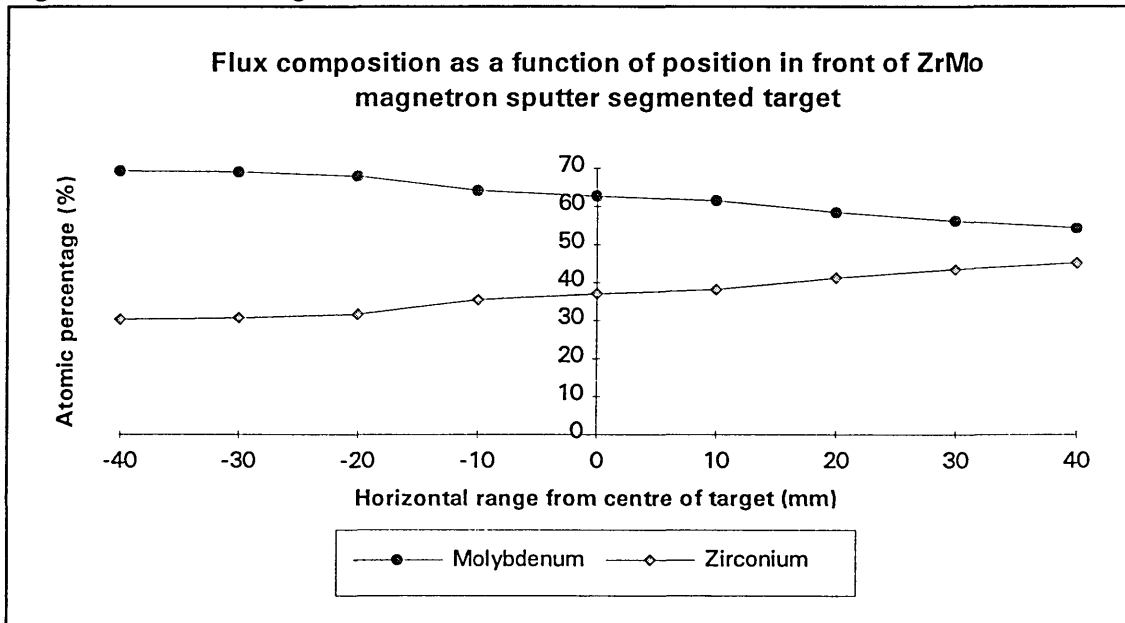


Figure 4.50a. ZrMo GDOES spectrum.

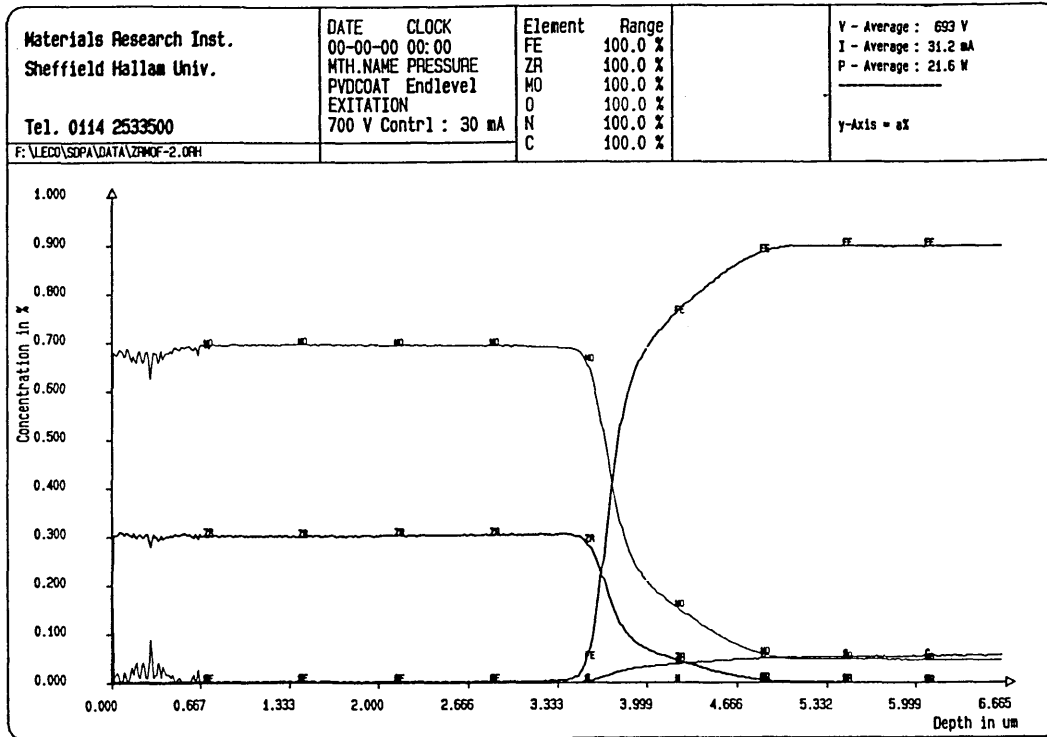
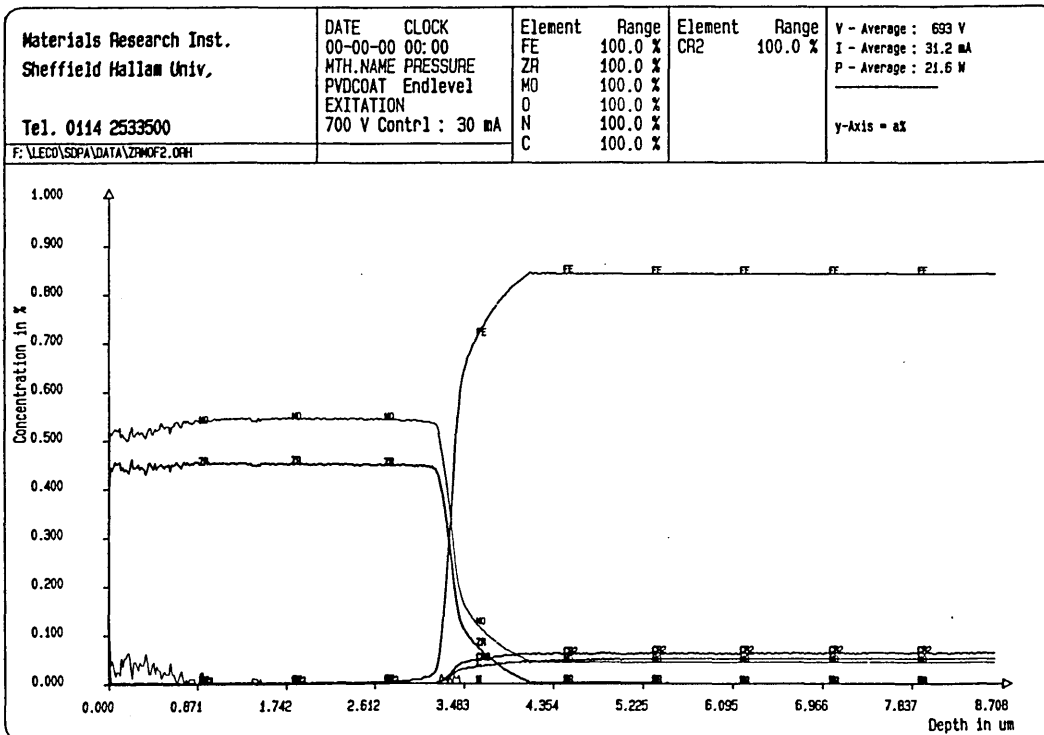


Figure 4.50b. ZrMo GDOES spectrum.



Analysis illustrated a highly linear composition distribution and hence strong line-of-sight nature of the sputtering process. At positions directly in front of each segment, the flux composition became dominated by that associated element (table 4.9), especially in the case of molybdenum which exhibited a significantly higher sputter yield ( $Y$ ) than titanium or zirconium. Composition analysis at the central position, aligned with the metal / metal interfaces, also revealed elemental constitutions which related well to values predicted by Monte-Carlo simulations (section 4.4.1).

Table 4.9

Target composition	GDOES coating sputter measurement	TRIM coating sputter prediction
$Ti_{0.57}Zr_{0.43}$	$Ti_{0.47}Zr_{0.53}$	$Ti_{0.49}Zr_{0.51}$
$Ti_{0.47}Mo_{0.53}$	$Ti_{0.40}Mo_{0.60}$	$Ti_{0.34}Mo_{0.66}$
$Zr_{0.40}Mo_{0.60}$	$Zr_{0.38}Mo_{0.62}$	$Zr_{0.34}Mo_{0.66}$

## References.

1. J.D.Fast - *Rec.Trav.Chim.Pays-Bas*, 1939, 58, 973.
2. P.Duwez - *J.Inst.Met*, 1952, 80, 525.
3. J.P.Biersack, L.G.Haggmark - *Nucl.Instrum.Methods*, 1980, 174, 257.
4. J.P.Biersack, W.Eckstein - *Appl.Phys*, 1984, A34, 73.
5. I.G.Brown, X.Godechot - *IEEE Trans.Plasma.Sci*, 1991, 19, 5, 713-717.

## **CHAPTER FIVE**

### **INVESTIGATION OF THE $Ti_xZr_yN$ SYSTEM.**

This chapter presents the results of various investigations on the fabrication and characterisation of  $Ti_xZr_yN$  thin films deposited on high speed steel and stainless steel substrates. The intention of the study was to critically examine the relationships between micro-structure, composition and the mechanical and physical properties of  $Ti_xZr_yN$  films produced from pure metallic and segmented targets by steered cathodic arc evaporation (SCAE), unbalanced magnetron sputtering (UBM) and arc-bond sputtering (ABS) techniques and compare against first generation ZrN and TiN binary coatings. This section also presents typical results from repeated analyses on the effects of changing two variable parameters during reactive UBM processing : reactive gas partial pressure and substrate bias voltage. Also included are the results of coating trials where partial substitution of Al into the  $Ti_xZr_yN$  lattice was undertaken to improve oxidation resistance properties.

#### **5.1. Examination of $Ti_xZr_yN$ coatings deposited by SCAC, UBM and ABS techniques.**

A single HTC 1000-4 ABS PVD unit had the flexibility to deposit all coatings in the trial. For this study 600 x 190 x12mm targets were used of the following compositions (chapter 3.2);

- (a) Grade 2 titanium (purity > 99.7%)
- (b) Grade 702 zirconium (purity > 99.6%)
- (c)  $Ti_{0.8}Zr_{0.2}$  HIPped segmented target.

The reactive gas used was nitrogen (purity 99.999%) and the working gas used to sputter the targets or aid arc ignition was argon (purity 99.999%). The gas flow was controlled by the P.I.D system with feedback to total pressure whilst the argon flow was kept constant. In the UBM and ABS coating modes, the reactive gas partial pressure required was determined by hysteresis analysis (figure 5.1a-c). In the SCAC coating mode, the partial pressure required was determined by a preliminary quantitative GDOES depth profiling where the reactive gas partial pressure had been varied as a function of deposition time.

Figure 5.1a

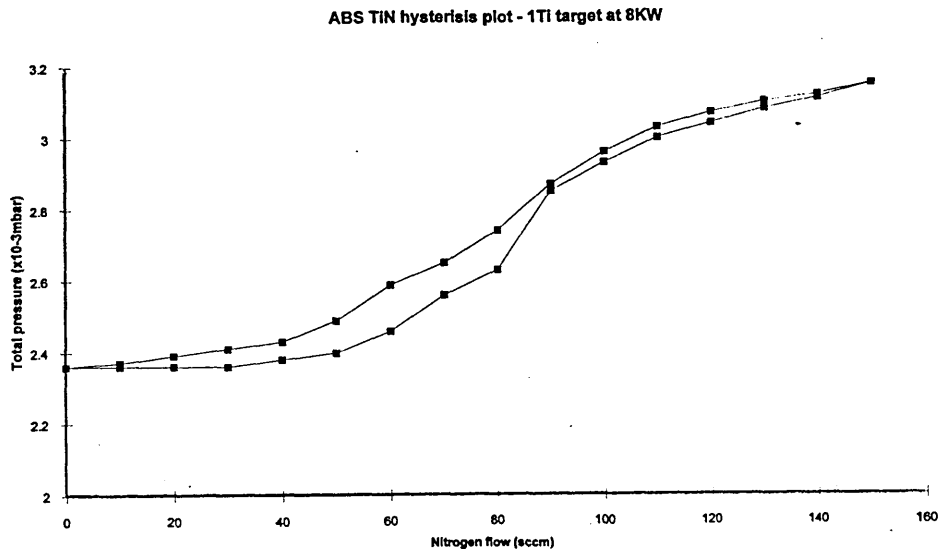


Figure 5.1b.

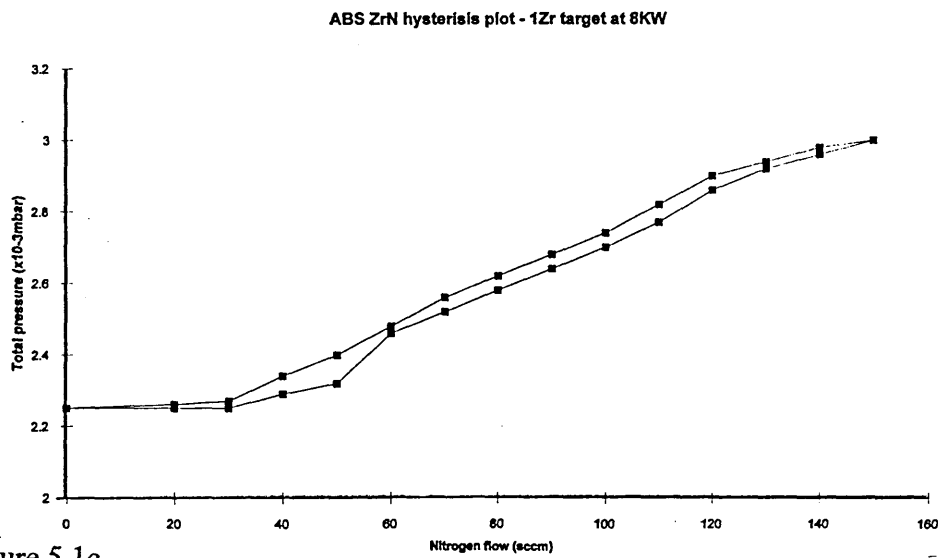


Figure 5.1c.

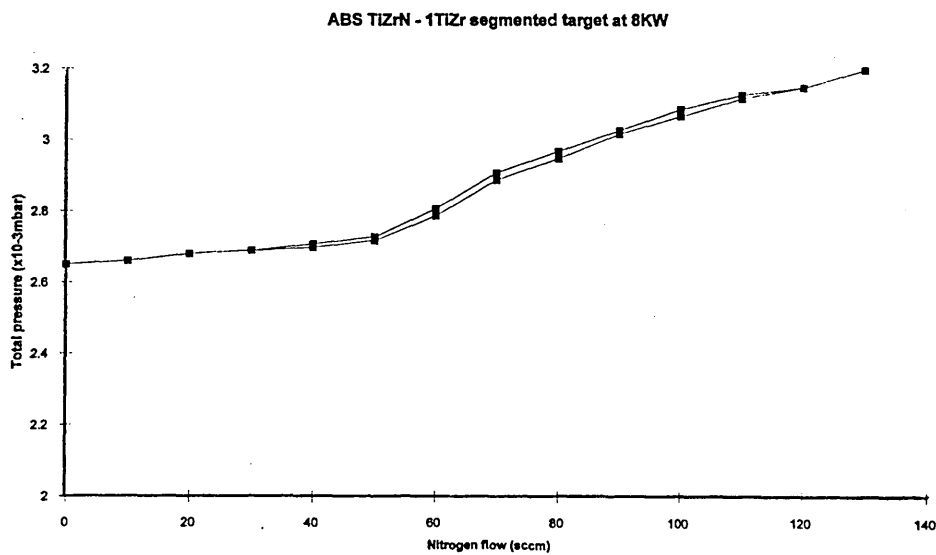


Table 5.1. Ti<sub>x</sub>Zr<sub>y</sub>N process.

Steered cathodic arc evaporation	Unbalanced magnetron sputtering	Arc-bond sputtering
<p>(1) Chamber heating &amp; argon glow discharge. Time = 30mins Temperature = 400°C Cathode voltage = -250V Substrate bias voltage = -1000V Ar flow = 220scm Pressure = 2.7 x10<sup>-3</sup>mbar</p> <p>(2) Glow discharge target cleaning. Time = 15mins Target shutter position = in front of target Power = 5KW Substrate bias voltage = 0V Unbalancing coil current = 0A Ar flow = 220scm Pressure = 2.7x10<sup>-3</sup>mbar Temperature = 400°C</p>	<p>(1) Chamber heating &amp; argon glow discharge. Time = 30mins Temperature = 400°C Cathode voltage = -250V Substrate bias voltage = -1000V Ar flow = 220scm Pressure = 2.7 x10<sup>-3</sup>mbar</p> <p>(2) Glow discharge target cleaning. Time = 15mins Target shutter position = in front of target Power = 5KW Substrate bias voltage = 0V Unbalancing coil current = 0A Ar flow = 220scm Pressure = 2.7x10<sup>-3</sup>mbar Temperature = 400°C</p>	<p>(1) Chamber heating &amp; argon glow discharge. Time = 30mins Temperature = 400°C Cathode voltage = -250V Substrate bias voltage = -1000V Ar flow = 220scm Pressure = 2.7 x10<sup>-3</sup>mbar</p> <p>(2) Glow discharge target cleaning. Time = 15mins Target shutter position = in front of target Power = 5KW Substrate bias voltage = 0V Unbalancing coil current = 0A Ar flow = 220scm Pressure = 2.7x10<sup>-3</sup>mbar Temperature = 400°C</p>
<p>(3) Steered arc metal ion etching. Time = 10 cycles each of 1 minute duration Arc current = 100A Substrate bias voltage = -1000V Temperature = 450°C Ar flow = 220scm Pressure = 2.7x10<sup>-3</sup>mbar</p>	<p>(3) Steered arc metal ion etching. No arc etching involved</p>	<p>(3) Steered arc metal ion etching. Time = 10 cycles each of 1 minute duration Arc current = 100A Substrate bias voltage = -1000V Temperature = 450°C Ar flow = 220scm Pressure = 2.7x10<sup>-3</sup>mbar</p>

<p>(4) <u>Steered arc evaporation interlayer coating</u></p> <p>Time = 5mins                  Thickness = 0.3-0.5µm                  Coil current = 0A                  Arc current = 100A                  Substrate bias voltage = -100V                  Temperature = 450°C                  Ar flow = 100scm</p>	<p>(4) <u>Unbalanced magnetron sputter interlayer coating</u></p> <p>Time = 5mins                  Thickness = 0.3-0.5µm                  Closed field geometry                  Unbalancing coil current = 8A                  Substrate bias voltage = -100V                  Power = 8KW                  Temperature = 450°C                  Ar flow = 220scm</p>	<p>(4) <u>Unbalanced magnetron sputter interlayer coating.</u></p> <p>Time = 5mins                  Thickness = 0.3-0.5µm                  Closed field geometry                  Unbalancing coil current = 8A                  Substrate bias voltage = -100V                  Power = 8KW                  Temperature = 450°C                  Ar flow = 220scm</p>
<p>(5) <u>Steered arc reactive evaporation coating.</u></p> <p>Thickness = 3-4µm                  Coil current = 0A                  Arc current = variable 60-100A                  Substrate bias voltage = -100V                  Temperature = 450°C                  Ar flow = 100scm</p>	<p>(5) <u>Unbalanced magnetron reactive sputter coating</u></p> <p>Thickness = 3-4µm                  Closed field geometry                  Unbalancing coil current = 8A                  Substrate bias voltage = -100V                  Power = variable 5-10KW                  Temperature = 450°C                  Ar flow = 220scm</p>	<p>(5) <u>Unbalanced magnetron reactive sputter coating.</u></p> <p>Thickness = 3-4µm                  Closed field geometry                  Unbalancing coil current = 8A                  Substrate bias voltage = -100V                  Power = variable 5-10KW                  Temperature = 450°C                  Ar flow = 220scm</p>

Table 5.2. Ti<sub>x</sub>Zr<sub>y</sub>N deposition conditions.

Technique	Coating	Target	N <sub>2</sub> flow (scm)	Deposition condition	Pressure (mbar)	Arc current (A)	Cathode power (KW)
SCAE	TiN	Ti	250	Static	1.50 x10 <sup>-3</sup>	100	
SCAE	ZrN	Zr	250	Static	1.87 x10 <sup>-3</sup>	100	
SCAE	Ti <sub>x</sub> Zr <sub>y</sub> N	TiZr segmented	250	Static	1.95 x10 <sup>-3</sup>	100	
SCAE	Ti <sub>x</sub> Zr <sub>y</sub> N (ARCCO1)	Ti & Zr co-evaporated	250	3-fold rotation	1.90 x10 <sup>-3</sup>	Ti=100, Zr=100	
SCAE	Ti <sub>x</sub> Zr <sub>y</sub> N (ARCCO2)	Ti & Zr co-evaporated	250	3-fold rotation	1.90 x10 <sup>-3</sup>	Ti=60, Zr=100	
UBM	TiN	Ti	83	Static	2.63 x10 <sup>-3</sup>		10
UBM	ZrN	Zr	68	Static	2.40 x10 <sup>-3</sup>		10
UBM	Ti <sub>x</sub> Zr <sub>y</sub> N	TiZr segmented	67	Static	2.98 x10 <sup>-3</sup>		10
UBM	Ti <sub>x</sub> Zr <sub>y</sub> N (UBMCO1)	Ti & Zr co-sputtered	100	3-fold rotation	2.63 x10 <sup>-3</sup>		Ti=10, Zr=10
UBM	Ti <sub>x</sub> Zr <sub>y</sub> N (UBMCO2)	Ti & Zr co-sputtered	85	3-fold rotation	2.52 x10 <sup>-3</sup>		Ti=5, Zr=10
UBM	Ti <sub>x</sub> Zr <sub>y</sub> N (UBMCO3)	Ti & Zr co-sputtered	74	3-fold rotation	2.70 x10 <sup>-3</sup>		Ti=10, Zr=5
ABS	TiN	Ti	83	Static	2.63 x10 <sup>-3</sup>		10
ABS	ZrN	Zr	68	Static	2.40 x10 <sup>-3</sup>		10
ABS	Ti <sub>x</sub> Zr <sub>y</sub> N	TiZr segmented	67	Static	2.98 x10 <sup>-3</sup>		10
ABS	Ti <sub>x</sub> Zr <sub>y</sub> N (ABSCO1)	Ti & Zr co-sputtered	100	3-fold rotation	2.63 x10 <sup>-3</sup>		Ti=10, Zr=10
ABS	Ti <sub>x</sub> Zr <sub>y</sub> N (ABSCO2)	Ti & Zr co-sputtered	85	3-fold rotation	2.52 x10 <sup>-3</sup>		Ti=5, Zr=10
ABS	Ti <sub>x</sub> Zr <sub>y</sub> N (ABSCO3)	Ti & Zr co-sputtered	74	3-fold rotation	2.70 x10 <sup>-3</sup>		Ti=10, Zr=5

Co-sputtered and co-evaporated films developed from multiple target deposition processes, segmented target and binary coatings developed from single target processes.

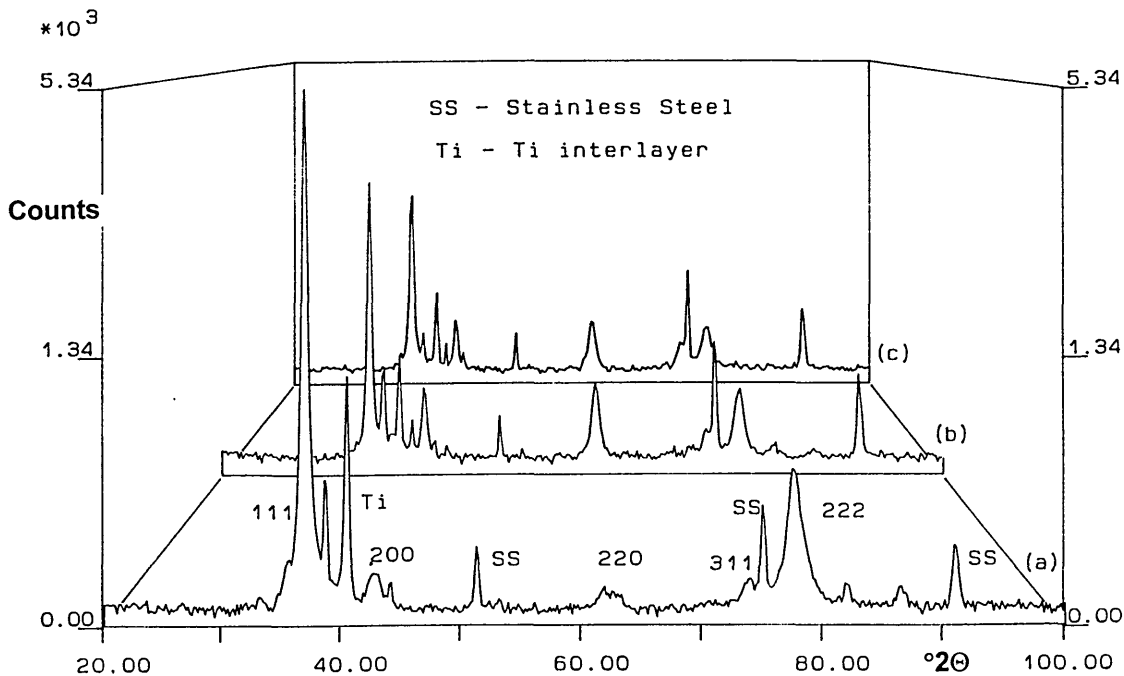
Standard polished HSS stubs, drill blanks and stainless steel coupons were chosen for use in the trial and individually cleaned using the routine outlined in section 3.3, before mounting onto one of six sub-turnstile assemblies at a nominal distance of 250mm from the targets.

The SCAE, UBM and ABS deposition regimes used are illustrated in table 5.1 and produced a range of compositions by manipulation of the cathode power, arc current and coating pressure as shown in table 5.2.

### 5.1.1. X-ray diffraction results.

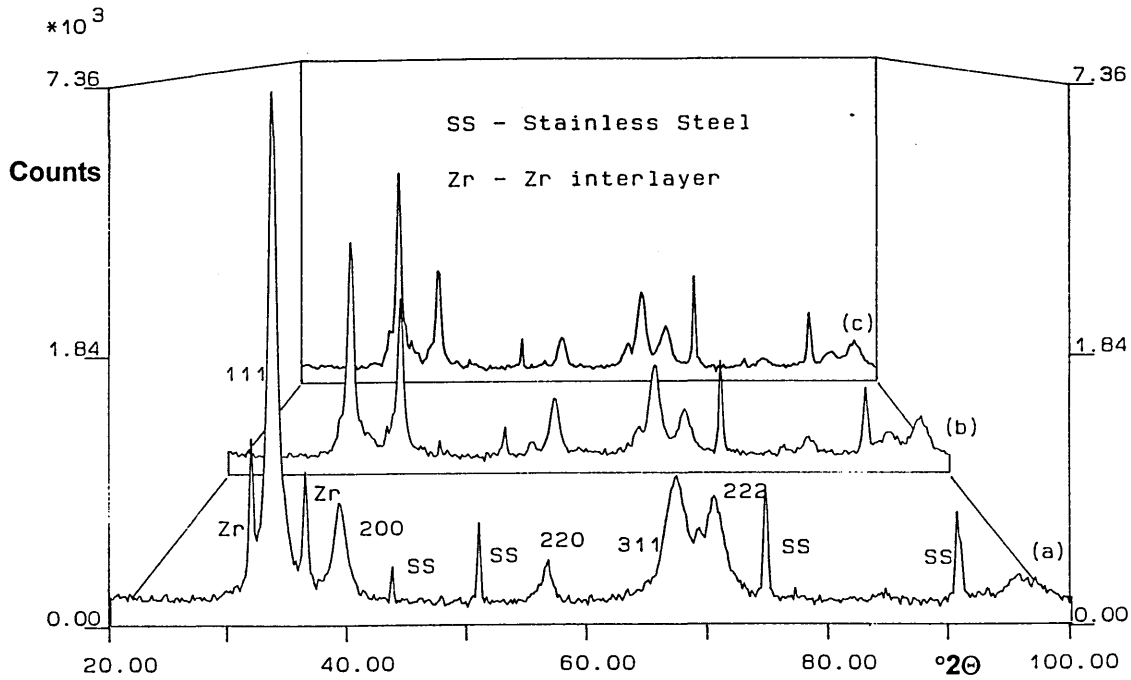
X-ray diffraction traces developed using Cu  $K\alpha$  radiation between  $20-100^\circ 2\theta$  showed that all coatings exhibited a preferred orientation in the  $\langle 111 \rangle$  direction irrespective of the coating system or deposition technique. Steered cathodic arc evaporated (SCAE) coatings had the strongest  $\langle 111 \rangle$  orientation with minimal contribution to the traces from (200), (220) and (311) reflections (figure 5.2-5.4). However, both the unbalanced magnetron sputtered (UBM) and arc-bond sputtered films (ABS) showed modest increases in (220) and (311) peak intensities and significant increases in the (200) reflections (figures 5.5 and 5.6) (table 5.3).

Figure 5.2. TiN X-ray diffraction traces.



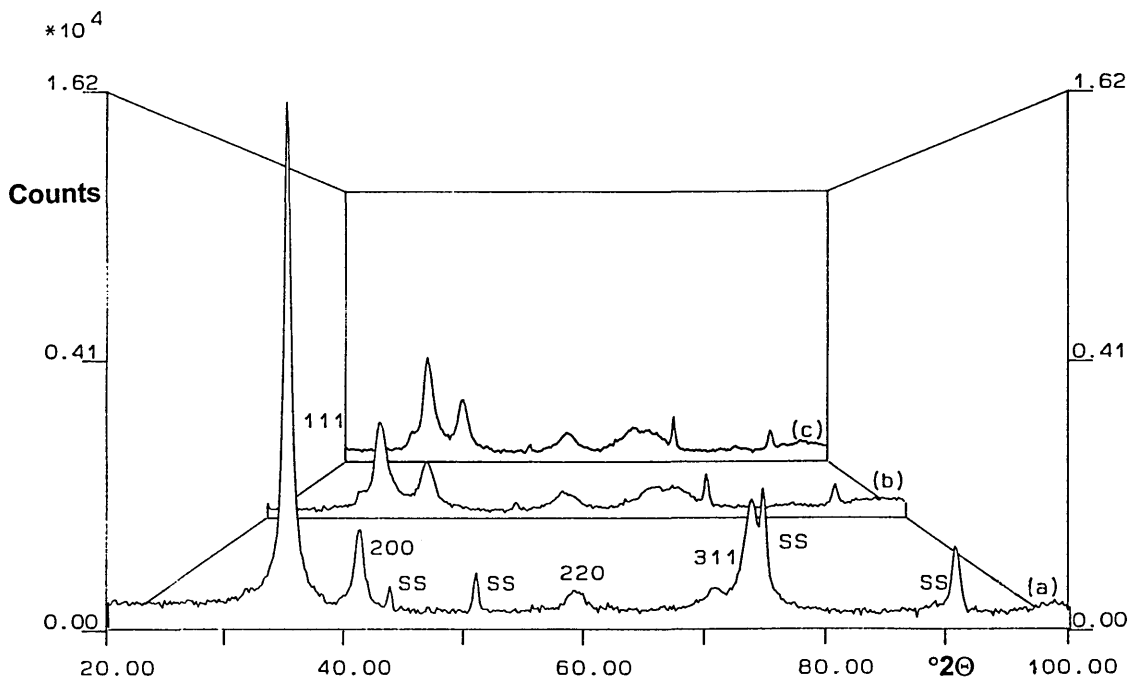
(a) ARC TiN, (b) UBM TiN, (c) ABS TiN

**Figure 5.3. ZrN X-ray diffraction traces.**

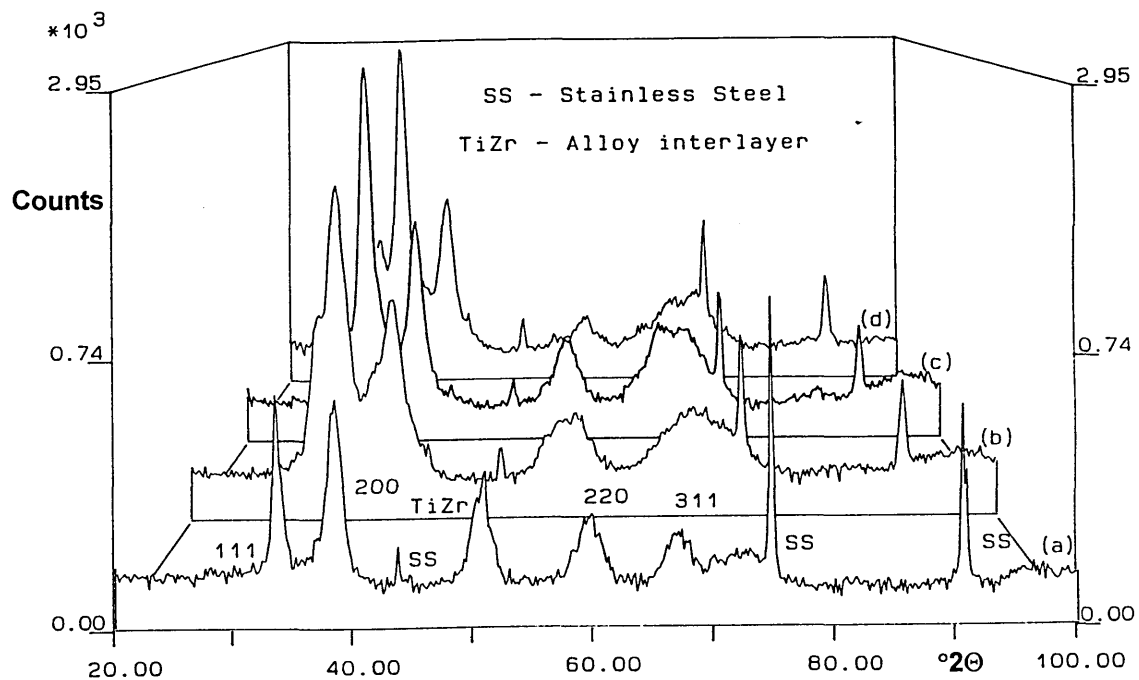


**(a) ARC ZrN, (b) UBM ZrN, (c) ABS ZrN**

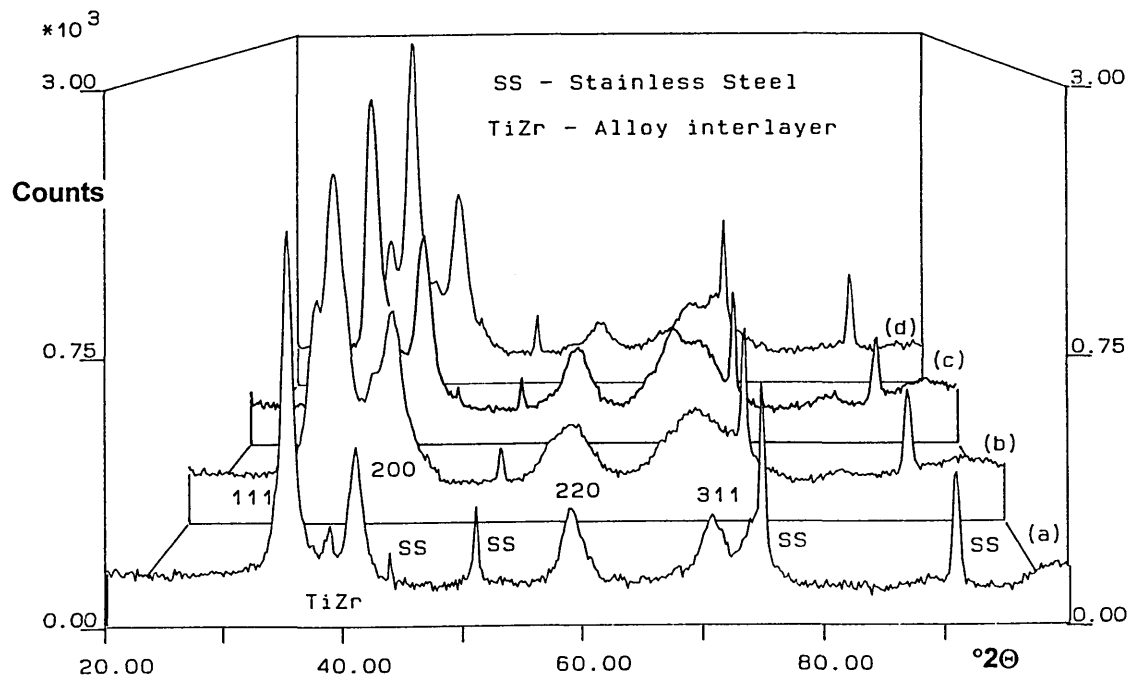
**Figure 5.4. Steered arc evaporation  $Ti_xZr_yN$  X-ray diffraction traces.**



**(a) ARC  $Ti_xZr_yN$  Segmented target  
(b) ARC  $Ti_xZr_yN$  Co-evaporation 1.  
(c) ARC  $Ti_xZr_yN$  Co-evaporation 2.**

Figure 5.5. Unbalanced magnetron sputter  $Ti_xZr_yN$  X-ray diffraction traces.

- (a) UBM  $Ti_xZr_yN$  Segmented target  
 (b) UBM  $Ti_xZr_yN$  Co-sputter 1.  
 (c) UBM  $Ti_xZr_yN$  Co-sputter 2.  
 (d) UBM  $Ti_xZr_yN$  Co-sputter 3.

Figure 5.6. Arc bond sputter  $Ti_xZr_yN$  X-ray diffraction traces.

- (a) ABS  $Ti_xZr_yN$  Segmented target  
 (b) ABS  $Ti_xZr_yN$  Co-sputter 1.  
 (c) ABS  $Ti_xZr_yN$  Co-sputter 2.  
 (d) ABS  $Ti_xZr_yN$  Co-sputter 3.

Table 5.3. X-ray diffraction relative intensity and unit cell data.

Coating	111 (%)	200 (%)	220 (%)	311 (%)	222 (%)	400 (%)	$a_0/\text{\AA}$ $\pm 0.01$	Expansion (%)	Structure
SCAE TiN	100	0.9	0.4	0.3	7.9	0.2	4.25	0.23	f.c.c
UBM TiN	100	9.3	9.4	1.8	6.6	0.1	4.26	0.47	f.c.c
ABS TiN	100	9.1	8.3	2.9	6.3	0.3	4.29	1.18	f.c.c
SCAE ZrN	100	4.2	1.1	6.9	5.2	0.4	4.63	1.53	f.c.c
UBM ZrN	100	53.8	9.4	18.0	5.1	3.7	4.61	1.09	f.c.c
ABS ZrN	100	30.3	3.2	17.3	5.6	2.5	4.62	1.32	f.c.c
SCAE SEG TiZrN	100	3.4	1.0	5.3	6.8	1.4	4.40	0.73	f.c.c
UBM SEG TiZrN	100	18.3	8.1	4.8	4.2	0.8	4.40	0.73	f.c.c
ABS SEG TiZrN	100	18.7	6.9	5.1	5.0	0.8	4.40	0.73	f.c.c
SCAE TiZrN (ARCCO1)	100	6.1	2.3	4.0	6.2	0.9	4.55	1.89	f.c.c
SCAE TiZrN (ARCCO2)	100	5.4	2.2	2.5	1.7	1.1	4.59	2.05	f.c.c
UBM TiZrN (UBMCO1)	100	41.0	4.7	4.2	3.0	1.5	4.52	1.95	f.c.c
UBM TiZrN (UBMCO2)	100	15.2	2.5	5.3	2.9	1.2	4.59	2.05	f.c.c
UBM TiZrN (UBMCO3)	100	30.5	3.6	5.0	4.8	1.2	4.38	0.27	f.c.c
ABS TiZrN (ABSCO1)	100	35.4	4.5	4.0	4.0	2.1	4.53	2.16	f.c.c
ABS TiZrN (ABSCO2)	100	32.8	3.7	5.7	4.0	1.7	4.59	2.05	f.c.c
ABS TiZrN (ABSCO3)	100	31.5	2.3	2.2	2.0	1.0	4.38	0.27	f.c.c

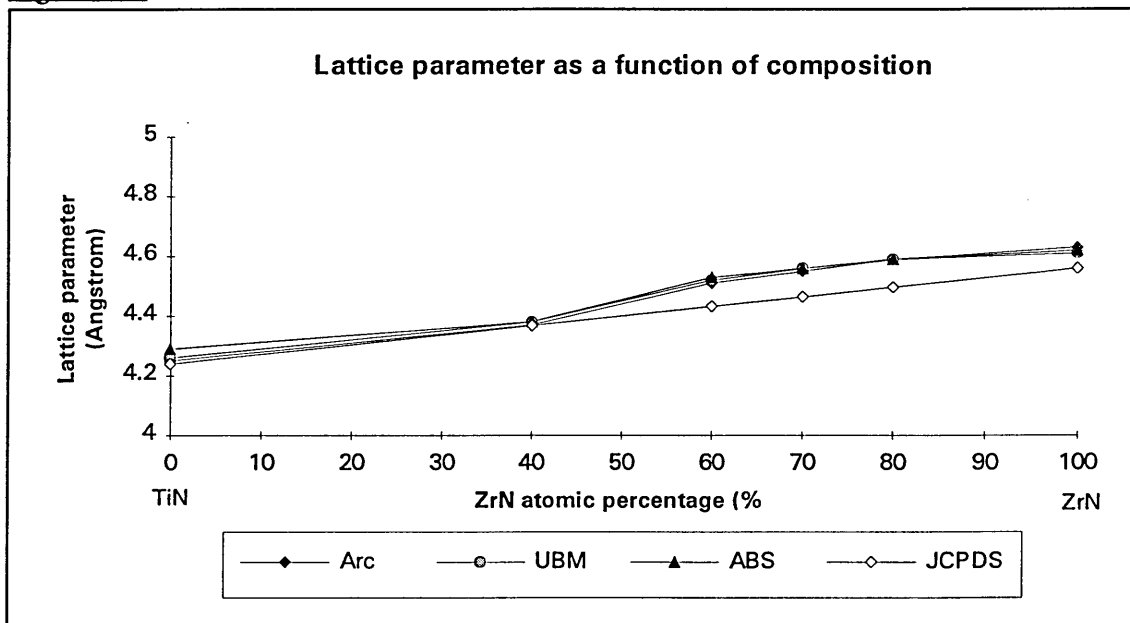
Where SEG indicates the TiZr segmented target used to deposit the film and CO indicates co-deposition from Ti & Zr pure metal targets.

Diffraction patterns from  $Ti_xZr_yN$  coatings (figures 5.4-5.6) indicated that in all cases only one f.c.c phase was present, confirming that the complete solid solubility exhibited by the Ti-Zr alloy system was also shown by the TiN-ZrN thin film system and indicated that the behaviour of the nitride system was isotropic. .

Further examination revealed that the Zr content in the coatings was given by  $y=1-x$  (where  $x$  = titanium fractional composition and  $y$  = zirconium fractional composition) and the unit cell dimensions followed Vegard's law, i.e. the linear dependence of ternary lattice spacings on composition follow a straight line joining the values for the binary system spacings (figure 5.7). Lattice parameter measurements showed that in all cases the unit cell dimensions were in excess of JCPDS unstressed powder standard data, indicating that lattice expansion had occurred causing the development of a compressive residual stress.

Measurements on the level of lattice expansion as a function of composition when compared against unstressed powder diffraction data ( JCPDS No. 6-6042 & 2-0956) indicated the largest increases in unit cell dimensions, and hence the highest compressive residual stresses occurred when the Zr content of the film was high.

Figure 5.7.



### 5.1.2. GDOES results.

The GDOES spectra showed that all coatings deposited were of similar thickness (3-4 $\mu$ m) and stoichiometric, i.e. the reactive gas : metal was 1:1 ( $\pm 0.05$ ) (figures 5.8a-c).  $Ti_xZr_yN$  sputtered coatings co-deposited from pure metal targets showed significant variation in the metal ratio as a function of applied power (figure 5.9 and 5.10). However, the metal ratio developed from the 80at% Ti, 20at% Zr segmented target proved constant at approximately 60at% Ti, 40at% Zr as the zirconium had a higher intrinsic sputter yield .

The results were in good agreement with Monte-Carlo sputter yield simulations conducted in the previous chapter using the TRIM-95 code. Alteration of the elemental composition of co-evaporated  $Ti_xZr_yN$  coatings deposited from pure metal targets could also be achieved by variation of the individual arc currents.

Figure 5.8a. GDOES depth profile of TiN on a steel substrate.

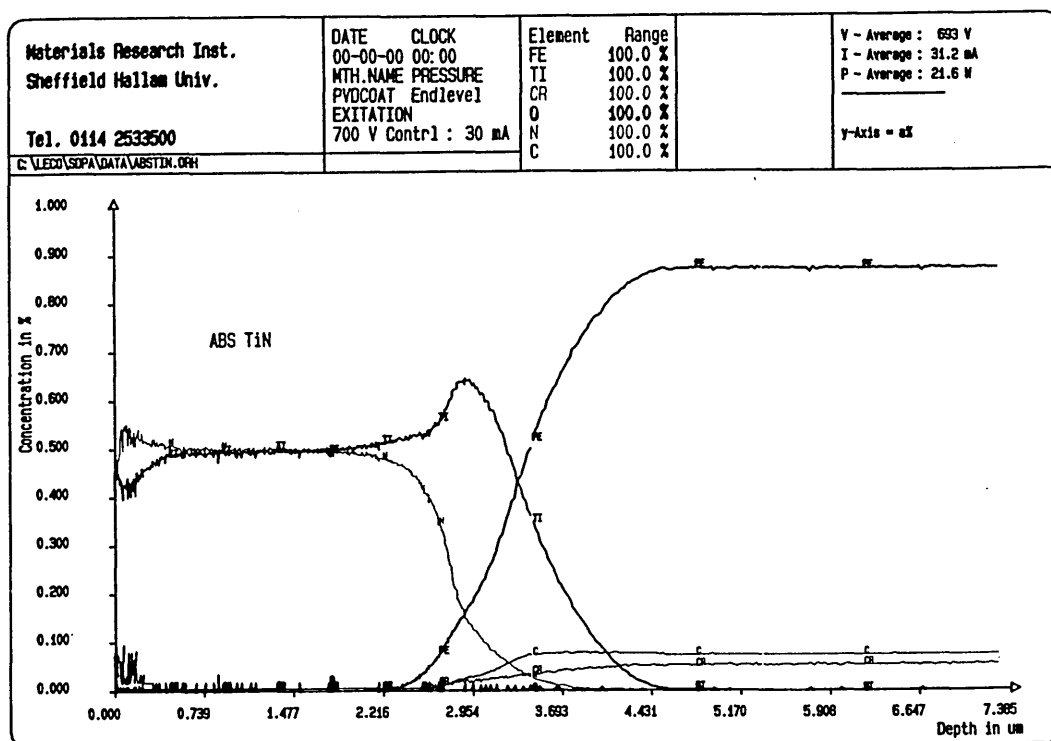


Figure 5.8b. GDOES depth profile of ZrN on a steel substrate.

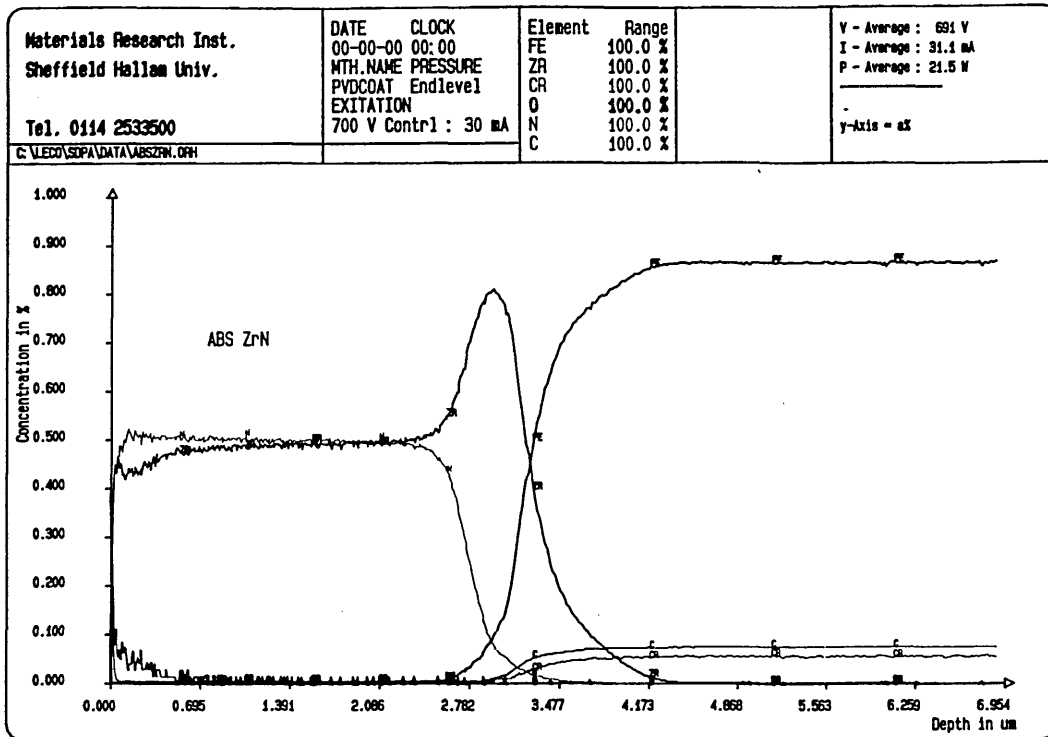


Figure 5.8c. GDOES depth profile of  $Ti_xZr_yN$  (segmented target) on a steel substrate.

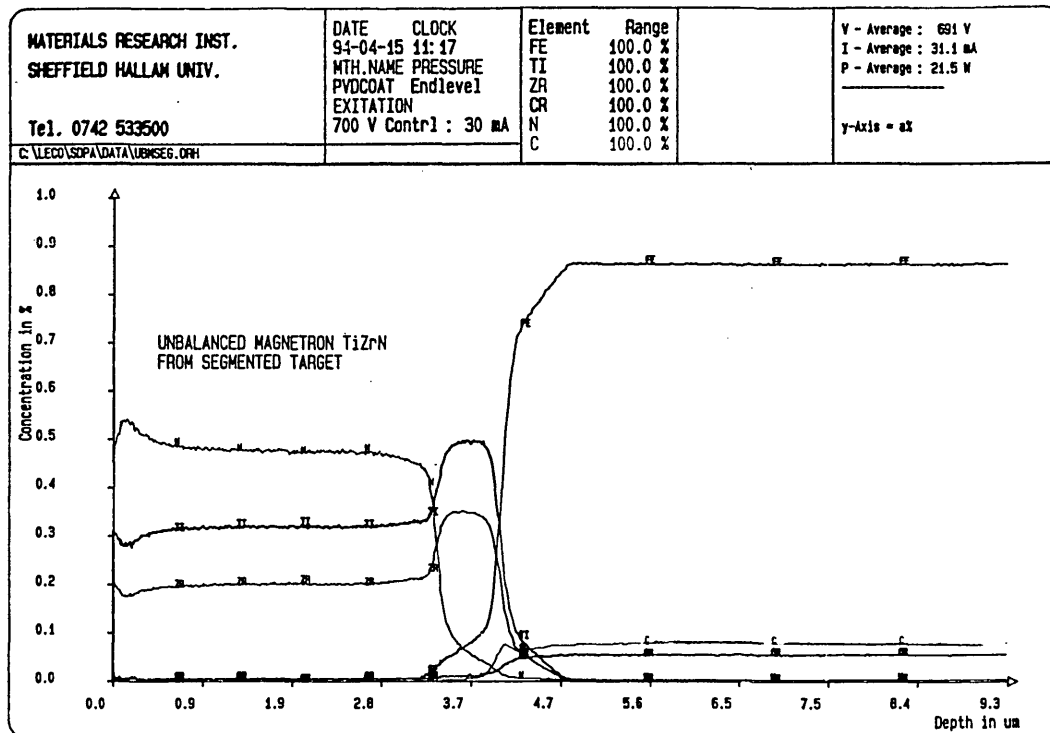


Figure 5.9. GDOES depth profile of co-sputtered  $Ti_xZr_yN$  on a steel substrate.

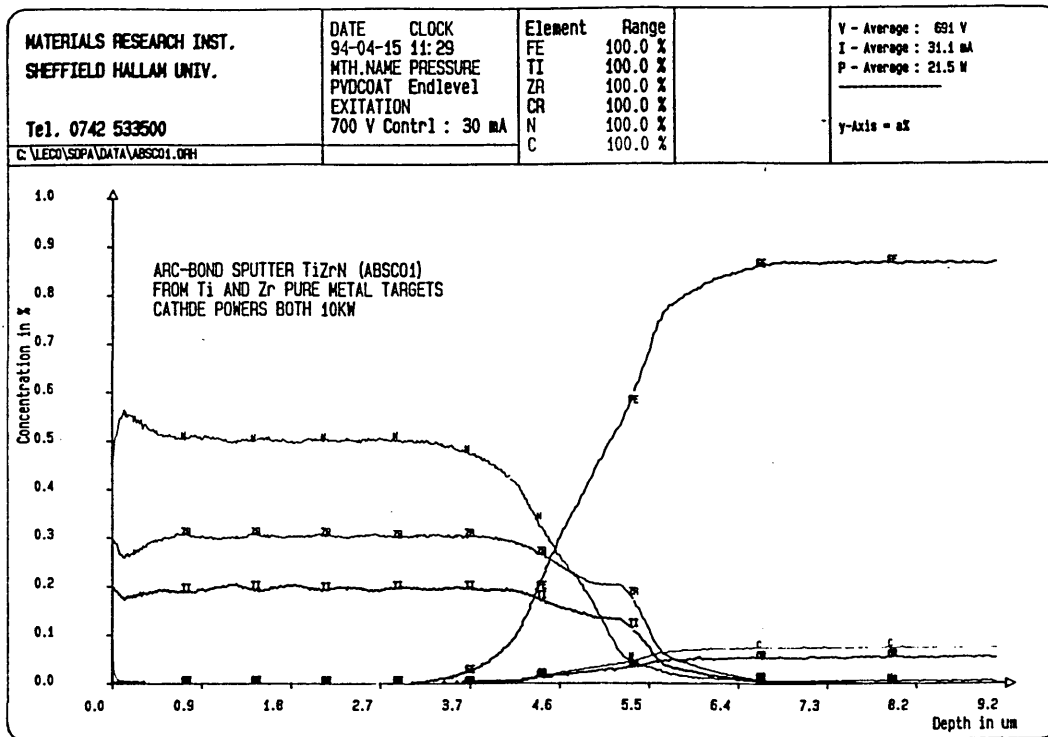
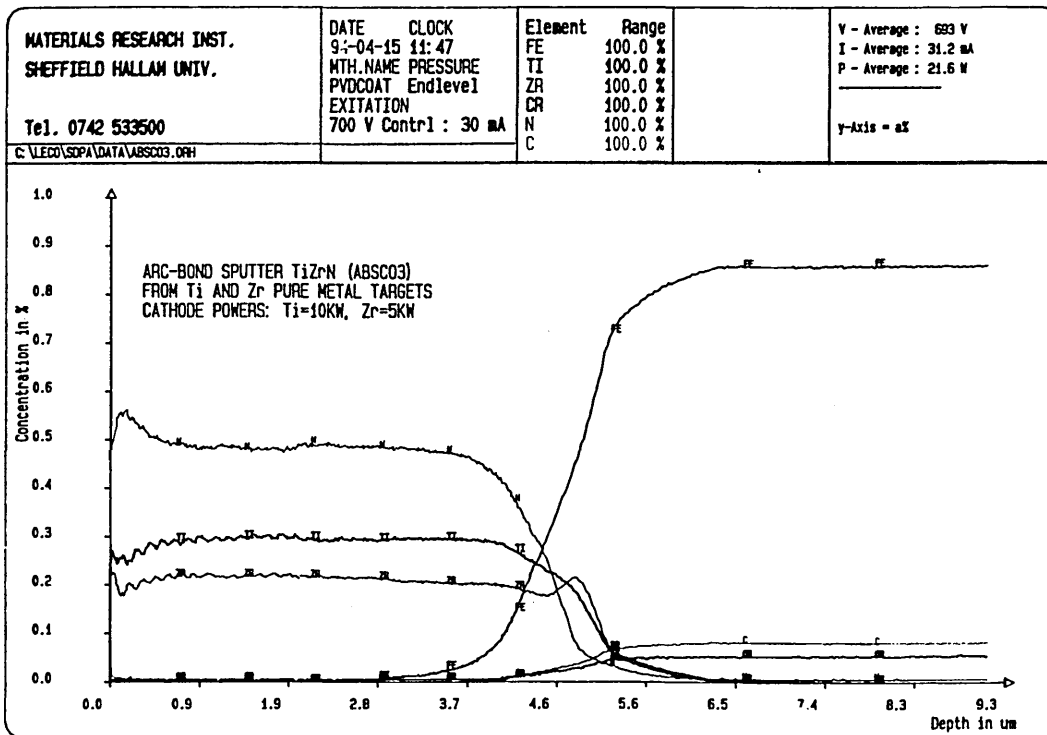


Figure 5.10. GDOES depth profile of co-sputtered  $Ti_xZr_yN$  on a steel substrate.

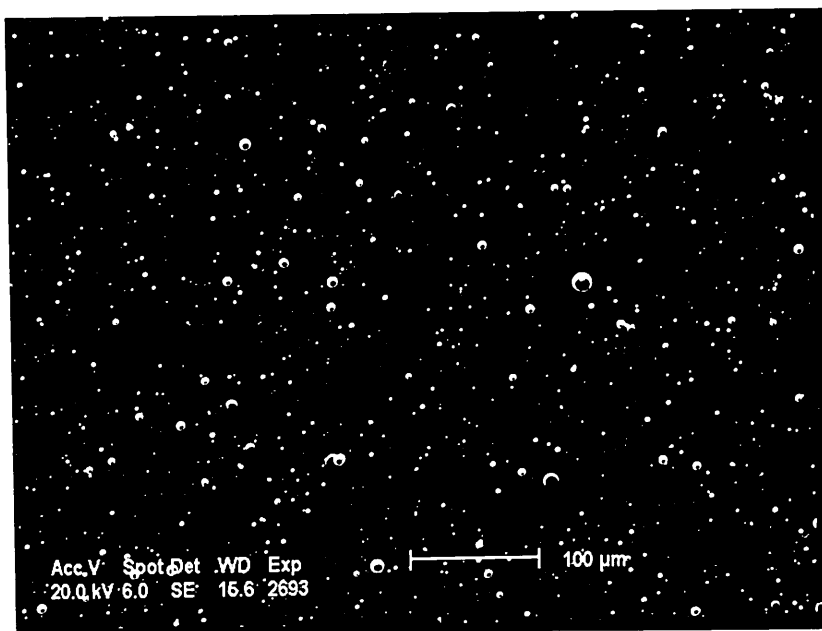


### 5.1.3. Scanning electron microscopy results.

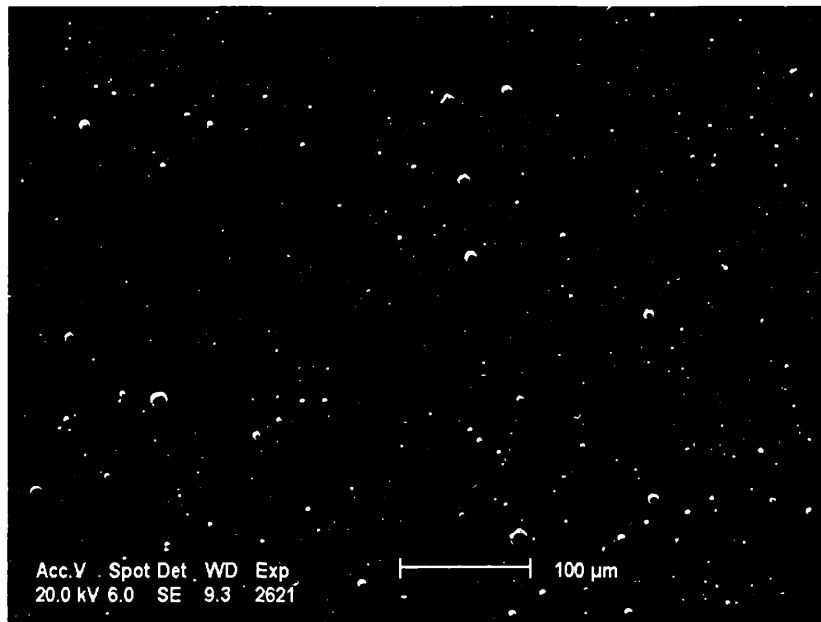
The SEM was used to analyse both the surface topography of the coatings, i.e. to measure the number of macro-particles and surface deformation, and the film micro-structure and density using the cross-sectional technique.

The highest density of macro-particles was recorded on SCAE coatings, significantly reduced in the ABS processes (incorporated only by the cyclic metal ion etch stage prior to deposition) and almost totally removed in the UBM films. The macro-particle density was also dependent on the type of target material, with the highest numbers of particles per centimetre recorded on SCAE TiN, intermediate numbers of smaller dimensions on arc evaporated  $Ti_xZr_yN$  films and the lowest number recorded on steered arc ZrN coatings (figures 5.11a-c). This behaviour is probably related to the individual target melting points and arc stalling at segmented target interfaces.

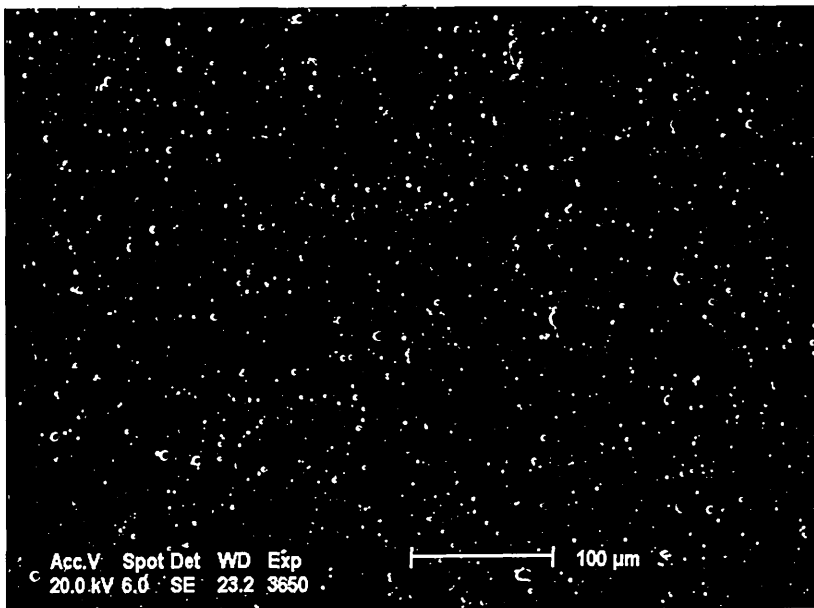
#### 5.11a. Macro-particles on the surface of a SCAE TiN coating.



5.11b. Macro-particles on the surface of a SCAE ZrN coating.

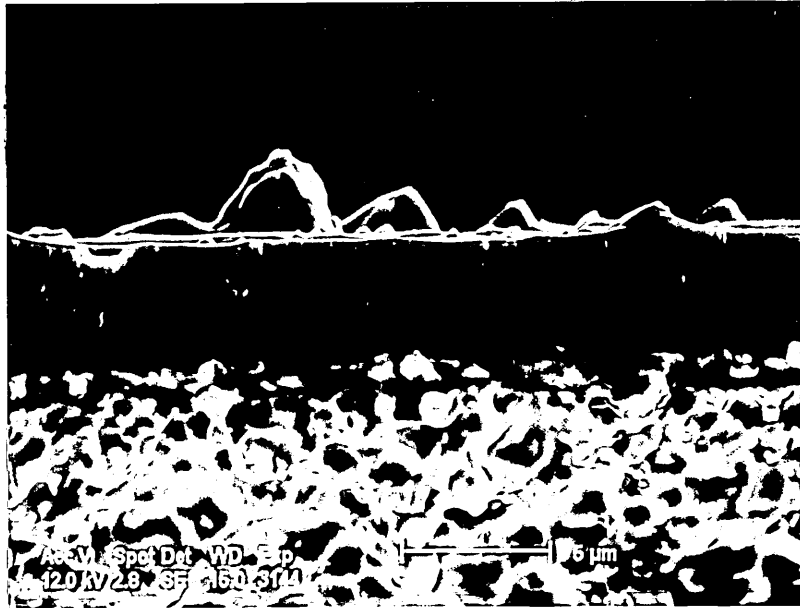


5.11c. Macro-particles on the surface of a SCAE Ti<sub>x</sub>Zr<sub>y</sub>N (segmented target) coating.



Cross-section analysis showed that all coatings exhibited a zone-T dense columnar micro-structure with the  $Ti_xZr_yN$  showing a finer grain size than the binary systems (figure 5.12).

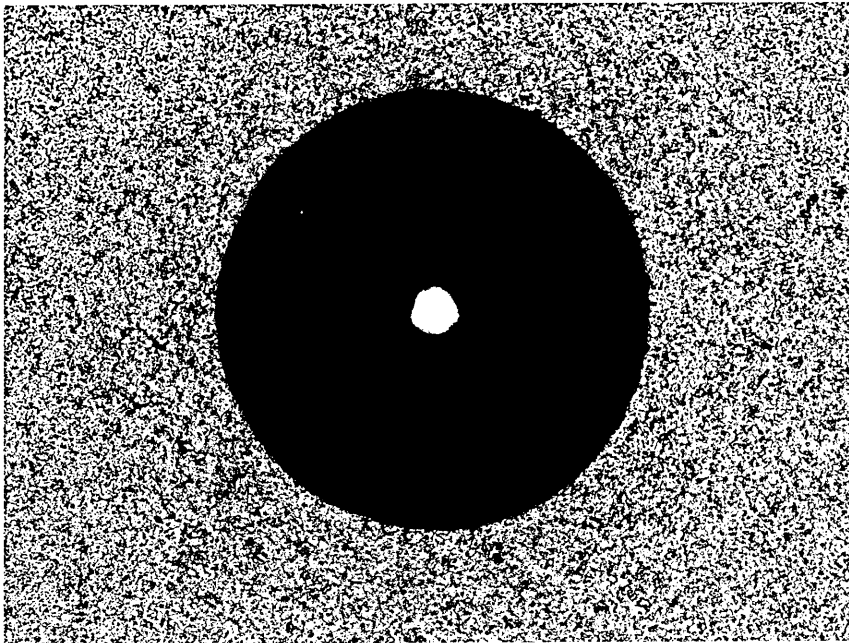
Figure 5.12. SEM cross-section micrograph of SCAE  $Ti_xZr_yN$  coating on HSS.



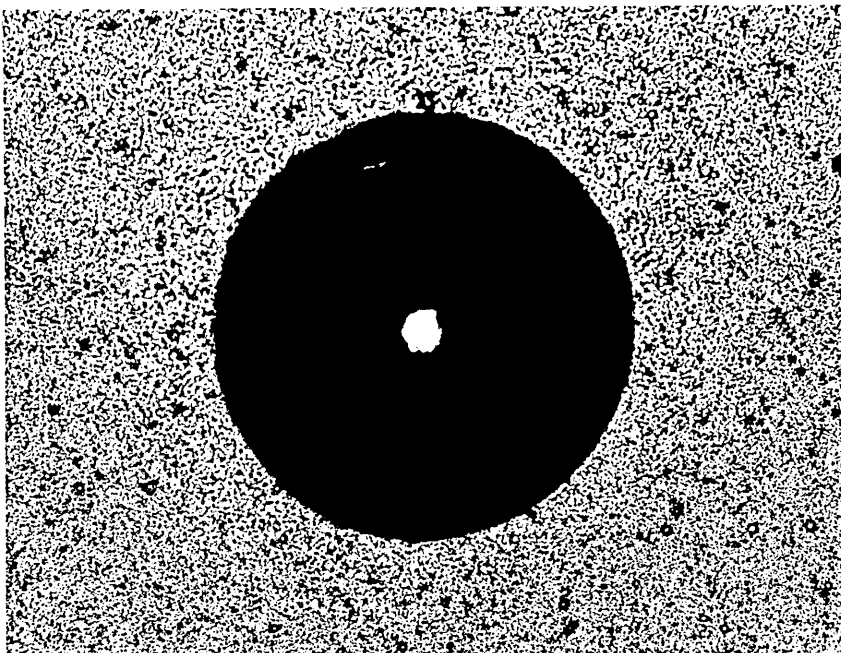
#### 5.1.4. Mechanical and physical properties.

A series of coating adhesion trials were undertaken using 150Kgf Rockwell-C indents which revealed that all coatings demonstrated HF1 standard indents at 100 times magnification with no signs of surface cracking, spallation and adhesive or cohesive failure (figures 5.13 and 5.14). The indentations also showed that the M2 high speed substrate hardness had not been altered during processing and remained at minimum  $R_C64$ . The results were verified by the scratch adhesion technique (figure 5.15 and 5.16) which showed that all coatings failed via a brittle fracture mechanism at critical loads which varied between 45-65N. SCAE and ABS coatings exhibited the highest critical load values and were comparable, whilst films deposited by the UBM technique had generally lower adhesion values (table 5.4). The investigations revealed that the critical loads of  $Ti_xZr_yN$  ternary coatings showed small increases over the binary systems, particularly when the titanium content in the coating was high.

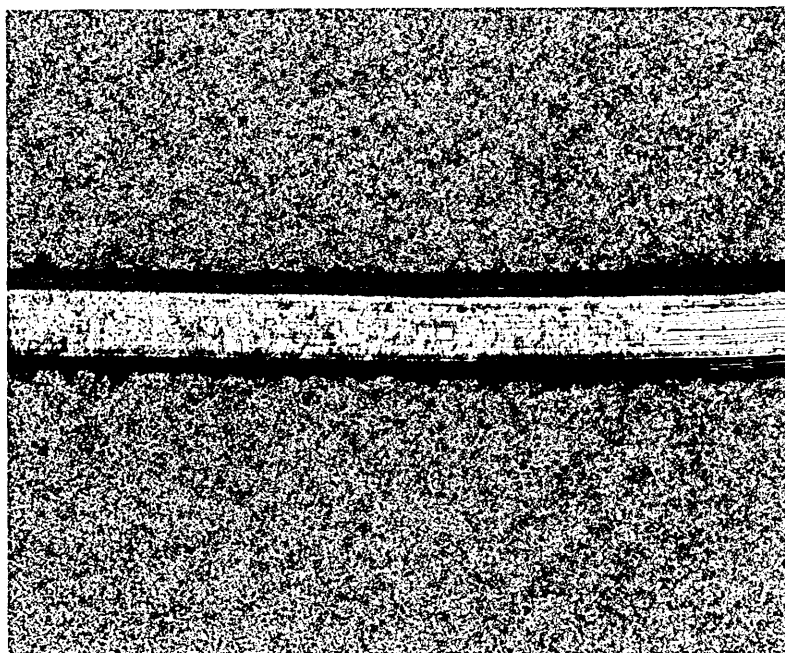
Figures 5.13. UBM  $Ti_xZr_yN$   $R_c$  indent.



Figures 5.14. ABS  $Ti_xZr_yN$   $R_c$  indent.



Figures 5.15. UBM Ti<sub>x</sub>Zr<sub>y</sub>N scratch.



Figures 5.16. ABS Ti<sub>x</sub>Zr<sub>y</sub>N scratch

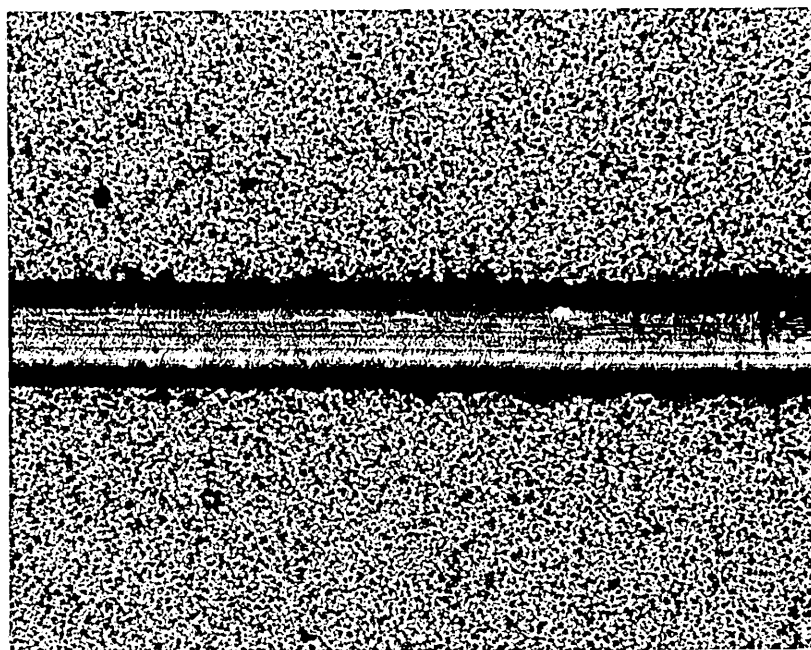


Table 5.4. Binary and ternary coating properties.

Coating	$R_a/\mu\text{m}$ $\pm 0.01$	$R_z/\mu\text{m}$ $\pm 0.05$	$R_t/\mu\text{m}$ $\pm 0.05$	$(H_{k0.025})$ $\pm 200\text{Kgmm}^{-2}$	Composition $\pm 5\%$	$L_c / N$ $\pm 2N$
SCAE TiN	0.105	2.73	3.45	2400	1:1	55
UBM TiN	0.063	1.04	1.26	2300	1:1	50
ABS TiN	0.073	1.67	2.66	2300	1:1	55
SCAE ZrN	0.095	2.67	3.25	2200	1:1	55
UBM ZrN	0.065	0.68	0.93	2000	1:1	45
ABS ZrN	0.070	2.15	2.45	2200	1:1	55
UBM SEG TiZrN	0.026	0.83	1.05	2950	$\text{Ti}_{0.6}\text{Zr}_{0.4}\text{N}$	50
ABS SEG TiZrN	0.057	1.58	2.32	3600	$\text{Ti}_{0.6}\text{Zr}_{0.4}\text{N}$	55
SCAE SEG TiZrN	0.098	2.70	3.45	3450	$\text{Ti}_{0.6}\text{Zr}_{0.4}\text{N}$	65
SCAE TiZrN (ARCCO1)	0.083	2.52	3.48	2800	$\text{Ti}_{0.3}\text{Zr}_{0.7}\text{N}$	55
SCAE TiZrN (ARCCO2)	0.081	2.51	3.46	2750	$\text{Ti}_{0.2}\text{Zr}_{0.8}\text{N}$	55
UBM TiZrN (UBMCO1)	0.060	2.00	3.18	3100	$\text{Ti}_{0.4}\text{Zr}_{0.6}\text{N}$	50
UBM TiZrN (UBMCO2)	0.065	2.08	3.35	2800	$\text{Ti}_{0.2}\text{Zr}_{0.8}\text{N}$	50
UBM TiZrN (UBMCO3)	0.065	2.08	3.47	3250	$\text{Ti}_{0.6}\text{Zr}_{0.4}\text{N}$	55
ABS TiZrN (ABSCO1)	0.070	2.31	3.45	3000	$\text{Ti}_{0.4}\text{Zr}_{0.6}\text{N}$	60
ABS TiZrN (ABSCO2)	0.072	2.32	3.42	2800	$\text{Ti}_{0.2}\text{Zr}_{0.8}\text{N}$	55
ABS TiZrN (ABSCO3)	0.070	2.31	3.46	3300	$\text{Ti}_{0.6}\text{Zr}_{0.4}\text{N}$	60

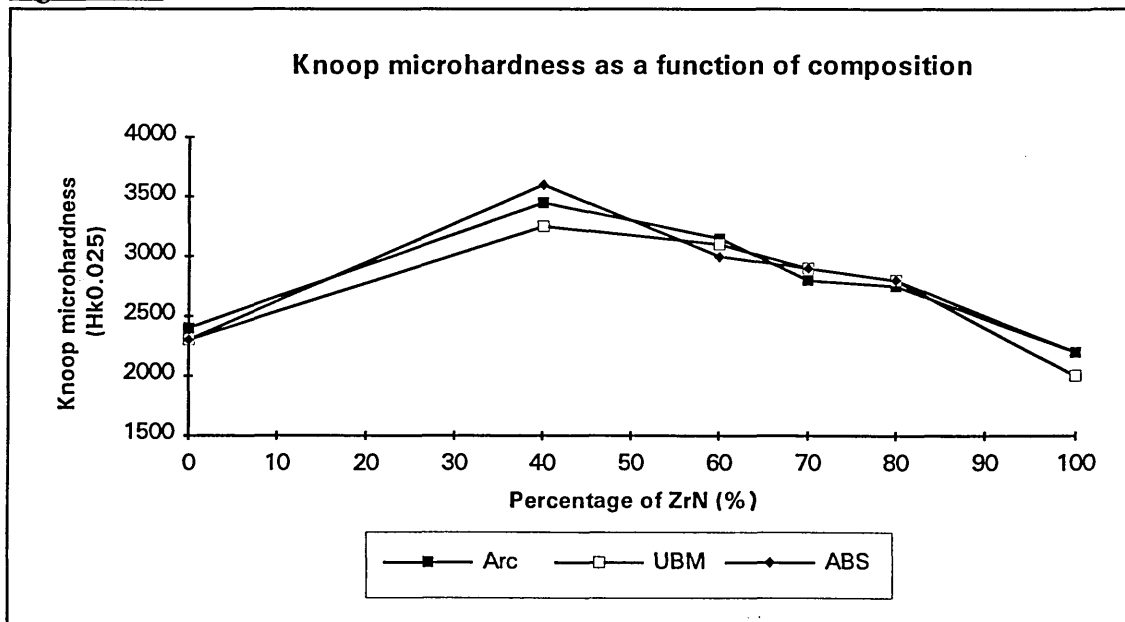
Where SEG indicates TiZr segmented target used to deposit the film.

Where CO indicates co-deposition from Ti & Zr pure metal targets.

Talysurf profiles across coated HSS substrates revealed several surface roughness trends. The highest  $R_a$ ,  $R_z$  and  $R_t$  values were always obtained from SCAE coatings deposited on static substrates and correlated well with the SEM investigations. The lowest surface roughness was developed from UBM coatings which were highly smooth, particularly when using the segmented target in static deposition mode. Comparison of static and rotating deposition shows that UBM and ABS  $R_a$  values were comparable but  $R_z$  and  $R_t$  values increased when the coating was co-sputtered. SCAE coatings exhibited a considerable decrease in surface roughness when rotational deposition was undertaken due to lower macro-particle incorporation in the growing film.

Knoop indentation measurements identified little change in coating hardness as a function of PVD processing technique; however, in all cases the  $Ti_xZr_yN$  films showed significantly higher hardness values when compared with either of the binary coatings deposited under equivalent process conditions. In general,  $Ti_xZr_yN$  coatings with near equal Ti : Zr ratios gave the highest hardness values (figure 5.17), demonstrated by the ABS  $Ti_{0.6}Zr_{0.4}N$  coating from the TiZr segmented target exhibiting  $\sim 3600H_k$ . This increased hardness in the ternary system was probably due to a solid solution strengthening mechanism which provided an energy barrier to the movement of dislocations throughout the crystals by distortion of the periodic lattice.

Figure 5.17.



L\*a\*b\* data indicated only small variations in film colour and lustre as a function of deposition technique (figure 5.18 and 5.19). ZrN coatings exhibited the highest L\* and the lowest a\* values of all coatings examined, whilst TiN showed the lowest L\* and the highest a\* values. Colour data recorded from  $Ti_xZr_yN$  coatings generally varied as a function of the metallic composition (x,y).

Figure 5.18

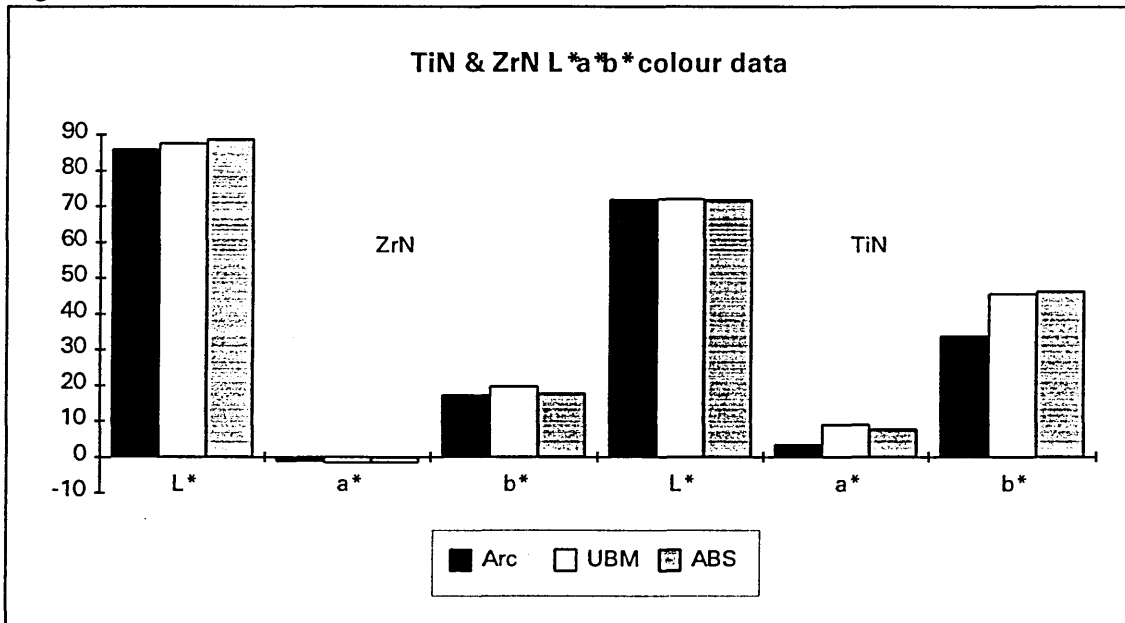
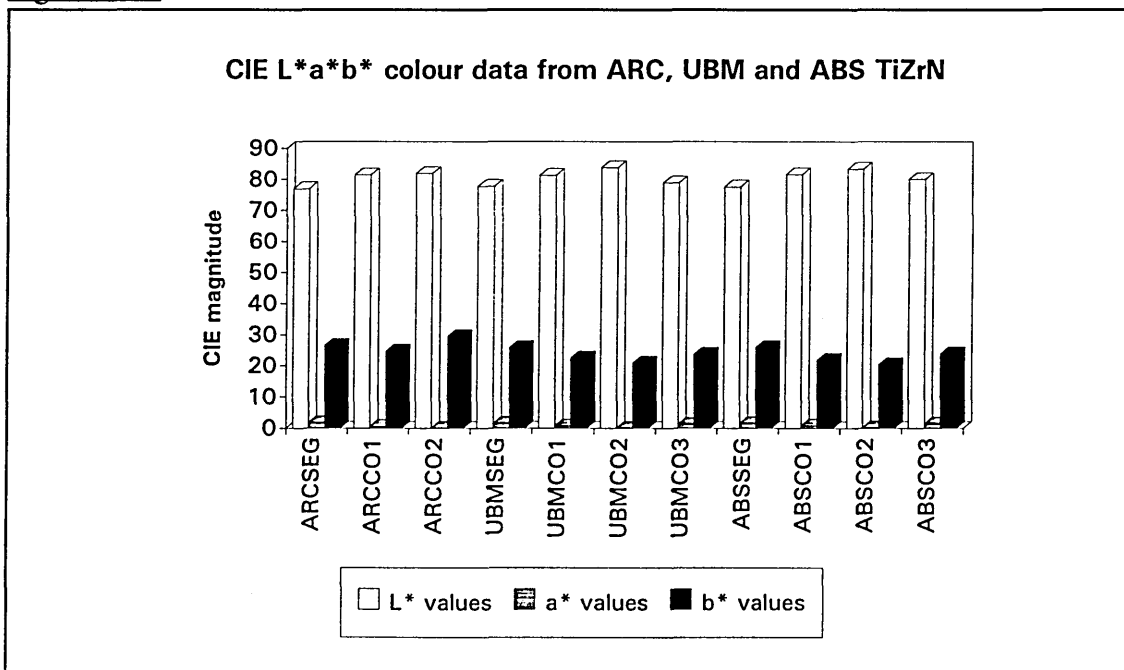


Figure 5.19.



## 5.2. Parameter study.

This section presents the results from a series of investigations on the influence of reactive gas pressure and substrate bias voltage on the mechanical and physical properties of  $Ti_xZr_yN$  coatings deposited by a static unbalanced magnetron sputtering technique (Leybold Z-700). The coating parameters were developed from a systematic 5x3 process matrix which comprised 5 different substrate bias voltages (ranging from 0 to -200V in increments of -50V) and 3 different  $N_2$  pressures (figure 5.20), whilst all other deposition conditions remained constant (table 5.5). High speed steel and stainless steel substrates were cleaned and degreased using the standard method (section 3.3) and mounted on assemblies which could be rotated around the perimeter of the chamber to positions directly in front of a radiant heater, a double cathode glow discharge etching source or the circular unbalanced magnetron sputter coating source at a target to substrate distance of 80mm.

Figure 5.20. 5x3 process parameter matrix.

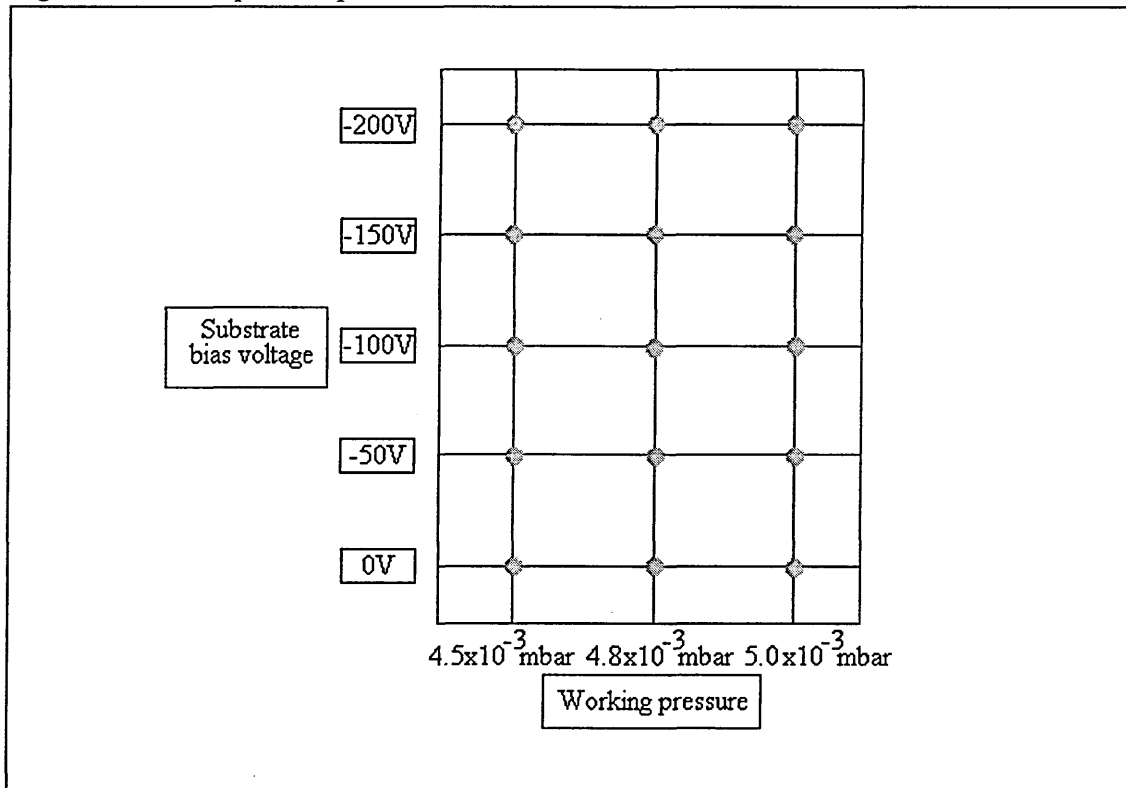


Table 5.5

<b>Static Ti<sub>x</sub>Zr<sub>y</sub>N unbalanced magnetron sputter process parameters (Z-700)</b>
<p><u>(1) Chamber pump down and radiant heating</u>            Substrates rotated directly in front of heaters            Time = 75 mins            Pressure = <math>&lt; 1 \times 10^{-5}</math> mbar            Temperature = 350°C</p>
<p><u>(2) Glow discharge target cleaning</u>            Substrates rotated through 270°            Shutter directly in front of target            Substrate bias voltage = 0V            Power = 1KW            Ar flow = 150sccm            Pressure = <math>\sim 4 \times 10^{-3}</math> mbar            Time = 5 mins            Temperature = 300°C</p>
<p><u>(3) Glow discharge substrate ion etching</u>            Substrates rotated through 270°            Substrates directly between double magnetron cathodes            Power = 0.15KW            Ar flow = 300sccm            Substrate bias voltage = -1000V            Time = 10mins            Pressure = <math>\sim 6 \times 10^{-3}</math> mbar            Temperature = 350-400°C</p>
<p><u>(4) Unbalanced magnetron sputtered metal interlayer deposition</u>            Substrates rotated through 270°            Substrates directly in front of circular unbalanced magnetron source            Power = 1.1KW            Ar flow = 150sccm            Time = 2mins            Substrate bias voltage = 0 to -200V            Pressure = <math>\sim 4.5 \times 10^{-3}</math> mbar            Temperature = 350°C</p>
<p><u>(5) Unbalanced magnetron reactive sputter deposition</u>            Substrate position as in stage 4            Power = 1.1KW            Ar flow = 150sccm            Quadrupole RGA partial pressure control ion probe current = <math>0.8 - 3.2 \times 10^{-10}</math> A            N<sub>2</sub> flow = 9-22sccm            Time = 30mins            Substrate bias voltage = 0 to -200V            Pressure = <math>\sim 4.5 \times 10^{-3}</math> mbar - <math>\sim 5 \times 10^{-3}</math> mbar            Temperature = 350°C</p>

### 5.2.1 X-ray diffraction results.

All coatings were found to exhibit a single phase face centred cubic NaCl type structure with unit cell parameters ( $a_0$ ) which varied as a function of substrate bias voltage and nitrogen gas flow (figures 5.21a-c).

In general, films deposited using the lowest nitrogen gas pressure showed the smallest lattice parameters, coatings fabricated using the intermediate gas pressure showed modest increases over its low pressure equivalent, whilst films deposited at the highest nitrogen pressure exhibited the largest unit cell dimensions.

Figure 5.21a. X-ray diffraction analysis of  $Ti_xZr_yN$  (9sccm  $N_2$ ,  $4.5 \times 10^{-3}$  mbar)

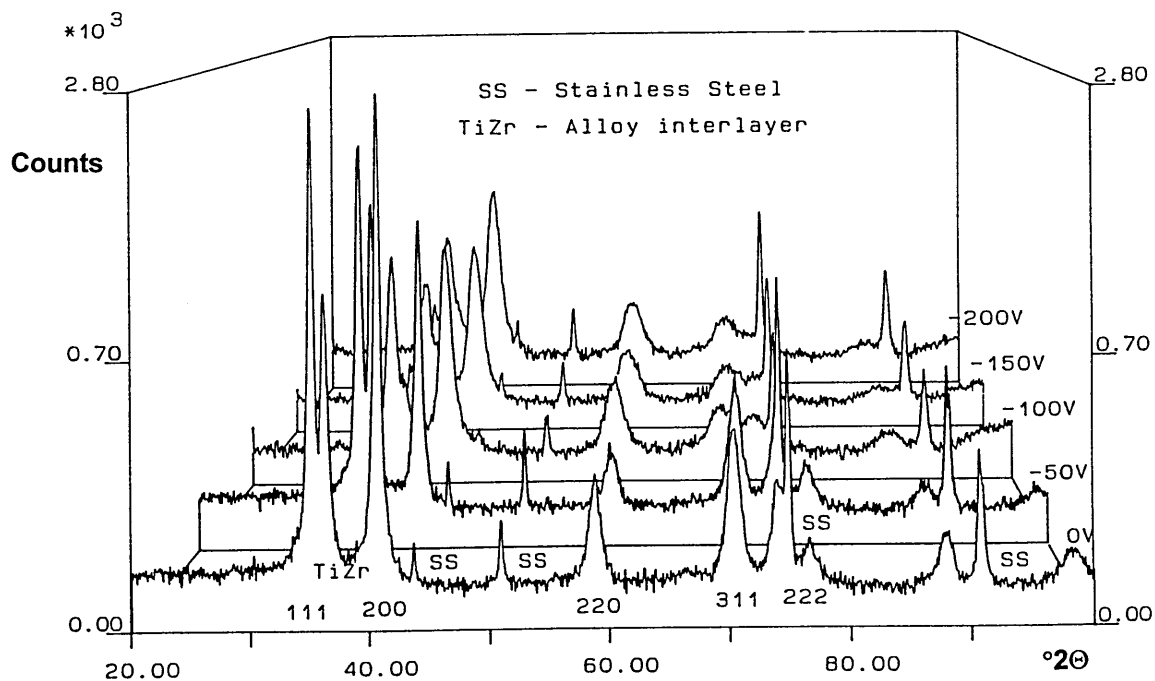
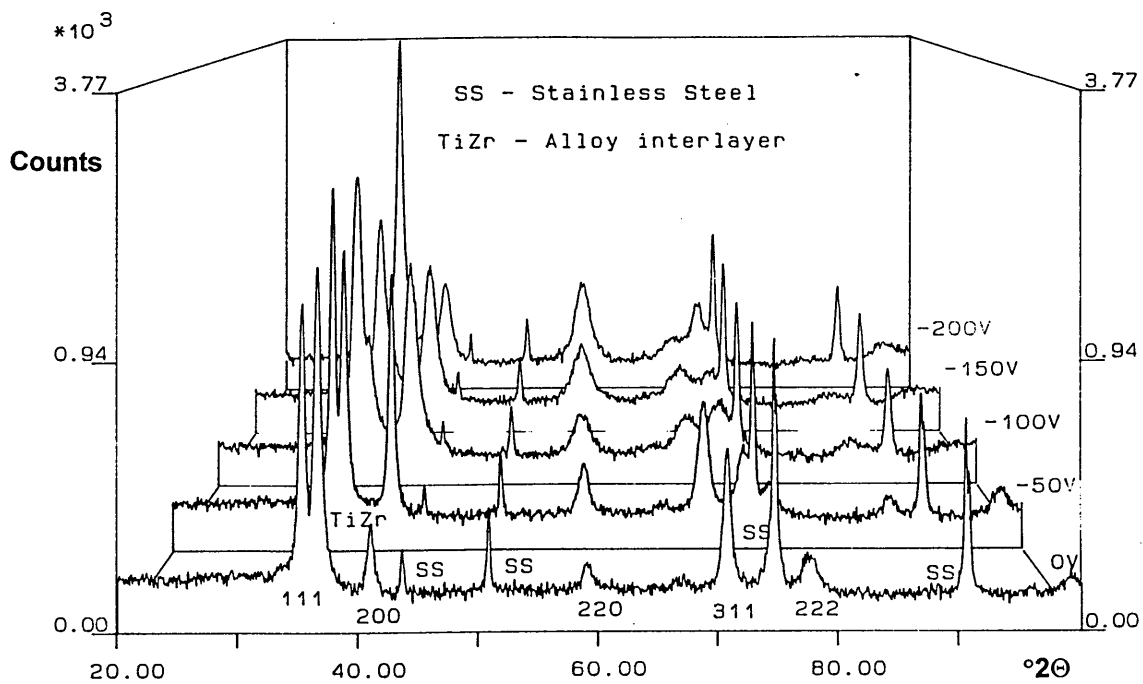
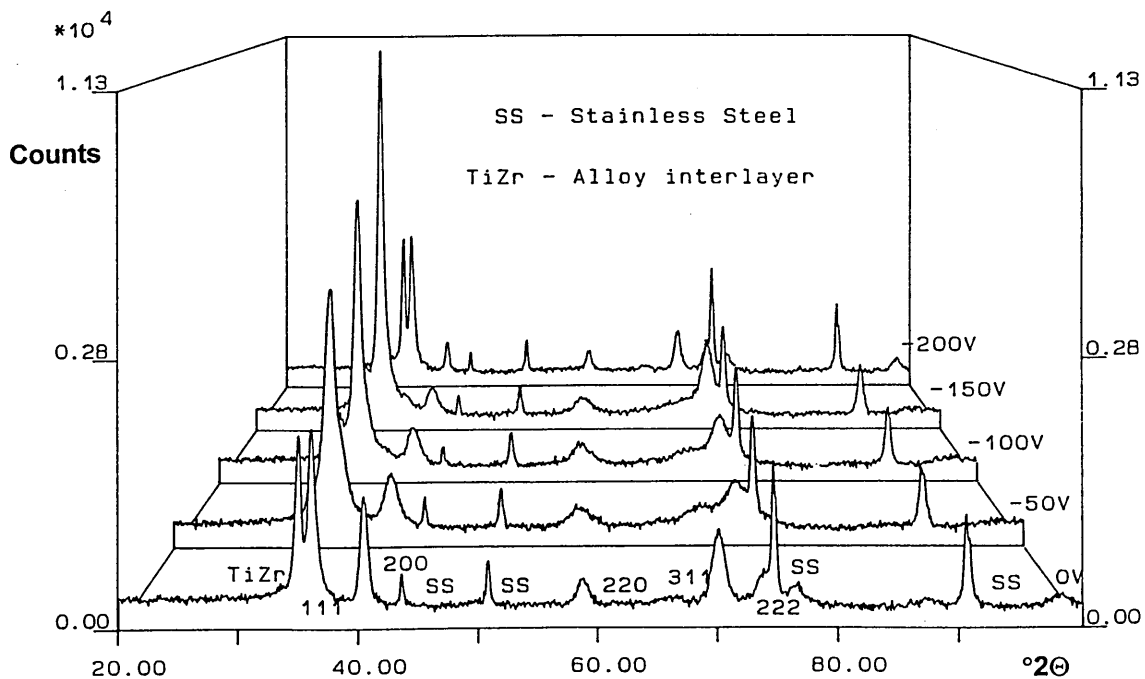


Figure 5.21b. X-ray diffraction analysis of  $Ti_xZr_yN$  (15sccm  $N_2$ ,  $4.8 \times 10^{-3}$  mbar)Figure 5.21c. X-ray diffraction analysis of  $Ti_xZr_yN$  (22sccm  $N_2$ ,  $5 \times 10^{-3}$  mbar)

All coatings demonstrated an increase in unit cell dimension as a function of increasing substrate bias voltage from 0-150V caused by an increase in the level of energetic ion bombardment during film growth which provided greater lattice expansion and an increase in compressive residual stress (figure 5.22). However for films deposited with intermediate and high reactive gas pressures at a substrate bias voltage of -200V, the level of adatom mobility, re-sputtering rate and ion bombardment became excessive, producing coating annealment, a reduction in compressive stress and a decrease in lattice parameter.

The texture and lattice strain of the  $Ti_xZr_yN$  coatings was also found to be strongly influenced by combination of substrate bias voltage and nitrogen gas pressure. Coatings produced at the lowest nitrogen gas pressure ( $4.5 \times 10^{-3}$  mbar & 9 sccm  $N_2$  flow) generally exhibited a  $\langle 100 \rangle$  preferred orientation which generally became stronger with increasing negative substrate bias voltage (table 5.6). These deposition conditions correspond to the greatest metal vapour flux, the most metallic film nature and energetic ion impingement on the substrate surface. At increased nitrogen pressures, the films always showed a preferred orientation in the  $\langle 111 \rangle$  direction which became strongest in coatings deposited at  $5 \times 10^{-3}$  mbar (22 sccm  $N_2$  flow).

Figure 5.22.

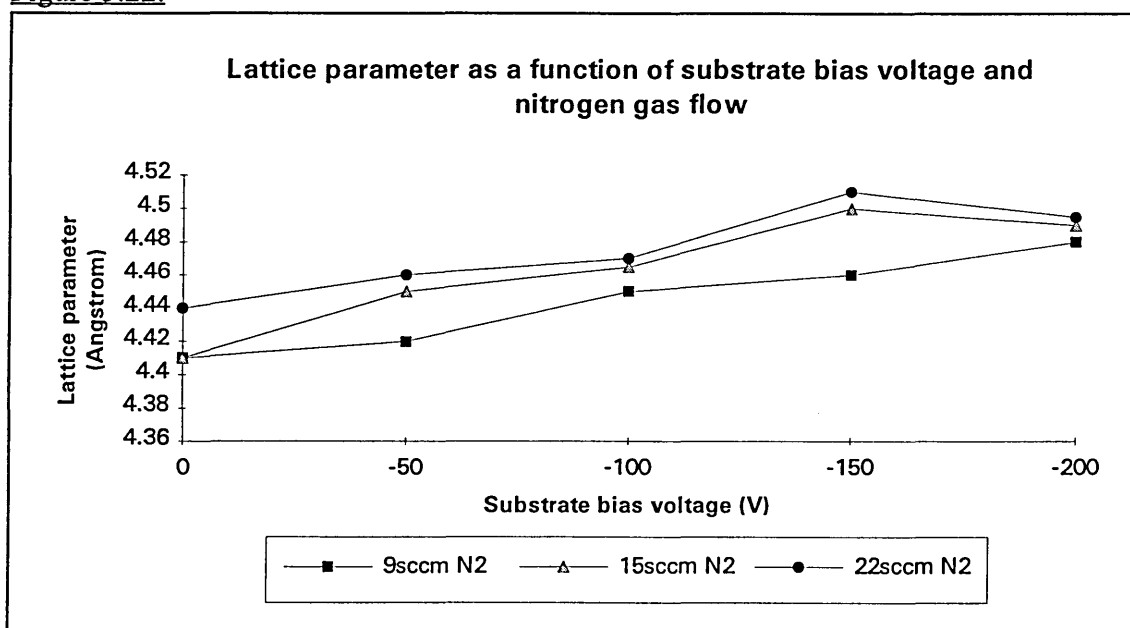
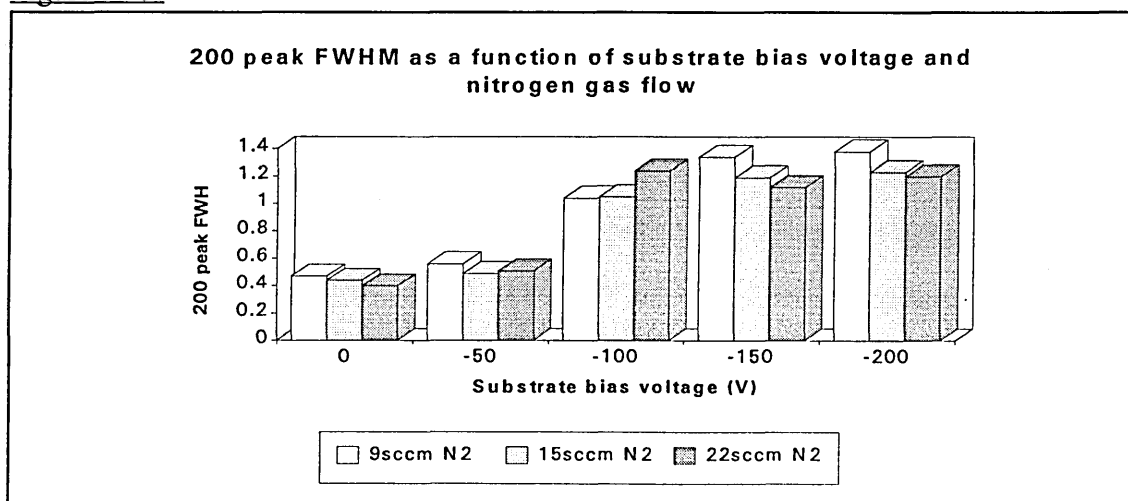


Table 5.6.  $Ti_xZr_yN$  parameter study relative intensity and structure data

$Ti_xZr_yN$ coating parameters	111 (%)	200 (%)	220 (%)	311 (%)	Structure
0V 9sccm $N_2$	91.7	100	6.2	13.3	f.c.c.
-50V 9sccm $N_2$	100	68.4	4.3	14.7	f.c.c.
-100V 9sccm $N_2$	94.3	100	14.5	5.0	f.c.c.
-150V 9sccm $N_2$	60.4	100	20.2	12.4	f.c.c.
-200V 9sccm $N_2$	55.0	100	23.3	5.6	f.c.c.
0V 15sccm $N_2$	100	7.0	1.9	22.9	f.c.c.
-50V 15sccm $N_2$	100	58.2	5.1	15.3	f.c.c.
-100V 15sccm $N_2$	100	48.7	6.0	5.3	f.c.c.
-150V 15sccm $N_2$	100	60.2	11.4	4.6	f.c.c.
-200V 15sccm $N_2$	100	7.5	6.7	0.4	f.c.c.
0V 22sccm $N_2$	100	45.2	4.7	25.8	f.c.c.
-50V 22sccm $N_2$	100	6.8	1.3	0.6	f.c.c.
-100V 22sccm $N_2$	100	2.7	1.7	0.5	f.c.c.
-150V 22sccm $N_2$	100	0.9	0.8	0.3	f.c.c.
-200V 22sccm $N_2$	100	8.1	4.0	12.1	f.c.c.

Full width at half maximum analysis on (200) reflections [(200) chosen as TiZr interlayer peaks often caused interference with  $Ti_xZr_yN$  (111) reflection] showed that the largest peak widths (fig 5.23) were generally exhibited by the low pressure, under stoichiometric films which exhibited  $\langle 100 \rangle$  preferred orientation. Peak widths were also generally found to significantly increase as a function of increasing bias voltage.

Figure 5.23.



### 5.2.2. GDOES results.

Quantified GDOES analysis of the 15  $Ti_xZr_yN$  films revealed that coatings deposited at the lowest reactive gas pressure ( $4.5 \times 10^{-3}$  mbar &  $N_2$  flow  $\sim 9$  sccm) were slightly sub-stoichiometric, films deposited at the intermediate gas pressure ( $4.8 \times 10^{-3}$  mbar &  $N_2$  flow  $\sim 15$  sccm) were stoichiometric and coatings processed at the high gas pressure ( $5 \times 10^{-3}$  mbar &  $N_2$  flow  $\sim 22$  sccm) were slightly over stoichiometric (figure 5.24a-c). In general, all coatings showed a small degree of surface porosity and low level oxygen ingress, whilst the alloy interlayer deposited prior to reactive deposition was  $\sim 0.5 \mu\text{m}$  thick.

Figure 5.24a. GDOES depth profile of  $Ti_xZr_yN$  (-100V, 9sccm  $N_2$ ) on HSS.

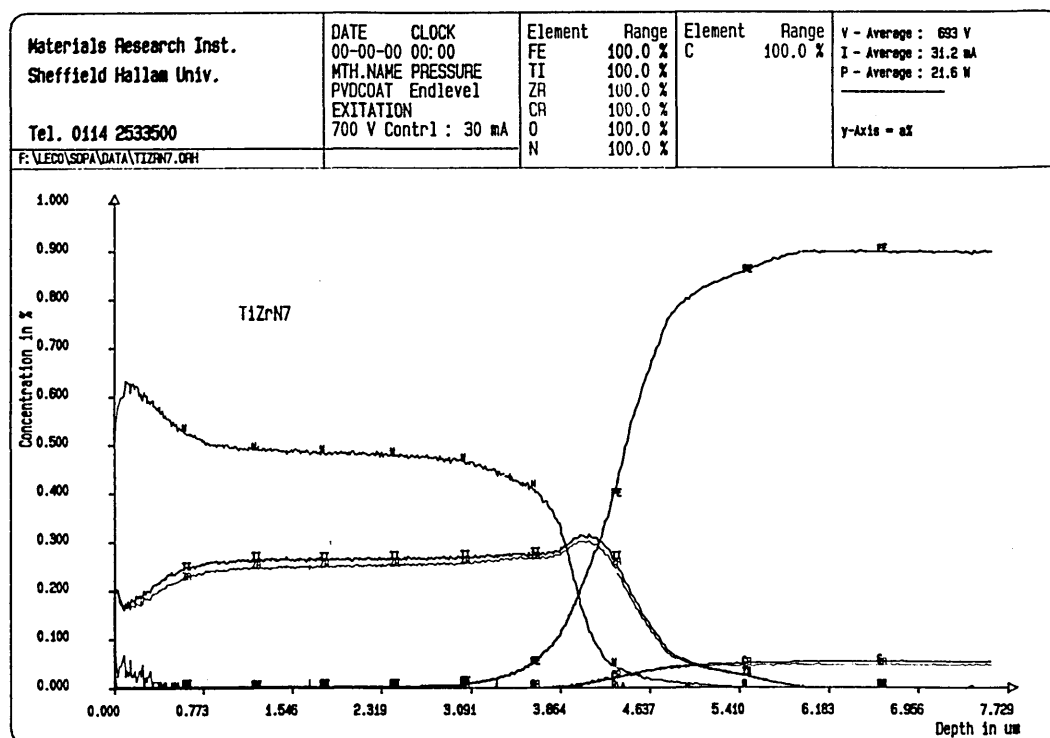


Figure 5.24b. GDOES depth profile of  $Ti_xZr_yN$  (-100V, 15sccm  $N_2$ ) on HSS.

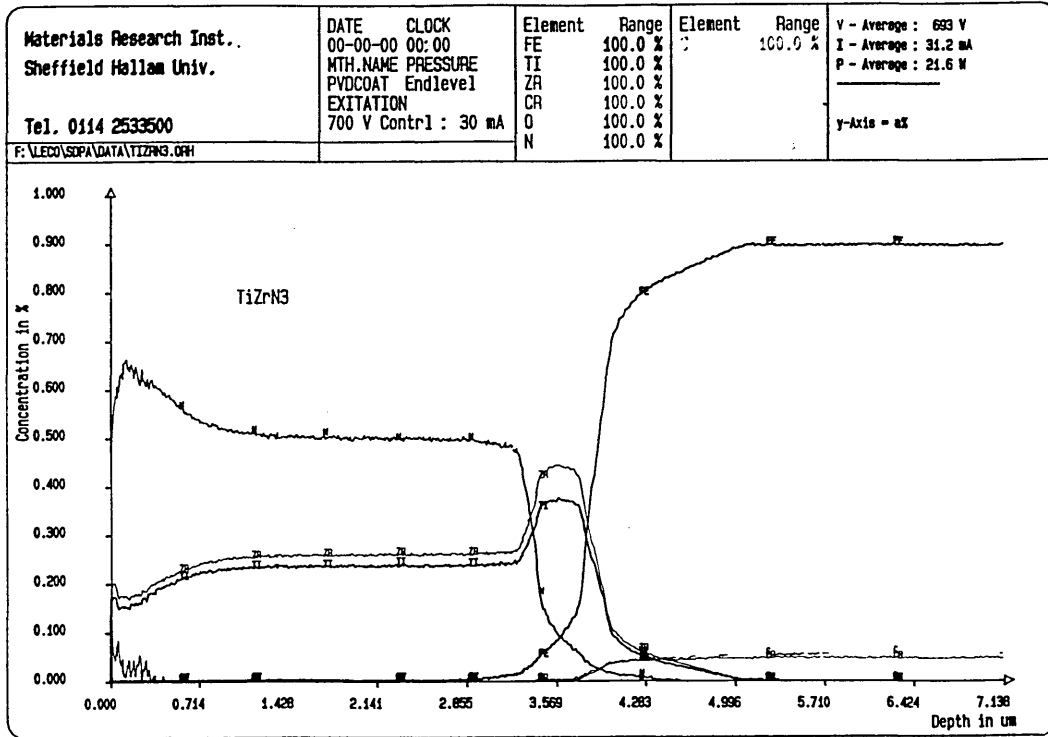
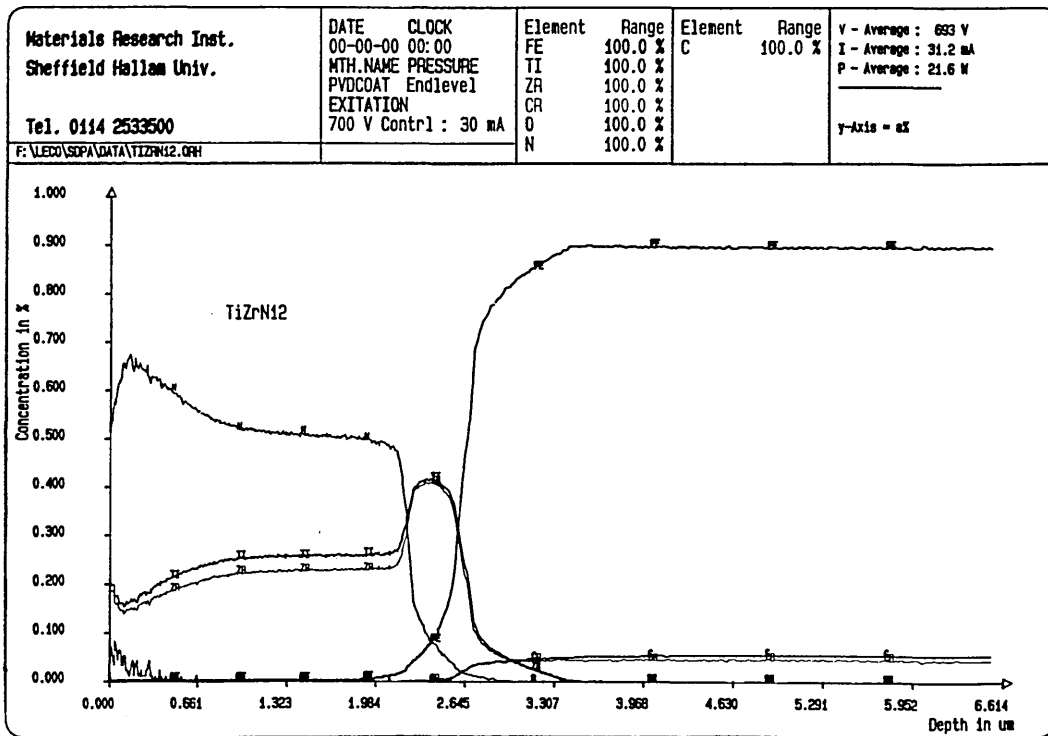


Figure 5.24c. GDOES depth profile of  $Ti_xZr_yN$  (-100V, 22sccm  $N_2$ ) on HSS.



The composition and thickness (measured at the mid point of the coating and iron profiles) of the films was found to be dependent on the level of substrate bias voltage and reactive gas pressure. The Zr content in both the interlayer and ceramic portions of the films increased as a function of increasing bias voltage such that at 0V bias the alloy composition was Ti rich whilst at bias greater than -100V the system became Zr rich. The film thickness decreased as a function of increasing bias voltage and gas pressure due to enhanced densification, increased re-sputtering and cathode poisoning effects (figures 5.25-5.30).

Figure 5.25. GDOES depth profile of  $Ti_xZr_yN$  (0V, 9sccm  $N_2$ ) on HSS.

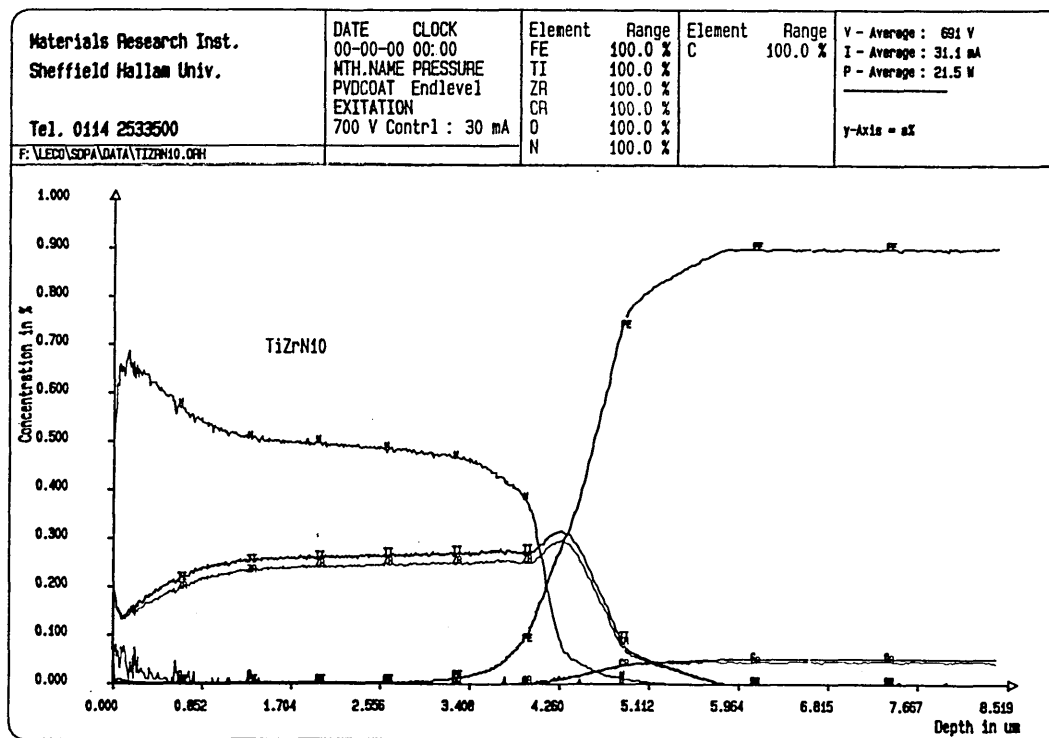


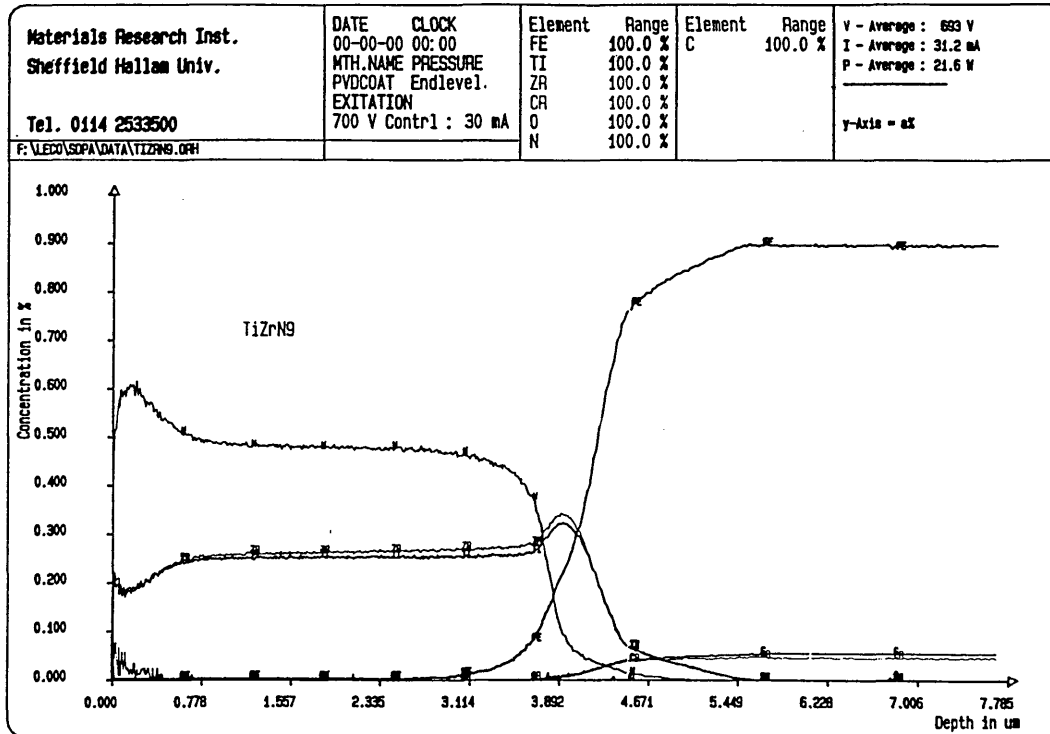
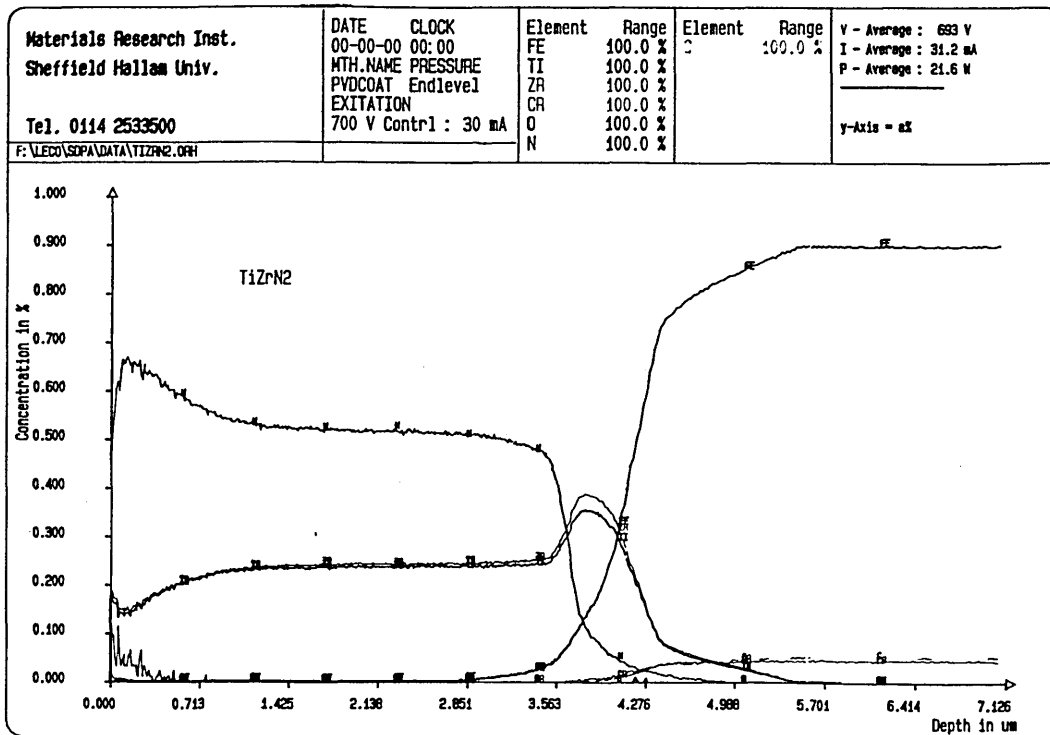
Figure 5.26. GDOES depth profile of  $Ti_xZr_yN$  (-200V, 9sccm  $N_2$ ) on HSS.Figure 5.27. GDOES depth profile of  $Ti_xZr_yN$  (0V, 15sccm  $N_2$ ) on HSS.

Figure 5.28. GDOES depth profile of  $Ti_xZr_yN$  (-200V, 15sccm  $N_2$ ) on HSS.

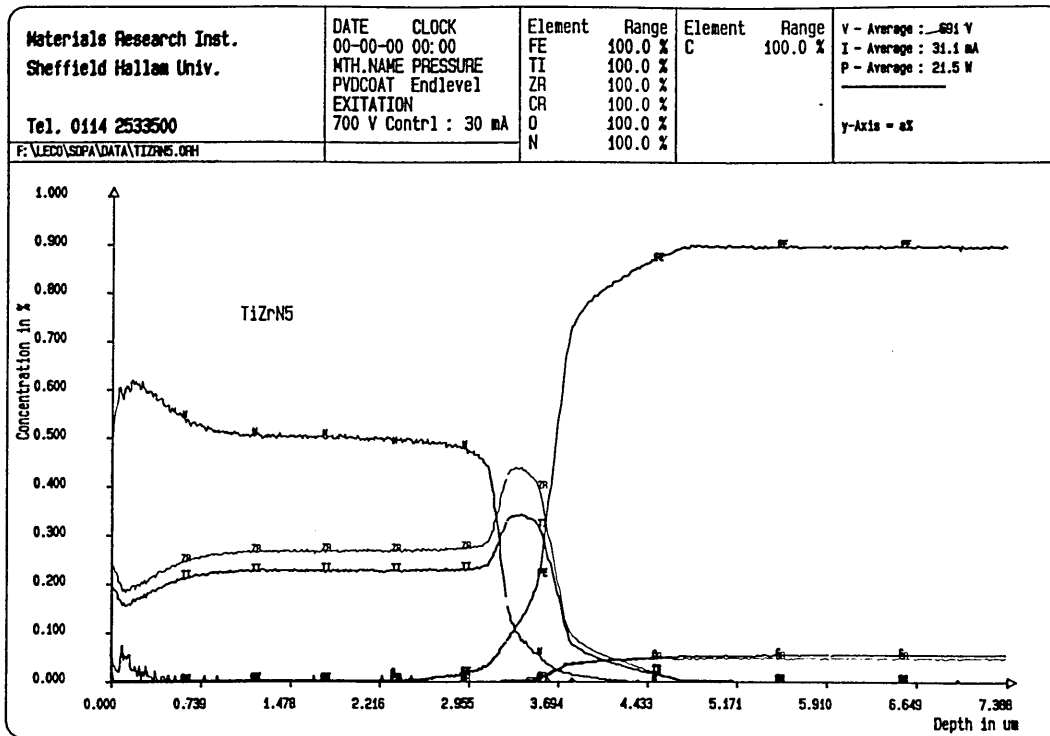


Figure 5.29. GDOES depth profile of  $Ti_xZr_yN$  (0V, 22sccm  $N_2$ ) on HSS.

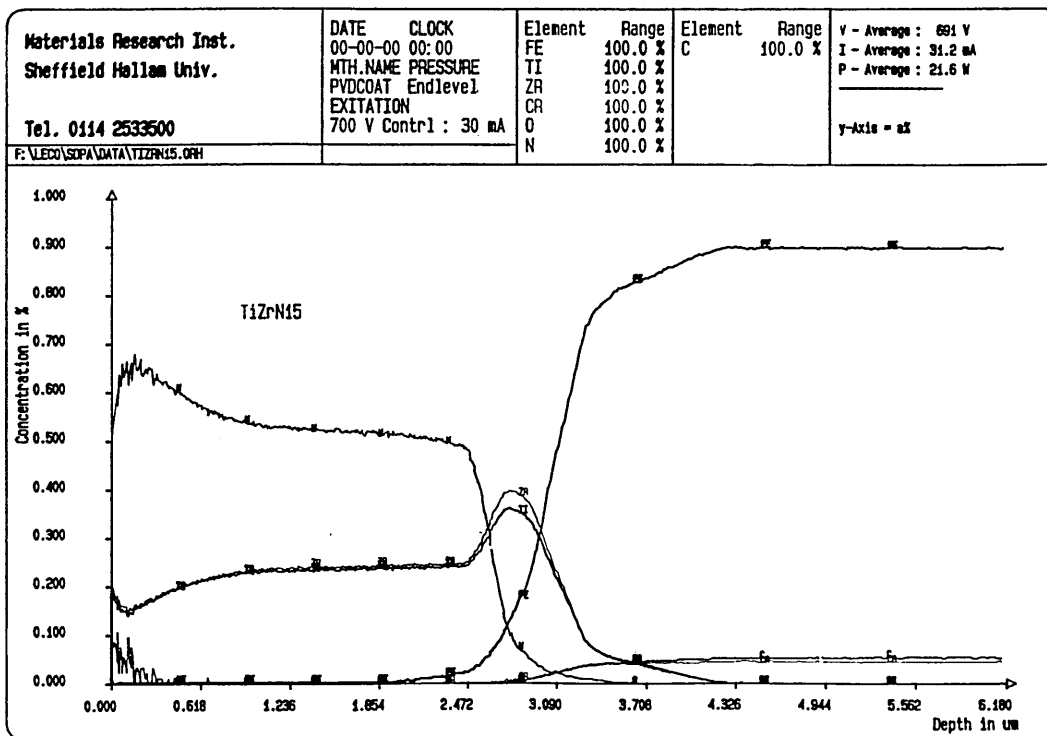
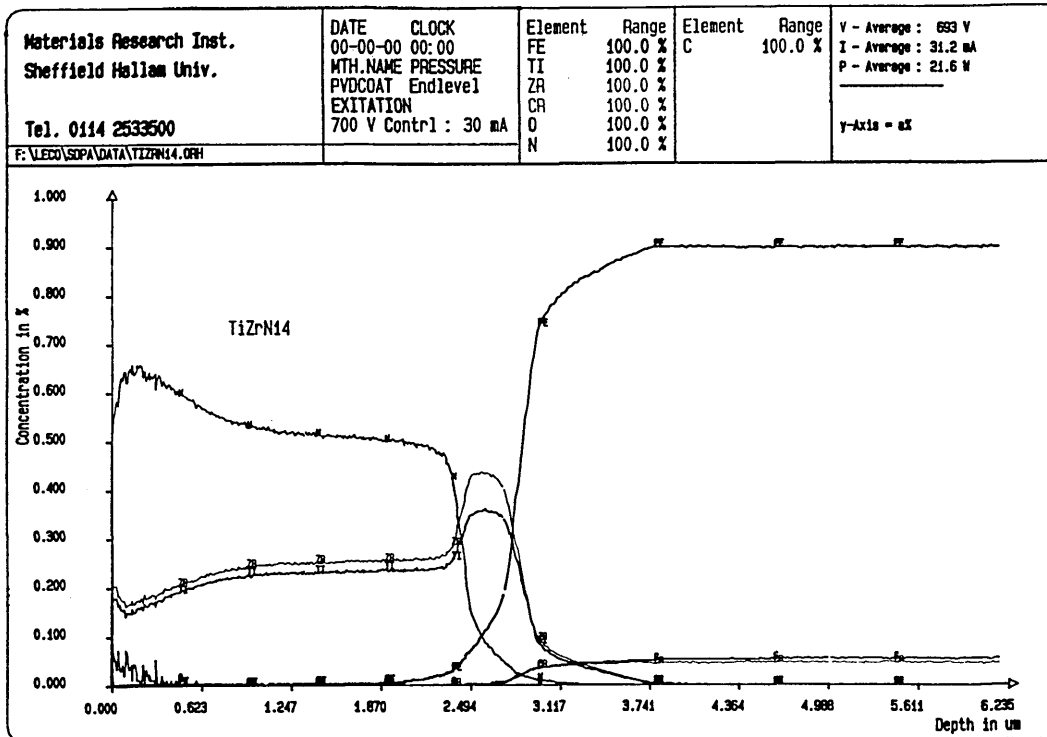


Figure 5.30. GDOES depth profile of Ti<sub>x</sub>Zr<sub>y</sub>N (-200V, 22sccm N<sub>2</sub>) on HSS.

The coating thickness values were found to be in good agreement with calotest values, where any discrepancies originated from depth resolution limits of the GDOES instrument (non-uniform analysis crater shape, surface roughness effects and high nitrogen composition standardisation).

### 5.2.3. Scanning electron microscopy results.

All films in cross-section appeared columnar and generally exhibited zone-T structures (figures 5.31-5.39). However, coatings deposited without bias (0V) appeared the most columnar (zone-1), porous and roughest of all coatings examined within the parameter study. The density, surface finish and porosity of the coatings was found to significantly improve at bias potentials between -50V and -150V, whilst coatings deposited at -200V became rougher as a result of excessive ion bombardment and re-sputtering effects. At high nitrogen partial pressures a tendency to produce more columnar structures was also observed due to an increase gas scattering and energy loss collisions.

Figure 5.31.  $Ti_xZr_yN$  (0V, 9sccm  $N_2$ ).

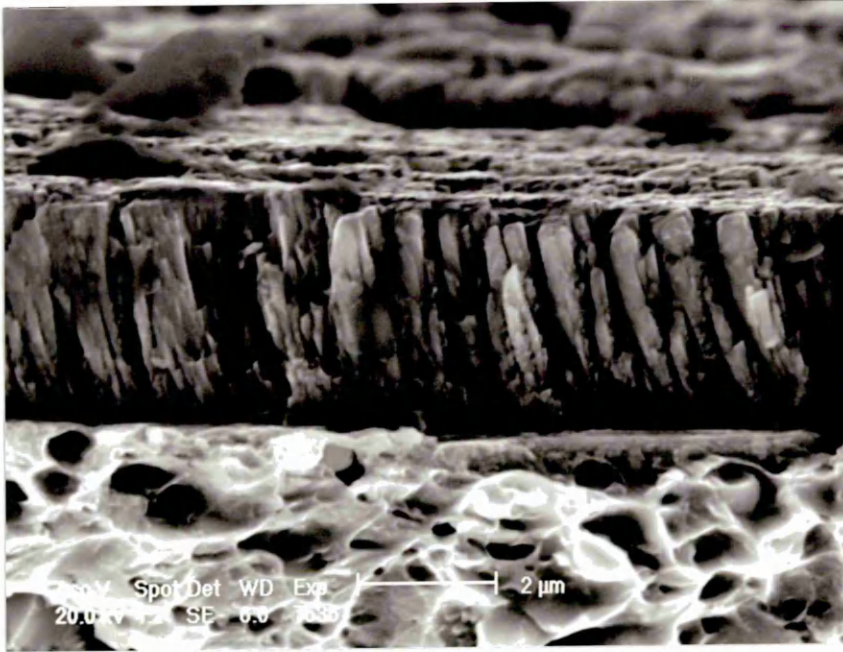


Figure 5.32.  $Ti_xZr_yN$  (-100V, 9sccm  $N_2$ ).

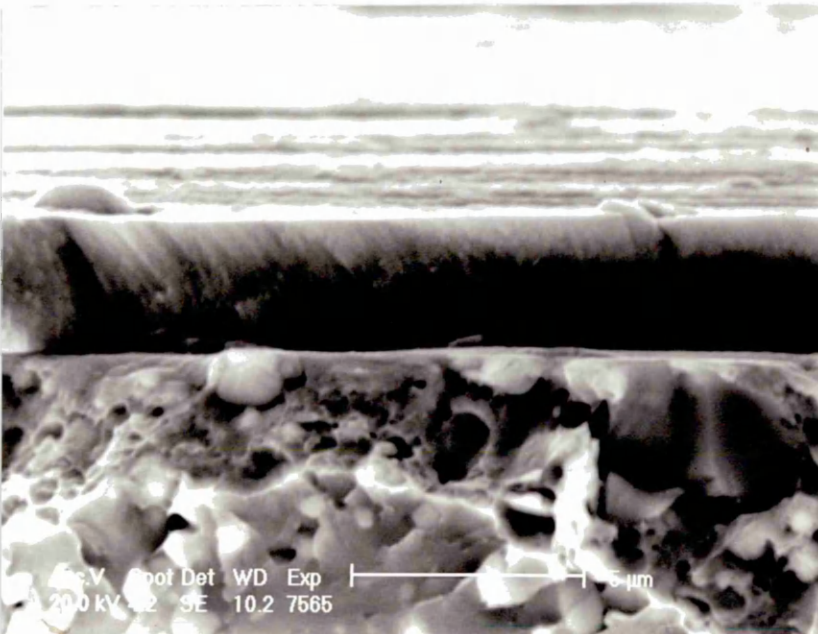


Figure 5.33.  $Ti_xZr_yN$  (-200V, 9sccm  $N_2$ ).

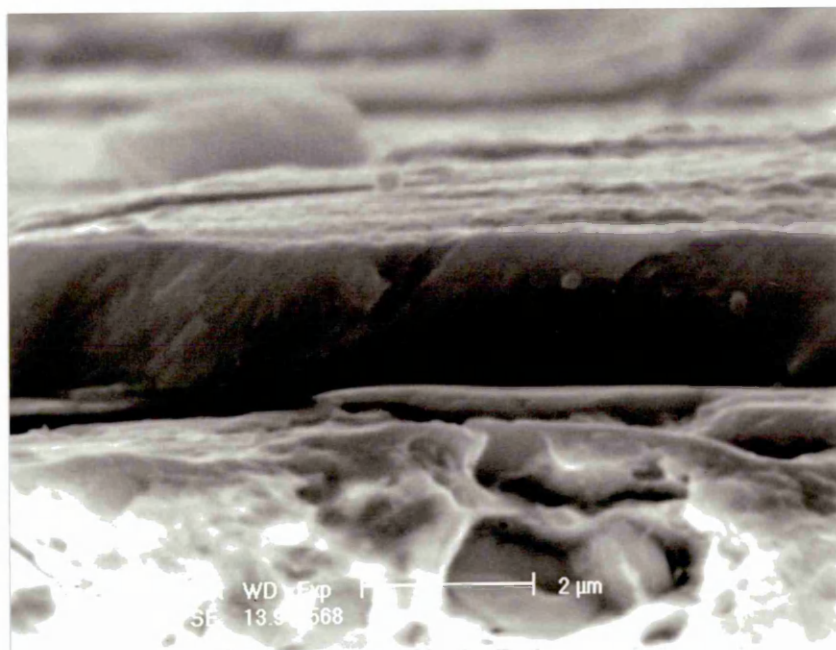


Figure 5.34.  $Ti_xZr_yN$  (0V, 15sccm  $N_2$ ).

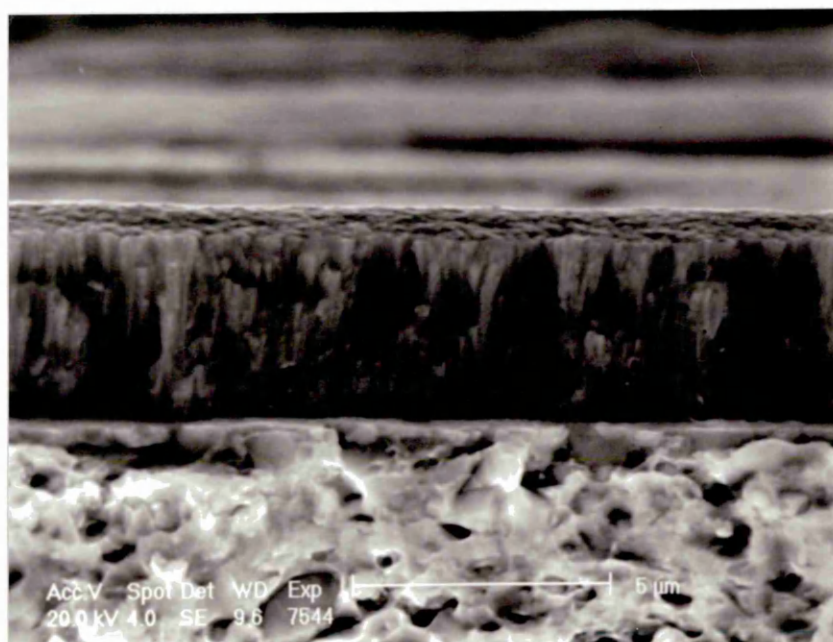


Figure 5.35.  $Ti_xZr_yN$  (-100V, 15sccm  $N_2$ ).

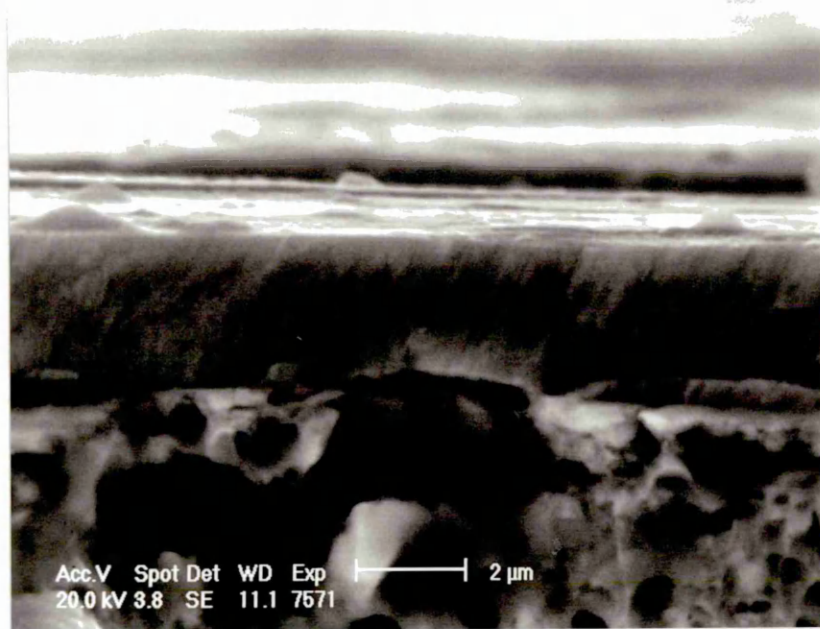


Figure 5.36.  $Ti_xZr_yN$  (-200V, 15sccm  $N_2$ ).

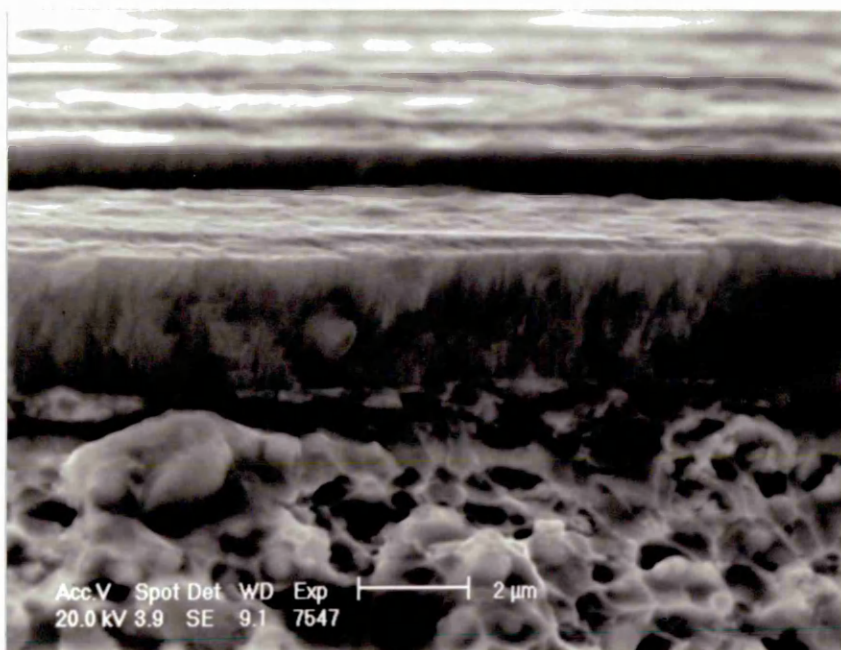


Figure 5.37.  $Ti_xZr_yN$  (0V, 22sccm  $N_2$ ).

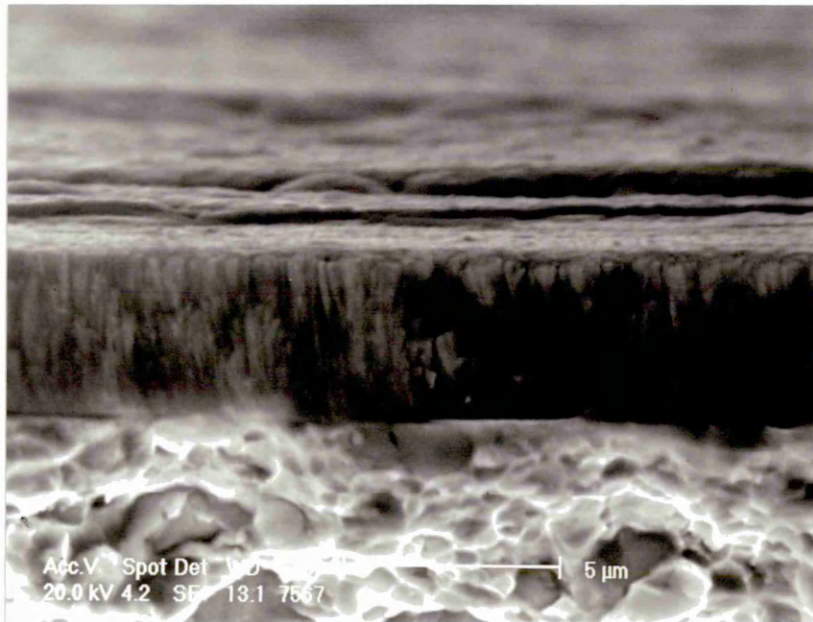


Figure 5.38.  $Ti_xZr_yN$  (-100V, 22sccm  $N_2$ ).

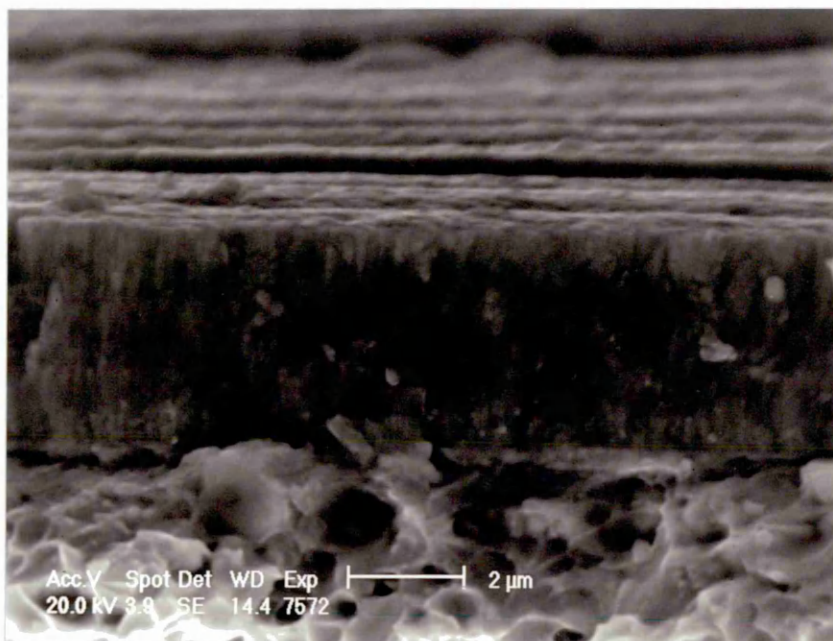
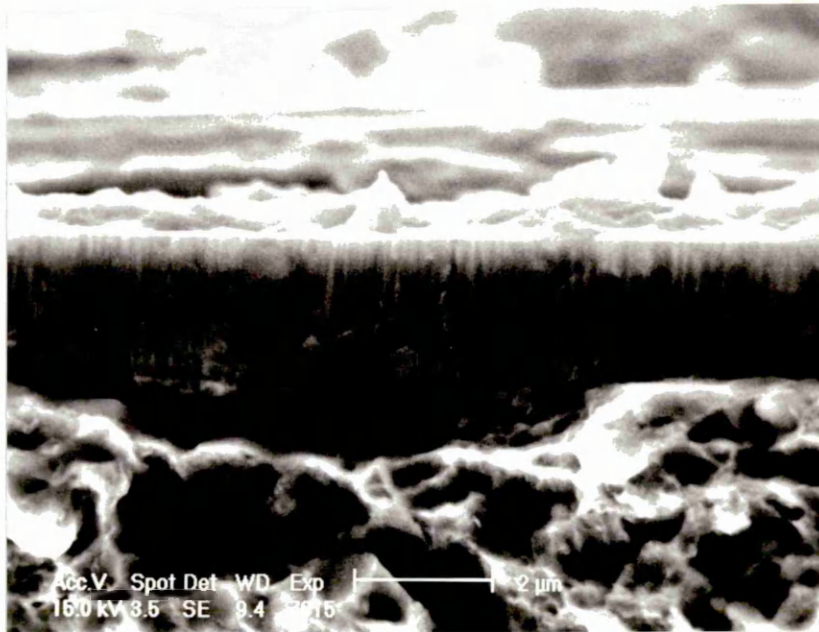


Figure 5.39.  $Ti_xZr_yN$  (-200V, 22sccm  $N_2$ ).



#### 5.2.4. Mechanical and physical properties.

All coatings exhibited satisfactory Rockwell-C indentation when related against the VDI criteria at 100 times magnification (table 5.7). Surprisingly, the worst indents were observed on films which were approximately stoichiometric at high or no substrate bias voltage (0V and -200V), whilst the best adhesion results were found on films which were slightly over-stoichiometric. Scratch testing showed that all coatings failed via a brittle fracture mechanism, with the lowest critical loads again recorded on the approximately stoichiometric, high or no substrate bias voltage films.

The coating hardness was found to be lowest in films deposited at 0V bias due to the lack of energetic ion bombardment during growth which caused the formation of an open, porous structure. The application of a negative bias voltage created significant film densification which resulted in substantial increases in Knoop hardness, typically in the range 3300-3700H<sub>k</sub>, comparable with results found in section 5.1.4 for films of similar composition. However, coatings deposited at -200V exhibited a reduction in hardness due to excessive ion bombardment and annealing effects, whilst stoichiometric and slightly overstoichiometric films were generally harder when compared against substoichiometric coatings.

Table 5.7.

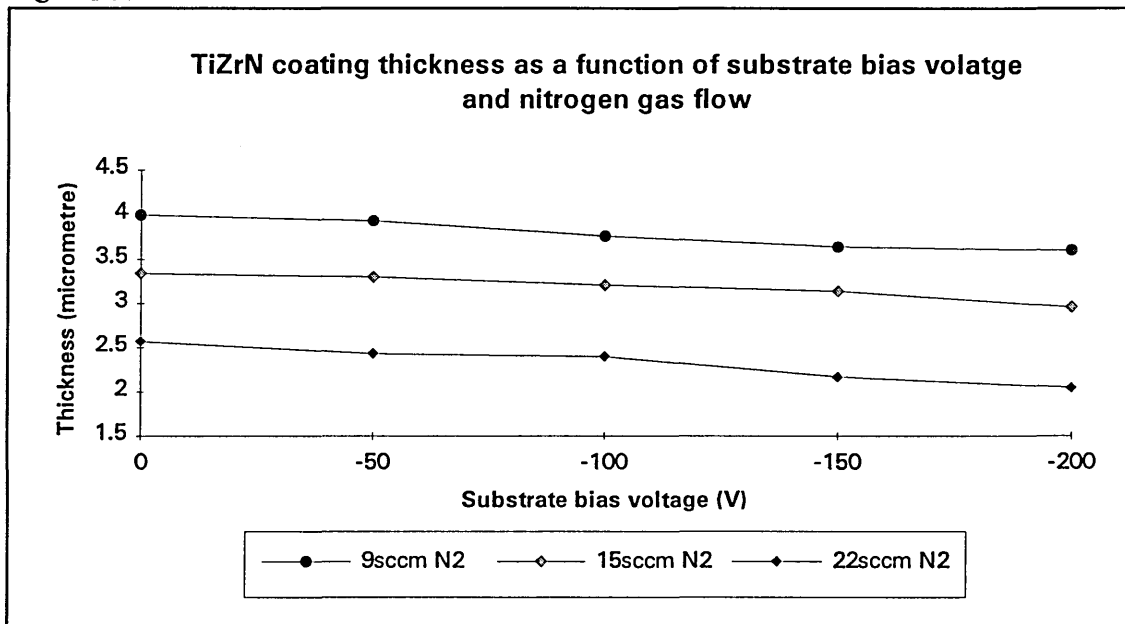
Coating	Rockwell quality	$L_c / N$ $\pm 2N$	$H_{k0.025}$ $\pm 300 \text{Kgmm}^{-2}$	$L^*$ $\pm 0.1$	$a^*$ $\pm 0.1$	$b^*$ $\pm 0.1$	$R_a / \mu\text{m}$ $\pm 0.01$
0V 9sccm $N_2$	1-2	50	2450	68.37	4.84	26.83	0.039
-50V 9sccm $N_2$	1-2	60	3440	74.77	3.63	28.19	0.027
-100V 9sccm $N_2$	1-2	60	3560	74.80	3.45	26.74	0.027
-150V 9sccm $N_2$	1-2	50	3545	75.77	2.90	25.67	0.029
-200V 9sccm $N_2$	1-2	45	3380	75.80	2.69	24.90	0.039
0V 15sccm $N_2$	2-3	40	2550	66.18	6.19	26.04	0.036
-50V 15sccm $N_2$	1-2	60	3530	72.86	5.24	29.37	0.023
-100V 15sccm $N_2$	1-2	50	3765	73.16	5.19	30.34	0.022
-150V 15sccm $N_2$	1-2	50	3735	73.98	5.04	30.58	0.022
-200V 15sccm $N_2$	2-3	45	3600	72.25	5.69	30.21	0.040
0V 22sccm $N_2$	1	50	2410	66.08	7.76	25.14	0.033
-50V 22sccm $N_2$	1	60	3480	71.08	6.43	27.70	0.025
-100V 22sccm $N_2$	1	60	3700	71.29	6.94	29.60	0.024
-150V 22sccm $N_2$	1	50	3720	72.22	6.96	29.65	0.029
-200V 22sccm $N_2$	1	45	3300	70.07	7.93	27.59	0.033

The surface roughness of all coatings was found to be very low, with  $R_a$  values considerably smaller than typical ABS or steered arc evaporated coatings. The highest surface roughness was demonstrated by 0V and -200V bias films due to the production of open porous structures and excessive re-sputtering and ion bombardment respectively.

Several trends could be detected from colour measurements performed during the trials. The lowest  $L^*$  values were recorded on the 0V bias films due to the formation of a porous, open columnar structure through the removal of energetic ion bombardment during deposition. Reduced  $L^*$  data could also be recorded on high bias, high  $N_2$  flow films due to excessive ion bombardment and target poisoning effects. The  $L^*$  value (brightness) was found to steadily increase as a function of increasing bias voltage, whilst the  $a^*$  (red-green) values generally decreased as the films became less red and more zirconium rich. The yellow levels ( $b^*$  = blue-yellow) within the films also increased with the use of a substrate bias voltage.

Coating thickness data generated using the calotest confirmed that all coatings reduced in thickness as a function of increasing substrate bias voltage and gas pressure as indicated in the GDOES analysis (figure 5.40).

Figure 5.40.



### 5.3. Investigation of the TiAlZrN system.

Research has shown that although the oxidation resistance of TiAlN coatings decreased if zirconium was incorporated as a substitute for aluminium (1), substantial increases in microhardness could be achieved making the film of academic and commercial interest (2). However, adhesion problems encountered during these earlier trials could only be satisfactorily resolved on cemented carbide substrates whilst films deposited on HSS were consistently inferior. This section reports on TiAlZrN coatings deposited on HSS and stainless steel substrates by ABS technology and examines their mechanical and physical properties and any improvements in film adhesion developed by a steered arc etching pre-coating stage and the deposition of a magnetron sputtered graded base layer.

#### 5.3.1. Experimental conditions.

A single HTC 1000-4 ABS unit was used to deposit all coatings in the trial and for this study 600 x 190 x 12mm targets were used for co-sputter deposition processing of the following compositions:-

3 Ti<sub>0.5</sub>Al<sub>0.5</sub> produced by a powder metallurgical route (section 3.2).

1 Zr grade 702 (purity >99.6%).

The reactive gas used was nitrogen (purity 99.999%) and the working gas used to sputter the targets or aid arc ignition was argon (purity 99.999%). Gas flow was controlled via a proportional integrating differential (P.I.D) controller with feedback to total pressure whilst the argon flow was kept constant. The reactive gas partial pressure required during deposition was determined from a nitrogen gas flow against total pressure hysteresis measurement (figure 5.41a&b).

Figure 5.41a.

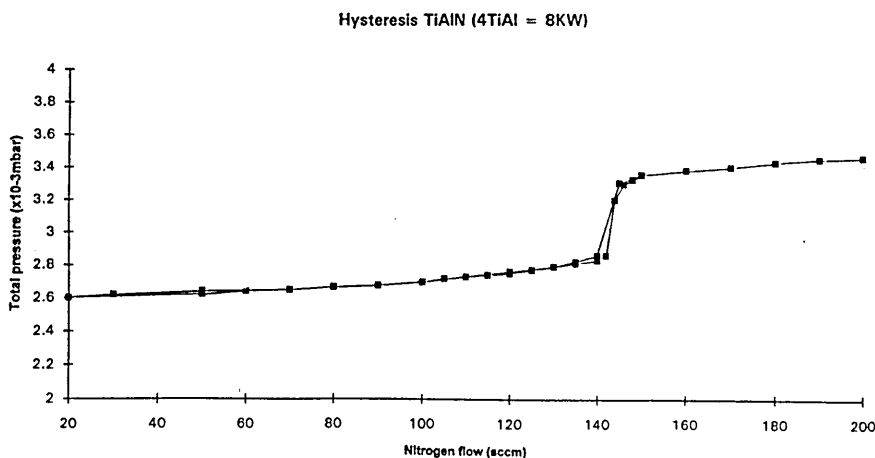
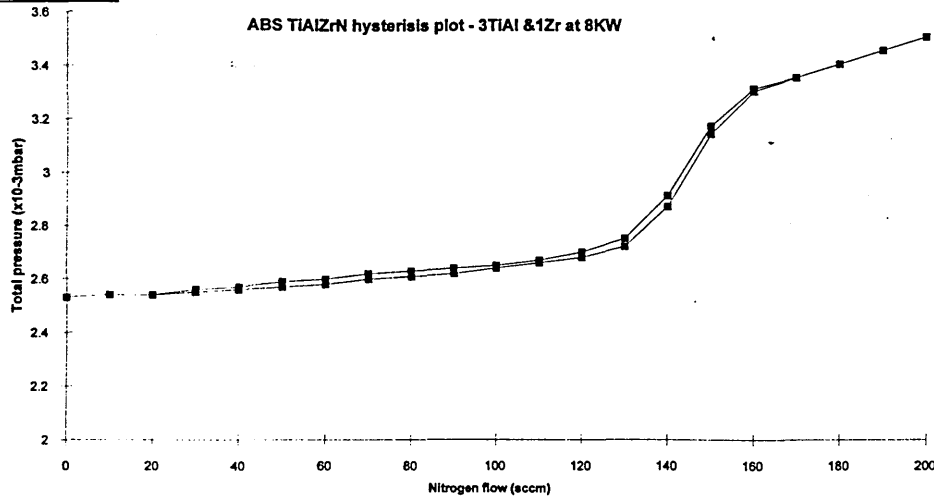


Figure 5.41b.



Standard polished HSS stubs, drill blanks and stainless steel coupons were chosen for use in the trial and individually cleaned using the routine outlined in section 3.3, before mounting onto one of six sub-turntable assemblies at a nominal distance of 250mm from the targets.

The deposition trial consisted of two coating processes where ABS TiAlZrN coatings were deposited both with and without a graded sputtered base layer between the quaternary coating and the metal ion etched substrate (figure 5.42). The coating regimes used are illustrated in table 5.8.

Figure 5.42.

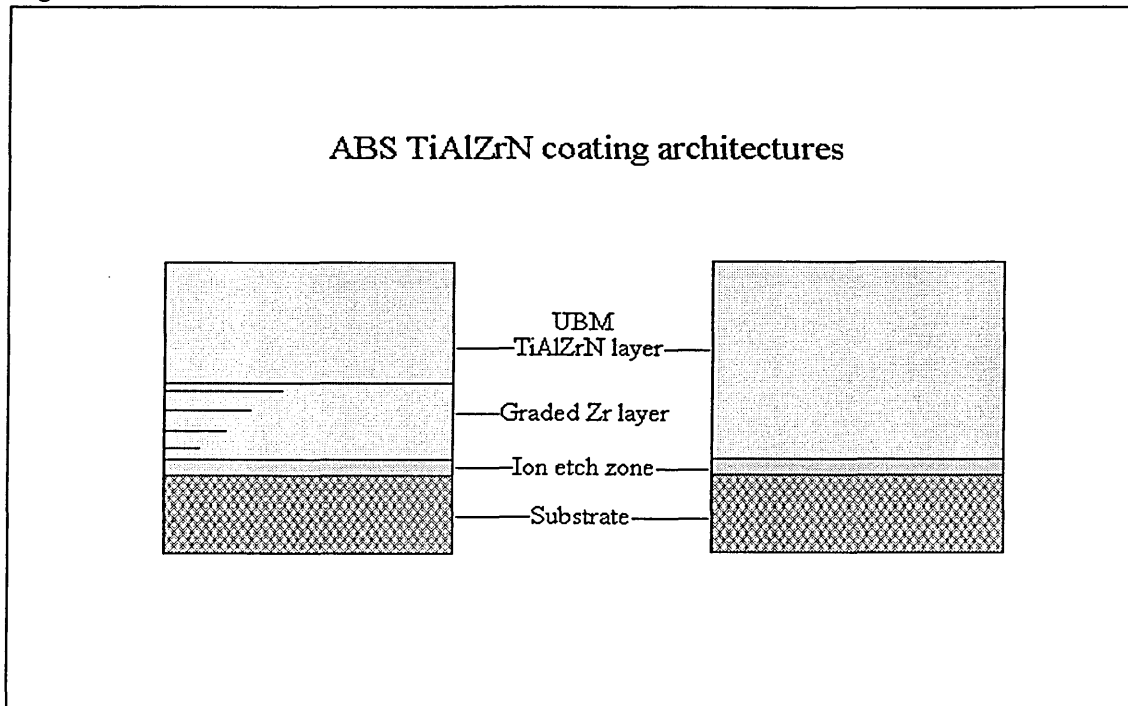


Table 5.8.

Standard Arc-Bond Sputter deposition	Arc-Bond Sputter deposition comprising base layer.
<p><b>1.Pump down and chamber heating</b>            Time = 75 minutes            Base pressure = <math>&lt;2 \times 10^{-5}</math> mbar            Temperature = 400°C</p> <p><b>2.Glow discharge target cleaning</b>            Shutter position = directly in front of targets            Time = 15 minutes            Power = 5KW            Substrate bias voltage = 0V            Unbalancing coil current = 0A            Argon flow = 220sccm            Pressure = <math>2.7 \times 10^{-3}</math> mbar            Temperature = 400°C</p>	<p><b>1.Pump down and chamber heating</b>            Time = 75 minutes            Base pressure = <math>&lt;2 \times 10^{-5}</math> mbar            Temperature = 400°C</p> <p><b>2.Glow discharge target cleaning</b>            Shutter position = directly in front of targets            Time = 15 minutes            Power = 5KW            Substrate bias voltage = 0V            Unbalancing coil current = 0A            Argon flow = 220sccm            Pressure = <math>2.7 \times 10^{-3}</math> mbar            Temperature = 400°C</p>
<p><b>3.Steered arc ion etching</b>            Arc etching using 2 TiAl targets only            Shutter position = moved away from targets            Arc current = 100A            Substrate bias voltage = -1200V            10 cycles of 1 minute duration            Argon flow = 220sccm            Pressure = <math>2.7 \times 10^{-3}</math> mbar            Coil current = 0A            Temperature = 450°C</p>	<p><b>3.Steered arc ion etching</b>            Arc etching using 2 TiAl targets only            Shutter position = moved away from targets            Arc current = 100A            Substrate bias voltage = -1200V            10 cycles of 1 minute duration            Argon flow = 220sccm            Pressure = <math>2.7 \times 10^{-3}</math> mbar            Coil current = 0A            Temperature = 450°C</p>

<p><b>4. Unbalanced magnetron sputter TiAlZrN coating</b></p> <p>All cathodes in magnetron mode</p> <p>Power = 8KW</p> <p>Closed field geometry</p> <p>Coil current = 8A</p> <p>Argon flow = 220sccm</p> <p>Pressure = <math>3.5 \times 10^{-3}</math> mbar</p> <p>Substrate bias voltage = -80V</p> <p>Coating time = 120 minutes</p> <p>Temperature = 450°C</p> <p>Primary rotation velocity = 80% of maximum (~6rpm)</p>	<p><b>4. Unbalanced magnetron sputter base layer coating</b></p> <p>All cathodes in magnetron mode</p> <p>3 TiAl target Power = 8KW</p> <p>1 Zr Power = 0.8KW in 1KW increments every 7.5 minutes</p> <p>Closed field geometry</p> <p>Coil current = 8A</p> <p>Argon flow = 220sccm</p> <p>Pressure = <math>3.5 \times 10^{-3}</math> mbar</p> <p>Substrate bias voltage = -80V</p> <p>Coating time = 60 minutes</p> <p>Temperature = 450°C</p> <p>Primary rotation velocity = 80% of maximum (~6rpm)</p>
<p><b>5. Chamber cooling, purging and venting</b></p> <p>Cooling cycle = 45 minutes</p> <p>Purging with Argon gas</p>	<p><b>5. Unbalanced magnetron sputter TiAlZrN coating</b></p> <p>All cathodes in magnetron mode</p> <p>Power = 8KW</p> <p>Closed field geometry</p> <p>Coil current = 8A</p> <p>Argon flow = 220sccm</p> <p>Pressure = <math>3.5 \times 10^{-3}</math> mbar</p> <p>Substrate bias voltage = -80V</p> <p>Coating time = 60 minutes</p> <p>Temperature = 450°C</p> <p>Primary rotation velocity = 80% of maximum (~6rpm)</p>
	<p><b>6. Chamber cooling, purging and venting</b></p> <p>Cooling cycle = 45 minutes</p> <p>Purging with Argon gas</p>

### 5.3.2. X-ray diffraction results

X-ray diffraction analysis using Cu  $K\alpha$  radiation was performed on each coated stainless steel coupon over a scan range from 20-100°2 $\theta$ . Both TiAlZrN coatings exhibited a single phase NaCl type face centred cubic structure and <100> preferred orientation (figure 5.43 and 5.44).

Figure 5.43. X-ray diffraction trace from ABS TiAlZrN coating on stainless steel.

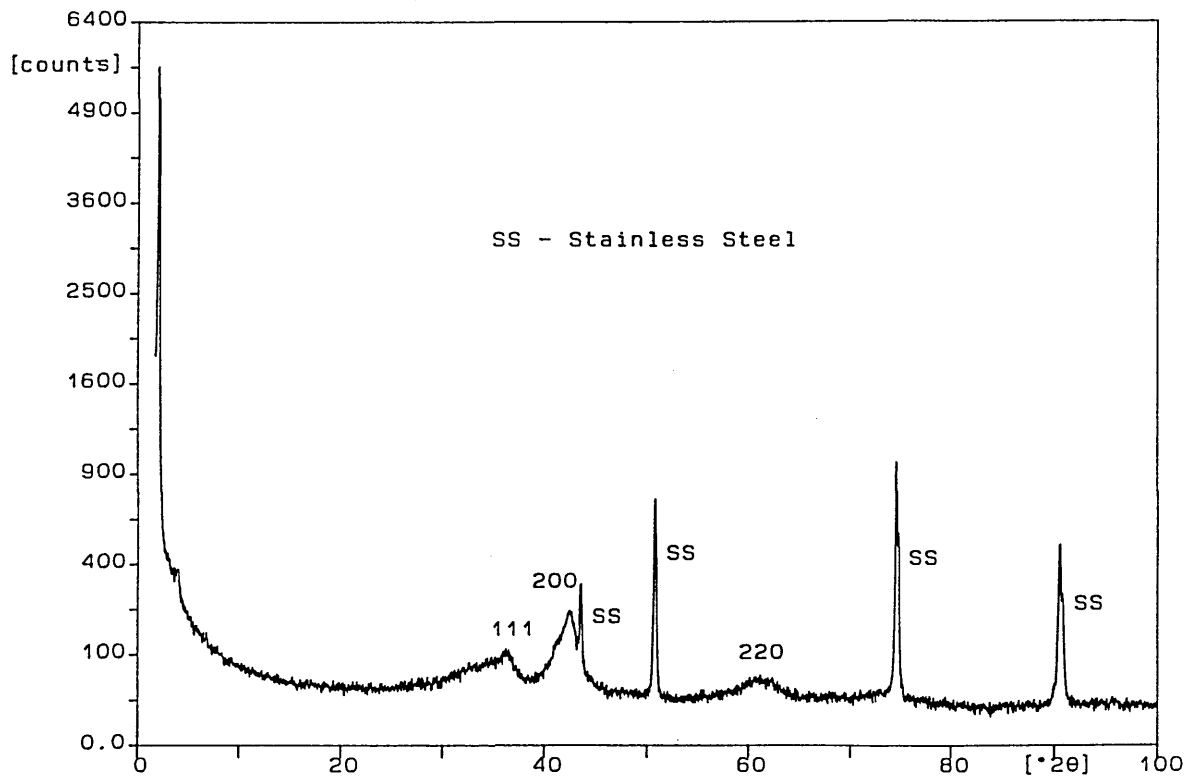
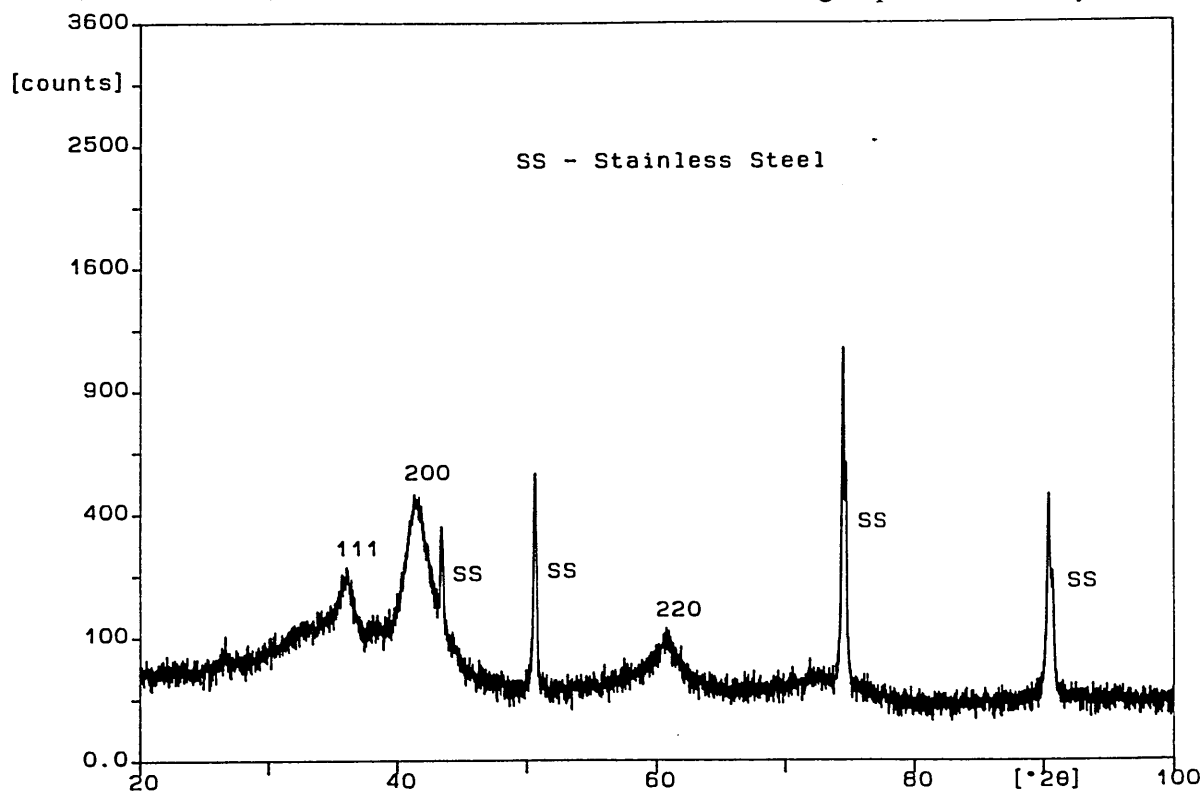


Figure 5.44. X-ray diffraction trace from ABS TiAlZrN using a sputtered base layer.



The lattice parameter of the ABS TiAlZrN coating deposited with a graded base layer was lower than the standard TiAlZrN coating due to the influence of the smaller TiAlN unit cell, however the (200) full width at half maximum was significantly reduced in the film comprising the base layer due to grading of the compressive residual stresses at the coating / substrate interface (table 5.9).

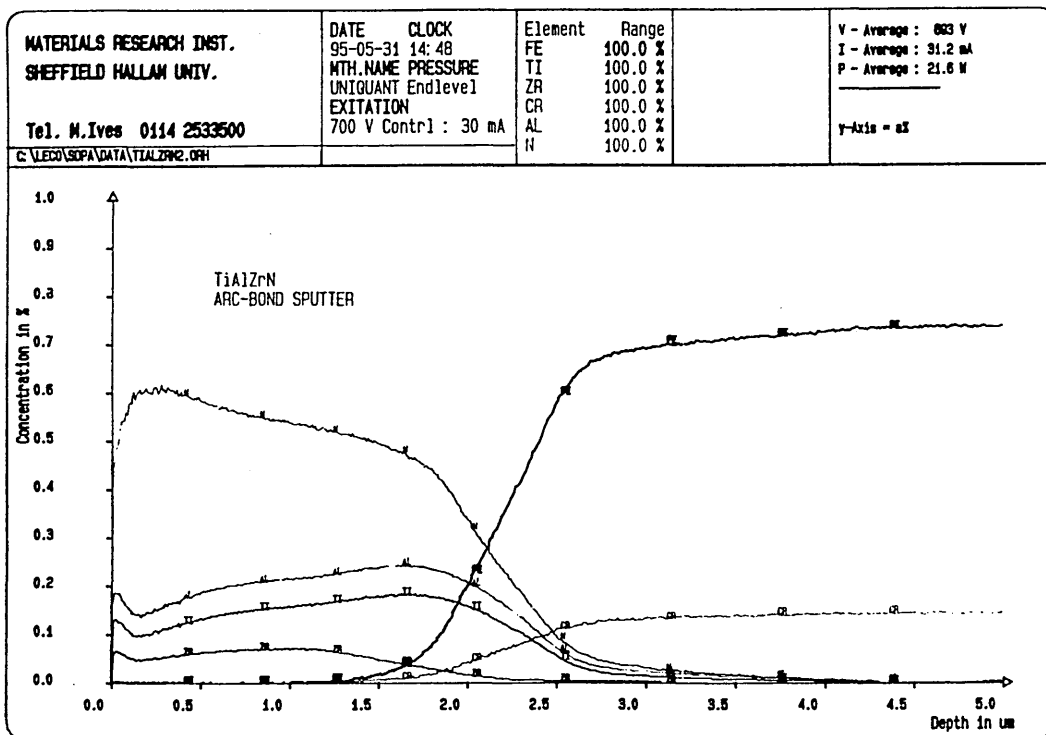
Table 5.9.

Coating type	Orientation	$a_0 / \text{\AA}$ $\pm 0.01$	(200) FWHM $\pm 0.10^\circ 2\theta$
ABS TiAlZrN	$\langle 100 \rangle$	4.31	1.89
ABS TiAlZrN + base layer	$\langle 100 \rangle$	4.27	1.54

### 5.3.3. GDOES results

Glow discharge depth profiles showed that the films were stoichiometric, of similar thickness ( $\sim 2\mu\text{m}$ ) where the metal ratio was predominantly composed of Ti and Al, with the Zr content typically around 10 atomic% (Ti $\sim$ 18%, Al $\sim$ 22%, N $\sim$ 50%) as a result of single zirconium target utilisation and target poisoning effects.

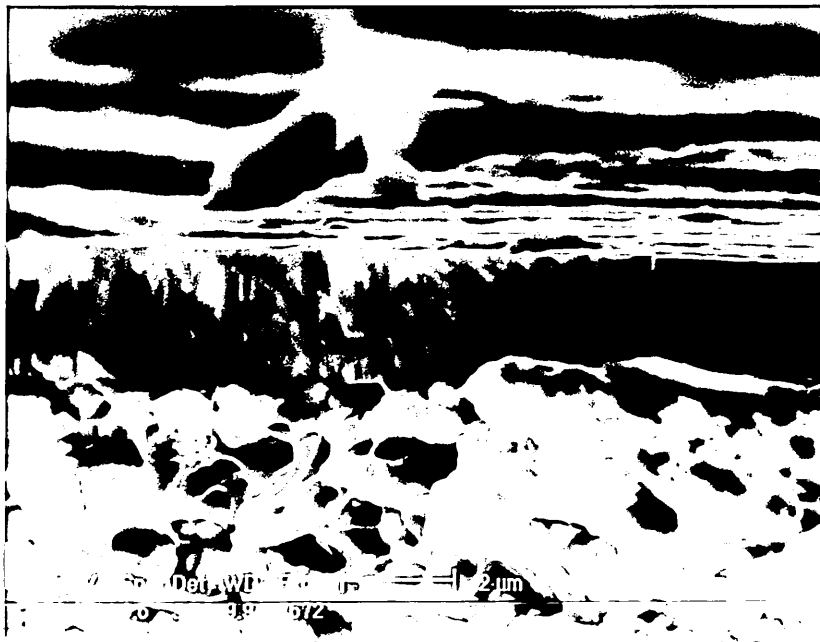
Figure 5.45. ABS TiAlZrN GDOES depth profile.



### 5.3.4. Scanning electron microscopy results

All films in cross-section appeared columnar and exhibited dense zone-T structures (figure 5.46). TiAlZrN coatings deposited with a TiAlN / graded Zr base layer showed evidence of increasing grain refinement as the Zr composition was increased due to further solid solution strengthening.

Figure 5.46. ABS TiAlZrN SEM cross-section micrograph.



### 5.3.5. TiAlZrN mechanical and physical properties

Adhesion measurements undertaken using the complementary scratch and Rockwell indentation techniques were found to be entirely consistent. TiAlZrN films deposited on high speed steel without an intermediate graded base layer were found to have poor adhesive properties due to the high levels of residual stress at the coating /substrate interface (table 5.10). However, the TiAlZrN coating using a base layer demonstrated a strong increase in film adhesion to levels comparable with standard ABS coatings such as ZrN and TiAlN.

Table 5.10.

Coating type	Indent quality	$L_c / N$ $\pm 2N$	$H_{k0.025}$ $\pm 300 \text{Kgmm}^{-2}$	$L^*$ $\pm 0.1$	$a^*$ $\pm 0.1$	$b^*$ $\pm 0.1$	$R_a / \mu\text{m}$ $\pm 0.01$
ABS TiAlN	1	55	2400	42.66	2.39	-0.25	0.14
ABS ZrN	1	50	2300	88.61	-1.57	17.65	0.07
ABS TiAlZrN	3-4	20	3600	40.08	3.16	-0.65	0.13
ABS TiAlZrN + base layer	1-2	50	3100	44.57	0.38	-1.12	0.13

Knoop hardness values indicated a significant increase in TiAlZrN film hardness over TiAlN and ZrN. Films deposited with the aid of a base layer had lower hardness than standard process films due to the influence of a softer (slowly increasing in hardness from TiAlN at 2400H<sub>k</sub>) intermediate layer and lower interfacial stress. The level of average surface roughness ( $R_a$ ) was also found to be consistent with TiAlN at 0.013 $\mu$ m and was higher than ZrN (~0.07 $\mu$ m) due to development of a higher macroparticle flux during the arc metal ion etching phase using the high aluminium content Ti<sub>0.5</sub>Al<sub>0.5</sub> targets. CIE lab colour measurements revealed that the films exhibited a blue-grey appearance of lightness,  $a^*$  and  $b^*$  similar to ABS TiAlN.

References.

- (1) W-D.Münz - *J.Vac.Sci.Technol*, 1986, A4(6), 2717-2725.
- (2) O.Knotek, W-D.Münz, T.Leyendecker - *J.Vac.Sci.Technol*, 1987, A5(4), 2173.

## CHAPTER SIX

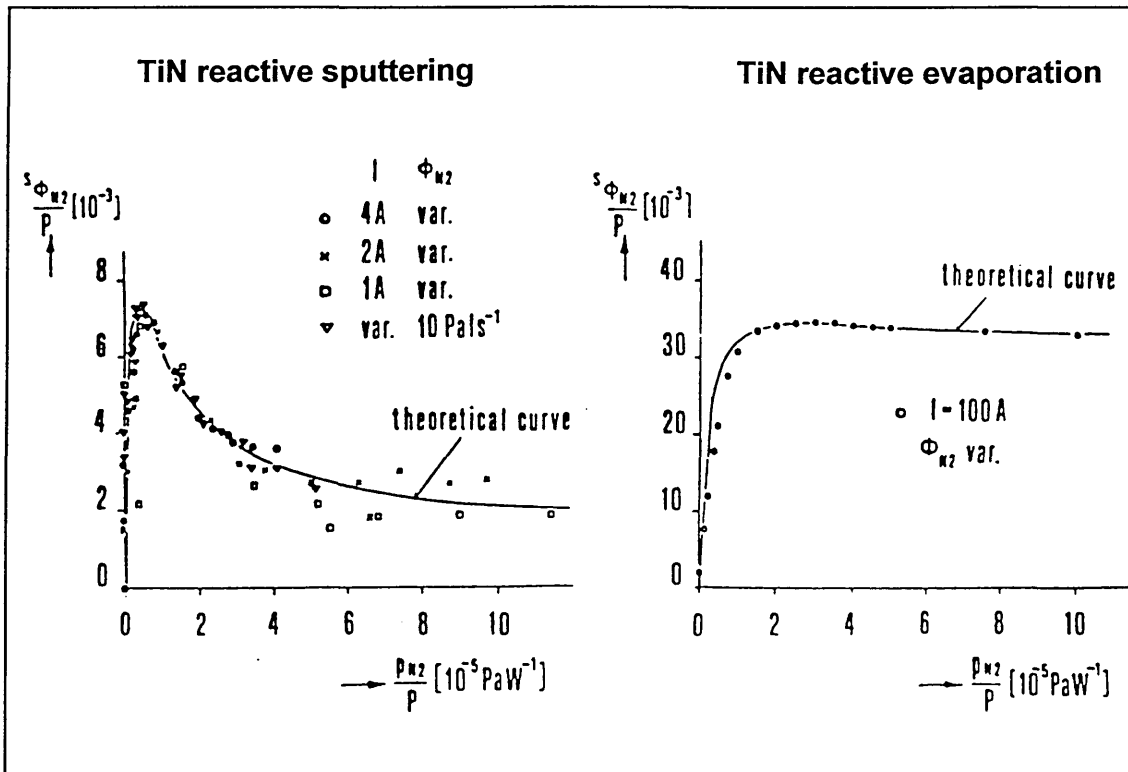
### THE GROWTH AND CHARACTERISATION OF TiAlN-ZrN AND TiAlN-TiN MULTI-LAYER THIN FILMS.

This chapter presents a new PVD technique for the reactive deposition of third generation TiAlN-ZrN and TiAlN-TiN multi-layer thin films at industrial scale by a combined steered arc evaporation and unbalanced magnetron sputtering process. The results from mechanical and physical characterisation of the coatings by a range of bulk and surface analysis techniques are illustrated along with bias current density measurements and computer modelling of the complex substrate rotation and normalised coating flux density.

#### 6.1. Multi-layer process conditions.

Earlier investigations by Vyskocil et al (1) on the consumption of nitrogen gas per unit power ( $\phi_{N_2}/p$ ) as a function of nitrogen partial pressure per unit power ( $p_{N_2}/p$ ) in reactive magnetron sputtering and steered arc evaporation trials demonstrated the importance of target deposition mode determination (figure 6.1).

Figure 6.1. Evaporation and sputter deposition mode behaviour.



Examination of the magnetron sputter process data obtained during TiN coating trials illustrated an initial sharp increase in  $\phi_{N_2}/p$  prior to target poisoning which rapidly lead to a decrease in secondary electron and sputter yield, deposition rate and  $N_2$  gas consumption after titanium target poisoning. Conversely, the arc evaporation trial undertaken at equivalent levels of  $p_{N_2}/p$  showed a sharp and larger magnitude rise in  $\phi_{N_2}/p$  which was maintained near the maximum value and was clearly significantly less sensitive to poisoning.

The effect is the result of fundamental differences between arc evaporated and magnetron sputtered vapour properties, outlined in chapter 2, which may be briefly summarised with the following arc flux characteristics:-

- High levels of mean charge state (2) e.g.  $Ti^{2.1+}$ ,  $Zr^{2.6+}$  and  $Nb^{3.0+}$ .
- High levels of metal ion energy typically  $\sim 50eV$ , metal atom energy  $\sim 0.1-1.0eV$ .
- High current density ( $\sim 10^8 Am^{-2}$ ) by a small active emitting area (cathode spot).
- Increased maximum vapour emission rates over sputtering.
- Macro-particle generation.
- High levels of radiant heating.

These reaction behaviours and physical properties are of key significance in multi-component processing and identify a basic mechanism which may be used in an original industrial scale technique for the deposition of pseudo ceramic - pseudo ceramic multi-layer films.

The multi-layer deposition technique relies on the flexibility of arc-bond sputter technology to simultaneously deposit a coating by the modulation of TiAlN layers from three unbalanced magnetron sputtering sources with ZrN or TiN layers from a single steered arc evaporation source. The method adopts a simple strategy in which materials of high reactivity with nitrogen (easily poisoned in high reactive gas partial pressures) are used in steered arc mode (i.e. group IVa transition and refractory metals such as Zr & Ti), and materials with less extreme nitrogen reactivity and hence less sensitive hysteresis behaviour (i.e. TiAl) are deposited in magnetron mode.

Following the results from investigations on TiAlZrN films demonstrated in section 5.3, processing consisted of a six step operation which incorporated a steered arc ion etch phase and an unbalanced magnetron sputtered graded base layer to control the high residual stresses generated at the coating / substrate interface. The optimum coating pressure ( $3.5 \times 10^{-3} mbar$ ) was obtained by performing a hysteresis test of gas flow

against total pressure and operating near the critical point (close to the "knee") prior to the onset of TiAl target poisoning (figure 5.41, chapter 5.3). Below this pressure insufficient gas scattering, excessive ion bombardment, sub-stoichiometry and deleterious levels of residual stress were developed. The chamber configurations and full process parameters are illustrated in figure 6.2.a&b and table 6.1.

Figure 6.2a Closed field unbalanced magnetron sputtered base layer configuration.

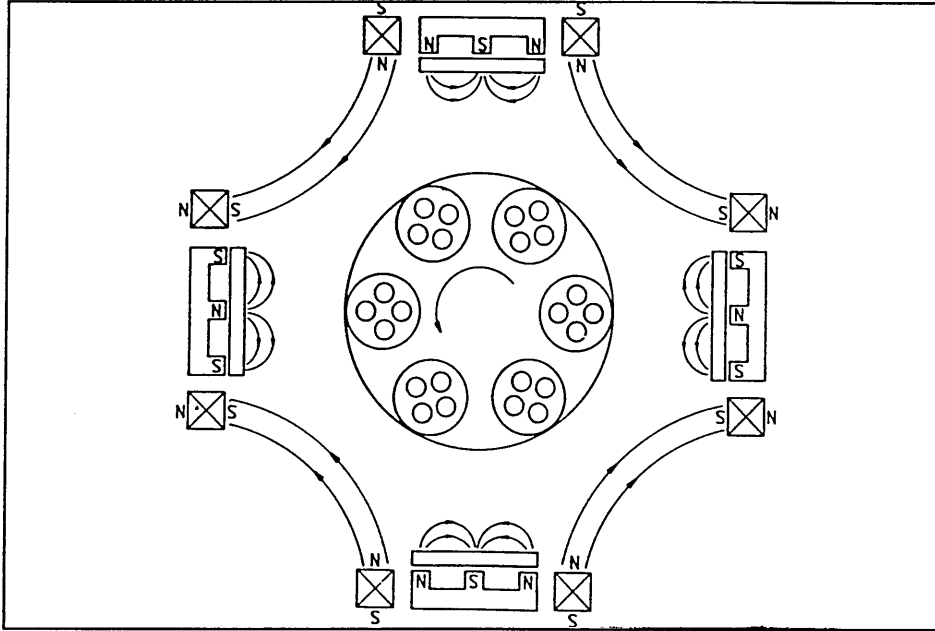


Figure 6.2b Combined arc / magnetron multi-layer coating configuration.

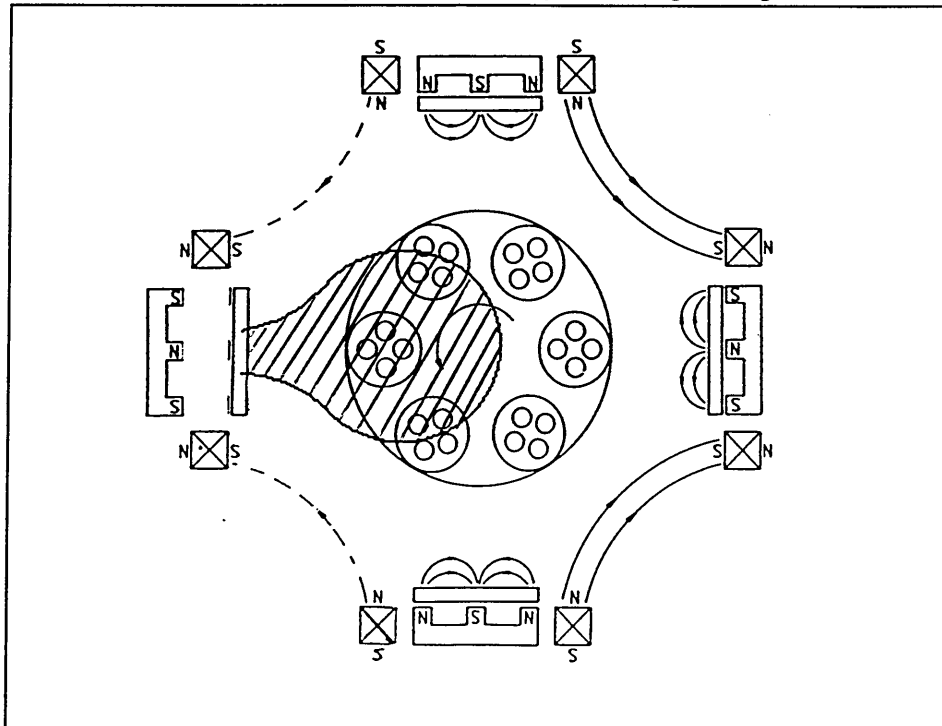


Table 6.1. Multi-layer process parameters.

<u>Combined steered arc / magnetron sputter deposition steps</u>
<p><u>1. Pump down and chamber heating</u>                      Time = 75 mins                      Base pressure = <math>3 \times 10^{-5}</math> mbar &amp; Leak rate <math>&lt; 1 \times 10^{-3}</math> mbar.l.s<sup>-1</sup>                      Temperature (radiant heating) = 400°C</p>
<p><u>2. Glow discharge target cleaning</u>                      Time = 15minutes                      Shutter position = directly in front of targets                      Power to each target = 5KW                      Argon flow = 220 sccm                      Working pressure = <math>2.7 \times 10^{-3}</math> mbar                      Substrate bias voltage = 0V &amp; Unbalancing coil current = 0A                      Temperature = 400°C</p>
<p><u>3. Steered arc ion etching</u>                      Arc etching using 2 TiAl targets only                      Fixed magnet array position = moved away from targets                      Shutter position = moved away from targets                      Arc current = 100A                      Substrate bias voltage = -1200V                      Substrate temperature = 450°C                      Argon flow = 220 sccm &amp; Working pressure = <math>2.7 \times 10^{-3}</math> mbar                      Coil current = 0A                      10 cycles of 1 minute duration</p>
<p><u>4. Unbalanced magnetron reactive sputtered base layer.</u>                      Fixed magnet array position = moved directly behind targets                      Shutter position = moved away from targets                      All targets in magnetron mode                      Power to 3 TiAl targets = 8KW                      Power to 1 Zr (or Ti) target = 0-8KW ( increments of 1 KW every 7.5minutes)                      Substrate bias voltage = -80V                      Temperature = 450°C                      Working pressure = <math>3.5 \times 10^{-3}</math> mbar                      Reactive gas = Nitrogen                      Argon flow = 220 sccm                      Unbalancing coil current = 8A per coil (closed field geometry)                      Coating time = 1 hour</p>

5. Combined reactive steered arc / unbalanced magnetron sputtering

3 TiAl targets in magnetron mode, 1 Zr (or Ti) target in steered arc mode

Magnetron power = 8KW, Arc current = 80A (unless stated)

Substrate bias voltage = -80V

Unbalancing coil current = 8A on magnetron cathodes, 0-2A on arc cathode

Argon flow = 220 sccm

Reactive gas = Nitrogen

Working pressure =  $3.5 \times 10^{-3}$  mbar

Temperature = 450°C

Coating time = 1 hour

6. Cooling cycle

Cooling time = 45 minutes

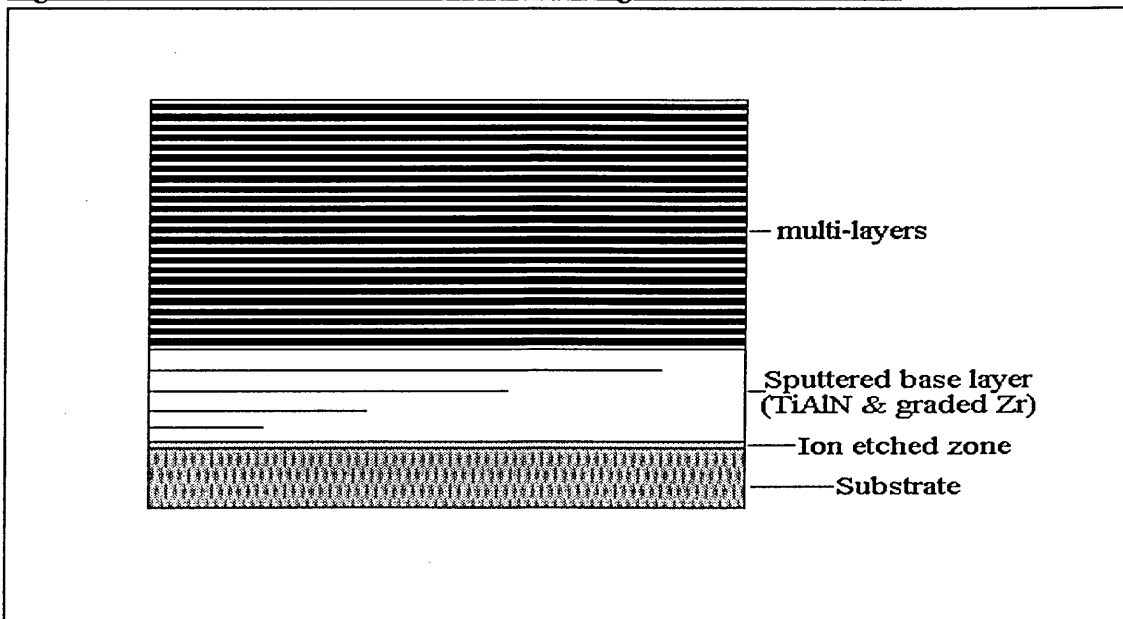
Purging = Argon

Pressure =  $2.7 \times 10^{-3}$  mbar

Temperature = 450-150°C

During the deposition of the sputtered base layer, the standard closed field linking configuration of the four cathodes was adopted and the power applied to the Zr or Ti target increased in increments of 1KW every 7.5 minutes to create a graded film composition prior to arc evaporation. However, in the multi-layer deposition stage of step five, the field linkage was only between the 3 TiAl targets operating in magnetron mode (figure 6.2b). The result was a film of architecture shown in figure 6.3.

Figure 6.3. Schematic of the combined arc / magnetron film structure.

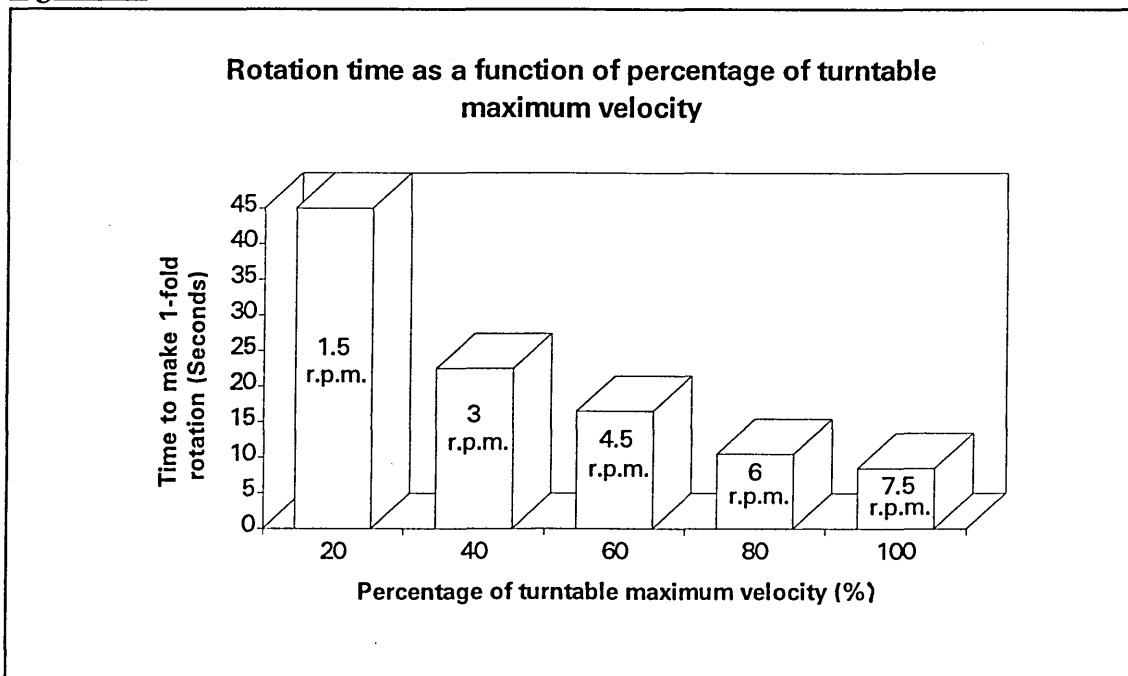


TiAlN-ZrN multi-layer coatings were deposited in a trial consisting of several processes where variation in the deposition rate was achieved by altering the substrate rotation velocity, the type of rotation (1-fold & 3-fold) and the arc current. The TiAlN-TiN trial involved a single combined arc / magnetron deposition process involving steered arc evaporation of a titanium target and 3-fold rotation at a primary rotation velocity of 6 r.p.m (80%).

## **6.2. The effect of rotation velocity and type of rotation on TiAlN-ZrN multilayer films.**

The coating trial consisted of five reactive deposition processes each with a different primary turntable rotation velocity, increasing in increments of 1.5 r.p.m (20%) to a maximum of 7.5 r.p.m.(figure 6.4). Each test sample was individually cleaned, degreased and rinsed using the standard method (section 3.3) and positioned in one of six sub-turntable assemblies to undergo three fold rotation at a nominal distance of 250mm from the targets. The 2<sup>nd</sup> fold of rotation was a 3.6:1 increase in velocity over the single fold and turned in the same anti-clockwise direction, whilst the 3<sup>rd</sup> fold revolved in a clockwise direction 1/6<sup>th</sup> of a revolution every full rotation of the 2<sup>nd</sup> fold. In each coating trial a 304 stainless steel coupon was also mounted in a fixed position to undergo single fold rotation with a target to substrate distance of 250mm.

Figure 6.4.



### 6.2.1. X-ray diffraction results.

The period of a multi-layer / superlattice can be calculated in the high angle region of an X-ray diffraction trace using the equation:-

$$\sin\Theta_a = \sin\Theta_b \pm (n\lambda / 2\Delta) \quad \dots\text{equation 6.1.}$$

where;  $\Theta_a$  and  $\Theta_b$  are the diffraction angles of the relative satellite peaks.

$\lambda$  is the X-ray wavelength.

$\Delta$  is the multi-layer / superlattice period.

$n$  is the order.

However, direct measurement of the layer period can also be made in the low angle region using the standard Bragg equation:-

$$\Delta = (n\lambda / 2\sin\Theta) \quad \dots\text{equation 6.2.}$$

Hence, Cu  $K\alpha$  X-ray diffraction was performed on all coated stainless steel coupons using two different scan ranges:-

- (1) High angle scan ( $20-100^\circ 2\Theta$ ) for lattice strain and preferred orientation analysis.
- (2) Low angle scan ( $2-5^\circ 2\Theta$ ) for layer confirmation and period measurement.

Figure 6.5a&b shows the high angle traces from TiAlN-ZrN films deposited in 3-fold and 1-fold rotation at five different rotation velocities. All coatings exhibited a face centred cubic (f.c.c) unit cell structure and texture analysis indicated a  $\langle 100 \rangle$  preferred orientation. Full separation of the peaks corresponding to TiAlN and ZrN was only observed in the largest period film undergoing single fold rotation at a velocity of 1.5 r.p.m (20%). At the higher rotation velocities, individual peaks corresponding to TiAlN and ZrN could not be resolved and traces showed single peaks at positions of the weighted average of the constituent layers.

**Figure 6.5a** High angle X-ray diffraction traces of 1-fold rotation TiAlN-ZrN

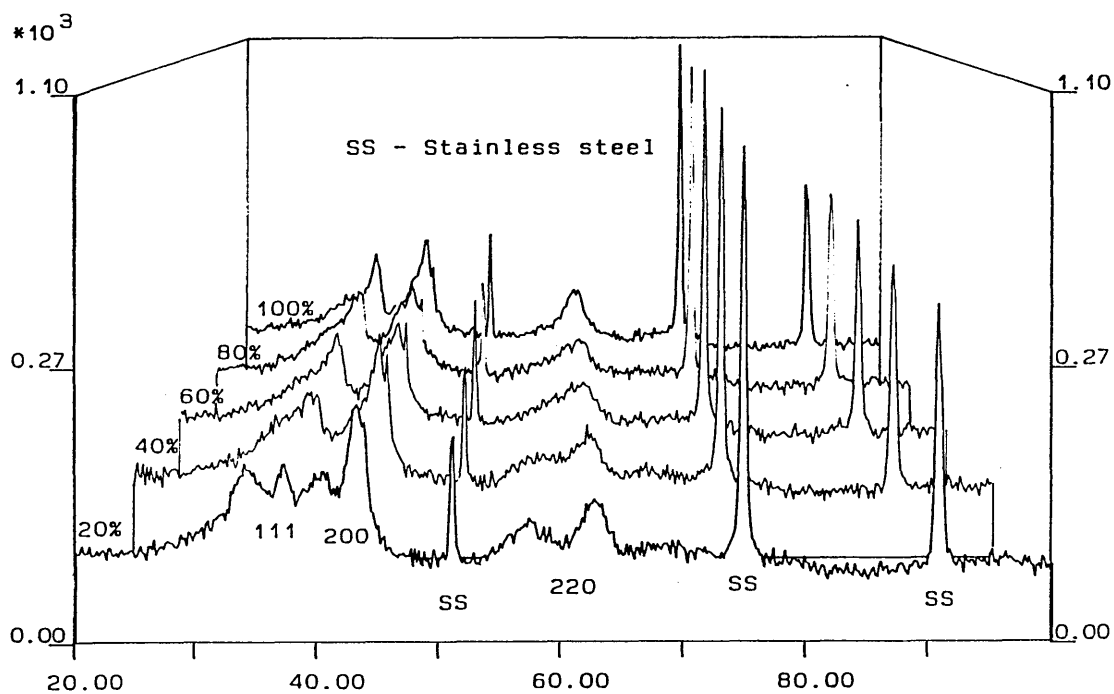


**Figure 6.5b** High angle X-ray diffraction traces of 3-fold rotation TiAlN-ZrN

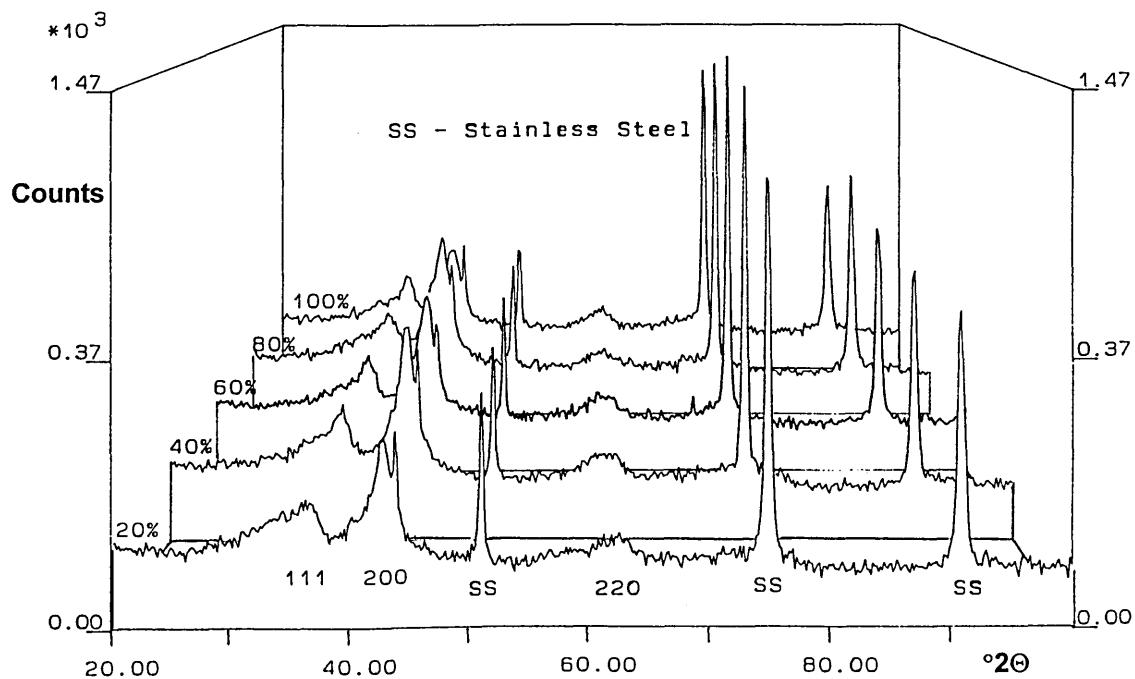
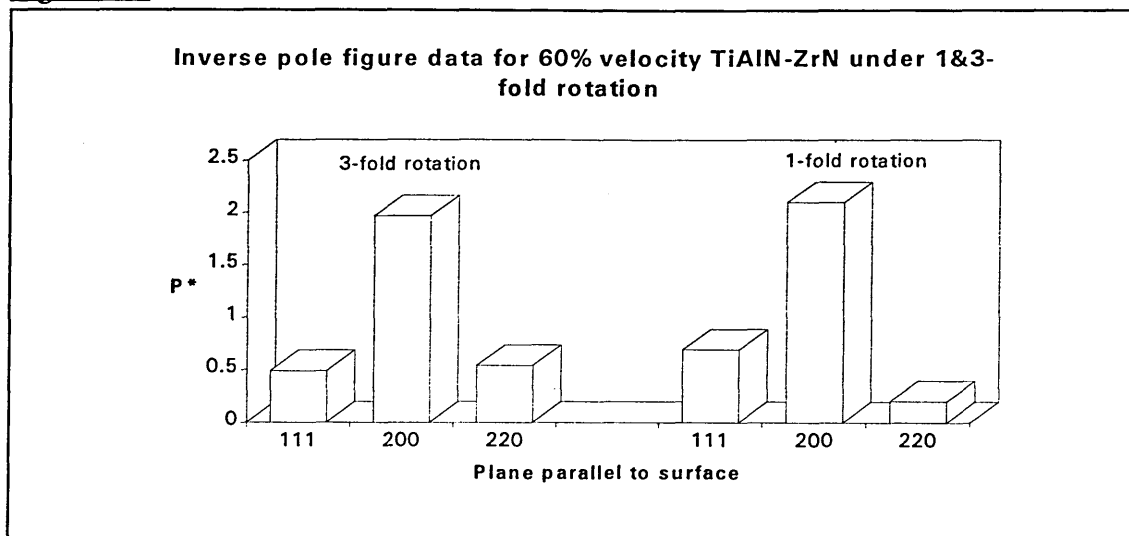
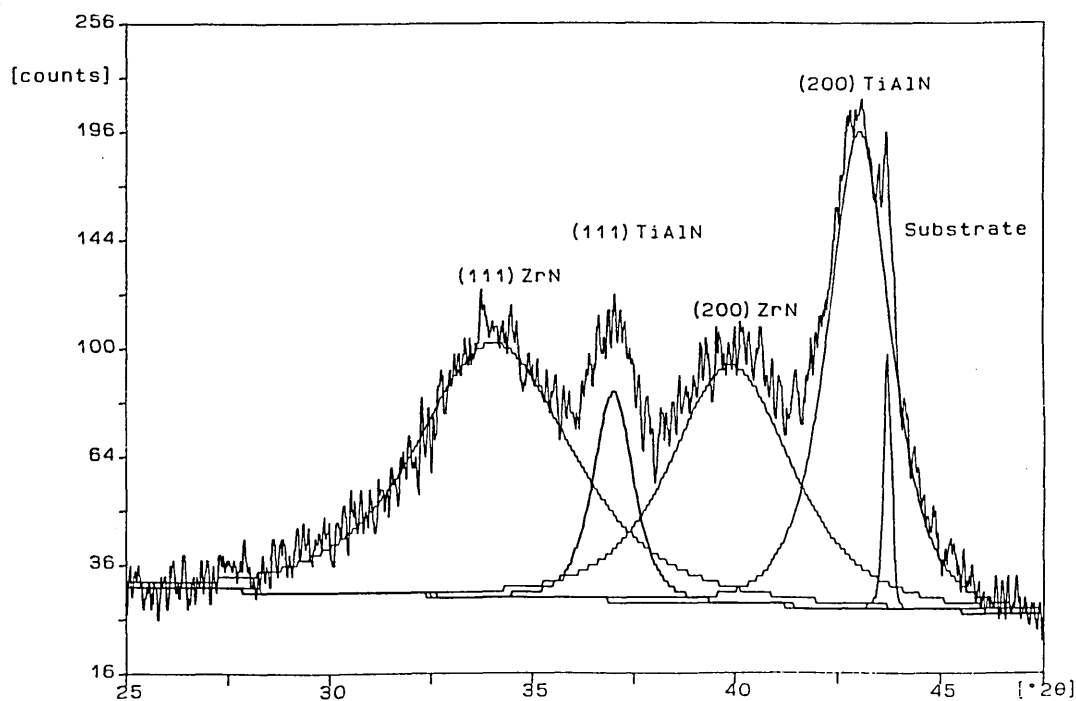


Figure 6.6.



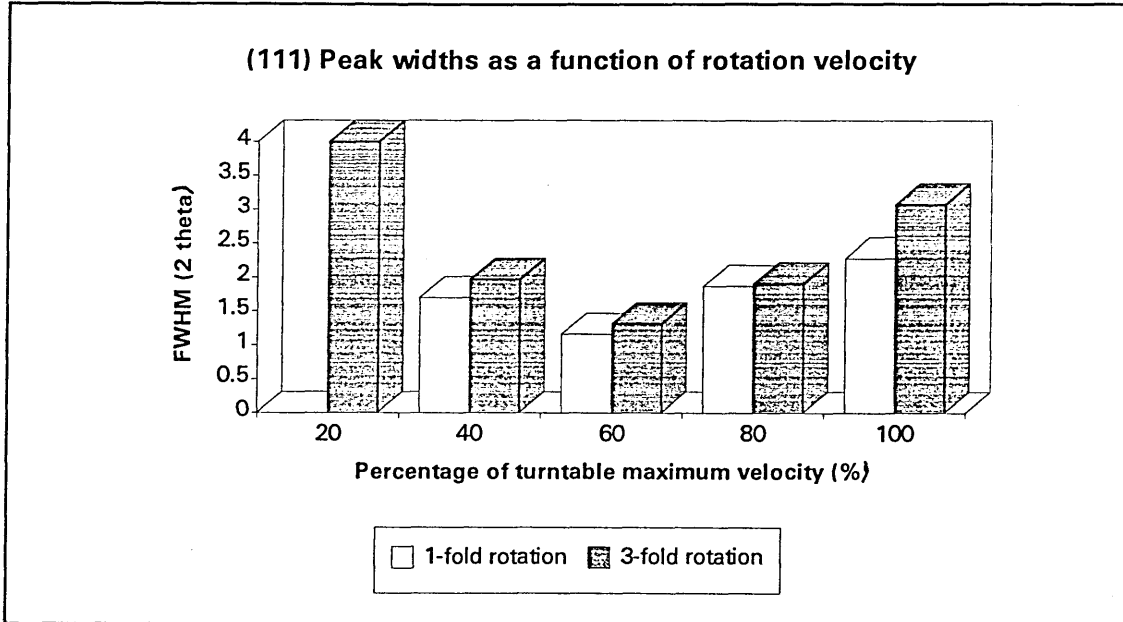
Inverse pole figure analysis of X-ray traces from 60% (4.5 r.p.m) velocity TiAlN-ZrN films deposited under 1 and 3-fold rotation identified a strong  $\langle 100 \rangle$  orientation for both films (figure 6.6). Examination of  $P^*$  values revealed a higher ratio of 200/111 probability when deposited using 3-fold rotation (4.02 for a layer period of 36Å) than single fold rotation (3.04 for a layer period of 64Å). Further analysis of the single fold rotation film deposited at 1.5 r.p.m (figure 6.7) showed that the ZrN layers exhibited more peak broadening than the TiAlN layers i.e. mean FWHM of  $3.54^\circ$  of  $2\theta$  and  $1.27^\circ$  of  $2\theta$  for ZrN and TiAlN respectively, indicating higher lattice strain, grain size effects and inter-diffusion.

Figure 6.7. FWHM analysis of 1-fold rotation 1.5 r.p.m TiAlN-ZrN film.



The average (111) peak full width at half maximum (FWHM) in single fold rotation was also found to be significantly less than in 3-fold rotation due to the production of a larger and more uniform layer period (figure 6.8).

Figure 6.8.



The FWHM data revealed a reduction in (111) peak width with increasing rotation velocity between 20-60% caused by a diminishing multi-layer period and subsequently greater superposition of the individual TiAlN and ZrN peaks. At velocities greater than 60% an increase in peak width was observed due to reducing grain size and higher lattice strain effects.

Lattice parameter measurements were performed using equation 6.3.

$$a_0 = d (h^2 + k^2 + l^2)^{0.5} \quad \text{.....equation 6.3.}$$

where:  $a_0$  = Lattice parameter for a particular set of planes &  $d$  = Interplanar spacing.

Analysis of the ZrN and TiAlN peaks shown in figure 6.7, indicated a ZrN unit cell smaller than the unstressed JCPDS standard data due to the development of an opposing residual stress state from constraining TiAlN layers and interfacial mixing of elements with smaller atomic radii. The TiAlN unit cell dimension was larger than that predicted by a Vegards law calculation (the linear dependence of ternary lattice spacings on composition follows a straight line joining the values for the binary system spacings) indicating a compressive residual stress (table 6.2).

Table 6.2.

TiAlN lattice parameter $\pm 0.01\text{\AA}$	ZrN lattice parameter $\pm 0.01\text{\AA}$
Vegards law prediction - $a_0 = 4.17\text{\AA}$	JCPDS data - $a_0 = 4.56\text{\AA}$
Measured data - $a_0 = 4.19\text{\AA}$	Measured data - $a_0 = 4.55\text{\AA}$
Percentage of expansion = 0.4%	Percentage of reduction = 0.2%

Analysis of the lattice parameters from the films exhibiting single peaks demonstrated a highly repeatable unit cell dimension of  $4.26 \pm 0.01\text{\AA}$  which remained constant with increasing velocity in both single and 3-fold rotation.

Low angle scan spectra from TiAlN-ZrN films deposited in 1-fold and 3-fold rotation at five different rotation velocities are shown in figures 6.9a&b. The 3-fold rotation showed only 1<sup>st</sup> order reflections ( $n=1$ ) whilst 1-fold rotation films showed higher order satellite reflections ( $n=2,3$ ,etc) due to a higher interfacial quality and improved uniformity of the multi-layer period. The general lack of strong high order reflections, the presence of peak broadening and the low relative intensities also suggests that a significant level of interfacial mixing and roughness and micro-grain size is present in the films.

Figure 6.9a. Low angle X-ray diffraction traces of 1-fold rotation TiAlN-ZrN

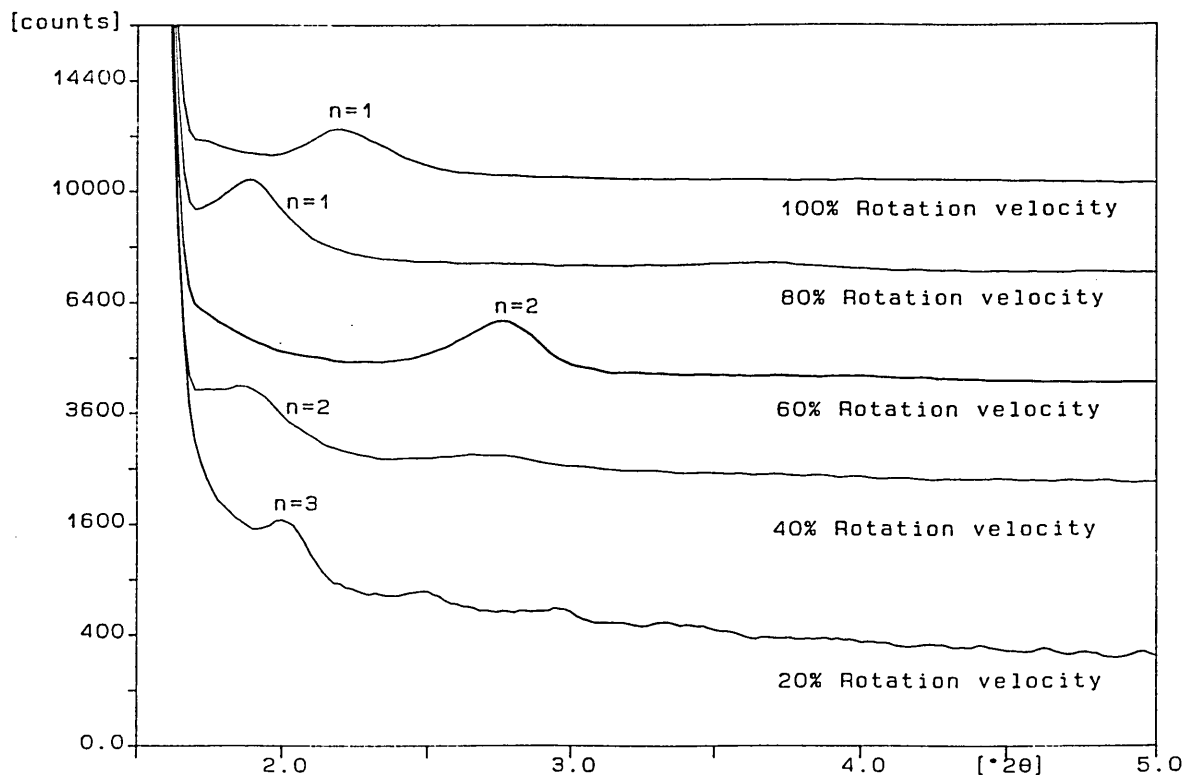
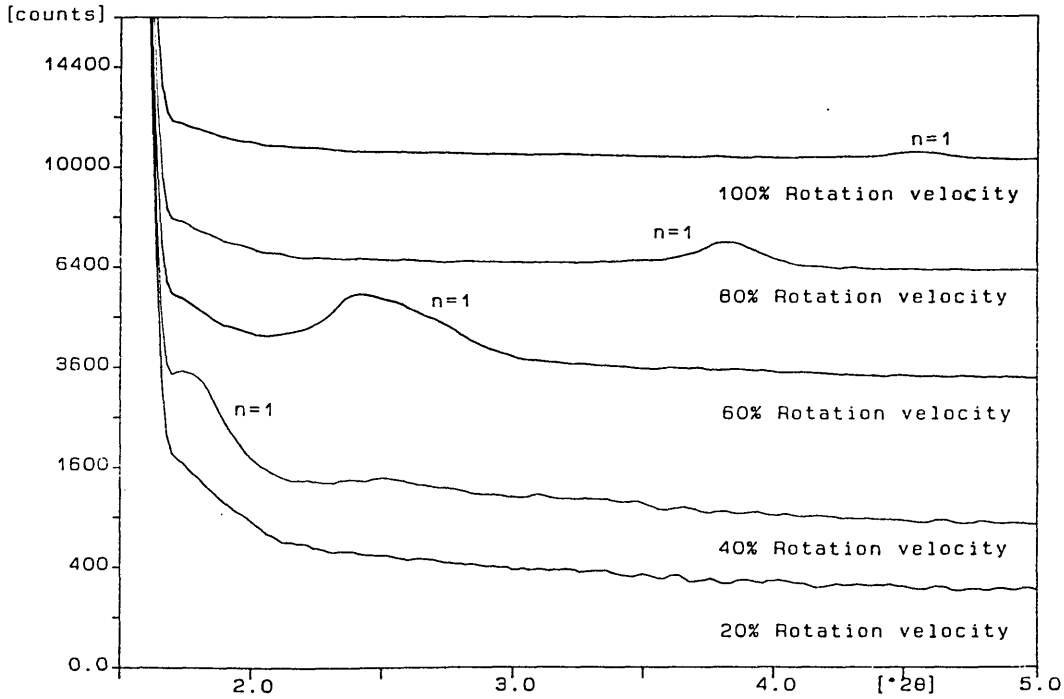
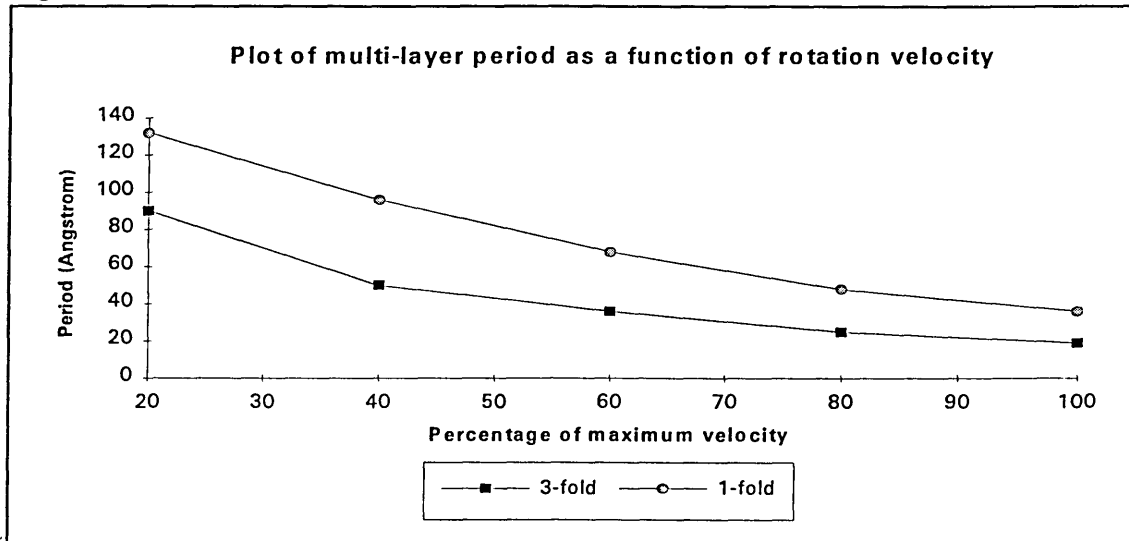


**Figure 6.9b. Low angle X-ray diffraction traces of 3-fold rotation TiAlN-ZrN**



In both single and 3-fold rotation, increasing the rotation velocity caused a decrease in the multi-layer period (figure 6.10). The coatings produced by single fold rotation had systematically larger periods than the 3-fold coating deposited at the equivalent rotation velocity. Control of the planetary rotation velocity and the type of rotation led to variation in the multi-layer period from 19-132Å.

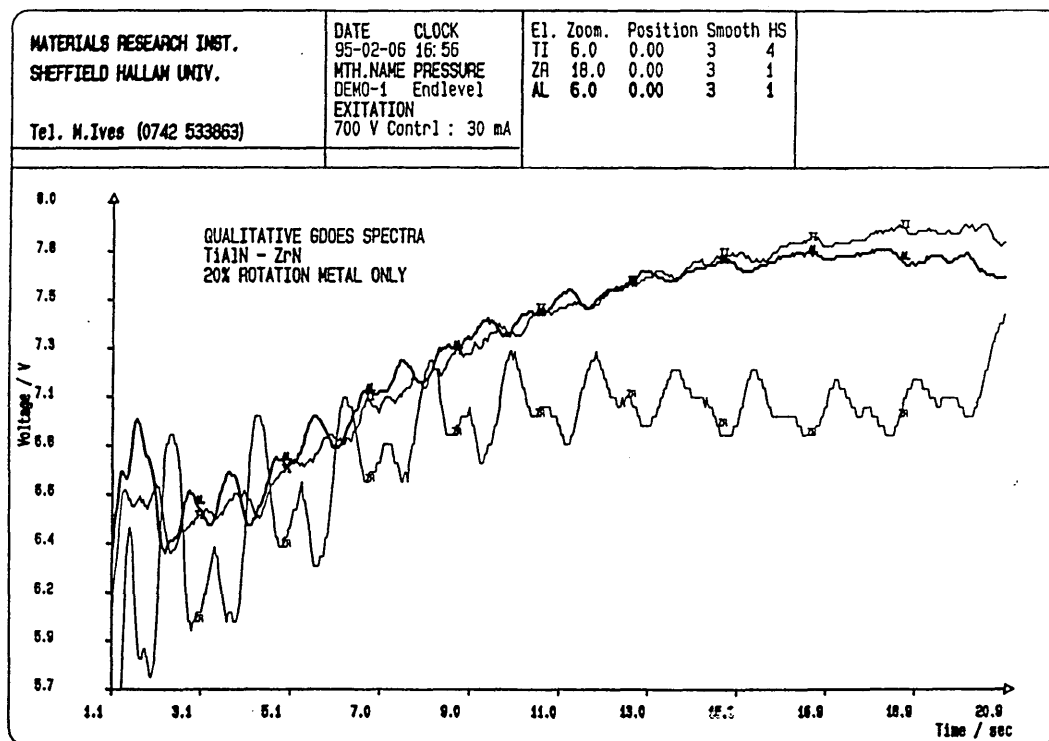
**Figure 6.10.**



### 6.2.2 GDOES results.

Figure 6.11 shows a typical qualitative profile of the metal contribution in the 3-fold, 1.5 r.p.m slow rotation TiAlN-ZrN film with a multi-layer period of approximately 90Å. The GDOES trace shows alternating TiAl and Zr rich layers where the TiAl maxima coincide with the sharp Zr minima. Further examination also reveals small doublets or secondary peaks which are believed to be produced from the influence of the second and third folds of rotation.

Figure 6.11. GDOES depth profile through 3-fold rotation 1.5rpm TiAlN-ZrN film.



Quantification of the depth profiles against a range of metal standards containing different nitrogen contents showed that all coatings were stoichiometric, demonstrated the existence of the graded Zr level to 9at% in the base layer and revealed that all the multi-layer regions had very similar average compositions of  $Ti_{0.18}Al_{0.24}Zr_{0.08}N_{0.50}$  (figure 6.12). The quantified spectra indicated that the ZrN layers were significantly thinner than the TiAlN layers and when related to low angle X-ray data allowed prediction of the mean layer thickness (figure 6.13). The results also demonstrate that films composed of only 2-3 monolayers of ZrN may be formed. However, a systematic error will occur in these calculations due to the influence of the 3-fold planetary rotation and the accuracy of measurement and calibration when using low angle XRD and GDOES.

Figure 6.12. Quantified GDOES spectra from 3-fold rotation 1.5rpm TiAlN-ZrN.

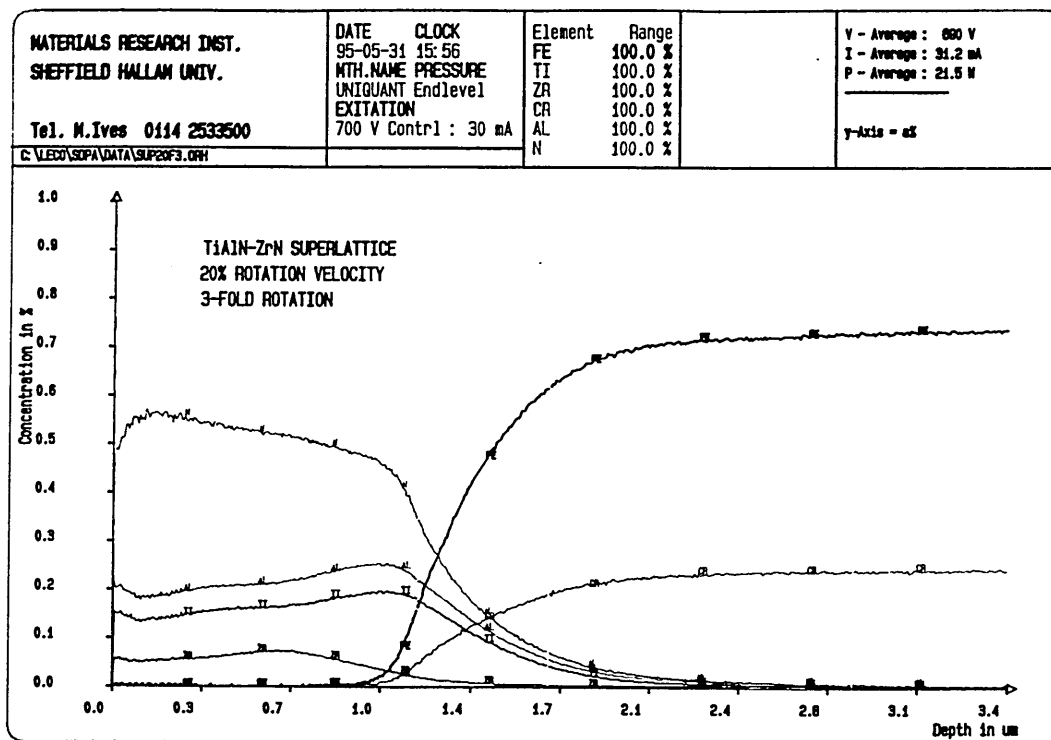
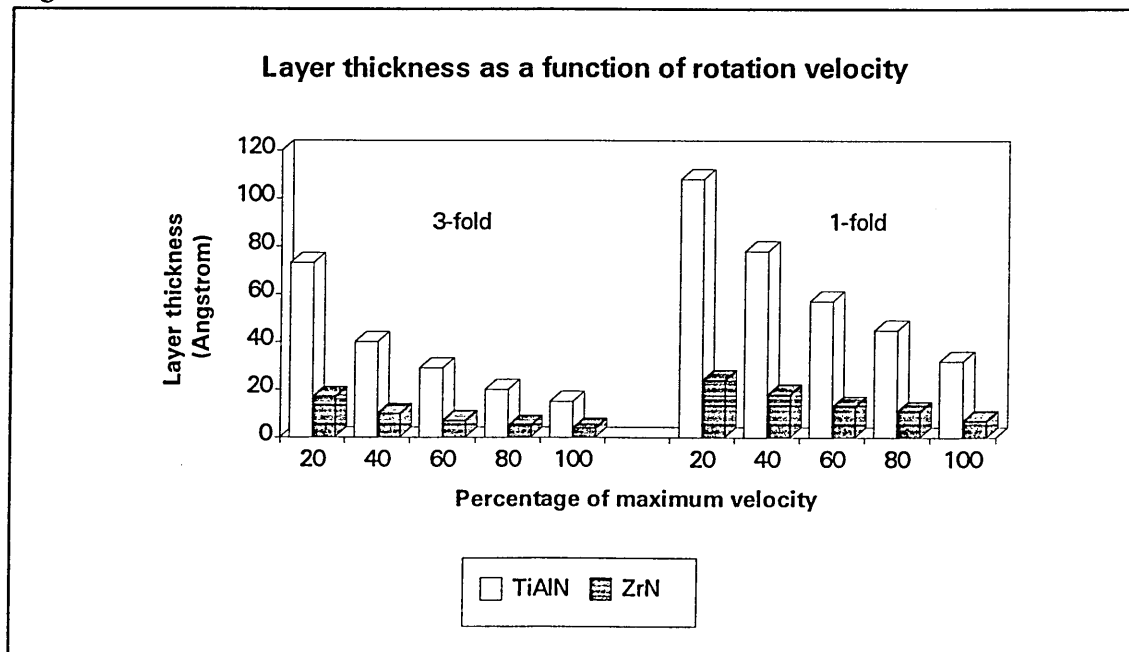


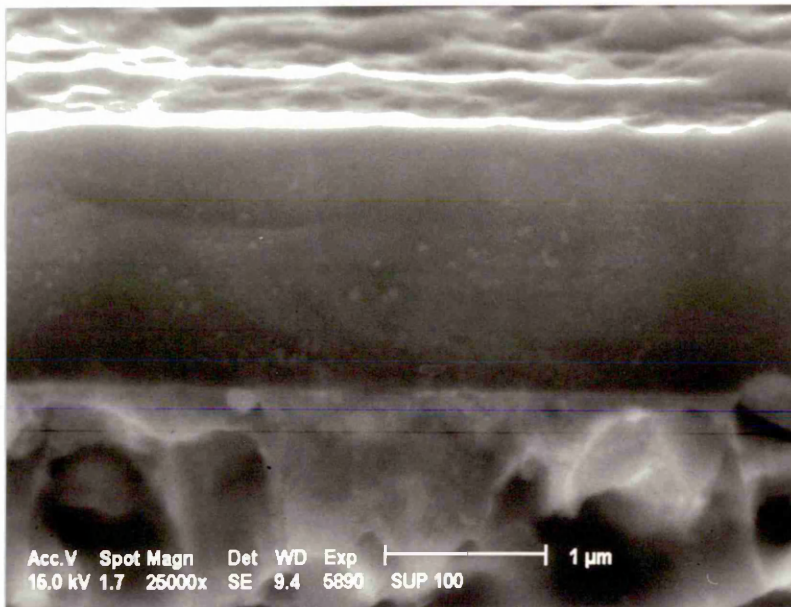
Figure 6.13.



### 6.2.3 Scanning electron microscopy results.

Cross-sectional scanning electron microscopy to examine coating structure revealed in all cases highly dense, smooth, uniform and featureless fracture faces where columnar morphology from even the largest multi-layer period had a lack of image contrast and was below the resolving power of the SEM (figure 6.14). Further analysis revealed surface and embedded macro-particle inclusions in the film of dimensions typically ranging from 0.1-3.0 $\mu\text{m}$  in diameter.

Figure 6.14. Cross-section micrograph of 3-fold rotation TiAlN-ZrN film.



Microscopic analysis of the surfaces of the films revealed a significantly higher macroparticle incorporation when deposition occurred under 1-fold rotation (figure 6.15a&b) than 3-fold rotation (6.16a&b). However no significant difference in macroparticle ingress as a function of increasing 3-fold rotation velocity was detected.

Figure 6.15a 1.5rpm 1-fold rotation.

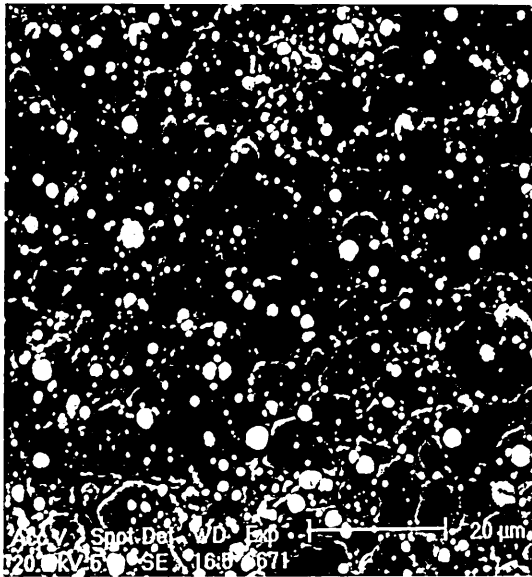


Figure 6.15b 7.5rpm 1-fold rotation.



Figure 6.16a 1.5rpm 3-fold rotation.

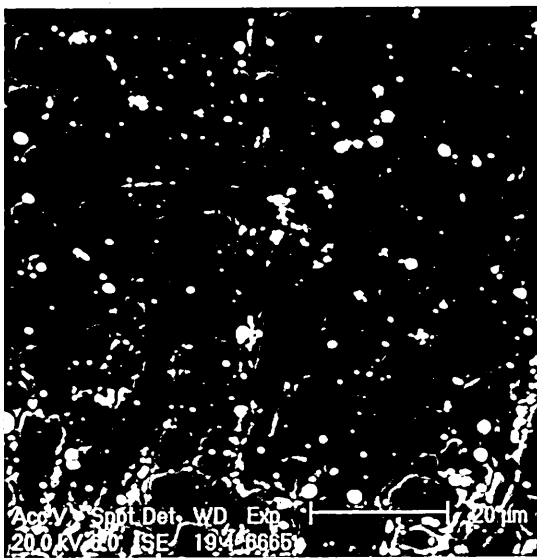
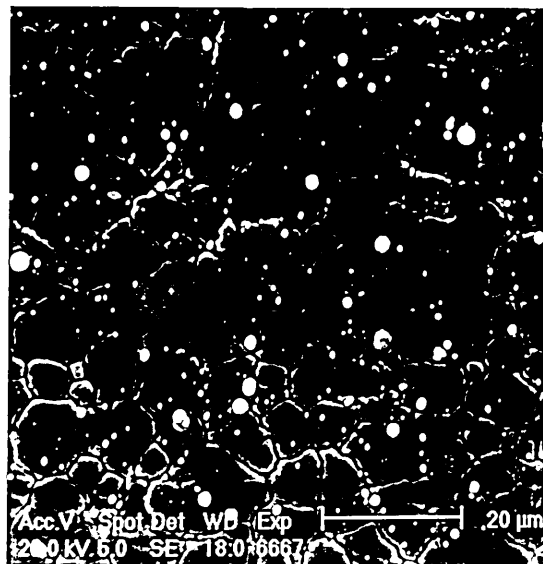


Figure 6.16b 7.5rpm 3-fold rotation.

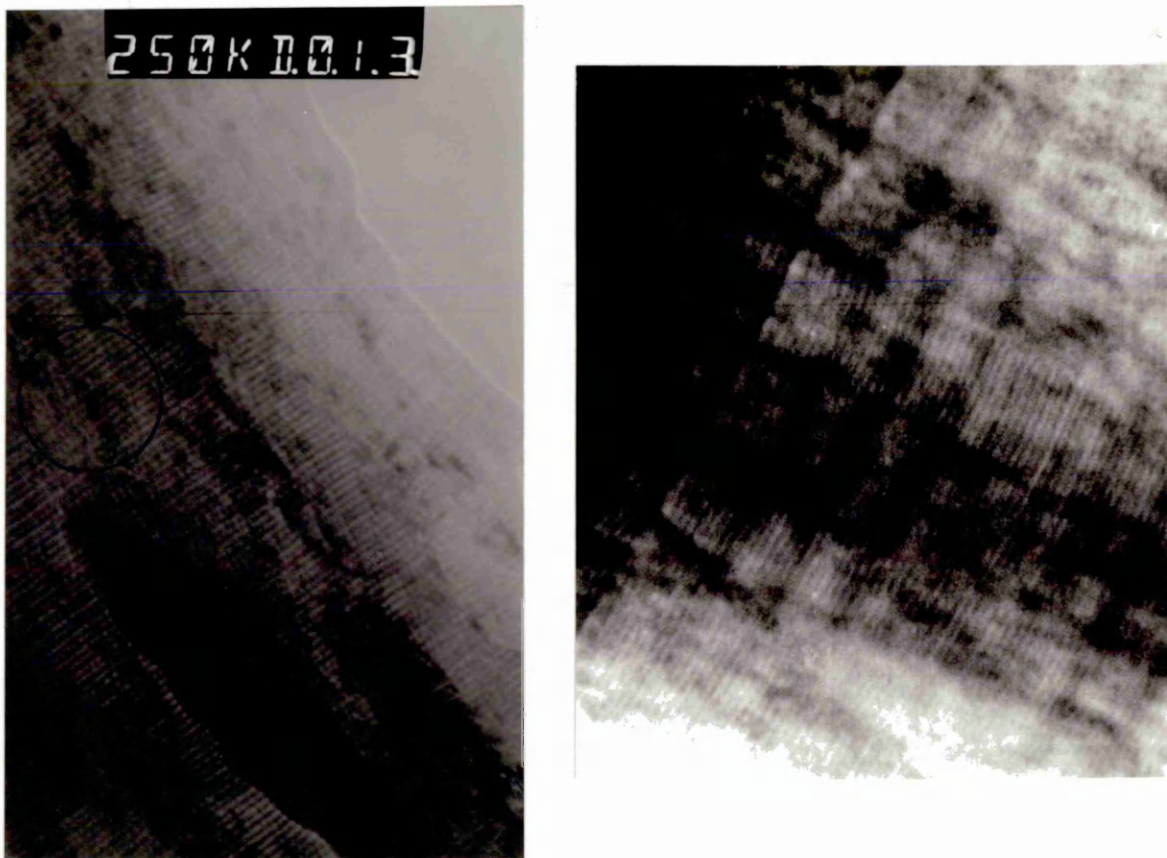


Examination of the cutting edges of coated drills also showed that the optimum negative bias voltage was -80V, as above this a red discoloration could occur from excessive re-sputtering of aluminium from the film.

#### 6.2.4 Transmission electron microscopy results.

Transmission electron microscopy was employed to study the structure of the coatings at high resolution. Fig 6.17a shows a bright field cross-sectional TEM micrograph (consistent with GDOES depth profiles) of the lamella nature, 6.0 r.p.m 3-fold rotation multi-layer film and clearly indicates that the thickness of the layers are unequal, the TiAlN (light layers) being larger at  $\sim 16 \pm 2 \text{ \AA}$  whilst the ZrN layers (dark) measure  $\sim 8 \pm 2 \text{ \AA}$ , giving a period of  $\sim 24 \pm 2 \text{ \AA}$ . This is in excellent agreement with GDOES results (section 6.2.2) and the low angle X-ray diffraction analysis which measured the layer period (distance from the centre of a TiAlN layer to the centre of an adjacent ZrN layer) at  $\sim 23 \pm 2 \text{ \AA}$ .

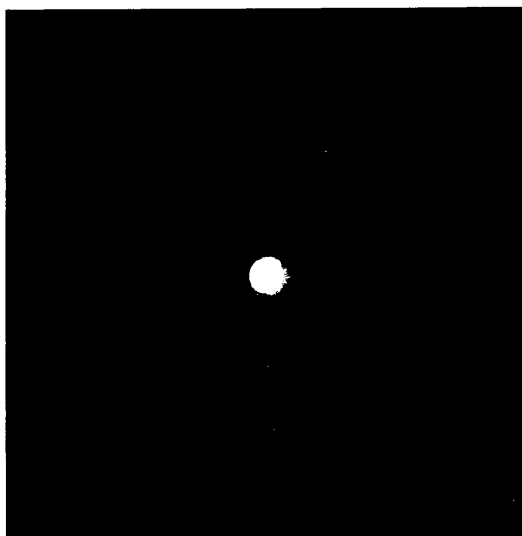
Figure 6.17a. XTEM micrograph (x250K)    Figure 6.17b. XSTEM micrograph (x200K)



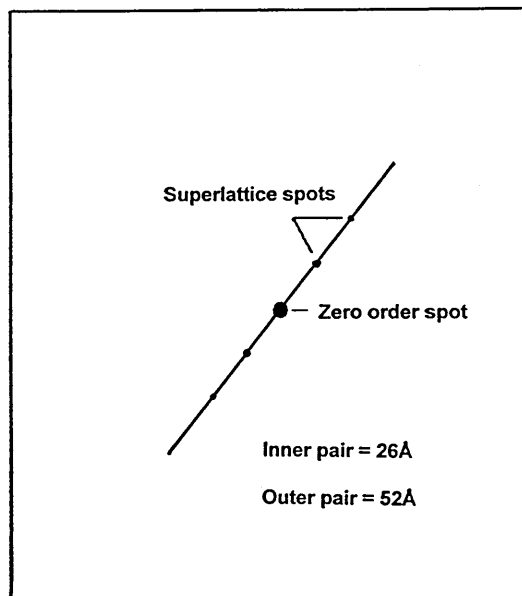
The columnar grain boundaries of the film, where the long axis is parallel to the flux direction and normal to the surface of the substrate, are just visible along with clear evidence of crystallographic high angle boundaries. The micrograph also reveals substantial long range integrity of the layers and implies that the growing front is extremely uniform.

Scanning transmission electron microscopy (STEM) on the same cross-section again revealed the lamella nature of the coating and showed clear evidence of columnar morphology. In addition, evidence of a secondary contrast mechanism was observed believed to be a result of a secondary beat frequency developed as a result of 3-fold planetary rotation of the substrate during deposition (figure 6.17b). Figure 6.18a&b show the selected area electron diffraction pattern taken from the region indicated on figure 6.17a and a schematic representation of the pattern. Consistent with the X-ray diffraction data, a series of spots appear close to the zero order spot representing the first, second and third order reciprocal lattice vectors of the layer period. These spots are sharp and therefore suggest that there is a high degree of coherency between the two layer structures and that the period possesses long range order. Layer spacing calculations taken from the inner set of spots gives a period of  $\sim 26 \pm 2 \text{ \AA}$  and is again in good agreement with X-ray diffraction results.

6.18a. SAED pattern.



6.18b. Schematic diagram.



Figures 6.19, 6.20 and 6.21 show the parallel electron energy loss (PEELS) jump ratio and filtered images performed on an outer region of the sample shown in figure 6.17a. These maps clearly indicate the presence of alternate layers of Zr and Ti rich material of the order of  $8 \text{ \AA}$  and  $16 \text{ \AA}$  respectively (demonstrating the remarkable spatial resolution obtained by this technique considering a sampling time of only a few seconds).

Figure 6.19. Ti PEELS jump ratio image.

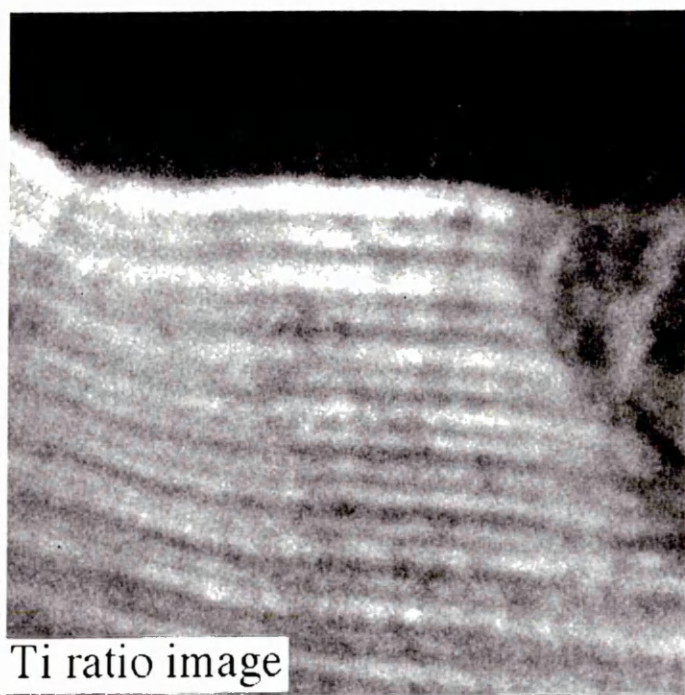


Figure 6.20. Zr PEELS jump ratio image.

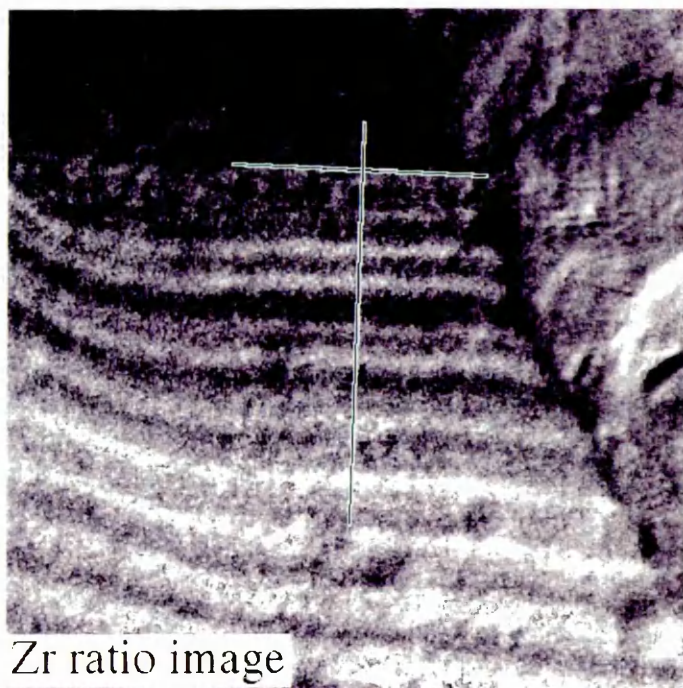
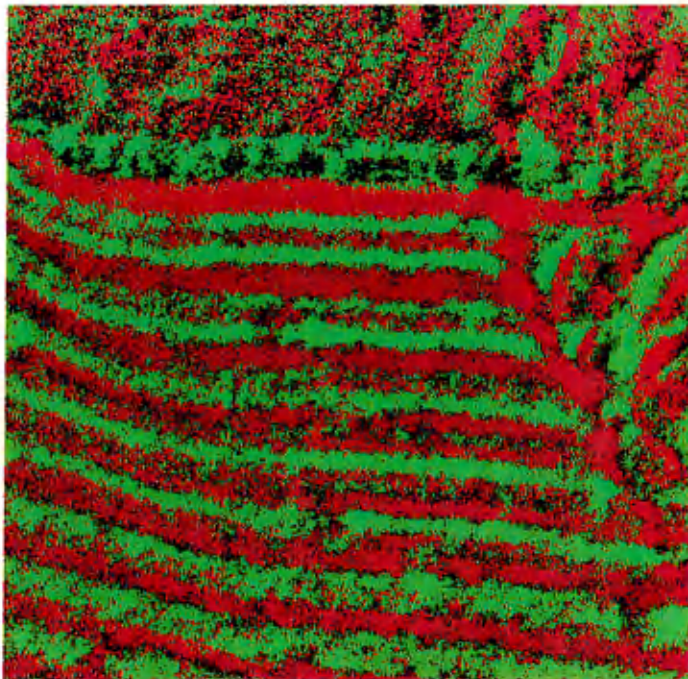


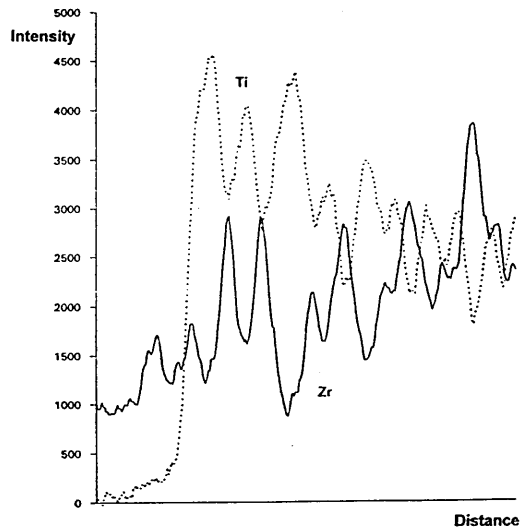
Figure 6.21. Combined PEELS jump ratio image.



Overlay map of Ti (red) elemental map and Zr (green) ratio map. These maps were shading corrected (removing gradual changes in overall brightness; note that this produces artefacts in the area of the substrate, but without the correction Zr is too strong in the bottom section and Ti in the middle section to give a good overlay map), aligned on the basis of the background images, and then put together in such a way that the brightest pixel of each map determines the colour.

Figure 6.22 shows a PEELS Ti and Zr linescan along a line normal to the film growth direction in the vicinity of the substrate. This result indicates distinct modulations of the compositions of both species again confirming the lamella nature of the multi-layer.

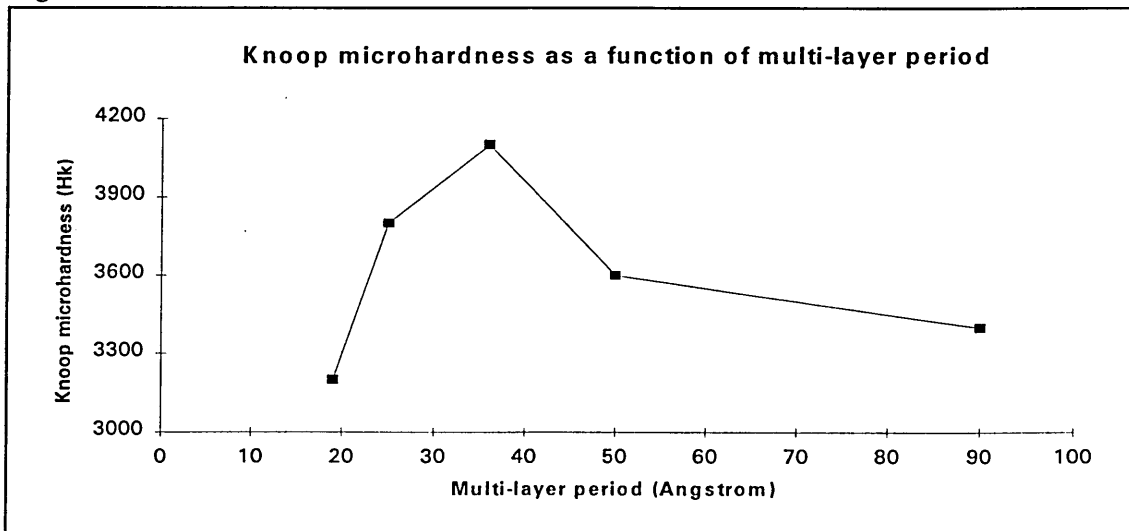
Figure 6.22. PEELS linescan across TiAlN-ZrN layers.



6.2.5. Knoop micro-hardness results.

Examination of the mean Knoop micro-hardness of the multi-layer coatings at 25gf ( $H_{k0.025}$ ) loading, deposited on high speed steel substrates undergoing 3-fold rotation are shown in figure 6.23. The mean hardness and standard deviation was found to increase steadily with decreasing period before reaching a maximum of approximately 4100 $H_k$  at a superlattice period between 30-50Å. At periods less than 30Å a significant reduction in microhardness was recorded.

Figure 6.23.

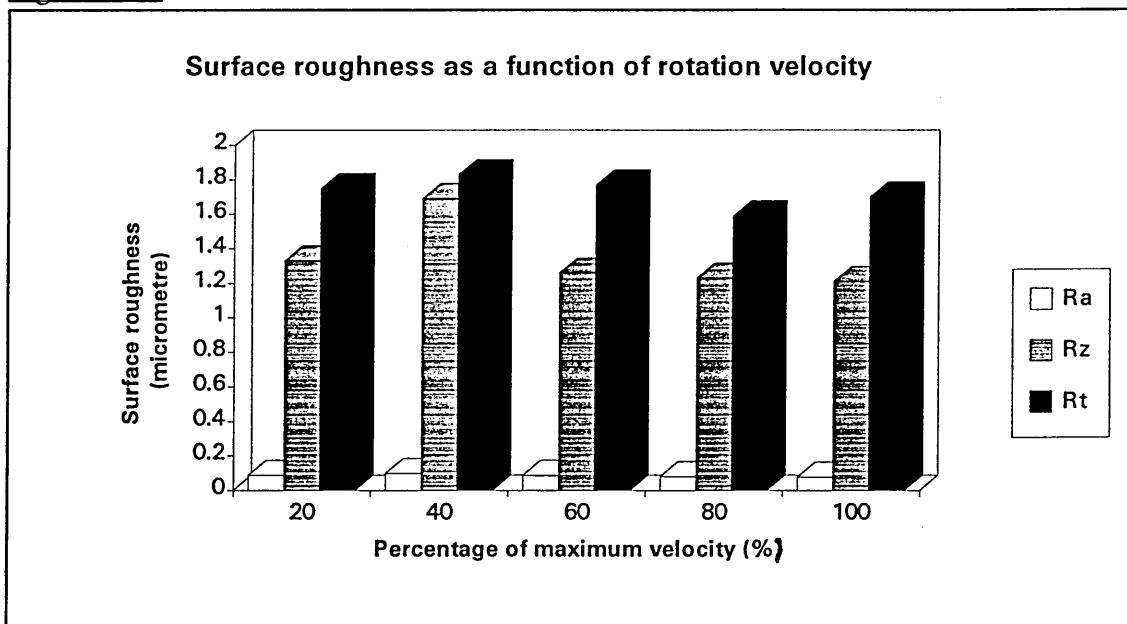


Typical Knoop indentation lengths were of the order of  $9\mu\text{m}$ , hence the virtual indentation depths (3) were of the order of  $3\mu\text{m}$  ( $\{9/30\} \times 10$ ). As the film thickness was typically  $1.5\text{-}2.0\mu\text{m}$ , the data was clearly influenced by the hardness of the HSS substrate. However, indentations made at a lower load of  $10\text{gf}$  ( $H_{k0.010}$ ) proved unreliable due to the small indent size, the resolution limits of the vernier optical microscope and the surface roughness.

#### 6.2.6. Surface roughness results.

The surface roughness data correlated well with the topographical studies carried out by scanning electron microscopy. Comparison of the  $R_a$ ,  $R_z$  and  $R_t$  values measured as a function of 3-fold rotation velocity revealed very similar and relatively low roughness values for all coated samples on polished HSS substrates despite arc evaporation for 1 hour (figure 6.24). The results were similar to values found earlier for various ABS coatings and indicated that the  $\langle 100 \rangle$  preferred orientation and high bias current densities obtained by combined arc / magnetron processing may have a beneficial smoothing effect and a low macroparticle flux was generated from Zr targets.

Figure 6.24.



#### 6.2.7. Thickness and deposition rate.

Calotest and GDOES measurements on films deposited under 3-fold rotation showed that all coatings were of similar thickness at  $1.5\mu\text{m}$  and were developed at a mean sputtered base layer deposition rate of  $0.65\mu\text{mhr}^{-1}$  and a multi-layer deposition rate of

$0.85 \mu\text{mhr}^{-1}$ . Coatings deposited using single fold rotation showed in all cases a significantly enhanced thickness, typically around  $3.5\mu\text{m}$ , generated at a mean base layer rate of  $1.5 \mu\text{mhr}^{-1}$  and a multi-layer deposition rate of  $2.0 \mu\text{mhr}^{-1}$ . The relatively small rise in deposition rate achieved under combined arc / magnetron conditions was probably due to collimation of the cathodic arc vapour flux by a well worn erosion trench on the surface of the Zr target.

#### 6.2.8. Rockwell and scratch adhesion results.

In general, the investigations showed little alteration in the scratch critical load and VDI indent quality with varying high speed steel rotation velocity. The application of a sputtered base layer prior to multi-layer deposition provided average critical load values of approximately 50N (figure 6.25) which correlated well with a consistent indent quality for all coatings of 1-2 at 100 times magnification. The Rockwell tests consistently showed no signs of spallation around the circular indent (figure 6.26), however a phenomenon of very fine, concentric circular cracking was occasionally observed at the perimeter of the indentation thought to be consistent with the diameter of the deformation zone ("virtual indenter") created by the Rockwell-C diamond (3).

Figure 6.25

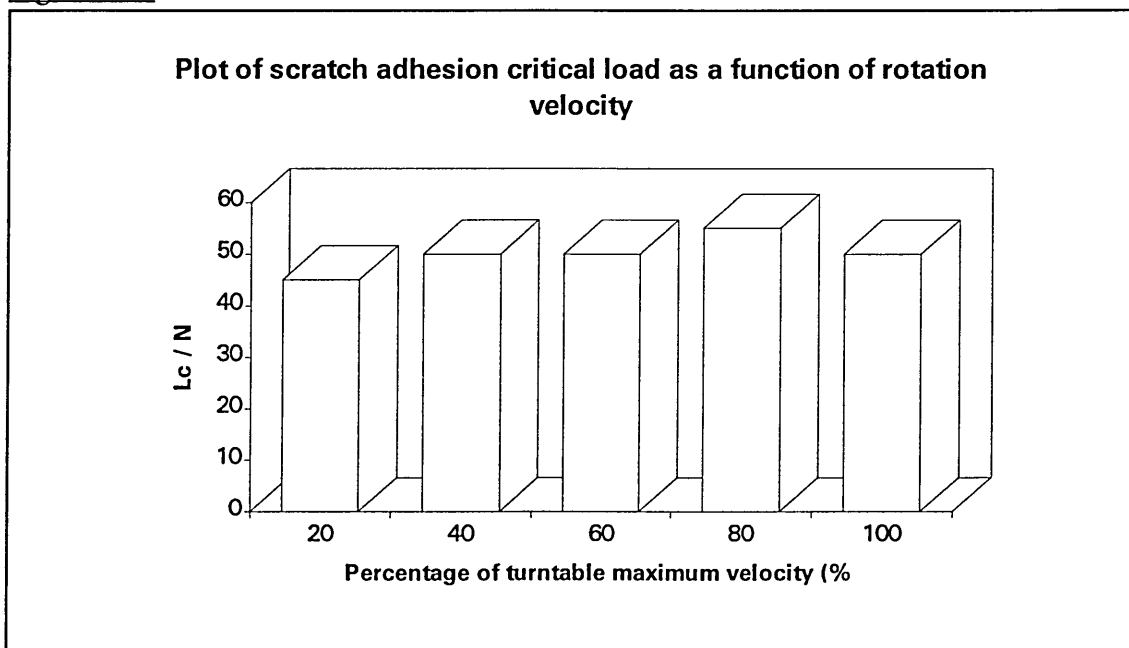
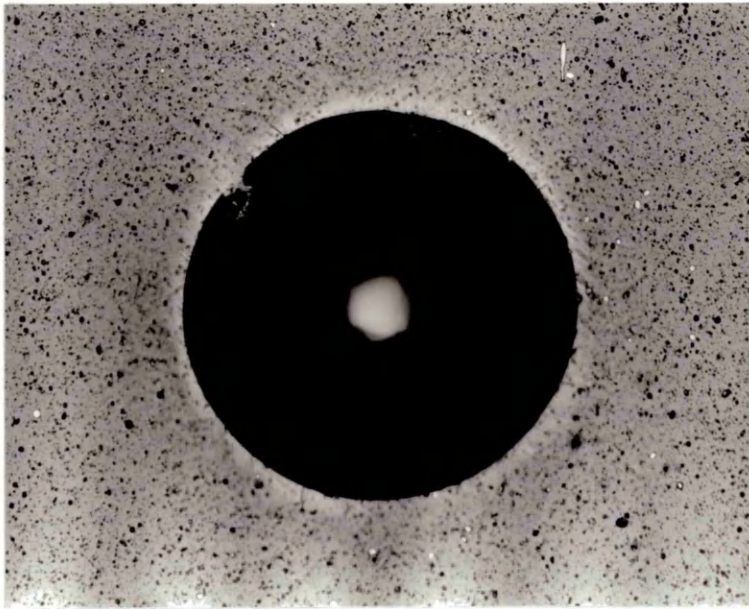
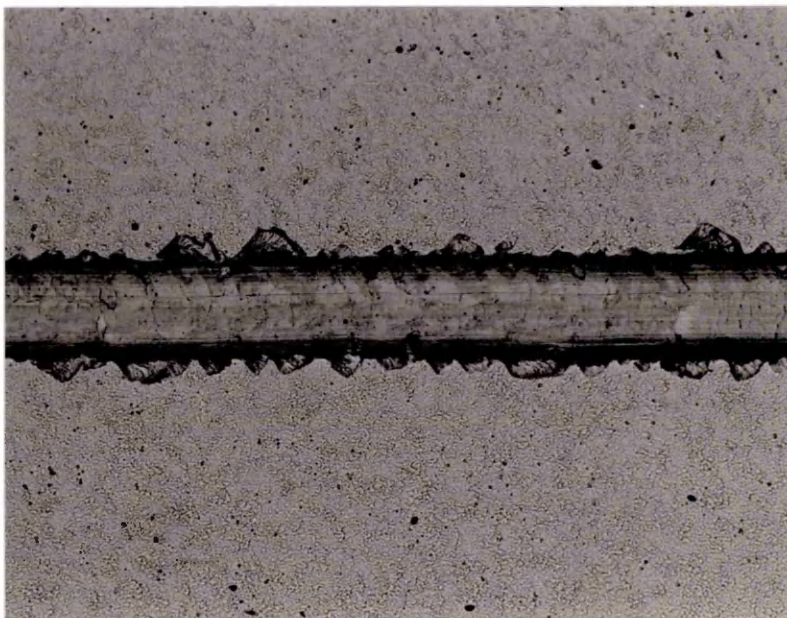


Figure 6.26a.



Analysis of the scratch channels (figure 6.27) revealed in all cases failure occurred via a brittle fracture mechanism.

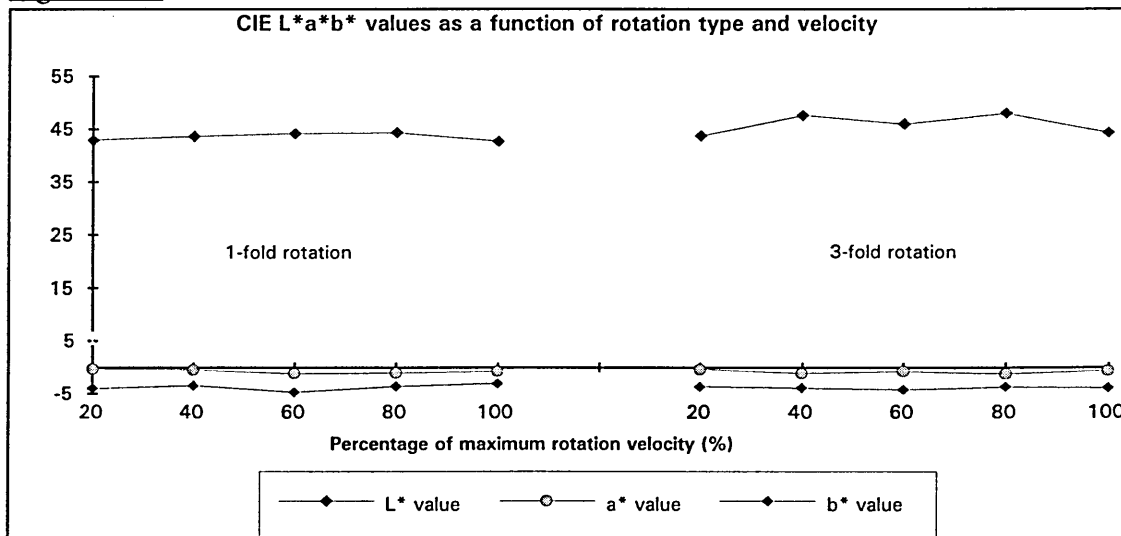
Figure 6.27.



### 6.2.9. Colour measurements.

Direct investigation of the variation in film colour with type of rotation could only be undertaken on coated 304 stainless steel substrates (grade 2B) which had a duller surface finish than the mirror polished HSS substrates. All TiAlN-ZrN coatings were found to have a high lustre metallic blue appearance and exhibited near constant  $a^*$  and  $b^*$  values as a function of single and 3-fold rotation velocity. The highest  $L^*$  values were recorded from 3-fold rotating substrates due a reduction in macro-particle incorporation from metal ion etching and combined arc / magnetron deposition (figure 6.28). Films deposited on HSS substrates under 3-fold rotation generally had  $L^* \sim 49$ ,  $a^* \sim 1$  and  $b^* \sim 4$ .

Figure 6.28.



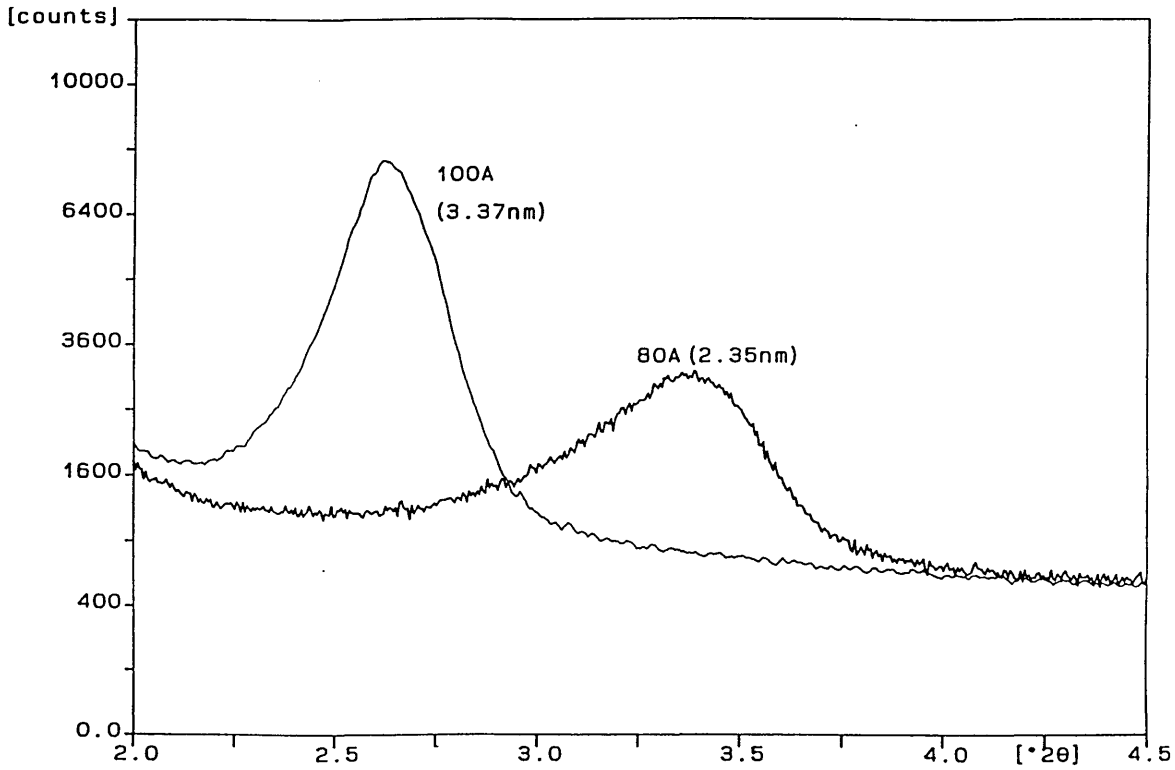
### 6.3. The effect of arc current on the period of TiAlN-ZrN superlattice films.

The effect of deposition rate on the period and properties of the TiAlN-ZrN multi-layer system was examined by comparison of coatings utilising steered arc currents of 80A and 100A during combined arc / magnetron deposition at 80% of the maximum rotation velocity (6 r.p.m).

#### 6.3.1. X-ray diffraction results.

Low angle X-ray analysis revealed a significant increase in layer period with increasing arc current (figure 6.29 and table 6.3).

**Figure 6.29. The effect of arc current on multi-layer period.**



High angle X-ray diffraction revealed an f.c.c unit cell structure where lattice parameter ( $a_0$ ) increased slightly with increasing arc current (figure 6.30). Texture analysis demonstrated both coatings had a strong  $\langle 100 \rangle$  preferred orientation.

**Figure 6.30. High angle X-ray diffraction trace 100A arc current TiAlN-ZrN.**

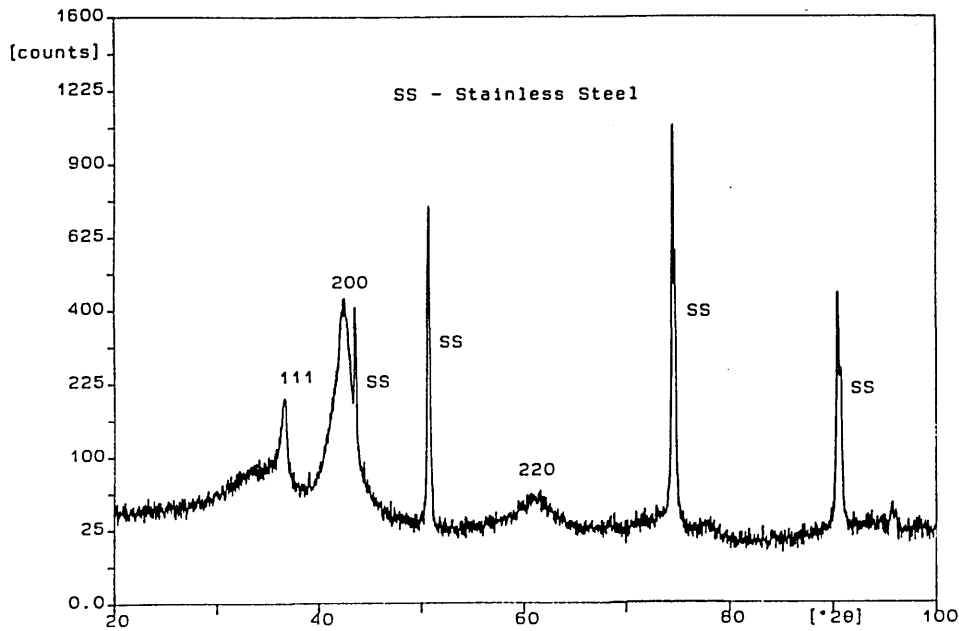


Table 6.3.

Coating	Orientation	$a_0 / \text{\AA} \pm 0.01\text{\AA}$	Period / $\text{\AA} \pm 2\text{\AA}$
TiAlN-ZrN (80A)	<100>	4.25	23
TiAlN-ZrN (100A)	<100>	4.26	34

### 6.3.2. Mechanical and physical properties.

Examination of the mechanical and physical properties of the films revealed that the microhardness reduced with increasing arc current, despite an increase in layer period, due to more extensive interfacial mixing, enhanced ion bombardment and higher bias current density which led to annealing of the film (table 6.4). Surface profiling data also showed an increase in average surface roughness with increasing arc current due to a higher number of macro-particles generated at the target and incorporated within the growing film. Scratch and Rockwell adhesion values remained constant and correlated well, whilst colourimetry revealed an increase in  $L^*$  value and a decrease in  $a^*$  and  $b^*$  values at 100A arc current indicating the formation of a brighter and more blue appearance of the coatings. Calotest investigations demonstrated that the higher arc current caused an increase in thickness from  $1.5\mu\text{m}$  to  $1.8\mu\text{m}$ .

Table 6.4.

Analysis.	TiAlN-ZrN (80A)	TiAlN-ZrN (100A)
Knoop microhardness ( $H_k0.025 \pm 350H_k$ )	3800	3500
Rockwell-C indent classification	1-2	1-2
Scratch adhesion $L_c / N \pm 2N$	50	50
Appearance	Metallic blue	Metallic blue
$L^* \pm 0.1$	48.93	49.34
$a^* \pm 0.1$	-0.96	-1.08
$b^* \pm 0.1$	-3.37	-3.76
Substrate bias current I / A $\pm 1A$	22	27
$R_a / \mu\text{m} \pm 0.01\mu\text{m}$	0.12	0.14

#### 6.4. The deposition and properties of arc / magnetron TiAlN-TiN coatings.

Utilisation of titanium as an unbalanced magnetron sputtering and steered arc evaporation source instead of zirconium, using identical deposition conditions to those outlined in section 6.1, allowed fabrication of TiAlN-TiN multi-layer coatings. The films were deposited on standard high speed steel and stainless steel substrates undergoing 3-fold rotation at a primary velocity of 6 r.p.m (80%) and analysed by a range of bulk and micro-analysis techniques.

##### 6.4.1. X-ray diffraction results.

High and low angle X-ray analysis (figure 6.31 and 6.32) indicated that small period, reproducible multi-layer TiAlN-TiN films could be fabricated by the same technique utilised in the production of the TiAlN-ZrN system. The TiAlN-TiN coatings exhibited  $\langle 100 \rangle$  orientation, face centred cubic structure and unit cells of dimension  $4.21 \text{ \AA}$  (table 6.5).

Figure 6.31. High angle X-ray trace from 6rpm 3-fold rotation TiAlN-TiN

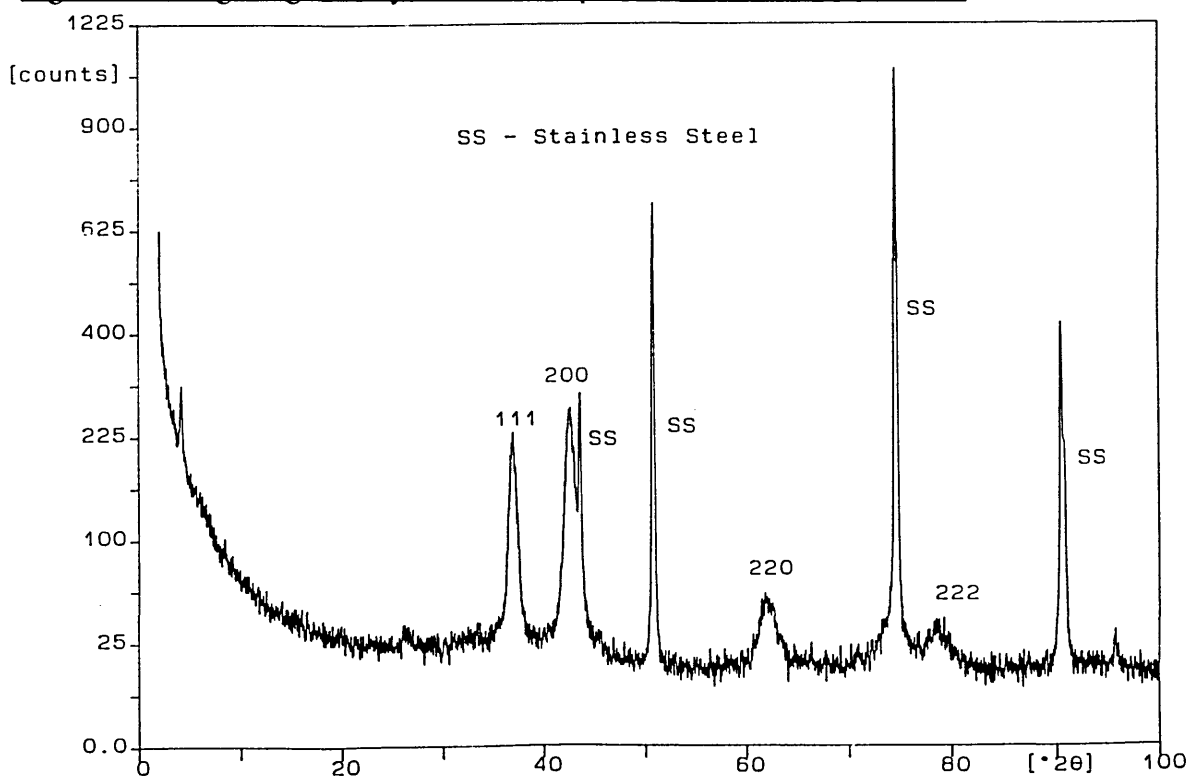
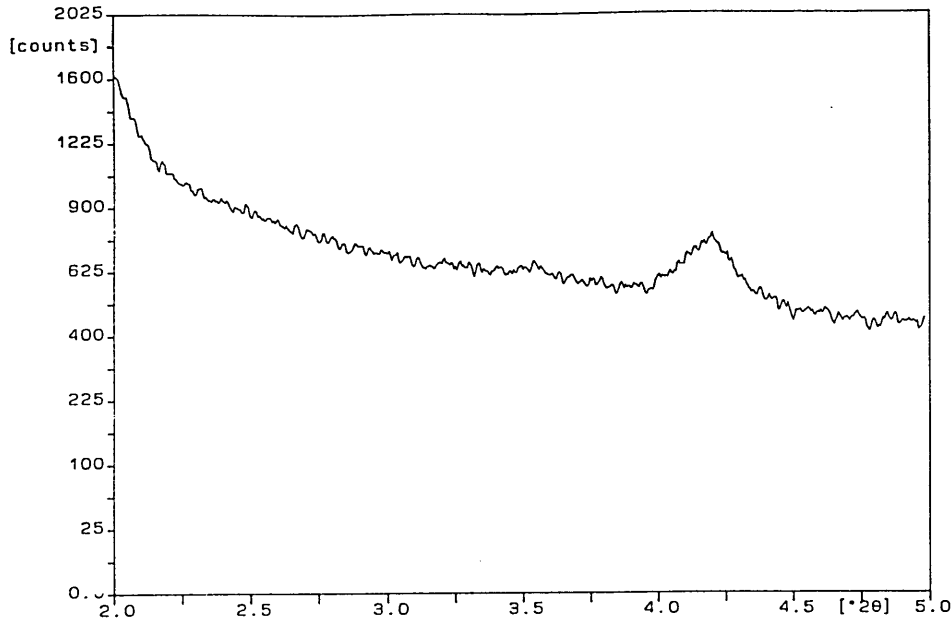


Table 6.5.

Coating	Orientation	$a_0 / \text{ \AA} \pm 0.01 \text{ \AA}$	Period / $\text{ \AA} \pm 2 \text{ \AA}$
TiAlN-TiN	$\langle 100 \rangle$	4.21	21.0

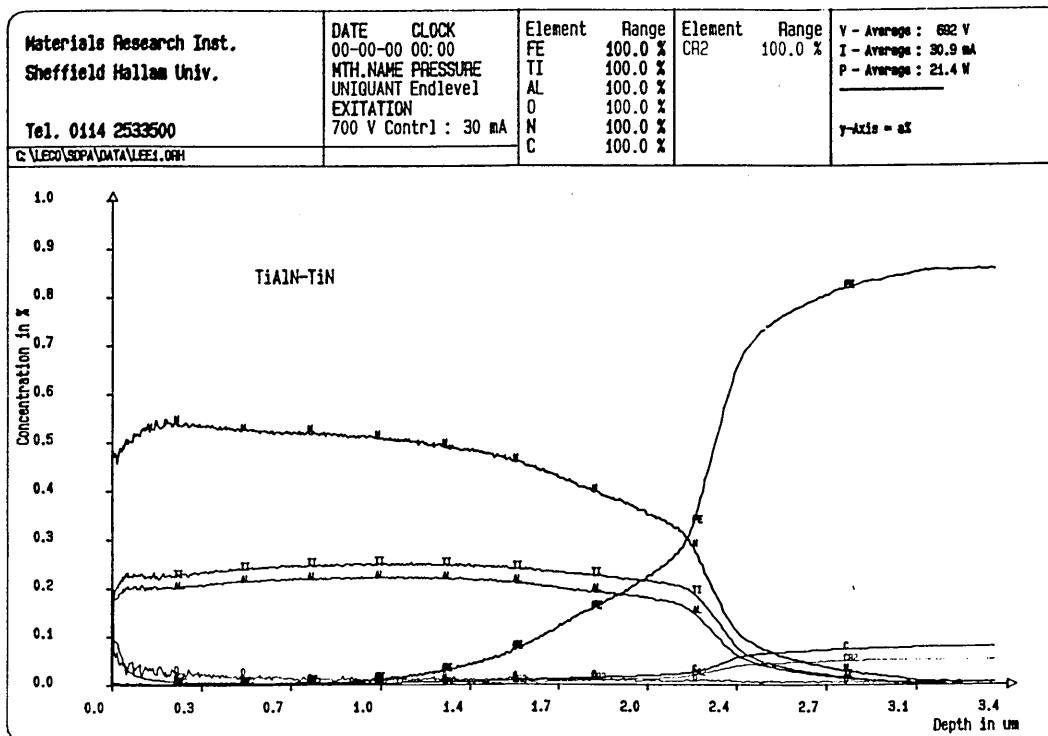
Figure 6.32. Low angle trace from 6rpm 3-fold rotation TiAlN-TiN



6.4.2. GDOES analysis.

Quantitative depth profiling through 3-fold rotation arc / magnetron TiAlN-TiN revealed a stoichiometric film had been developed of thickness similar to TiAlN-ZrN, metal composition ratio rich in titanium and a less well defined coating / substrate interface (figure 6.33).

Figure 6.33. Quantitative GDOES profile on arc / magnetron 6rpm 3-fold TiAlN-TiN.



### 6.4.3. Mechanical and physical properties.

Knoop diamond indentation data revealed that the TiAlN-TiN multi-layer structure had caused only a modest increase in microhardness (table 6.6) over standard ABS TiAlN values ( $2200H_{k0.025}$ ) and were significantly less than the corresponding TiAlN-ZrN coating ( $3800H_{k0.025}$ ). These values are in excellent agreement with the reduction in lattice mis-match (TiAlN-TiN  $\sim 1.6\%$ , TiAlN-ZrN  $\sim 9.3\%$ ). Adhesion measurements showed that the scratch and Rockwell values were comparable to TiAlN-ZrN values and colour measurements demonstrated a change towards a shiny, charcoal grey appearance. Talysurf profiles revealed an increase in roughness over the equivalent TiAlN-ZrN film due to the production of a higher macro-particle density from the lower melting point titanium target.

Table 6.6.

Analysis.	TiAlN-TiN data
Knoop microhardness ( $H_{k0.025} \pm 300H_k$ )	2500
Rockwell-C indent classification	1-2
Scratch adhesion $L_c / N \pm 2N$	45
Appearance	Charcoal grey
$L^* \pm 0.1$	49.54
$a^* \pm 0.1$	1.12
$b^* \pm 0.1$	-2.21
$R_a / \mu m \pm 0.01\mu m$	0.16

### 6.5. Multi-layer fabrication by co-sputter deposition without combined steered arc evaporation.

The importance of the combined arc / magnetron coating strategy when operating with highly reactive metals such as titanium or zirconium was demonstrated during investigations of TiAlN-ZrN and TiAlN-TiN films fabricated by four cathode unbalanced magnetron co-sputter deposition. Processing was identical to stages 1-4 of the regime outlined in section 6.1, however the second hour of deposition (stage 5) was changed to allow all four targets (3TiAl plus 1 Zr or Ti) to continue to operate in closed field unbalanced magnetron mode at a power 8KW.

### 6.5.1. X-ray diffraction results.

High angle X-ray diffraction analysis of ABS deposited films (figure 6.34 and 6.35) revealed an increase in (111) peak intensities and in the case of TiAlN-TiN a change in preferred orientation to the  $\langle 111 \rangle$  direction. The low angle diffraction traces identified small but discernible reflection peaks (figure 6.36 and table 6.7). The lack of intensity of the peaks is probably due to the ZrN or TiN based phase being very thin (because of a much reduced growth rate from sputtering a poisoned target) and thus mass effect considerations would generate only very weak reflections.

Figure 6.34. High angle X-ray diffraction trace on ABS TiAlN-ZrN

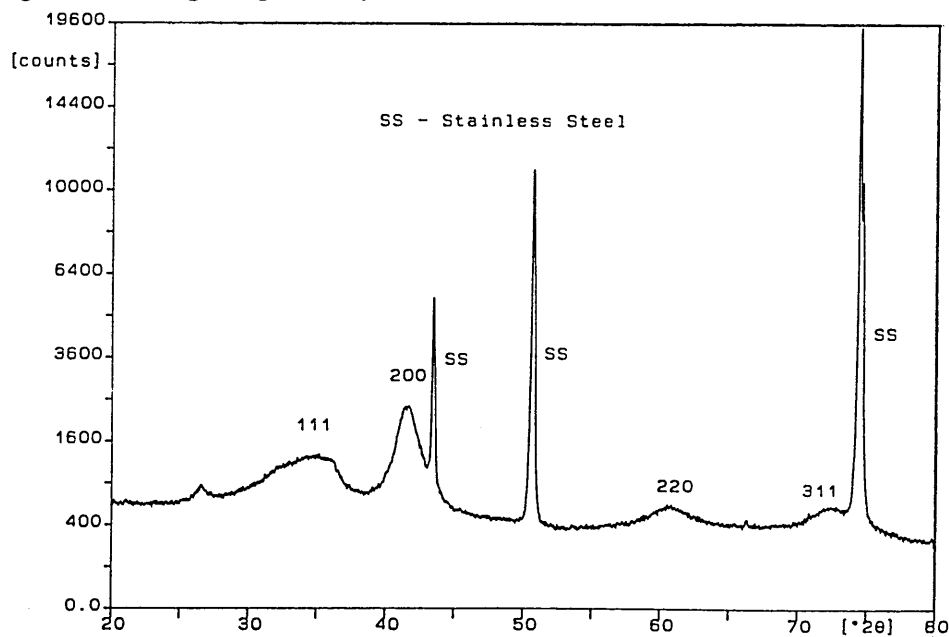


Figure 6.35. High angle X-ray diffraction trace on ABS TiAlN-TiN.

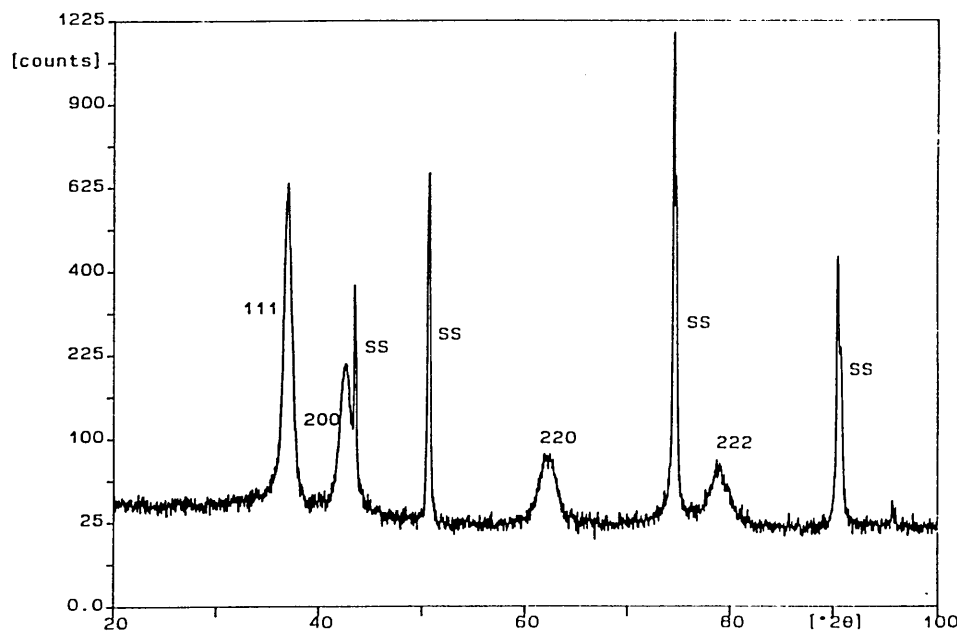


Figure 6.36. Low angle diffraction trace on ABS TiAlN-ZrN

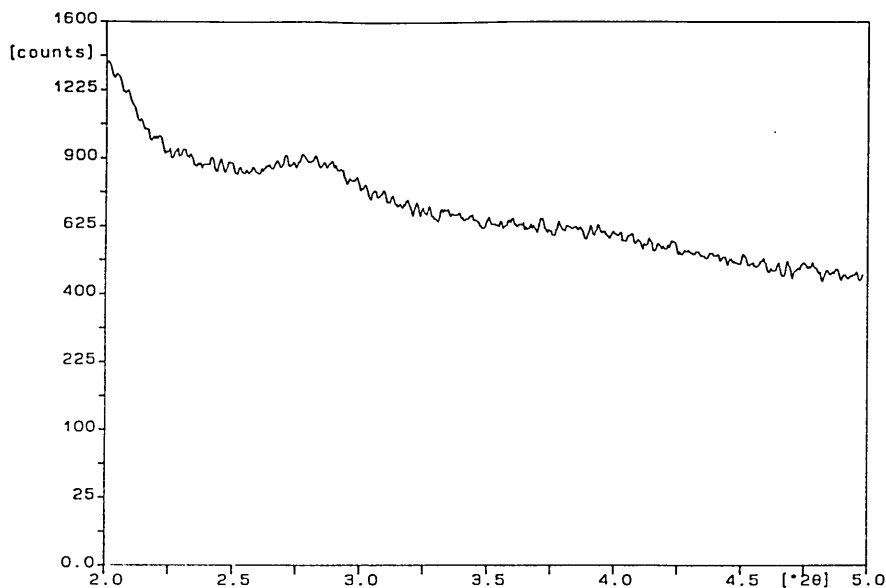


Table 6.7.

Coating	Orientation	$a_0 / \text{Å} \pm 0.01\text{Å}$	Period / $\text{Å} \pm 2\text{Å}$
ABS TiAlN-ZrN	<100>	4.27	23
ABS TiAlN-TiN	<111>	4.23	24

### 6.5.2. GDOES analysis.

ABS TiAlN-ZrN and TiAlN-TiN coatings both showed a reduction in Ti and Zr content within the films when compared against the equivalent arc / magnetron coatings due to enhanced reactive gas poisoning effects during sputter deposition. In both cases the result of co-sputtering was the formation of slightly over-stoichiometric films.

### 6.5.3. Mechanical and physical properties.

The effect of sputtering a poisoned zirconium or titanium target in a high nitrogen partial pressure, producing a weakly pronounced and low period multi-layer structure, had important consequences for the coating properties (table 6.8). Microhardness values in both cases showed significant reductions over the equivalent combined arc / magnetron multi-layer coating. The graded base layer still maintained good levels of scratch and Rockwell adhesion, however the reduction in bias current density and Ti or Zr deposition rate caused a reduction in coating brilliance. TiAlN-ZrN coatings suffered a decrease in  $L^*$ ,  $a^*$  and  $b^*$  values whilst TiAlN-TiN showed a similar decline in  $L^*$  and  $b^*$  and a small increase in  $a^*$ . Co-sputter deposition also generally created a lower degree of surface roughness than arc / magnetron processing.

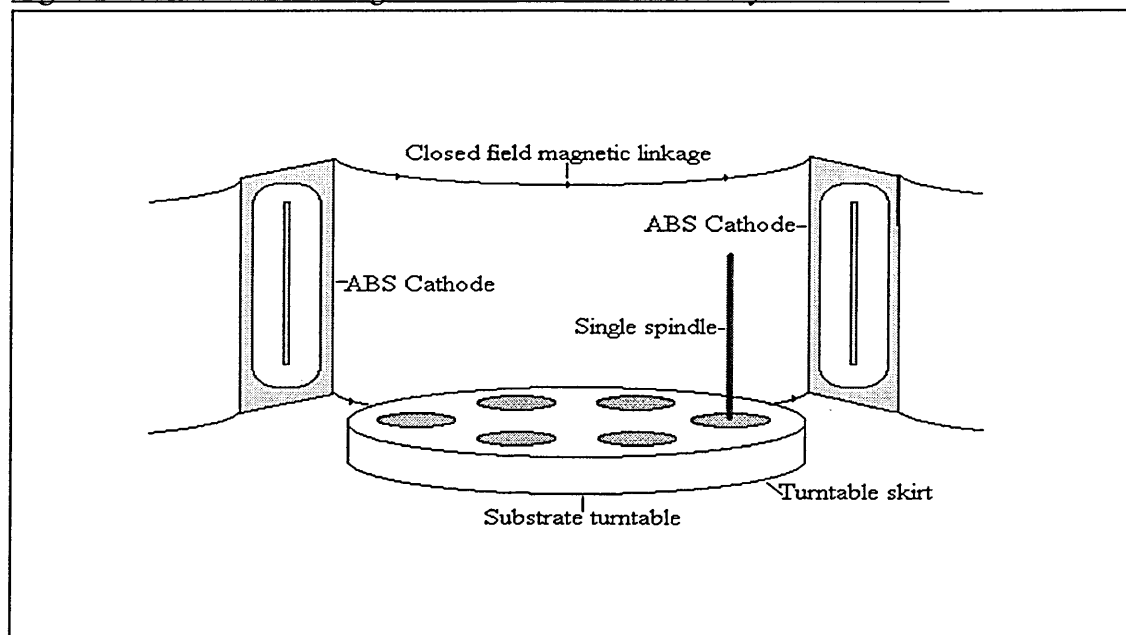
Table 6.8.

Analysis.	ABS TiAlN-ZrN	ABS TiAlN-TiN
Knoop microhardness ( $H_k0.025$ ) $\pm 350H_k$	3300	2300
Rockwell-C indent classification	1-2	1
Scratch adhesion $L_c / N \pm 2N$	50	50
Appearance	Blue/grey	Charcoal grey
$L^* \pm 0.1$	44.57	43.60
$a^* \pm 0.1$	0.38	3.69
$b^* \pm 0.1$	-1.12	-0.33
$R_a / \mu\text{m} \pm 0.01\mu\text{m}$	0.10	0.13

### 6.6. Bias current measurements

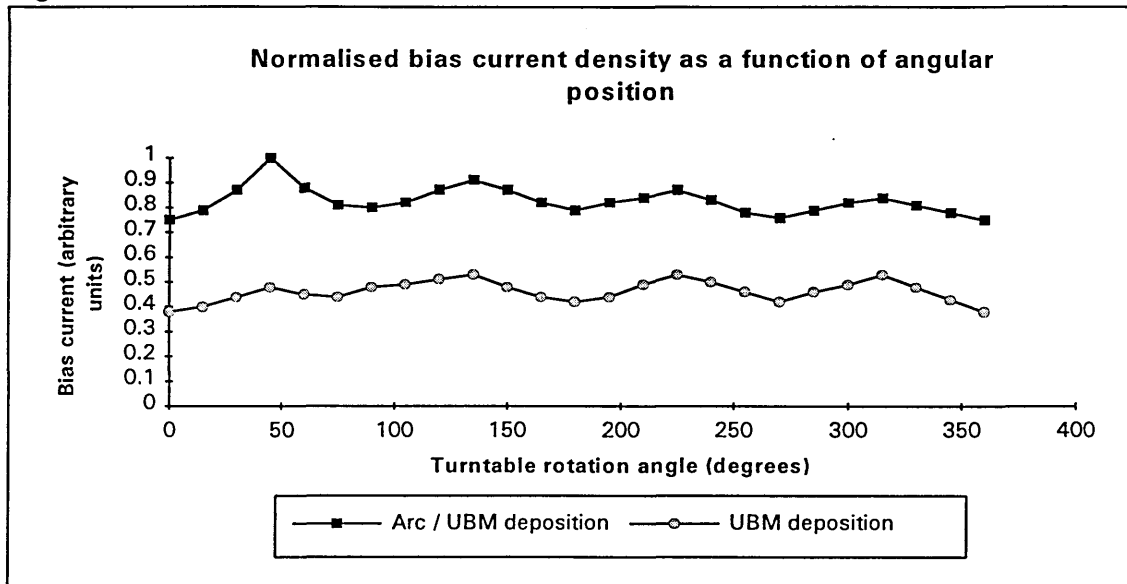
Bias current measurements were performed within the arc-bond sputter chamber to determine the plasma uniformity with varying position of the rotating substrate turntable.

Figure 6.37. Chamber arrangement for bias current density measurement.



Bias current intensity as a function of time measurements were made under slow rotation TiAlN-ZrN combined arc / magnetron and ABS co-sputter deposition conditions where the chamber contained only a single substrate spindle linked directly to an X-Y plotter (figure 6.37).

Figure 6.38.



The plot of bias current density as a function of angular position clearly demonstrates a significantly higher normalised bias current density in combined arc / magnetron processes when compared against all four cathodes operating in UBM deposition mode (figure 6.38). The bias current density was found to peak in intensity when the substrate spindle moved directly in front of each target (positions at 45°, 135°, 225°, 315°). However, examination of the standard UBM mode plot over the range 30-60° illustrates the effect of sputtering a poisoned Zr target, whilst investigation of the arc / magnetron process over the same range reveals an increased bias current density due to evaporation of the Zr target.

### **6.7. Modelling of the substrate rotation and coating flux density.**

Adaptation of an original mathematical treatment by Rother et al (4,5) allowed vector analysis and computer modelling of the 3-fold rotation path, normalised vapour flux density and film growth rate (to a first approximation) on a substrate positioned at a nominal distance of 250mm from each cathode as it was periodically exposed to four orthogonal sources within an arc-bond sputter chamber.

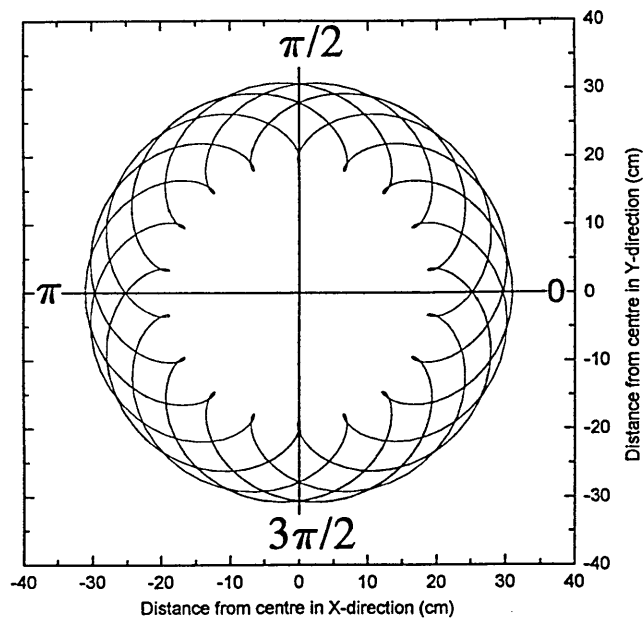
The calculation model (appendix 1) was implemented using a MATHCAD™ commercial PC-based programming package and the calculation program developed permitted the computation and visualisation of the normalised magnitude of the particle current densities and growth rates of the source material. Because of the markedly differing numbers of revolutions of the individual contributions to the substrate rotation

and to reduce processing time, the coating conditions were computed in a finite time scale.

Figure 6.39 shows a typical result from modelling the path of a substrate undergoing 3-fold rotation at a primary turntable velocity of 5.2 r.p.m in a HTC 1000-4 ABS chamber over a period of 90 seconds when started from the position  $(d_1, d_2, d_3) = (0,0,0)$ .

Figure 6.39.

Plot of the path a substrate undertakes during 3-fold rotation in an Arc-Bond Sputter deposition chamber



Knowledge of the exact position of a substrate with respect to the four orthogonal sources at any moment in time allowed three sets of flux density and growth rate modelling experiments to be carried out.

Figures 6.40a-6.40d illustrate the normalised coating flux density and growth rate delivered by four sources delivering identical vapour yields, simulating a standard ABS TiAlN or TiN deposition process on a 3-fold rotating substrate, as a function of various starting position  $(d_1, d_2, d_3)$ .

Figure 6.40a.

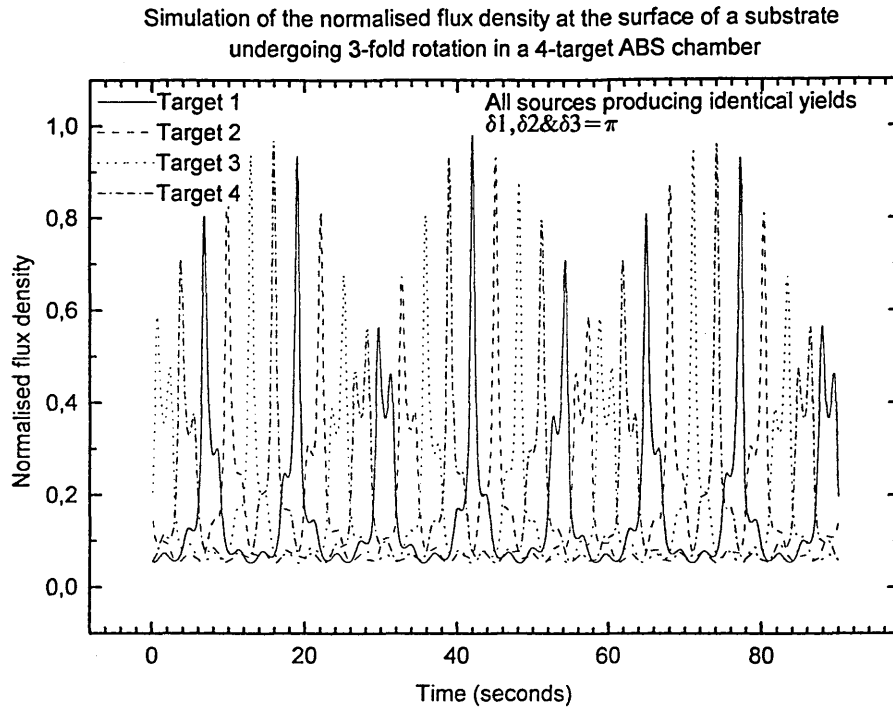


Figure 6.40b.

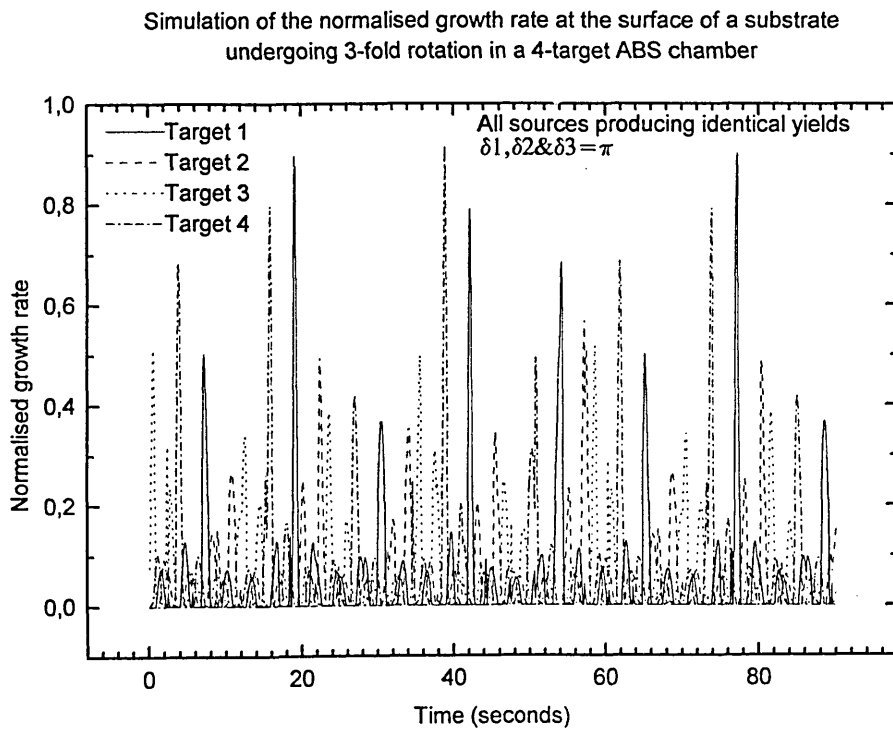


Figure 6.40c.

Simulation of the normalised flux density at the surface of a substrate undergoing 3-fold rotation in a 4-target ABS chamber

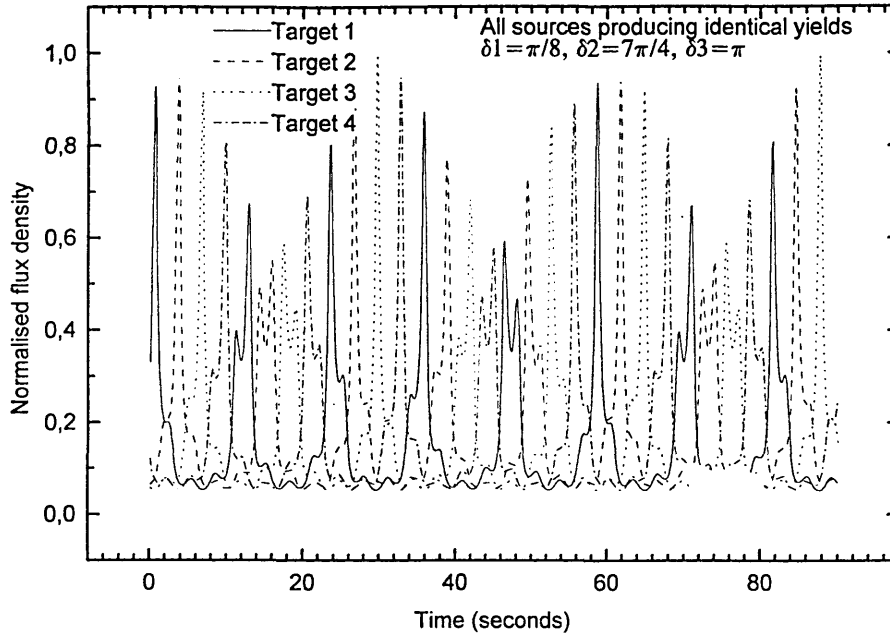
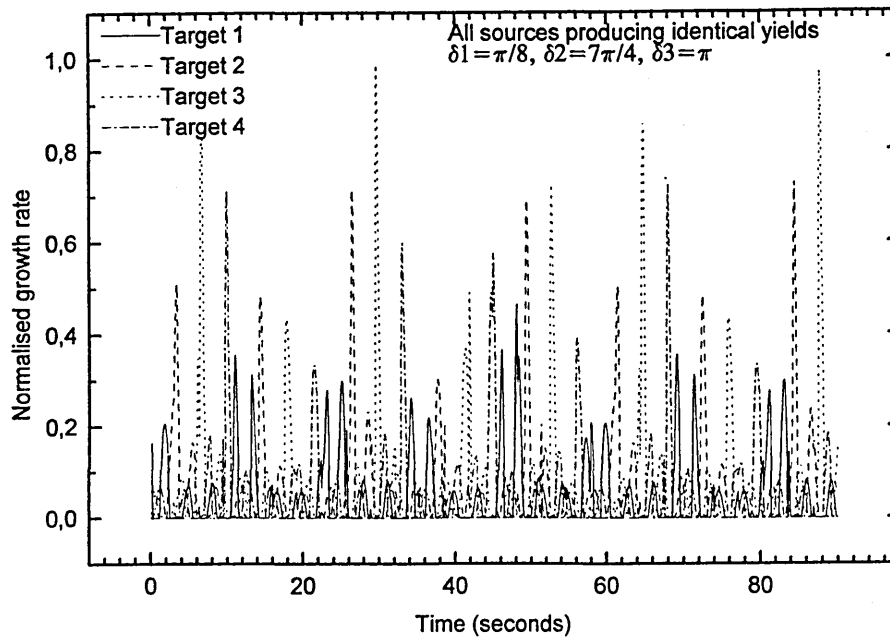


Figure 6.40d.

Simulation of the normalised growth rate at the surface of a substrate undergoing 3-fold rotation in a 4-target ABS chamber



Figures 6.41a-6.41d illustrate the normalised coating flux density and growth rate delivered by three sources delivering identical vapour yields and the fourth delivering twice the yield, simulating arc / magnetron deposition of TiAlN-ZrN on a 3-fold rotating substrate, as a function of various starting position ( $d_1, d_2, d_3$ ).

Figure 6.41a.

Simulation of the normalised flux density at the surface of a substrate undergoing 3-fold rotation in a 4-target ABS chamber

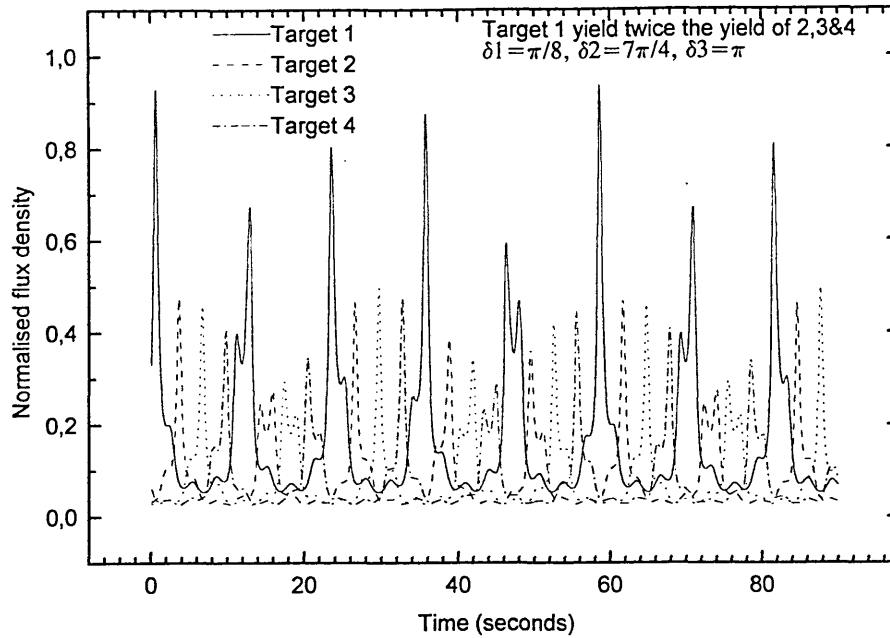


Figure 6.41b.

Simulation of the normalised growth rate at the surface of a substrate undergoing 3-fold rotation in a 4-target ABS chamber

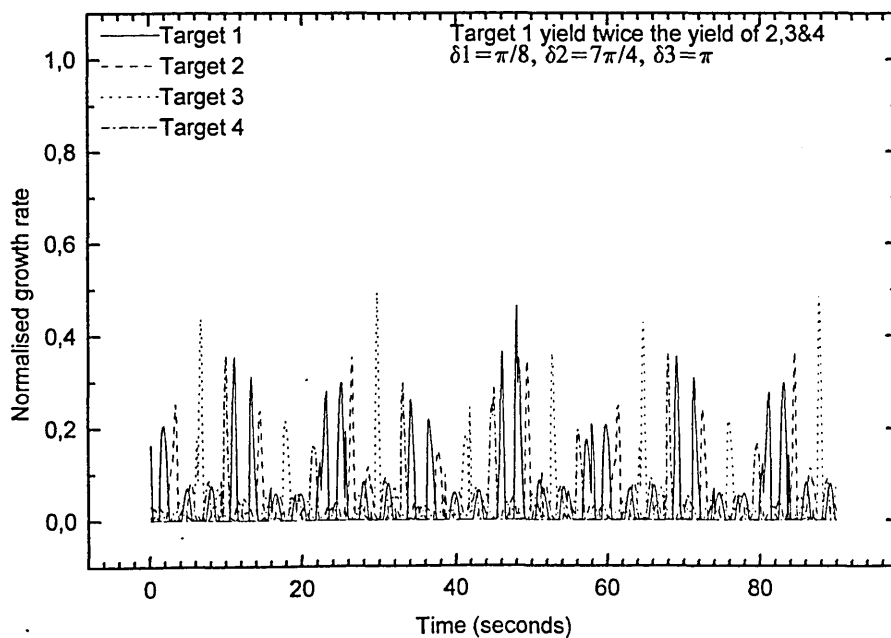


Figure 6.41c.

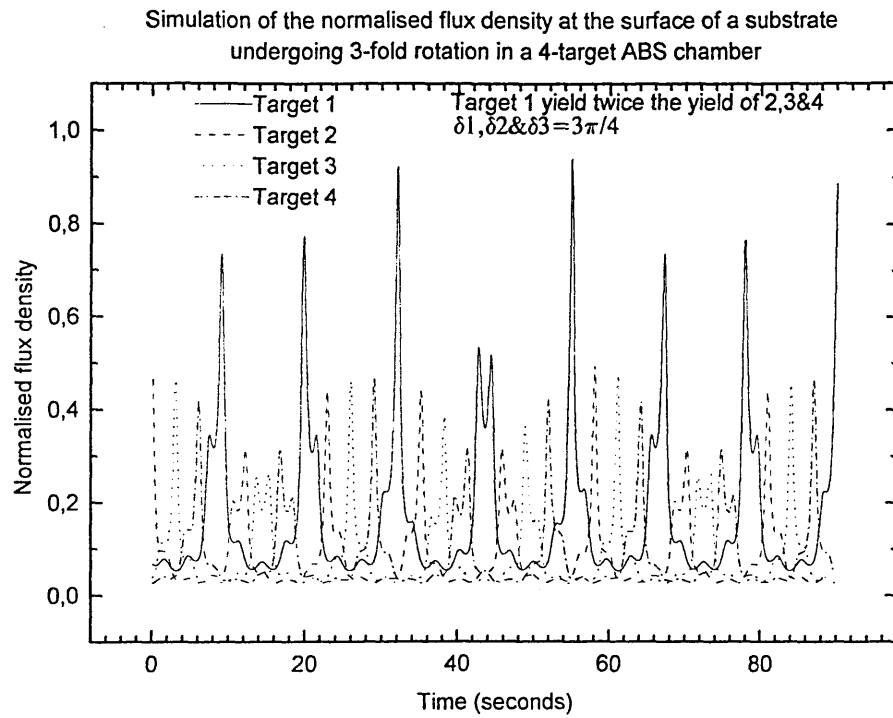
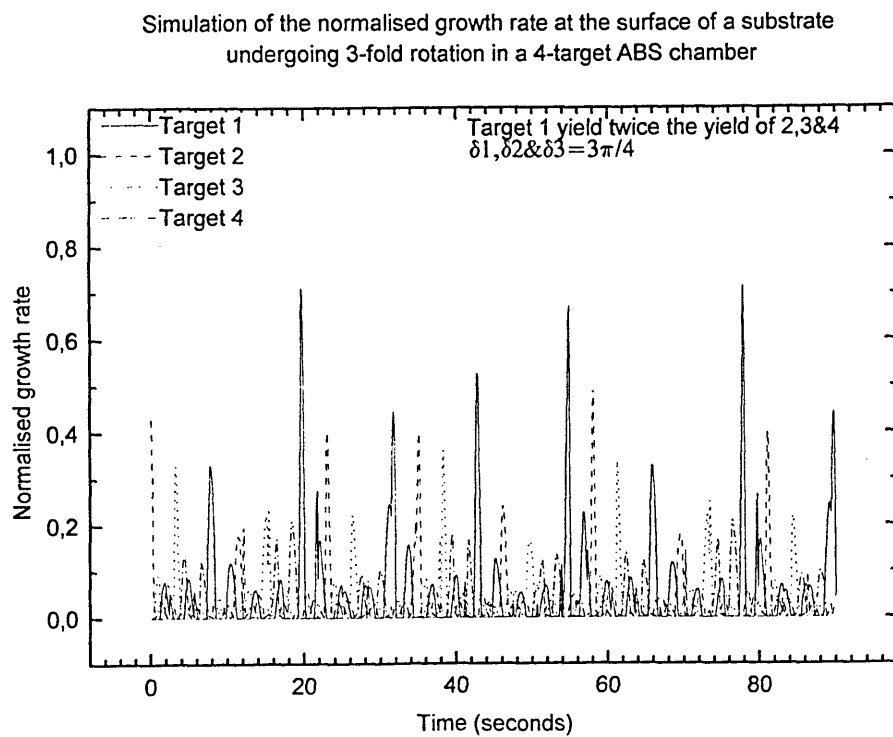


Figure 6.41d.



Figures 6.42a-6.42d illustrate the normalised coating flux density and growth rate delivered by three sources delivering identical vapour yields and the fourth delivering half the yield, simulating UBM deposition of TiAlN-ZrN on a 3-fold rotating substrate, as a function of various starting position ( $d_1, d_2, d_3$ ).

Figure 6.42a.

Simulation of the normalised flux density at the surface of a substrate undergoing 3-fold rotation in a 4-target ABS chamber

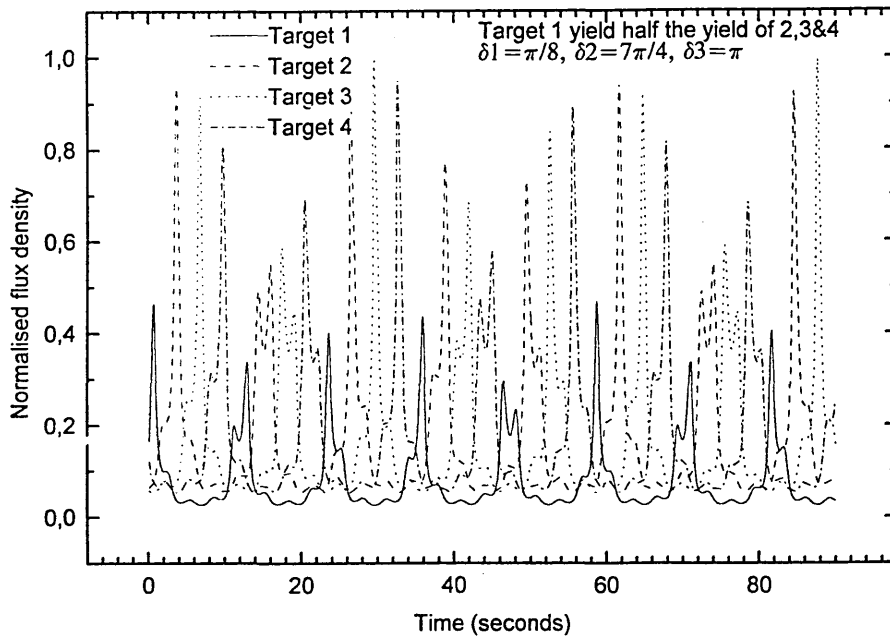


Figure 6.42b.

Simulation of the normalised growth rate at the surface of a substrate undergoing 3-fold rotation in a 4-target ABS chamber

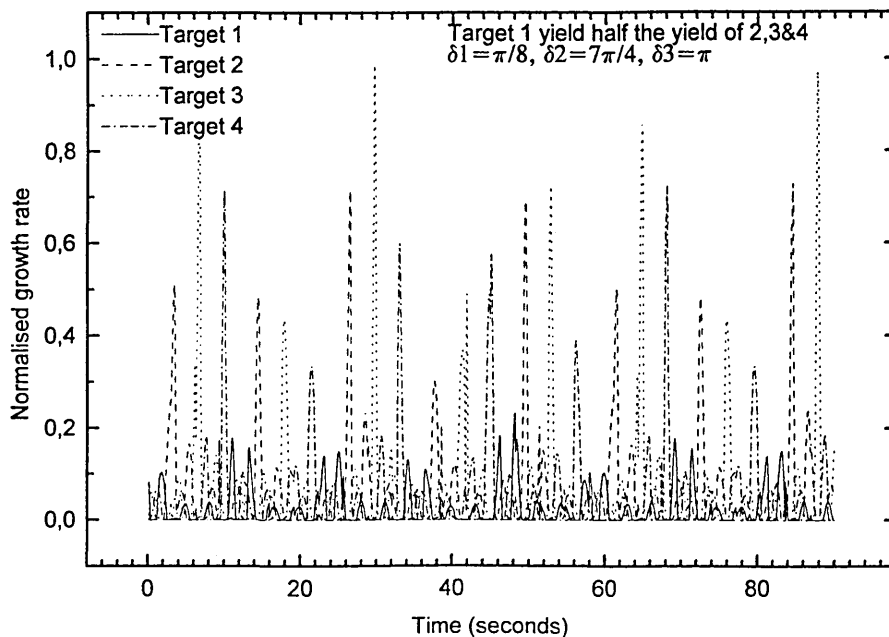


Figure 6.42c.

Simulation of the normalised flux density at the surface of a substrate undergoing 3-fold rotation in a 4-target ABS chamber

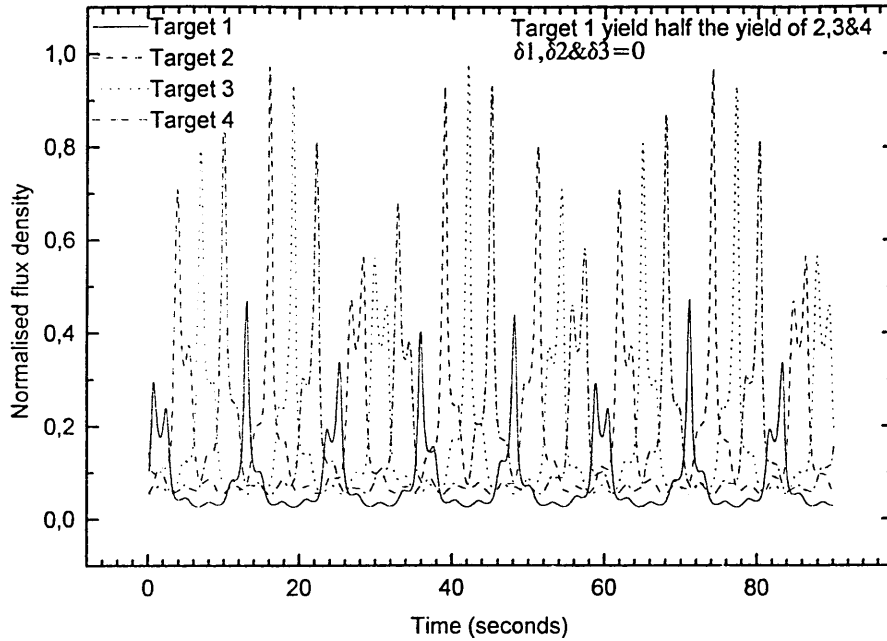
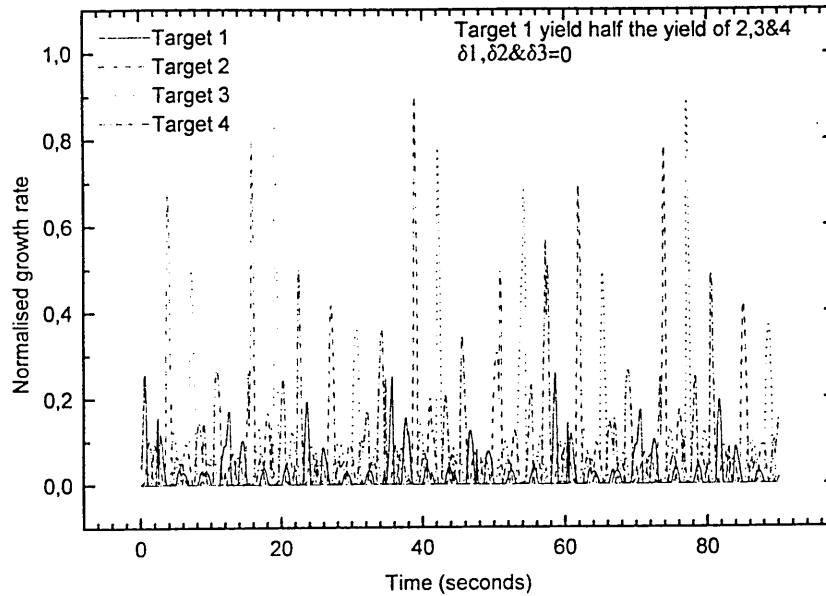


Figure 6.42d.

Simulation of the normalised growth rate at the surface of a substrate undergoing 3-fold rotation in a 4-target ABS chamber



The normalised flux density spectra illustrates how the substrate rotation frequencies were directly replicated in the oscillations of the arriving vapour fluxes to produce a strong beat frequency. The influence of substrate starting position served to simply create a shift in the time axis, whilst the effect of increasing or decreasing target yield caused a proportional change in flux density.

Analysis of the normalised growth rate spectra illustrates the large variations which can be caused by changes in starting position or target yield. The data again demonstrate a beat frequency from an oscillating coating flux and explains the production of non-uniform superlattice periods during 3-fold rotation processes. Further examination reveals that the highest deposition rates occur when the substrate is directly in-line with a target and its vapour flux and the minimum rates occur at positions  $45^\circ$  between targets and positions where the substrate points directly away from the target (e.g. at positions such as  $d_1 \& d_2 = \pi/4, d_3 = 5\pi/4$ ).

Investigations using one target with a lower yield than the other three targets (simulating ABS TiAlN-ZrN when sputtering a poisoned Zr target) in 3-fold rotation gives an explanation of the production of thin, non-uniform thickness ZrN layers and the development of a weak superlattice structure.

Analysis of slower rotation velocity ( $\sim 3.8$ rpm) revealed a beating behaviour in the normalised flux density and normalised growth rate but with reduced frequency (figures 6.43a&b).

Figure 6.43a.

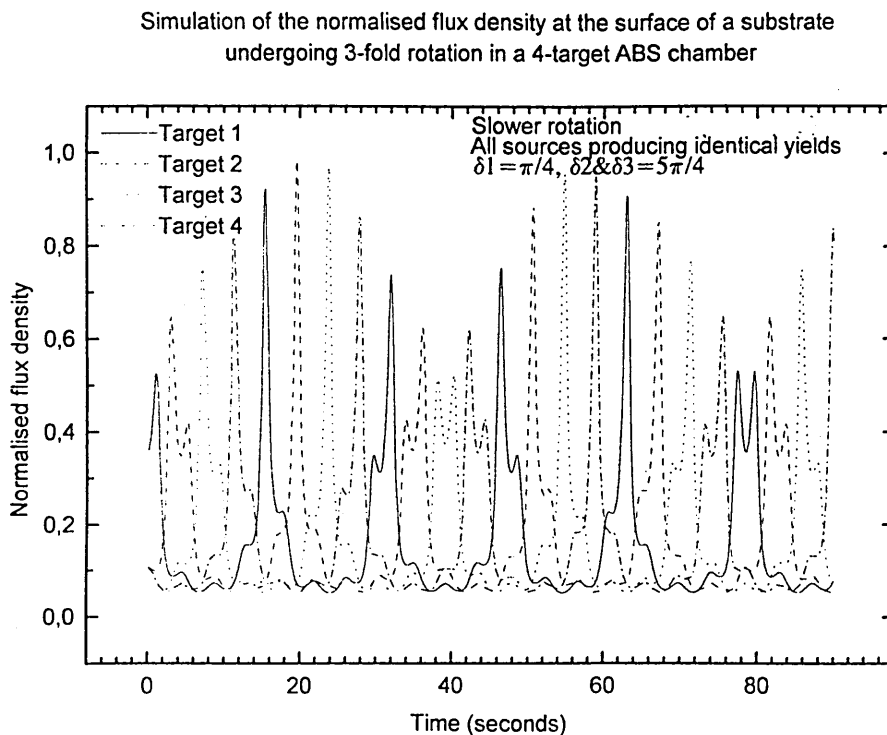
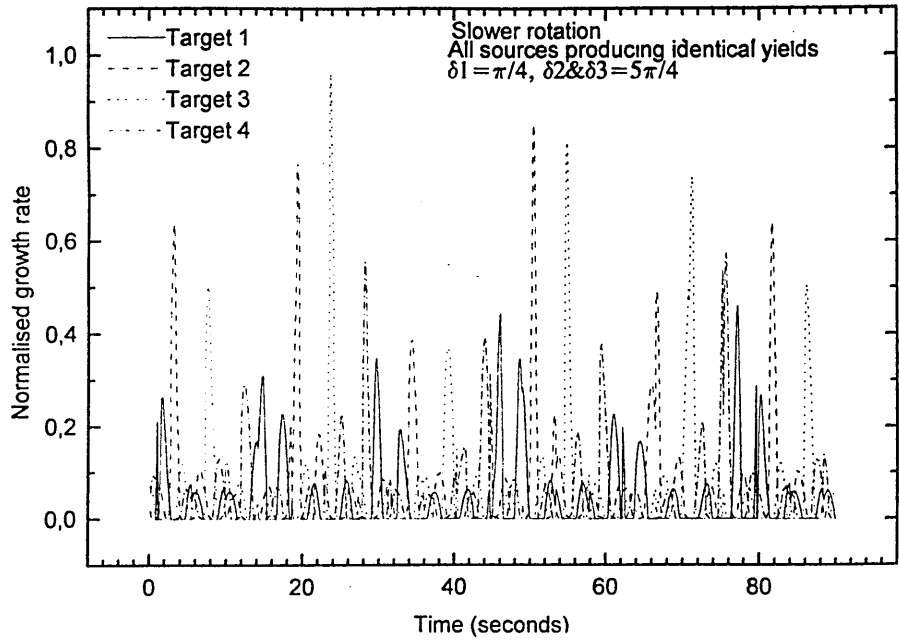


Figure 6.43b.

Simulation of the normalised growth rate at the surface of a substrate undergoing 3-fold rotation in a 4-target ABS chamber



## **References.**

1. J.Vyskocil, J.Musil, S.Kadlec, W-D.Münz - *Proc. 1st. Intl. Conf. Plasma Surface Engineering*, 1988, Garmisch-Partenkirchen, Germany, 661-668, DGM Informationsgesellschaft Verlag.
2. I.G.Brown, X.Godechot - *IEEE Trans. Plasma.Sci*, 1991, 19, 5, 713-717.
3. B.Rother, D.A.Dietrich - *Surf.Coat.Tech*, 1995, 74-75, 614-617.
4. B.Rother, H.A.Jehn - *Surf.Coat.Tech*, 1993, 62, 635-640.
5. B.Rother - *Surf.Coat.Tech*, 1994, 64, 155-159.

## **CHAPTER SEVEN**

### **DISCUSSION AND CONCLUSIONS**

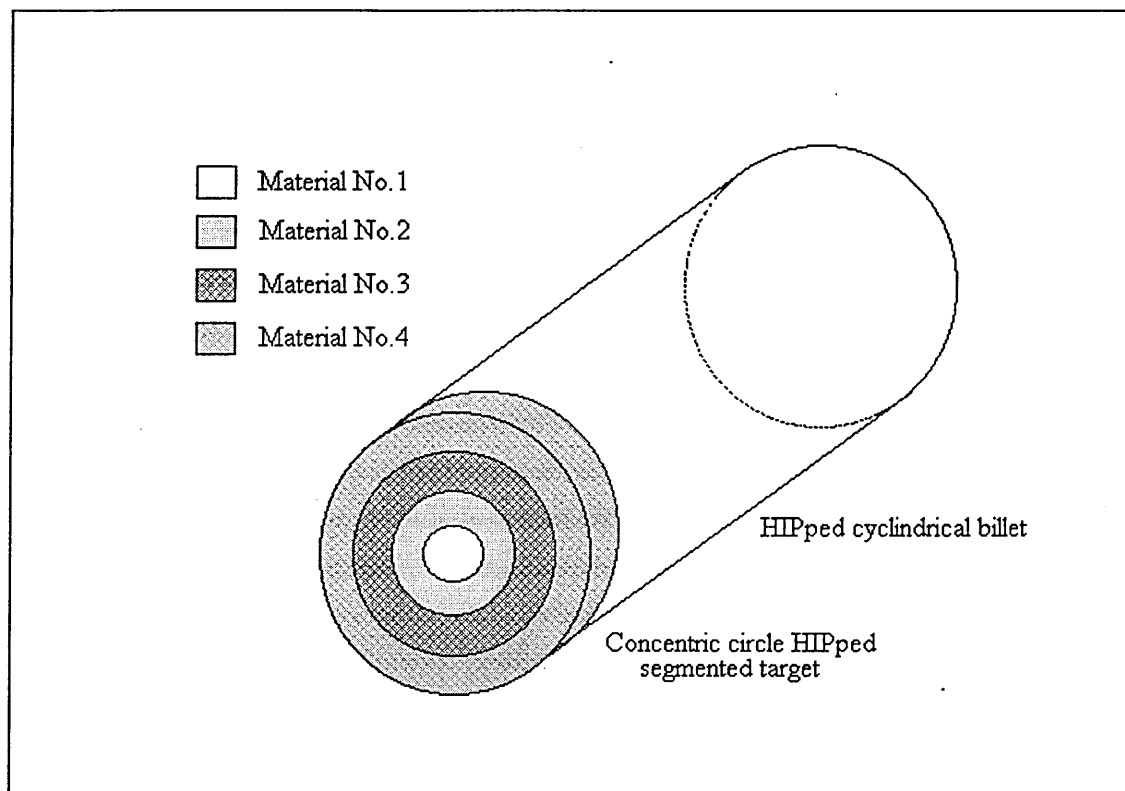
#### **7.1. The fabrication and performance of segmented targets.**

Metallurgical investigation of appropriate stable alloy systems suitable for the production of transition and refractory metal nitride hard coatings has been undertaken prior to the manufacture of a range of TiZr, TiMo and ZrMo segmented targets by an original diffusion bonding hot isostatic pressing technique. Target performance was evaluated during a series of steered arc evaporation, unbalanced magnetron sputtering and arc-bond sputter trials which allowed examination of the cathode spot motion across dissimilar metal junctions, study of the evaporative and sputter yields, investigation of preferential target poisoning effects and characterisation of coating properties.

The initial aim of the project was to produce segmented targets which could provide a high level of flexibility in steered arc coating material and allow the controlled production of second and third generation films without utilising co-evaporative techniques. Hence the first objective was simply to establish the metallurgical properties of a range of transition and refractory metals and study the viability of a segmented target manufacturing route utilising a hot isostatic pressing technique. The final goal was to produce a series of concentric circular segmented targets which could be sliced from a large cylindrical billet (thereby reducing HIPping costs) and utilised in electromagnetic steered arc evaporation to deliver binary, alloy and multi-layer coatings by control of the arc radii through variation in local coil currents (figure 7.1). Prior to large scale target production, performance trials were initiated to study the fundamental interaction of the steered cathode spot across a variety of dissimilar metal junctions and analyse the effect of variation in interfacial crossing angle.

Metallurgical and physical property analysis of titanium, zirconium and molybdenum revealed that the materials exhibited appropriate elemental and thermal stability for use in HIP diffusion bonding provided adequate levels of material purity and vacuum pressure were used. Elevated temperature studies indicated that a HIPping temperature above the  $\alpha/\beta$  transus (1280°C chosen) could be used to initiate a diffusion bonding mechanism without a reduction in mechanical properties, whilst HIPping trials demonstrated that a range of target geometries could be developed where the degree of surface roughness of the bonding faces significantly affects the range of inter-diffusion.

Figure 7.1. Schematic of concentric circular segmented target.



The critical aspect observed from steered arc evaporation trials was the propensity for the cathode spot to "stall" for a short period of time when traversing across an interface from a material with higher vapour pressure to lower vapour pressure, yet having no problem in traversing the junction in the reverse direction. Results have indicated that the larger the difference in segment material vapour pressures, the greater the arc dwell time at the interface region and the more extensive the deleterious erosion trench formed. However, other physical and chemical properties of the individual metals may be responsible for the complex differences in cathode spot behaviour and likely interrelated properties are thought to be variations in work function, heat of vapourisation, electrical resistivity and thermal conductivity.

This interfacial behaviour appears to agree with a possible adaptation of a simplified model first postulated by Ecker (1). Asymmetric confinement of the arc plasma by self and confining fields causes low energy positive charged ions to be drawn back to the cathode (target) with a circular deflection on the retrograde side. This creates energetically favourable sites for new spot ignition in the direction opposite to that given by  $\mathbf{J} \wedge \mathbf{B}$  (Ampere's law). Work carried out by Beilis on the temperature field at

the cathode spot has also shown that the radius of the heated region around the spot is of the order of 0.5mm and independent of the current density (2).

As the cathode spot approaches close to the segment junction in the high-low vapour pressure direction, within a distance of the heating radius, the local temperature of the target materials will rise. This sets up a competitive mechanism between evaporation of the higher vapour pressure segment material, which requires a lower cathode voltage to volatilise material at energetically favourable evaporation sites, and increasing resistivity of the high vapour pressure material. Whilst sites on the high vapour pressure segment remain favourable, the cathode spot (maintained at current of 85A) velocity decreases and deleterious erosion at the interface region occurs. After a short period of time the local resistance of the high vapour pressure segment is such that an increase in cathode voltage is required if emission levels from the target are to be maintained. Hence, sites on the lower vapour pressure segment become energetically favourable and the arc crosses the junction. The extent of the vapour pressure mismatch (refractory nature of the materials) simply serves to increase or decrease the cathode spot dwell time required to form energetically favourable sites across the junction. When traversing in the opposite direction, evaporation sites on the higher vapour pressure segment will always remain energetically favourable and the cathode spot crosses the junction without impediment.

Sputtering yield investigations undertaken by GDOES analysis and Monte-carlo simulation using TRIM95 software were found to be in excellent agreement. Variable  $N_2$  partial pressure trials showed a strong tendency for preferential segment poisoning of the high reactivity metals (Ti or Zr) and serve to identify a basic disadvantage in unbalanced magnetron co-sputter processing which may limit the materials which can be accommodated in such reactive sputtering systems. Analysis of the coating composition distribution from a range of segment targets has indicated the line-of-sight nature of the sputtered vapour flux. GDOES investigation of the composition of a series of directly aligned substrates at constant substrate-target distance has illustrated a highly linear decay in elemental content as a function of substrate angular position.

Characterisation of the PVD films developed from TiZr, TiMo and ZrMo segmented target coating trials has confirmed the possibility of their use in reactive steered arc evaporation, unbalanced magnetron sputtering and hybrid arc-bond sputter processing. The properties of original  $Ti_xMo_yN$  and  $Zr_xMo_yN$  coatings have been investigated as a function of increasing nitrogen partial pressure. The results indicate that greatest

optimisation of hardness, adhesive and colour properties occurred just prior to the onset of group IV segment poisoning.

However, the use of segmented targets in both arc evaporation and unbalanced magnetron sputter processes continues to exhibit intrinsic and economic disadvantages which make the use of homogeneous alloy and powder metallurgical targets more desirable. Deleterious erosion problems at bi-metallic junctions and preferential segment poisoning still remain inherent which have prevented full scale manufacture of cylindrical billets. The need for a more flexible steered arc evaporation process, capable of producing a wide range of second and third generation coatings remains essential and possible methods to reduce the interfacial erosion may lie in the use of preferential localised segment heating to reduce the extent of apparent vapour pressure mismatch.

### 7.2. The TiZrN system.

The mechanical and physical properties of the second generation TiZrN ternary coating system has been investigated as a function of substrate bias voltage, nitrogen gas partial pressure and deposition technique.

The TiZrN system was found to simultaneously exhibit two stable forms of solid solution, that is a homogeneous mixture of two or more species of atoms in the solid state (figure 7.2). A complete substitutional solid solution across the entire phase field was formed by the TiZr alloy as the titanium and zirconium atoms were of similar radii, whilst an interstitial solid solution was also produced, where the solute atoms (nitrogen) entered into the octahedral interstices between the solvent atoms (titanium or zirconium) as the ratio of titanium or zirconium to nitrogen was high.

Metal structure	Interstitial site	Min radius ratio	Max radius ratio
f.c.c	octahedral	0.41	0.59
f.c.c	tetrahedral	0.23	---

Atomic radius of titanium = 0.146nm

Atomic radius of zirconium = 0.160nm

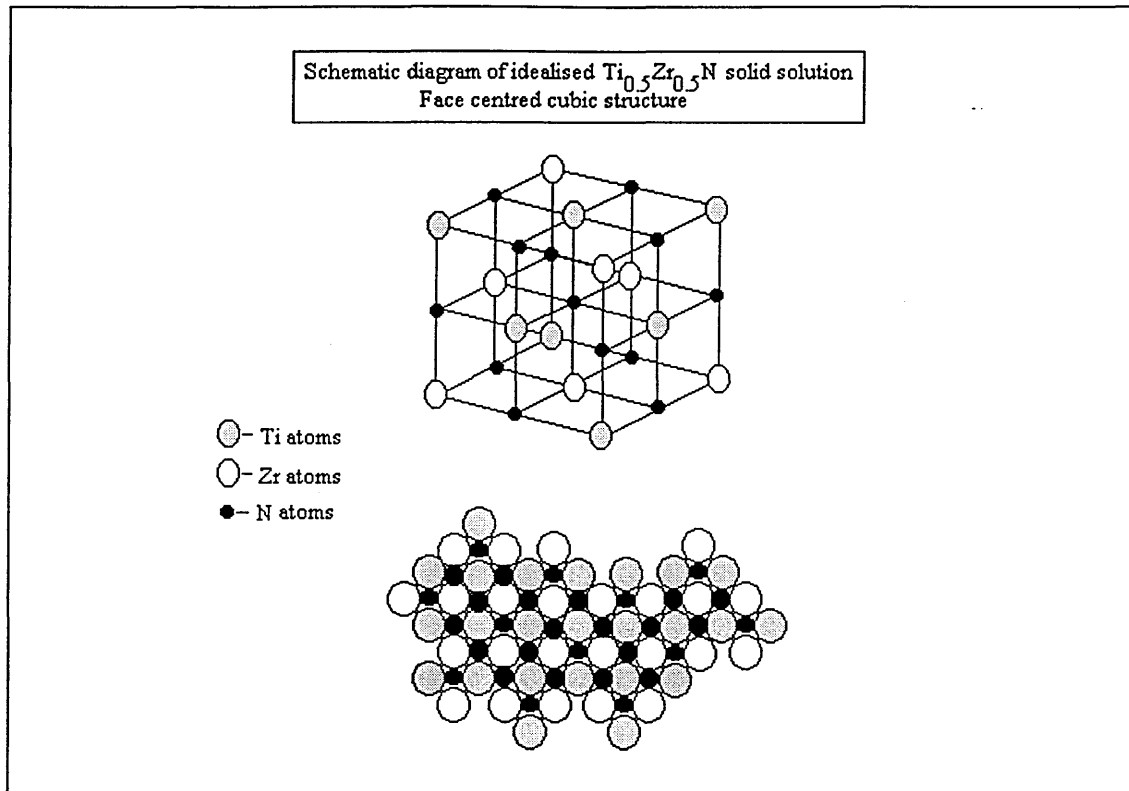
Atomic radius of nitrogen = 0.071nm

Radius ratio N / Ti = 0.486

Radius ratio N / Zr = 0.444

Radius ratio Ti / Zr = 0.913

Figure 7.2.



The exact nature of bonding in solid solution systems is not fully understood. However, it is clear that solid solution additions generally result in a significant hardening which tends to vary as a function of ratio of solute : solvent atomic radii, differences in valency and the extent of preferential grouping of solute atoms around dislocations and stacking faults. In the TiZrN system, the maximum solid solution strengthening was exhibited as the ratio of Ti :Zr approached 1:1. This may be explained in terms of a maximising of the dislocation density in the 60 / 40 alloy which allowed interstitial atoms to collect in expanded regions around the slip planes of positive edge dislocations. Because the local energy is lower when a dislocation is surrounded by solute atoms, a higher stress is required to make the dislocation move than would be required if there were no interaction between the dislocation and the solute atom (3). Thus a locking mechanism ("Cottrell locking") is generated from elastic interactions between solute atoms and dislocations which provides an energy barrier to the movement of dislocations throughout the crystals by distortion of the periodic lattice and this is manifest as a hardness increase. The hardness of the TiZrN films was typically found to be of the order of  $1000H_k$  larger than the equivalent TiN, ZrN or TiAlN film which provides obvious benefits for cutting tool operations.

The adhesion of the coatings was generally excellent, with the best Rockwell adhesion and critical load values found on steered arc and arc-bond sputtered films. This can be attributed to the influence of high bias voltage metal ion etching of the substrate, prior to coating. Trim-95 computer simulations have indicated that low level implantation ( $<100\text{\AA}$ ) of metal ions may occur as a result of arc etching which can be followed by a strong thermal diffusion of the metal significantly further into the substrate matrix (substrate temperature of  $450^{\circ}\text{C}$  corresponds to a significantly higher surface temperature). Hence the metal ion etching step engineered a graded layer in the substrate surface region which allowed greater lattice matching to the PVD film, a reduction in residual stress at the coating / substrate interface and provided a clean and slightly roughened surface giving greater surface area and the possibility of keying. The use of pure metal and alloy interlayers prior to reactive deposition also served to provide good coating adhesion to high speed steel substrates. Adhesion values appeared to maximise when the composition of the interlayer was titanium rich, which may be attributed to relatively close lattice spacings of the face centred cubic TiZrN (111) plane and the hexagonal close packed (0002) titanium plane.

X-ray diffraction analysis has indicated that the TiZrN system was isotropic and always exhibited a single phase,  $<111>$  preferred orientation and an enlarged lattice parameter following Vegard's law indicating a compressive residual stress. The strongest  $<111>$  orientation was shown by steered arc evaporated and ABS coatings. Unbalanced magnetron sputtered coatings developed under process conditions of high substrate bias voltage ( $-200\text{V}$ ) or low reactive gas partial pressure ( $4.5 \times 10^{-3}\text{mbar}$  &  $9\text{sccm N}_2$  flow) both underwent changes in preferred orientation towards  $<100>$  direction. This behaviour corresponds to an increased ion flux density and ion energy impinging on the substrate surface i.e. higher bias-higher accelerating potential, lower pressure-reduced target poisoning, higher yield and less gas scattering.

GDOES depth profiles on unbalanced magnetron sputter deposited TiZrN coatings revealed that a range of metal to nitrogen gas ratios could be achieved through variation in the reactive gas flow. Films generated at intermediate gas flows ( $15\text{sccm}$ ) provided sufficient nitrogen to form fully filled interstitial TiZrN. However, at low nitrogen flows insufficient filling provided sub-stoichiometric coatings and exhibited a more metallic nature, whilst at high gas flows over-stoichiometric films were observed due to gas entrapment within the growing film (in voids or pores etc). Coatings grown by the steered arc technique were always stoichiometric and exhibited remarkable tolerance to any variation in reactive gas flow. The profiles also showed a slight drop in nitrogen concentration with depth throughout the reactive deposition region of the traces, due to

outgassing and water vapour contamination effects. The spectra also demonstrated an increase in oxygen signal near the coating surface due to GDOES anode / vacuum sealing effects and the possibility of a small degree of micro-porosity within the coatings.

The best TiZrN mechanical and physical properties appeared to be provided by coatings generated from the HIPped segmented target. This is attributed to greater homogeneity and uniformity of the coating flux from the segmented target and the possible development of a layered and hence higher stressed film by the co-sputter or co-evaporation process technique

Coatings deposited using unbalanced magnetron sputtering at low bias voltages and high nitrogen flows, producing low ad-atom mobility and high levels of gas scattering, appeared porous and highly columnar in structure, corresponding to a zone-1 morphology. However, as the bias voltage was increased, a microstructure transition to a zone-T morphology was evident where the level of porosity decreased and the film density and surface finish improved significantly. Low nitrogen flow coatings appeared highly dense and smooth due to the more metallic nature of the films. At extreme biasing conditions, the microstructure reverted to a dense, fibrous morphology due to excessive ion bombardment, formation of inter-granular voids and re-sputtering effects. This allowed micro-structure optimisation of the TiZrN to be undertaken as the best morphology was generated in the medium bias (-50V & -100V) stoichiometric films. Steered arc and arc-bond sputter films demonstrated significant increases in surface roughness when compared to magnetron sputtered films as a result of macro-particle incorporation during the evaporation process. The highest macro-particle densities were always recorded on steered arc coatings whilst ABS films exhibited less incorporation due to shorter evaporation times (arc only running during cyclic ion etching for 10 minutes).

The TiZrN films deposited showed a peak in both the reflectance (or lightness  $L^*$ ) and the yellowness ( $b^*$ ) which coincided with the optimised deposition conditions in terms of substrate bias and stoichiometry. At low (0V) and excessive bias voltages (-200V) and high nitrogen flows (22sccm) enhanced ion bombardment and over stoichiometry produced a reduction in film colour properties due to the formation of open and porous columnar structures, preferential poisoning effects and re-sputtering effects. Little variation in optimum colour properties were found as a function of deposition technique, however variation in the metal : nitrogen and alloy content (Ti:Zr ratio) provided significant changes in  $L^*$ ,  $a^*$  and  $b^*$ .

In general, stoichiometric TiZrN had a platinum gold appearance which could be varied between the yellow gold of TiN to the champagne gold colour of ZrN through alteration of the alloy composition. Thus, the film could also be utilised as a bright candidate system for the decorative coating industry which also exhibits high levels of wear resistance.

The arc-bond sputter technique could essentially be characterised as a hybrid process which utilised the flexibility of the closed field unbalanced magnetron sputter technique (wide variety of target materials which can be sputtered, large degree of composition and micro-structure control, etc) combined with adhesion levels comparable to the steered arc evaporation technique and generally higher than unbalanced magnetron sputtering. The arc evaporation technique proved very well suited for the deposition of first generation binary coatings such as TiN and ZrN. However, the controlled production of complex alloy nitride or carbide coatings and third generation coatings by arc techniques remains considerably more difficult. The main drawback involved in both the steered arc and ABS techniques was an undesirable increase in surface roughness (ABS  $R_a$  values significantly higher than UBM processing but considerably less than steered arc evaporative coating) due to macro-particle incorporation during the cyclic steered arc ion etch phase. This may mean that for some coating applications (e.g. decorative, medical) the system should be used in closed field unbalanced magnetron mode only.

### **7.3. The growth and characterisation of pseudo-ceramic multi-layer thin films.**

Most reported investigations on the physical vapour deposition of multi-layer and superlattice thin films have been undertaken at experimental scale using dual unbalanced magnetron or evaporation sources in opposed cathode or multiple crucible configurations which have limited the substrate size, geometry and quantity which can be accommodated. These systems often required complex and expensive reactive gas partial pressure control and chamber reciprocating shutters to create controlled atmosphere separation and restrain cross-contamination and preferential target poisoning. In many cases ultra high vacuum and interrupted deposition conditions had to be applied and a compromise was required between the deposition rate and coating uniformity.

Following earlier investigations by Vyskocil et al (4) on the consumption of nitrogen gas per unit power as a function of nitrogen partial pressure per unit power in reactive magnetron sputtering and steered arc evaporation trials, an understanding of the

importance of target deposition mode determination was obtained. The effect of fundamental differences between arc evaporated and sputtered vapour properties (charge state, ion energy, current density etc) and their reaction behaviours identified a basic mechanism which was developed for the deposition of pseudo-ceramic multi-layer thin films.

If the coating requirement was a combination of materials which exhibited large differences in the target reactivity, such that excessive poisoning of individual materials may occur when sputtering at high reactive gas partial pressures (group IVa metals such as Ti or Zr), then deposition using the high reactivity materials in steered arc evaporation mode can be achieved whilst continuously coating the less reactive materials by an unbalanced magnetron sputtering technique. The utilisation of a multi-cathode geometry, where the spacial arrangement is such that the vapour sources are at 90° to one another, combined with the strong line-of-sight nature of the metal vapour fluxes can cause coating modulation and multi-layered films to be developed.

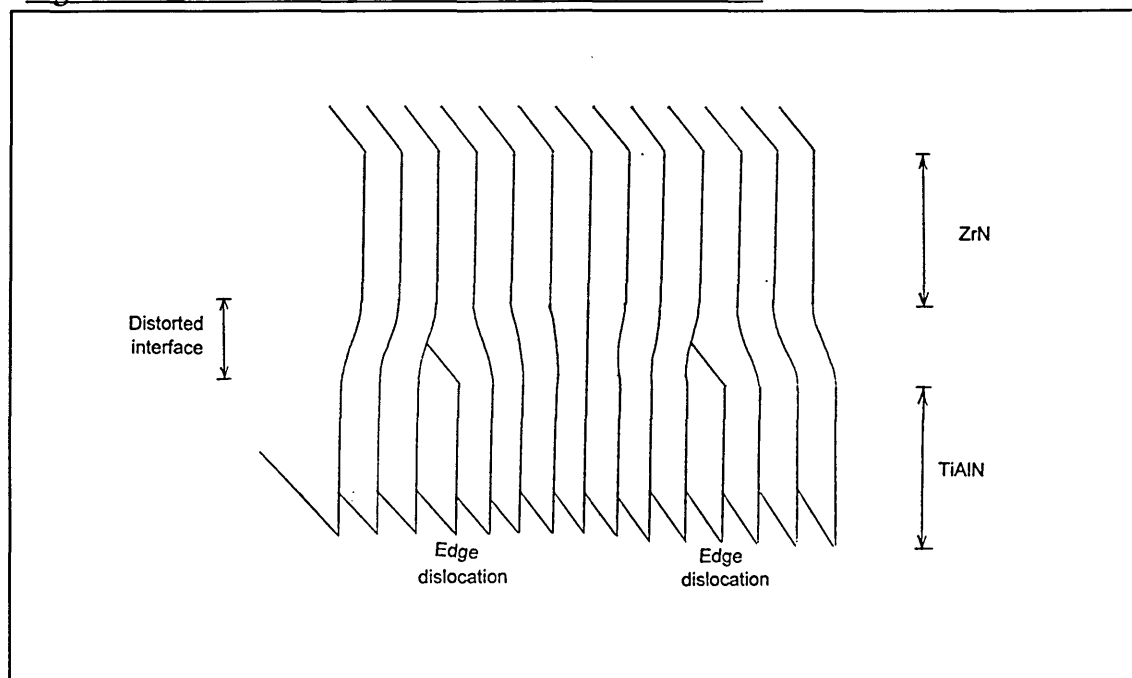
The recent development of arc-bond sputter technology provided a capability to simultaneously deposit by independent steered arc evaporation or unbalanced magnetron sputtering at industrial scale. Hence, examination of the ion assisted growth and characteristics of TiAlN-ZrN and TiAlN-TiN multi-layer systems fabricated by combined steered arc evaporation and unbalanced magnetron sputtering could be undertaken.

The deposition parameters for a range of multi-layer structured hard coatings have been outlined and the influence of target deposition mode, substrate rotation velocity and rotation type and composition has been studied. The application of relatively simple tests such as hardness and roughness, combined with the sophistication of X-ray and electron beam techniques has provided a powerful method of examining and evaluating the sub-structure of multi-layer coatings. An understanding of the crystallography and elemental distribution nearing the atomic scale has produced a detailed interpretation of the mechanisms responsible for enhanced coating properties and allowed initial optimisation of the coating process parameters. Much of this work is in its infancy, but the analysis carried out has already lead to a clearer understanding of the mechanisms which produce hard coatings by understanding the role of dislocations and vacancies. The complex relationships between the effect of solute gradients and the nature of low and high angle boundaries within the sub-structure of iso-morphous TiAlN and ZrN layers, produced simultaneously by an adapted ABS process has been analysed.

The investigations have indicated that a reproducible and coherent multi-layered film structure can be fabricated without special means of atmosphere separation and shuttering. The strong line-of-sight nature of the PVD fluxes meant that significant modification (19-132Å) of the layer period can be achieved simply by control of the planetary turntable rotation velocity and the type of rotation (one-fold and three-fold).

X-ray diffraction, GDOES, XTEM and XSTEM techniques have confirmed the presence of distinct, coherent TiAlN-ZrN and TiAlN-TiN alternating layers. Whereas first and second generation coatings generally exhibited a <111> orientation, combined arc / magnetron multi-layer coatings, developed at significantly higher bias current densities, always showed a <100> orientation. The <100> preferred orientation was found to provide beneficial surface roughness properties however, its effect on wear resistance properties is as yet unclear as the closest packed plane for an f.c.c structure is (111) and Sue (5) has shown that the erosive wear resistance of TiN coatings increases when the (200) component is minimised relative to the (111) component. Analysis of the (111) and (200) interplanar spacings has indicated the presence of a mutual constraint mechanism from opposing residual stresses and interfacial mixing of the coating species shown schematically in figure 7.3. Investigation has demonstrated that lattice expansion of the magnetron deposited TiAlN layer created a compressive residual stress which combined with incorporation of elements with small atomic radii at layer interfaces caused a reduction in the ZrN lattice parameter to a level below JCPDS standard data.

Figure 7.3. Schematic of the interfacial stress mechanism



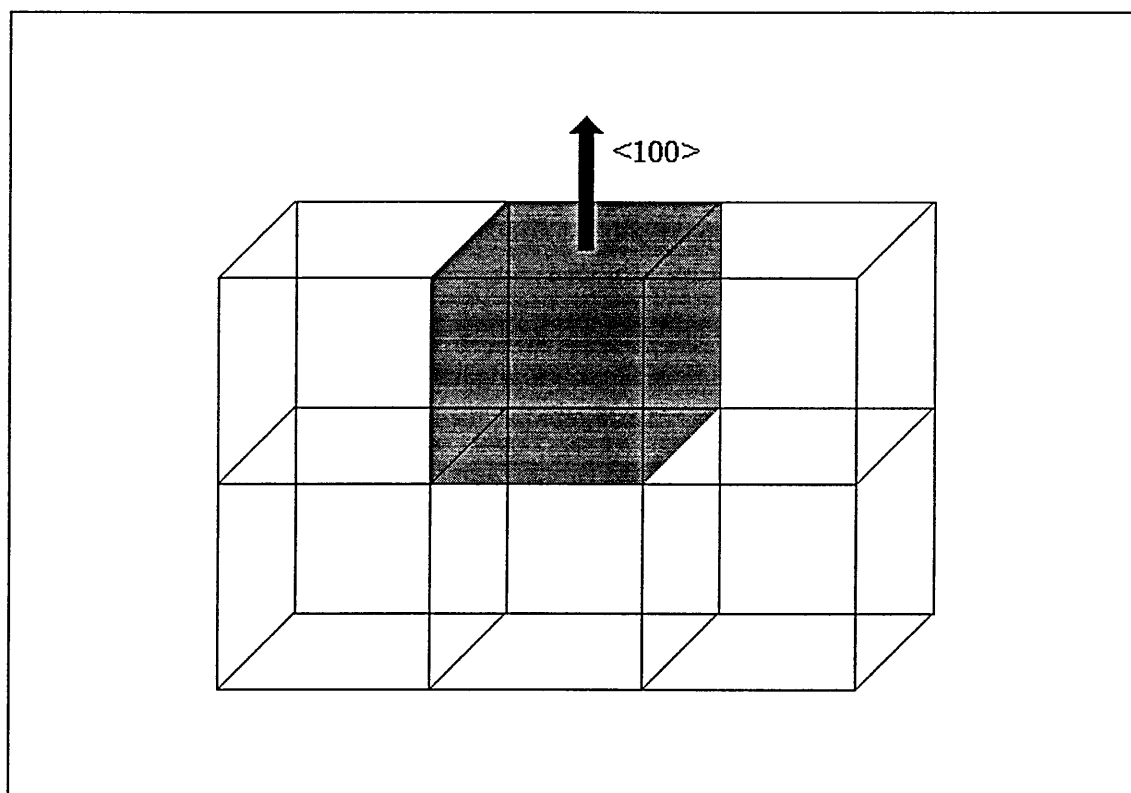
Full peak width at half maximum (FWHM) analysis of TiAlN-ZrN films has shown that the greatest period uniformity existed in single-fold rotation coatings and the highest lattice strain is produced by the arc deposited ZrN layers. The large degree of lattice mismatch (TiAlN-ZrN~9.3%, TiAlN-TiN~1.2% ) between individual layers caused the formation of high lattice strain fields and dislocation pile-up at layer interfaces. Hence the TiAlN-ZrN films were always significantly harder than the equivalent TiAlN-TiN film. However, differences in shear modulus and dislocation line energy, the level of layer coherency, interfacial mixing and composition fluctuations and Hall-Petch relationships also critically affect coating hardness. Results have shown that a hardness maximum occurs in the TiAlN-ZrN system as periods typically between 30-50Å followed by a significant reduction in hardness at lower periods. The hardness maximum is thought to be due to an optimised interaction of overlapping dislocation strain fields whilst the subsequent decrease in hardness at periods <30Å can be explained by a rapidly reducing dislocation density in the significant thinner ZrN layers i.e. a period of 20Å corresponds to a ZrN approximate layer thickness of 5Å (less than 2 unit cells).

Transmission electron microscopy has confirmed the lamella nature of the multi-layer films and established the existence of unique reciprocal lattice vectors. Energy loss image filtering has separated the layers in terms of elemental composition and demonstrated remarkable elemental resolving power. XTEM and XSTEM techniques have demonstrated the long range integrity of the individual layers and the highly uniform nature of the growing front. This has led to layer formation remaining parallel to substrate surface at distances of several micrometres, unlike dual magnetron coatings which generally show distinct layer curvature which increases as a function of film thickness. This behaviour is thought to be due to the significant enhancements in substrate bias current densities, higher ad-atom mobility and distinct re-nucleation events which occur due to the differing reaction behaviours of steered arc and magnetron sputtering processes. Dual magnetron systems generally produce films with a more "graded layer" type nature and are developed at lower bias current densities.

The TiAlN-ZrN multi-layer coatings investigated have shown significant enhancements in their mechanical and physical properties over first and second generation coatings and has clearly provided a number of academic and commercial possibilities. The application of a sputtered base layer, to control high residual stresses developed at the coating / substrate interface, has enabled acceptable adhesion levels to be reached on a variety of engineering components. The use of an arc evaporation technique generally leads to an increase in surface roughness from the development of metallic droplets or

macro-particle incorporation. Film growth with a  $\langle 100 \rangle$  preferred orientation, where the deposition occurs such that face-centred cubic unit cells are arranged cube on cube (figure 7.4), meant that a relatively low roughness coefficient was developed. This, combined with the use of zirconium as the arc target material which produces a relatively macro-particle density flux, produced coatings of roughness similar to standard ABS films. CIE lab colour measurements also indicated that a range of high lustre, metallic colours could be produced which may be of commercial interest.

Figure 7.4. Schematic of a  $\langle 100 \rangle$  preferred orientation f.c.c film



Monte-carlo simulation of the three-fold substrate rotation path, normalised flux density and growth rate has provided an understanding of the different vapour phase relationships. The formation of a strong beat frequency from orthogonal vapour sources has been predicted from a series of modelling trials and experimental confirmation of secondary periods due to the influence of second and third fold rotation has been achieved by scanning transmission electron microscopy.

The modulation of ZrN layers within the TiAlN coatings significantly influences the oxidation resistance properties of the TiAlN-ZrN system (unbalanced magnetron sputtered second generation TiAlZrN  $\sim 550^\circ\text{C}$  compared to TiAlN  $\sim 800^\circ\text{C}$ ) such that

the coating may not be suitable for application on components which operate in high temperature environments (i.e. dry cutting at high speeds and feed rates). A possible modification to the coating composition to increase the aluminium content, by sputtering  $Ti_{0.4}Al_{0.6}$  targets, may produce improved oxidation resistance properties. However, the present coating should be ideally suited to lower temperature wear and erosion resistance, decorative and possibly corrosion resistance applications. At present there is insufficient evidence available to critically assess coating performance on real devices (cutting, drilling operations and other wear resistance applications). However, preliminary results reported on similar multi-layer / superlattice systems (TiAlN-TiNbN) when deposited on cemented carbide and fine-blanking tools have shown outstanding performance when compared against  $\langle 111 \rangle$  orientated TiAlN coatings (6,7). Clearly, the deposition technique can be used to produce a range of other coating systems and their application for commercial applications is enormous. The grain structure and micro-columnar nature of the films also makes them an ideal candidate system for corrosion resistance operations.

- Improving the hardness properties of CrN by multi-layering with lattice mismatched second generation hard coatings (e.g. TiAlN) as a replacement for hard chrome plate.
- The development of carbo-nitride layered systems for improved wear and erosion resistance.

The target material - deposition mode philosophy which has been developed means that materials with less extreme differences in nitrogen reactivity can be successfully deposited in all magnetron sputtering processes. Publications on the deposition and characteristics of TiAlN-CrN and TiN-W<sub>2</sub>N superlattice thin films are already in press and component testing trials are already proving successful (8,9).

## **7.4. Conclusions.**

The following conclusions may be drawn from the research outlined in this thesis:-

- A hot isostatic pressing technique can be used to form TiZr, TiMo and ZrMo diffusion bonded segmented targets.
- Steered arc evaporation trials identified a propensity for the cathode spot to "stall" for a short period of time when traversing across an interface from a material with higher vapour pressure to lower vapour pressure, without the phenomenon occurring when traversing the junction in the reverse direction.
- Physical properties which may affect cathode spot motion across segment junctions are thought to be mis-matches in vapour pressure, electrical resistivity, thermal conductivity and work function.
- Reactive sputtering trials have identified a preferential segment poisoning mechanism on TiMo and ZrMo targets.
- All  $Ti_xZr_yN$  coatings exhibited single phase,  $\langle 111 \rangle$  orientation, compressive residual stress and lattice parameters which followed a Vegard's law relationship.
- $Ti_xZr_yN$  coatings showed significant improvements in coating hardness over binary TiN and ZrN films due to substitutional and interstitial solid solution strengthening mechanisms.
- ABS TiN, ZrN and  $Ti_xZr_yN$  coatings utilising a steered arc ion etch phase prior to reactive unbalanced magnetron sputter (UBM) deposition showed modest increases in scratch adhesion critical loads over standard UBM values and were comparable to steered arc coatings.
- ABS cyclic steered arc metal ion etching provided macro-particle incorporation within the growing films, giving increases in surface roughness ( $R_a$ ) to levels above UBM coatings but below steered arc evaporation coatings.
- ABS TiAlZrN coatings deposited with a (TiAlN- graded Zr content) base layer provided scratch adhesion critical loads above 50N on high speed steel substrates and 1-2 VDI Rockwell-C indent quality.

- Industrial scale deposition of a range of multi-layer thin films can be achieved using a combined steered arc evaporation and unbalanced magnetron sputter PVD technique without atmospheric separation or reciprocating shutter mechanisms.
- Control of the multi-layer period and hence the mechanical and physical properties can be achieved by modification of the planetary rotation velocity, the type of rotation and the deposition rate.
- The TiAlN-ZrN multi-layer system can exhibit hardness greater than  $4000H_k$ , scratch adhesion critical load values on high speed steel in excess of 50N and a highly dense, coherent and uniform lamella micro-structure.
- A coating strategy based on the reactivity of individual target materials allows a variety of third generation films to be deposited without a productivity loss in comparison to first and second generation coatings.

### **7.5. Further work.**

Examination of the results and discussion chapters has led to several areas requiring more detailed study. In addition to this several ideas are presented on research that might have been performed had this project moved in a different direction.

- (1) Elevated temperature studies on steered arc segmented targets and investigation of cathode spot motion across interfaces when subjected to localised heating of the low vapour pressure material.
- (2) Investigation of TiZrN and TiAlZrN coating performance in milling and low-moderate temperature cutting operations.
- (3) Plasma diagnostics evaluation of combined arc / magnetron deposition processing.
- (4) Studies on the mechanical and physical properties (hardness by nano-indentation etc) of multi-layer films with equal layer thicknesses. Epitaxial growth investigations by deposition on lattice matched substrates (e.g. MgO).
- (5) Multi-layer coating performance evaluation on a range of engineering components.
- (6) XTEM characterisation of multi-layer thermal stability, inter-diffusion and growth mechanisms.
- (7) Improved Monte-carlo simulation of flux density and growth rate calculations to allow layer period prediction by growth rate integration calculations.

**References.**

1. G.Ecker - "*Vacuum Arcs - Theory and Application*", 1980, Wiley Interscience Press.
2. I.I. Beilis, G.V.Levchenko, V.S.Potkin, V.I.Rakhovskii, I.N.Rykalin - *Fizika i Himia Orabotki*, 1966, 3, 19.
3. A.H.Cottrell - "*Relation of properties to microstructure*", 1954, ASM, Metals Park, Ohio, USA, pp131-162.
4. J.Vyskocil, J.Musil, S.Kadlec, W-D.Münz - *Proc.1st. Intl. Conf. Plasma Surface Engineering*, Garmisch-Partenkirchen, Germany, 1988, 661-668, DGM Informationsgesellschaft Verlag.
5. J.A.Sue, H.H.Troue - *Surf.Coat.Tech*, 1987, 33, 169-181.
6. Brite Euram Project No."CoCo" BE-4118, to be published.
7. Technical Information, Hauzer Techno Coating Europe B.V, Venlo, Netherlands.
8. T.Hurkmans, T.Trinh, D.B.Lewis, J.S.Brooks, W-D.Münz - *Proc. ICMCTF-95 Conf*, San Diego, California, USA, In Press Surf.Coat.Tech.
9. I.Smith, J.S.Brooks, W-D.Münz, S.Harvey, R.Goodwin - To be presented at *ICMCTF-96*, San Diego, USA.

## **Appendix 1. ABS coating flux density and substrate rotation model.**

### Primary assumptions.

(1) The relationship between the condensation of the vapour flux and the growth rate is given by:

$$\begin{aligned} \dot{d}_c &= j_{pf}(H-S) \frac{M_c}{\rho_c} \cos\alpha & 0^\circ < \alpha < 90^\circ \\ \dot{d}_c &= 0 & 90^\circ < \alpha < 180^\circ \end{aligned}$$

where:-

$j_{pf}$  = The film forming particle flux density.

$H, S$  = The sticking and sputtering coefficients of impinging particles respectively.

$M_c$  = The average mass of the film forming particles.

$\rho_c$  = The mass density of the condensed material.

$\alpha$  = The angle between the particle flux and the substrate normal vector.

$\dot{d}_c$  = The growth rate.

(2) The particle sources may be considered as point sources.

(3) The lateral distribution of the particle fluxes starting from the individual sources follows the equation:

$$j_v = \frac{A}{r^2} (\cos\varphi)^n$$

where:

$j_v$  = The particle vapour flux density.

$r$  = The distance between source and considered point in the vapour cloud.

$\varphi$  = The angle between the source normal and the actual direction considered.

$n$  = The lateral vapour distribution coefficient.

$A$  = Characteristic of the absolute value of the flux.

(4) No scattering or shadowing effects exist.

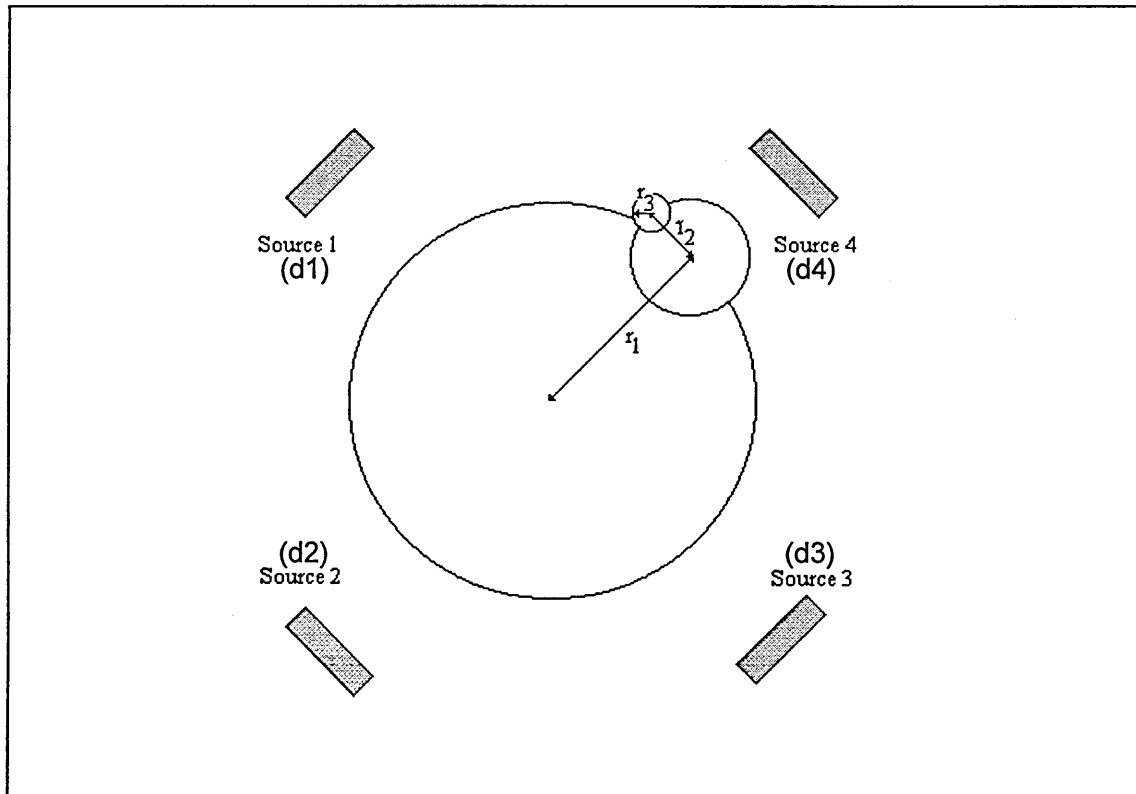
(5) The arrangement is in the x-y plane and flux extensions in the z-direction are not considered.

(6) Normalised growth rate and flux density and their time dependence can be reasonably considered.

### The calculation model.

The minimum distance between an ABS vapour source and the surface of a rotating substrate may be expressed by the equation;

$$a_{\min} = 50 - |r_1| - |r_2| - |r_3|$$



where:

50 = The distance between the centre of the chamber and the vapour source (50cm).

$r_1, r_2, r_3$  = The radii of the rotation circles defined in the 3-fold rotation system.

The positions of the sources and the substrates can be described by their cartesian co-ordinates in the form;

$$\vec{r} = \begin{pmatrix} x \\ y \\ z \end{pmatrix}$$

Hence, for a substrate with rotation in the x-y plane at  $Z_s$ :-

$$\overline{r_s(t)} = \sum_{i=1}^K r_{s_i} \begin{Bmatrix} \cos(\omega_i t + \delta_i) \\ \sin(\omega_i t + \delta_i) \\ Z_s \end{Bmatrix}$$

where,  $K$  = The number of rotations,  $r_{s_i}$  = Individual rotation radii.

$\omega_i$  = The rotation frequencies ( $\omega = 2\pi f$ ),  $\delta_i$  = Angular shift of the rotations.

Thus we can express the following individual vectors:-

For rotation 1

$$\overline{r(1)t} = r_1 \begin{Bmatrix} \cos(\omega_1 t + \delta_1) \\ \sin(\omega_1 t + \delta_1) \\ 0 \end{Bmatrix}$$

For rotation 2 (fixed to rotation 1)

$$\overline{r(2)t} = r_2 \begin{Bmatrix} \cos[(\omega_1 + \omega_2)t + \delta_2] \\ \sin[(\omega_1 + \omega_2)t + \delta_2] \\ 0 \end{Bmatrix}$$

For rotation 3 we must take account of the switching action of 3<sup>rd</sup> fold i.e. always acts at 90° to  $r_1$  in a fixed position every full rotation of  $r_2$  (- indicates rotation in opposite direction).

$$\overline{r(s)t} = r_1 \begin{Bmatrix} \cos\left[(\omega_1 t + \delta_1) - \frac{\pi}{2}\right] \\ \sin\left[(\omega_2 t + \delta_1) - \frac{\pi}{2}\right] \\ 0 \end{Bmatrix}$$

Thus the switching time can be calculated by equating  $\overline{r(2)t}$  with  $\overline{r(s)t}$ .

$$\omega_1 t + \omega_2 t + \delta_2 = \omega_1 t + \delta_1 - \frac{\pi}{2}$$

$$\omega_2 t = (\delta_1 - \delta_2) - \frac{\pi}{2}$$

hence;

$$t(\text{switching}) = \frac{(\delta_1 - \delta_2) - \frac{\pi}{2}}{\omega_2}$$

Also, the time to make one revolution of the circle described by  $r_2$  is given by:-

$$T_2 = \frac{2\pi}{\omega_2}$$

For speed of computation, only positive integral numbers of the switches made must be calculated. Thus the number of 3<sup>rd</sup> fold switches made in a given time (t) is:-

$$\text{Int}(t) = \frac{t - t(\text{switching}) - |(t - t(\text{switching}) / T_2)|}{T_2}$$

As each switch causes a 1/6<sup>th</sup> rotation in the ABS system, we may define:-

$$o(t) = \frac{2\pi}{6} \text{Int}(t)$$

Thus the third fold rotation vector can be expressed as the following:-

$$\overline{r(3)t} = r_3 \cdot \overline{ns(t)}$$

where,

$$\overline{ns(t)} = \begin{Bmatrix} \cos([( \omega_1 + \omega_2 )t - o(t)] + \delta_3) \\ \sin([( \omega_1 + \omega_2 )t - o(t)] + \delta_3) \\ 0 \end{Bmatrix}$$

Thus the 3 rotation vectors have been found and the total rotation vector may be given by:-

$$\overline{r(123)t} = \overline{r(1)t} + \overline{r(2)t} + \overline{r(3)t}$$

The vapour source normal vectors may be simply expressed as:

$$\overline{nv_1} = \begin{Bmatrix} \cos(\pi/4) \\ \sin(\pi/4) \\ 0 \end{Bmatrix} \quad \overline{nv_2} = \begin{Bmatrix} \cos(3\pi/4) \\ \sin(3\pi/4) \\ 0 \end{Bmatrix} \quad \overline{nv_3} = \begin{Bmatrix} \cos(5\pi/4) \\ \sin(5\pi/4) \\ 0 \end{Bmatrix}$$

$$\overline{nv_4} = \begin{Bmatrix} \cos(7\pi/4) \\ \sin(7\pi/4) \\ 0 \end{Bmatrix}$$

The position of a point like vapour source is given by

$$\overline{d_1} = 50\overline{nv_1}, \quad \overline{d_2} = 50\overline{nv_2}, \quad \overline{d_3} = 50\overline{nv_3}, \quad \overline{d_4} = 50\overline{nv_4}$$

Thus the distance vector between source and substrate at time (t) is;

$$\overline{a_1(t)} = \overline{d_1} - \overline{r(123)t}, \quad \overline{a_2(t)} = \overline{d_2} - \overline{r(123)t}, \quad \overline{a_3(t)} = \overline{d_3} - \overline{r(123)t}, \quad \overline{a_4(t)} = \overline{d_4} - \overline{r(123)t},$$

and the angle between the source normal and the distance vector at time (t) can be calculated using the scalar product equation:-

$$\overline{P_1} \cdot \overline{P_2} = |\overline{P_1}| \cdot |\overline{P_2}| \cos \phi$$

hence, for the case where  $\overline{a_1(t)} = \overline{P_1}$  and  $\overline{nv_1} = \overline{P_2}$  and by re-arrangement we find;

$$\phi_1(t) = \arccos \left[ \frac{1}{|\overline{a_1(t)}|} \cdot \overline{a_1(t)} \cdot \overline{nv_1} \right]$$

and similarly,  $\phi_2(t) = \arccos\left[\frac{1}{|a_2(t)|} \cdot \overline{a_2(t) \cdot nv_2}\right]$ ,  $\phi_3(t) = \arccos\left[\frac{1}{|a_3(t)|} \cdot \overline{a_3(t) \cdot nv_3}\right]$ ,

$$\phi_4(t) = \arccos\left[\frac{1}{|a_4(t)|} \cdot \overline{a_4(t) \cdot nv_4}\right]$$

From previous experiments source exponents  $n_1, n_2, n_3, n_4 \sim 2$ .

Thus, it is also possible to multiply the  $\phi(t)$  terms by a factor ( $f$ ) to take account of variable yield from each source and generate normalised flux density ( $j_v$ ) and normalised growth rate ( $d_s$ ) data as a function of angular position.

$$j_{v1}(t) = \frac{|a_{min}|^2}{|a_1(t)|} \cdot \cos(\phi_1(t))^{n_1} \cdot f_1 \quad \text{and} \quad d_{sv1}(t) = j_{v1}(t) \cdot \frac{a_1(t)}{|a_1(t)|} \cdot ns(t)$$

and similarly for 2,3&4 combined with the following ABS chamber constants:

Radii :-  $r_1 = 25\text{cm}$ ,  $r_2 = 6\text{cm}$ ,  $r_3 = 0.3\text{cm}$ .

Rotation frequencies for  $\sim 5.2$  r.p.m primary rotation velocity :-

$r_1 = 5.2\text{min}^{-1}$ ,  $r_2 = 3.6 \times 5.2\text{min}^{-1}$ ,  $r_3 = 60^\circ(\pi/3)$  per full 2nd fold revolution.

Start angles :-  $\delta_1, \delta_2, \delta_3 = \text{variable from } 0-2\pi$ .